Localization in random media and its effect on the homogenized behavior of materials

François Willot

To cite this version:

François Willot. Localization in random media and its effect on the homogenized behavior of materials. Materials. Université Paris Sorbonne, 2019. ⟨tel-02412623⟩

HAL Id: tel-02412623
https://hal.science/tel-02412623v1

Submitted on 15 Dec 2019

Mémoire d'habilitation à diriger des recherches

École Doctorale 391, Université Paris Sorbonne
Spécialité : Sciences pour l'Ingénieur
par François Willot

Localization in random media and its effect on the homogenized behavior of materials

La localisation dans les milieux aléatoires et ses effets sur la réponse homogénéisée des matériaux

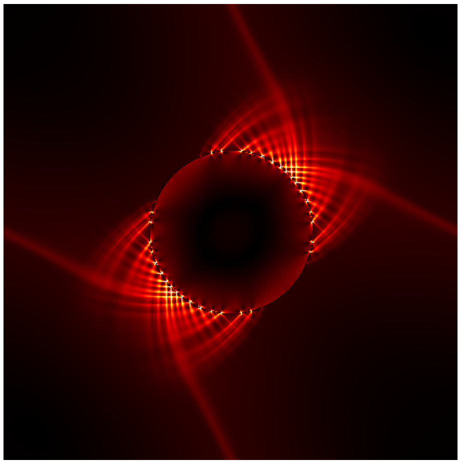

Soutenue le 8 octobre 2019 devant le jury composé de MM. :

Stéphane Berbenni	Directeur de recherche CNRS, Université de Lorraine
Sébastien Brisard	Chercheur, IFSTTAR
Djimédo Kondo	Professeur, Sorbonne Université
Renaud Masson	Directeur de Recherche, CEA Cadarache
Yann Monerie	Professeur, Université de Montpellier
Pedro Ponte Castañeda	Professeur, Université de Pennsylvanie, États-Unis
Stéphane Roux	Directeur de recherche, ENS Paris Saclay
Volker Schmidt	Professeur, Université d'Ulm, Allemagne
Pierre Suquet	Directeur de recherche CNRS émérite

Remerciements

Je remercie Sébastien Brisard, Yann Monerie et Stéphane Roux qui me font l'honneur de participer à mon jury d'HDR en tant que rapporteurs. J'ai l'honneur également de compter dans mon jury Stéphane Berbenni, Djimédo Kondo, Renaud Masson, Pierre Suquet, Volker Schmidt et Pedro Ponte Castañeda. J'ai formé un jury de chercheurs dont la créativité scientifique est pour moi un modèle et les remercie beaucoup d'avoir accepté de faire partie de mon jury. J'ai une pensée particulière pour Pedro Ponte Castañeda et Yves-Patrick Pellegrini, qui m'ont donné l'esprit de la recherche. Je souhaite également remercier chaleureusement Dominique Jeulin, avec lequel j'ai de nombreuses collaborations scientifiques et de projets communs, Fernand Meyer et Michel Bilodeau, directeurs du Centre de Morphologie Mathématique, Anne-Marie De Castro et tous les membres de l'équipe “morpho math”, et Christian Lantuéjoul. Je remercie également Samuel Forest, l'équipe “simulation” du Centre des Matériaux ainsi qu'Anthony Chesnaud et l'équipe “interfaces”, et Jérôme Crépin, directeur du centre des matériaux, Matthieu Mazières, ainsi qu'Hervé Trumel, Francis Blanc et les nombreux étudiants en thèse et en stage qui se sont associés à ces travaux.

Abstract

The present manuscript is submitted in partial fulfillment of my application to the degree of *Habilitation à diriger des recherches* at Sorbonne University. Its main contribution is a study in theoretical mechanics devoted to homogenization problems in the context of degenerate (non-strictly convex) local response of one of the phases, which can serve as idealized models for porous or rigidly-reinforced materials exhibiting perfectly-plastic behavior. In these situations plastic flow preferentially concentrates along shear bands; as a result the material effective response is governed by those regions within the material where the field localizes. A form of localization also occurs in linear problems governed by asymptotically hyperbolic partial derivative equations, where the strain field is found to develop banding patterns. The solutions are relevant to strongly-anisotropic elastic or thermoelastic media. Such a linear problem is studied in the present work in the context of a random microstructure, specifically a polycrystal containing cracks. A related topic is whether incipient localization may develop as a result of the microstructure itself. This question is investigated in the case of a Stokes flow occurring in a porous medium around a set of obstacles exhibiting unusual spatial distribution, characterized by long-range correlations. The different model problems are addressed by means of various techniques. Limit analysis bounds are combined with integral geometry to provide insight on the material behavior. Comparisons with rigorous bounds and estimates of homogenization theories, and full-field “Fourier-based” numerical results, allow us to interpret and assess the response of certain random microstructures. Although a complete solution is out-of-reach, the interplay between field localization and microstructure is elucidated in specific cases.

Contents

Chapter 1

Introduction

1.1 Research and teaching at Mines ParisTech

I would like to briefly describe here the different activities I have had as a researcher, teacher and supervisor of PhD students at Mines ParisTech and École des Mines since 2010. But before I proceed and enumerate some of my activities, it is useful to point out that the *Center for Mathematical Morphology* where I am located is a research center common to Mines ParisTech and the research association Armines. Beside academic research, the purpose of the Armines and Mines ParisTech centers is the development of applied research and its transfer to industry. This transfer occurs thanks to collaborative projects, grants from French or European agencies, "direct contracts" with industry and partnership through chairs and collaborative projects. The same philosophy holds at the Center of Materials, which is a center common to CNRS, Mines and Armines, and in which I also work as a research associate, on a weekly basis.

After my PhD thesis at the Commissariat à l'Énergie atomique, in the *Département de Physique Théorique et Appliqué* and the *Laboratoire de Mécanique des Solides* of École Polytechnique, and after a subsequent post-doctoral position at University of Pennsylvania, I have, as soon as I became a tenure track at Mines ParisTech, contributed to and directly managed several national and international research projects. Some of the projects I contributed to are listed in Appendix (B). The project topics are quite diverse, ranging from the modeling of optical properties for paint layers in automotive industry (LIMA ANR project), microstructure modeling and optimization for the development of low-temperature fuel cells (EVOLVE European project), the study and modeling of damage in TATB polycrystals (CEA Le Ripault), microstructure optimization of the viscoelastic properties of tires (Yokohama Rubber Cie), the modeling of cosmetics at the microscopic scale (L'Oréal), transport properties of mesoporous alumina (IFPEN), the conducting properties of cold-spray materials (US Air Force grant), the mechanical properties of concrete (EDF MAI grant), the prediction of piezoelectricity in woven (FUI), classification of defects in wielding (CEA Valduc) to the study of damage in reservoirs (ministry grant). Although many of these projects are actually collaborations with colleagues scientists, I have taken an active part in obtaining grants so that the research may be carried out.

Obviously, my role and activities have evolved with time, but a key aspect consists in keeping a good equilibrium between academic and applied research. On the one hand, state-of-the-art academic research is required for applied research to be useful to industry. On the other hand, many examples show that industrial problems are at the origin of breakthrough in mathematical morphology and in the wide domain of material and engineering science. An example of industrial problems which have motivated new theoretical developments are the modeling of anode layers and other components of fuel cells. The later have led to the developments of new methodologies for simulating n-phase random sets [3], image analysis tools specific to FIB-SEM and interesting optimization problems [150]. Today, these developments continue [43] and have led to a fruitful international collaboration [179, 180].

The main topics of my research activities cover the development of spectral, Fourier-based numerical methods in homogenization [14, 249, 254, 78] and the modeling of heterogeneous microstructures (see e.g. [76, 1, 240]). A summary of my recent activities in this domain is provided in Appendix (A).

Another aspect of my work as a research scientist is teaching. I organize a one-week course at École des Mines devoted to random sets microstructure modeling and homogenization. The course includes theoretical lectures as well as training sessions carried out with the Fourier code I develop for homogenization. The courses I give take the point of view of numerical analysis (PDEs, convex analysis, optimization etc.) rather than that of algebra. The same philosophy is followed in the one-week course I contribute to, which is part of the course “Ingénierie Digitale des Systèmes Complexes”[1] in Mines ParisTech, organized by D. Ryckelynck and É. Hachem. The one-week course, organized together with H. Proudhon and B. Figliuzzi, aims at predicting and simulating the properties of materials based on images (microtomography etc.).

I wish to pursue my teaching activities and if possible, enlarge them. I would also like to not only teach, but *organize* courses, and invite scientists to deliver top-level lectures in topics that are rarely taught. One example is the course on nonlinear homogenization in the Athens week “Physics and Mechanics of Random Media”[2] that PhD students as well as students from the international “Athens” University network attend. In that respect, I have been pleased to organize (with the invaluable help of Samuel Forest) the international workshop in honor of Dominique Jeulin “Physics and mechanics of random structures: from morphology to material properties”[3] which was held in the Peninsula of Oléron in 2018. A book was published at the occasion [257] at Presses de l’École des Mines as well as a special topic in *Image Analysis & Stereology* [218] and a special issue of the *International Journal of Solids and Structures*[4] (Elsevier).

To guarantee a global coherence in this HDR thesis manuscript, I have decided to focus on the homogenization of the mechanical response and transport properties of heterogeneous media, in the context of field localization. As a result of this choice, part of my research work, some of which is briefly summarized in Appendix (A) has been left out. Nevertheless, the present HDR study includes developments in integral geometry, which, while they are relevant to the homogenization problems at stake, are also of interest, I believe, to microstructure simulations and probabilistic models.

This HDR manuscript therefore does not constitute a program of the research activities I would like to pursue in the future. In particular, I am presently working on the implementation of Stokes flow solvers in Fourier-based methods, and, thanks to the ongoing PhD thesis of F. Rabette, on a FFT implementation [197] of phase-field methods for the initiation and propagation of cracks in

---

[1] `http://mms2.ensmp.fr/option_IDSysCo/accueil_option.php`

[2] `http://www.cmm.mines-paristech.fr/ESPRM/`

[3] `http://www.cmm.mines-paristech.fr/~willot/PMRM/`

[4] `https://www.sciencedirect.com/journal/international-journal-of-solids-and-structures/special-issue/103QGG5T8J0`

quasi-brittle materials, based on the variational theory of Francfort and Marigot [80] and by the works of Bourdin et al. [33] and Miehe et al. [164]. The PhD thesis of É. Kaeshammer, focusing on wave propagation in energetic materials is another important domain of research [122] that I would definitely like to pursue. I hope to be able to develop these topics of research in the future and have new interesting collaborations with other researchers.

The following section gives a short introduction to the main topic of this HDR thesis.

1.2 An investigation of localization in random media

A broad range of physical phenomena in material science involve the emergence of surfaces or paths of minimal energy. Examples include domain walls in random Ising systems [108], current localization in varistors (or non-Newtonian fluid flow) [66], the onset of voltage in polycrystals [102], or ductile fracture [58, 32]. Some of these problems have been addressed using idealized random network models (see [66, 70] and references therein). In nonlinear networks relevant to varistors and superconductors, localized flow paths emerge at special points, which act as thresholds for the network's macroscopic response [66]. As noted by Duxbury et al. [70], these paths are the solutions of the “shortest-path” and “minimum-cut” problems. The equivalence between a network's effective response and an optimization problem on graphs is demonstrated by the min-cut/max-flow theorem [73]. Interestingly, the optimal surfaces exhibit, in the presence of disorder, rich self-affine structures, characterized, notably, by non-standard scaling laws [34, 5]. In the continuum, the maximal flow of a vector field through a domain is likewise related to a minimal cut problem [227].

In a numerical and theoretical study of an “analog electric network” that mimic perfect-plasticity, Roux and Hansen [206] have used the connection between minimal surface problems and effective yield stress. In the continuum, limit analysis results obtained by Drucker [68] in a periodic problem in plane strain highlight a similar non-analytic dependence. Drucker's bounds demonstrate that the leading-order term to the effective flow stress y_0 of a periodic arrangement of pores of volume fraction f scales as $\sim f^{1/2}$ in the limit of vanishingly small porosity f:

$$y_0 = y\left[1 - af^{1/2} + o(f^{1/2})\right], \qquad f \to 0, \tag{1.1}$$

with prefactor a depending on the geometry of the inclusions. This results holds for a rigid, perfectly-plastic matrix. The infinite slope of the flow stress ($\partial y_0/\partial f = \infty$) when $f = 0$ underlines the strong effect of the voids in this limit. The trial displacement fields used to derive the upper-bound are piecewise-constant and present surface discontinuities in the matrix [79]. *Optimal* upper-bounds are thus attained by *minimal* surfaces. In antiplane strain, these surfaces reduce to minimal paths, or in geometrical terms, geodesics. The paths are minimal in the sense that they have smallest cut in the matrix and span the array of pores in a direction that depends on the applied macroscopic loading. Examples relevant to a 2D square array of pores with prescribed “simple” and “pure shear” (45°-rotated) strain loadings are given in [112]. The strain field in porous materials tends to localize in bands seeking to pass through the pores in order to minimize the plastic dissipation (see example Fig. 1.1). In this case, the interaction between the pores is obviously quite strong and dependent on the geometry of the configuration as well as the relative orientation of the loading. As a consequence of the strong interaction between shear bands and pores, a slight increase of the porosity leads, in specific configurations, to a sudden rearrangement of the shear bands, as demonstrated by limit analysis and Fourier computations [112]. Consequently, the

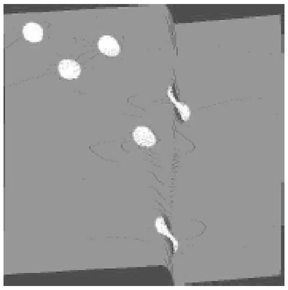

Figure 1.1: A shear band going through two pores in plane strain. Perfectly-plastic medium. Numerical computation.

response of the material is essentially driven by the geometry rather than details of the material law. In the rigid case, in periodic structures, the shear bands may avoid inclusions entirely while spanning the medium, highlighting a much lower influence of the rigid reinforcement.

Despite the aforementioned works, the role of a random distribution of heterogeneities (typically pores) on the effective behavior of perfectly-plastic media, is not completely elucidated. Theoretical results suggest that the effective yield stress of 2D random porous media also exhibits power-laws with non-integer exponents, in the dilute porosity limit $f \to 0$. Different exponents however have been proposed, depending on the problem at hand. In a square lattice model made of broken bonds in proportion f, optimal surfaces are obtained by minimizing the sum of the capacity (analog to the yield stress) taken over each bond that crosses the surface. Thus, it is in principle possible to infer the behavior of the effective response of heterogeneous materials by solving minimal paths problems. In a two-phase resistor lattice with a dilute proportion of “broken” (insulating) bonds, the effective response exhibits interesting non-analytic behavior. The exponent characterizing the leading-order term correction in the dilute limit $f \to 0$ is found to be 1 for minimal paths oriented along the directions of the lattice, and 1/2 along the diagonal [205]. Dilute limit singularities, of a different type, have been reported in the dielectric breakdown of square and cubic networks [71] and in the continuum [72]. More recently, the non-analytical behavior of the effective response characterizing nonlinear ionic transport has been discussed by Sillamoni and Idiart [225]. The authors obtain an exponent 2/3 as the result of their application of the nonlinear homogenization theory of P. Ponte Castañeda [190].

The “second-order” nonlinear homogenization theory, which provides analytical estimates based on variational principles, indeed predicts a fractional exponent 2/3 in the dilute limit $f \to 0$, in the plane strain [191] and anti-plane [83] problems. The result has been confirmed in plane strain by numerical Fourier computations on a pixel-based porous material [258, 248]. As pointed out in [225], this suggests a lower influence of the pores in a random configuration rather than in the periodic problem. Nevertheless, the exact role of the pores in a random medium and the onset of a non-analytical powerlaw has not been elucidated. The studies developed in the following chapters, devoted to various problems relevant to minimal paths and random structures, give partial answers, in the porous and rigid problems.

It is interesting to note that the second-order nonlinear homogenization theory is based on a linear comparison composite material and underlying linear homogenization theory. In the perfectly-plastic limit, the linear comparison composite makes use of phases that are in general anisotropic [112]. Nonlinearity is therefore approached by a locally (elastic or thermoelastic) anisotropic matrix phase. In effect, in the limit of certain "infinitely-anisotropic" constitutive laws (where the local potential looses strict convexity), the strain field organizes through banding patterns [260], which are of a different nature than plastic shear bands, but are nevertheless useful to study localization phenomena. This approach is followed in [259] in the case of a periodic arrangements of voids, and is pursued in the case of a random material in Chap. (2). The chapter is complemented by a study of elastic field distributions in random media (Chap. 3), which although not directly related to localization, is included because of the possible perspectives of this work. The two chapters, which form the first part of this manuscript is thus concerned by a linear behavior. The second part is devoted to nonlinear media for mechanical and transport properties, and the third part is devoted to Stokes flow.

1.3 Outline of the present dissertation

Some of the studies presented in this HDR thesis are reworked versions of previously-published journal articles. Chap. (2), based on reference [261], deals with self-consistent estimates for polycrystals containing cracks. It incorporates a figure and results taken from [259], with additional discussion. The study of elastic field distributions (Chap. 3) is part of a manuscript accepted for publication [256]. Chap. (4), a study of the length of geodesics in Boolean and Cox-Boolean models, is a part of ref. [250]. The link between minimal paths and effective yield stress is examined in Chap. (5), which is part of a recently accepted manuscript [252]. The effective yield stress occurring in multiscale random sets is the subject of Chap. (6). Bounds related to strongly-nonlinear media with periodic microstructures are presented in Chap. (7). These two chapters have not been published. Chap. (8) is concerned with the scaling properties of the covariance function, integral range and variance properties of a Boolean set of particles with high aspect ratio, namely oblate and prolate cylinders. This work, slightly amended in the present manuscript, is published in ref. [251]. Chap. (9) investigates the effective permeability of the corresponding porous media, making use of analytical upper-bounds. This last work has been published as a part of ref. [253], but also incorporates an additional section (9.3.3) which is new.

Part I

Strongly anisotropic, linear-elastic and thermoelastic media

Chapter 2

Self-consistent estimates for cracked polycrystals

This chapter is devoted to the influence of a population of randomly-oriented cracks on the macroscopic thermal and linear-elastic response of a polycrystal. Emphasis is put on crystals exhibiting hexagonal symmetry with strong anisotropy. The problem is addressed using a self-consistent method. Coupling between micro-cracks and crystal anisotropy is taken into account through an effective medium where all inhomogeneities are embedded. In the absence of cracks, the self-consistent estimates reduce to that of Berryman (2005), whereas the method is new in the case of a homogeneous cracked body. The accuracy of the present method is first assessed using numerical, Fourier-based computations. In the absence of crystal anisotropy, the estimates for the effective elastic properties are close to that obtained numerically for a homogeneous body containing a Boolean model of disk-shaped cracks. In the case, of homogeneous cracked bodies, the method is also compared to various other analytical estimates and bounds. The prediction of the self-consistent estimates are then investigated in the case of a strongly-anisotropic polycrystal in which the in-plane shear modulus of the crystal is much smaller than the elastic moduli related to other deformation modes. The cracks-density percolation threshold is found to diminish abruptly in this limit. This "advanced" percolation threshold is concomitant to the onset of large, weakly-loaded regions surrounding cracks.

2.1 Introduction

The present work focuses on a model problem of a polycrystal, involving open micro-cracks in a macroscopically isotropic material in its initial *and damaged* states as well, in a locally linear, thermoelastic framework. Initially isotropic materials should remain so if micro-cracking results from the application of a non-directional load, in particular by heating or cooling slowly enough for the temperature field to remain uniform. Such a situation may be encountered in materials made of strongly thermally and elastically anisotropic crystals, such as polycrystalline graphite [178, 60], or the energetic material 1,3,5-triamino-2,4,6-trinitrobenzene (TATB) [125, 8].

In the general case, elastic softening in quasi-brittle materials is accompanied by induced anisotropy, known to reflect the non-uniform distribution of micro-cracks orientations, itself the result of either the strong initial heterogeneity and anisotropy of the material or the directionality of the load. Modeling this softening effect is not straightforward, and has generated a large amount of work, either by phenomenological means (see in particular the brief review of Cormey and Welemane [52] or more recently [15, 53, 47]) or via micromechanical modeling (see [42, 105, 10, 130, 121], and the more recent studies [186, 67, 267, 173, 141] among many others). Most of these works have considered the damaged material as a homogeneous matrix containing a distribution of micro-cracks. However, real materials are not homogeneous in their initial state, and this assumption may be seen as being too restrictive, as noted for example by Ortiz [182], Pijaudier-Cabot and Bazant [188], or Challamel [47]. The problem however is potentially very complex, as it may involve open and closed cracks, strongly nonlinear unilateral effects, closed crack kinking, and friction. Therefore, the focus in this chapter will be restricted to isotropic polycrystals containing a population of open micro-cracks with isotropic distribution in space.

The following work is restricted to crystals with hexagonal symmetry (transverse isotropy). This choice is motivated by applications to polycrystalline graphite or TATB, and because hexagonal symmetry is amenable to a relatively simple analytical treatment. A previous attempt was made by Huang and Hu [107], aiming at predicting the elastic behavior of micro-cracked polycrystals, in the case of crystals of cubic symmetry.

The model derived in this chapter uses the self-consistent approach. Exact expressions for the Hill tensor (or equivalently Eshelby's tensor) have been derived for cracks embedded in a transversely-isotropic [136] or orthotropic case [98], for particular crack shape and orientations. Closed-form explicit solutions of Eshelby's problem for an ellipsoidal crack in a medium with arbitrary anisotropy are not available, although some analytical results are available in two dimensions [151]. Therefore we consider the grains, of any crystallographic orientation, and the randomly-oriented cracks as separate phases embedded in the homogeneous effective medium. Under this assumption, we do not take into account the exact interaction between an oriented crack and the crystallographic orientation of the surrounding medium.

The obtained formulation is first discussed in terms of its percolating behavior, and compared to previous models of microcracked materials. Quantitative model predictions are then confronted to numerical ones obtained by Fourier-based simulations, first on a homogeneous matrix in which (isotropic) populations of micro-cracks of various crack densities are embedded, then on polycrystalline microstructures representative of a TATB-based material, in which the same populations of micro-cracks as before are embedded. The confrontation uses the Bristow-Budiansky-O'Connell [41, 42] definition of micro-crack density, widely accepted to be a good quantifier (see for example [53]), up to relatively large crack densities (up to around 0.7) representing several thousands of micro-cracks at most.

2.2 Thermoelasticity problem for cracked polycrystals

Consider a polycrystal in a domain Ω of volume V, containing a population of frictionless cracks along a set of surfaces Γ and subjected to mechanical and thermal loading. In the rest of this chapter, it is assumed that the applied load results in the opening of all micro-cracks, so that:

$$\boldsymbol{\sigma}(\boldsymbol{x}) \cdot \boldsymbol{n} = 0, \qquad \boldsymbol{x} \in \Gamma \tag{2.1}$$

where $\boldsymbol{n}$ is the normal at point $\boldsymbol{x}$ along Γ (oriented indifferently) and $\boldsymbol{\sigma}$ is the stress tensor. Outside of the cracks, the strain field $\boldsymbol{\varepsilon}$ is determined as a function of the stress by the linear thermoelastic law:

$$\boldsymbol{\varepsilon}(\boldsymbol{x}) = \mathbf{S}(\boldsymbol{x}) : \boldsymbol{\sigma}(\boldsymbol{x}) + \boldsymbol{\alpha}(\boldsymbol{x})\Delta T, \qquad \boldsymbol{\sigma}(\boldsymbol{x}) = \mathbf{C}(\boldsymbol{x}) : [\boldsymbol{\varepsilon}(\boldsymbol{x}) - \boldsymbol{\alpha}(\boldsymbol{x})\Delta T], \qquad \boldsymbol{x} \in \Omega\backslash\Gamma, \tag{2.2}$$

where $\Delta T = T - T_0$ is the difference of temperature with respect to a reference temperature T_0. The permanent regime is attained at all time during cooling or heating, so that ΔT is homogeneous in Ω and represents a macroscopic thermal loading. Small deformation $\varepsilon_{ij} = (1/2)(\partial_i u_j + \partial_j u_i)$, with $\boldsymbol{u}$ the displacement vector, and quasi-static equilibrium, i.e. $\mathrm{div}\boldsymbol{\sigma} \equiv 0$ is assumed for all thermo-mechanical loadings. Hereafter, the compliance $\mathbf{S}$ and stiffness tensor $\mathbf{C} = \mathbf{S}^{-1}$ of the crystal in (2.2) have hexagonal (i.e. transversely-isotropic) symmetry. Equation (2.2) is rewritten as:

$$(\varepsilon_{11}, \varepsilon_{22}, \varepsilon_{33}, 2\varepsilon_{23}, 2\varepsilon_{13}, 2\varepsilon_{12})^{\mathrm{t}} = \mathbf{S} \cdot (\sigma_{11}, \sigma_{22}, \sigma_{33}, \sigma_{23}, \sigma_{13}, \sigma_{12})^{\mathrm{t}} + \boldsymbol{\alpha}^{\mathrm{t}}\Delta T, \tag{2.3}$$

where $\mathbf{S}$ is expressed, in the above Voigt notation, as the following 6×6 symmetric matrix:

$$\mathbf{S} = \begin{pmatrix} 1/E_p & -\nu_p/E_p & -\nu_{pz}/E_p & 0 & 0 & 0 \\ & 1/E_p & -\nu_{pz}/E_p & 0 & 0 & 0 \\ & & 1/E_z & 0 & 0 & 0 \\ & & & 1/G_{zp} & 0 & 0 \\ & \text{sym} & & & 1/G_{zp} & 0 \\ & & & & & 2(1+\nu_p)/E_p \end{pmatrix}, \tag{2.4}$$

in an orthonormal basis (e_1, e_2, e_3) local to each grain where e_3 coincides with the crystal's axis of symmetry. The compliance tensor $\mathbf{S}$ depends on five elastic moduli: the in-plane (E_p) and out-of-plane (E_z) Young moduli, the out-of-plane shear modulus G_{zp}, the in-plane (ν_p) and out-of-plane (ν_{pz}) Poisson ratios. In contrast to isotropic elasticity, Poisson effects depend on the loading direction, hence, the coefficients ν_p and ν_{pz} can exceed 1/2. They vary in the range:

$$-1 \leqslant \nu_p \leqslant 1 - 2\nu_{pz}^2 \frac{E_z}{E_p} \leqslant 1, \qquad |\nu_{pz}| \leqslant \sqrt{\frac{(1-\nu_p)E_p}{2E_z}} \leqslant \sqrt{\frac{E_p}{E_z}}. \tag{2.5}$$

With the condition $E_z \geqslant 0$, $E_p \geqslant 0$, $G_{zp} \geqslant 0$, the above guarantees that $\mathbf{S}$ (or $\mathbf{C}$) is positive semi-definite. The two Young moduli E_z and E_p vary in the range:

$$\frac{2\nu_{zp}^2}{1-\nu_p} E_p \leqslant E_z \leqslant \frac{1-\nu_p}{2\nu_{pz}^2} E_p, \qquad \frac{2\nu_{pz}^2}{1-\nu_p} E_z \leqslant E_p \leqslant E_z \frac{1-\nu_p}{2\nu_{zp}^2}, \tag{2.6}$$

where we have introduced $\nu_{zp} = \nu_{pz} E_z/E_p$, inequalities (2.5) and (2.6) being equivalent. When needed, we refer to the following Voigt notation for stiffness tensors, equivalent to (2.3):

$$(\sigma_{11}, \sigma_{22}, \sigma_{33}, \sigma_{23}, \sigma_{13}, \sigma_{12})^{\mathrm{t}} = \mathbf{C} \cdot \left[(\varepsilon_{11}, \varepsilon_{22}, \varepsilon_{33}, 2\varepsilon_{23}, 2\varepsilon_{13}, 2\varepsilon_{12})^{\mathrm{t}} - \boldsymbol{\alpha}^{\mathrm{t}}\Delta T\right], \tag{2.7}$$

where $\mathbf{C}$ is represented by the 6×6 matrix inverse of (2.4).

In the crystal, we assume that a purely-thermal loading induces transversely-isotropic dilation or contraction with the same axis of symmetry as that of $\mathbf{S}$. In the same basis used in (2.4), where

e_3 is the axis of symmetry of the crystal lattice, the thermal expansion tensor entering (2.3) reads, in vector notation:

$$\boldsymbol{\alpha}(\boldsymbol{x}) = (\alpha_{11}, \alpha_{11}, \alpha_{33}, 0, 0, 0)^{\mathrm{t}}, \tag{2.8}$$

i.e. $\alpha_{11} = \alpha_{22}$ and $\alpha_{12} = \alpha_{13} = \alpha_{23} = 0$.

The polycrystal is a space-tessellation of Ω, in which all grains are made from the same, randomly-oriented crystal. In an orthornormal basis (x_I) attached to the laboratory:

$$S_{IJ,KL}(\boldsymbol{x}) = R_{iI}(\boldsymbol{x})R_{jJ}(\boldsymbol{x})R_{kK}(\boldsymbol{x})R_{lL}(\boldsymbol{x})S_{ij,kl}, \quad \alpha_{IJ}(\boldsymbol{x}) = R_{iI}(\boldsymbol{x})R_{jJ}(\boldsymbol{x})\alpha_{ij}, \quad \boldsymbol{x} \in \Omega\backslash\Gamma, \tag{2.9}$$

where $\mathbf{R}(\boldsymbol{x})$ are constant-per-grain rotation matrix and where $S_{ij,kl}$ and α_{ij} are given by (2.3), (2.4) and (2.8).

The effective thermoelastic response of the polycrystal reads:

$$\overline{\boldsymbol{\sigma}} = \langle \boldsymbol{\sigma}(\boldsymbol{x}) \rangle = \widetilde{\mathbf{C}} : (\overline{\boldsymbol{\varepsilon}} - \widetilde{\boldsymbol{\alpha}} \Delta T), \tag{2.10}$$

where $\overline{\boldsymbol{\varepsilon}} = \langle \boldsymbol{\varepsilon}(\boldsymbol{x}) \rangle$ and $\overline{\boldsymbol{\sigma}}$ are the macroscopic strain and stress fields, computed by averaging the fields $\boldsymbol{\varepsilon}(\boldsymbol{x})$ and $\boldsymbol{\sigma}(\boldsymbol{x})$ over the domain Ω. In the following, the rotation matrix $\mathbf{R}$ and cracks's orientations are uniformly-distributed random variables in the space of 3D matrix rotations and in the sphere, respectively, and the polycrystal is statistically isotropic. In particular, the orientations of two different crystals are uncorrelated.

The effective stiffness tensor $\widetilde{\mathbf{C}}$ reduces to its bulk modulus $\widetilde{K}$ and shear modulus $\widetilde{G}$ or equivalently, its Young modulus $\widetilde{E}$ and Poisson ratio $\widetilde{\nu}$, and the effective thermal expansion tensor is diagonal with the unique eigenvalue $\widetilde{\alpha}_{11}$. The macroscopic volumetric expansion is $\widetilde{\alpha}_V = \mathrm{tr}(\widetilde{\boldsymbol{\alpha}}) = 3\widetilde{\alpha}_{11}$.

In the analytical treatment that follows, we use Eshelby-type solutions for the cracks, in a manner that model them as infinitesimally thin ellispoidal voids. Under this hypothesis, the strain field in the cracks is singular and each crack contributes to the spatial mean $\langle \boldsymbol{\varepsilon}(\boldsymbol{x}) \rangle$ by (see e.g. [121]):

$$\frac{1}{V} \int_{\Gamma_i} \mathrm{d}S \, \frac{\boldsymbol{b} \cdot \boldsymbol{n} + \boldsymbol{n} \cdot \boldsymbol{b}}{2}, \tag{2.11}$$

where V is the volume of Ω, Γ_i the surface along crack i, dS an elementary surface along Γ_i and $\boldsymbol{b}$ is the displacement jump at each point of Γ_i. In the above, denoting $\boldsymbol{u}^{\pm}(\boldsymbol{x})$ the displacement vector field on each side of the lips of the cracks, $\boldsymbol{b} = \boldsymbol{u}^{+} - \boldsymbol{u}^{-}$ where $\boldsymbol{n}$ is oriented positively from the $-$ to the $+$ side.

In a homogeneous body containing cracks, the effective elastic moduli depend on a non-dimensional cracks-density parameter η. This parameter arises naturally from Eshelby's single-inclusion problem in the "dilute limit" where cracks interaction are neglected [41] and has been subsequently used in most self-consistent schemes, e.g. [42]. When the cracks embedded in the polycrystal are equisized disks of radius a, the cracks-density parameter reads:

$$\eta = \frac{n_0 a^3}{V}, \tag{2.12}$$

where n_0 is the number of cracks in Ω and n_0/V the number of cracks per unit volume. The cracks's locations are arbitrary, in particular, cracks may interpenetrate with one another. In the rest of this work, we assume that the spatial distribution of cracks in the polycrystal and their morphology can be described by the cracks-density parameter $0 \leqslant \eta \leqslant \infty$.

2.3 Self-consistent estimate for cracked polycrystals

We now derive estimates for the homogenized thermoelastic response of a cracked polycrystal using classical self-consistent assumptions. Elastic moduli are first considered. Our method is based on Eshelby's problem for: (i) an isolated penny-shaped crack in an isotropic medium and (ii) a spherical grain with transversely-isotropic elastic response embedded in an isotropic medium. Assume for now that the grains and cracks are isolated from one another and that they are embedded in a homogeneous isotropic body of compliance tensor $\mathbf{S}^0$, subjected to an applied stress $\overline{\boldsymbol{\sigma}}$. The contributions of the cracks and grains to the material's macroscopic strain $\overline{\boldsymbol{\varepsilon}}$ are summed up as:

$$\overline{\boldsymbol{\varepsilon}} = \widetilde{\mathbf{S}} : \overline{\boldsymbol{\sigma}} = \mathbf{S}^0 : \overline{\boldsymbol{\sigma}} + f\langle \mathbf{H}(\mathbf{S};\mathbf{S}^0) : \overline{\boldsymbol{\sigma}}\rangle_{\mathcal{C}} + \eta\langle \mathbf{G}(\mathbf{S}^0) : \overline{\boldsymbol{\sigma}}\rangle_{\mathcal{O}}, \tag{2.13}$$

where the second-term on the r.h.s. represents the strain change due to the presence of grains, of volume fraction $0 \leqslant f \leqslant 1$, and the third-term on the r.h.s. the strain change due to the cracks. The contributions of individual grains (tensor $\mathbf{H}$) are averaged over all crystallographic orientations $\mathcal{C}$. Likewise, the contributions of the cracks (tensor $\mathbf{G}$) are averaged over all cracks orientations $\mathcal{O}$. The transversely-isotropic tensors $\mathbf{H}$ and $\mathbf{G}$ are obtained in terms of Eshelby's or Hill's tensor [103] for their respective problem. Tensor $\mathbf{H}$ reads (see e.g. [222]):

$$\mathbf{H}(\mathbf{S};\mathbf{S}^0) = \Big[\big(\mathbf{S} - \mathbf{S}^0\big)^{-1} + \mathbf{Q}(\mathbf{S}^0)\Big]^{-1}, \tag{2.14}$$

in which $\mathbf{Q}$ is the isotropic stiffness tensor defined by [176, Chap. 2]:

$$Q_{11} = Q_{22} = Q_{33} = \frac{16}{15}\frac{G^0}{1-\nu^0}, \qquad Q_{12} = Q_{23} = Q_{13} = \frac{2G^0}{15}\frac{1+5\nu^0}{1-\nu^0}, \tag{2.15}$$

where we refer to the Voigt notation (2.7). Other components are obtained from the above, e.g. $Q_{44} = Q_{55} = Q_{66} = (Q_{11} - Q_{12})/2$. The variables G^0 refer to the shear modulus associated to $\mathbf{S}^0$ and ν^0 to its Poisson ratio, i.e. $G^0 = 1/S^0_{44}$ and $\nu^0 = S^0_{44}/(2S^0_{11}) - 1$. An equivalent form is given in [142] for the reciprocal tensor:

$$\mathbf{P} = \mathbf{S}^0(\mathbf{I} - \mathbf{Q}\mathbf{S}^0), \tag{2.16}$$

whereas a more general expression for $\mathbf{Q}$ is given in [220] for an ellipsoidal inclusion with revolution symmetry.

Tensor $\mathbf{G}$ entering (2.13) is given in closed-form expression as [176, Chap. 5]:

$$G_{33} = \frac{8(1-\nu^0)}{3G^0}, \quad G_{44} = G_{55} = \frac{16(1-\nu^0)}{3G^0(2-\nu^0)}, \quad G_{11} = G_{22} = G_{12} = G_{13} = G_{66} = 0, \tag{2.17}$$

in the Voigt notation (2.3) where e_3 is normal to the crack.

Assume now that the embedding medium with compliance $\mathbf{S}^0$ has the same elastic response as the heterogeneous medium, so that $\mathbf{S}^0 = \widetilde{\mathbf{S}}$. Accordingly, when the material is subjected to the macroscopic stress $\overline{\boldsymbol{\sigma}}$, the deformation induced by the cracks compensates that of the grains:

$$\langle \mathbf{H}(\mathbf{S};\widetilde{\mathbf{S}})\rangle_{\mathcal{C}} + \eta\langle \mathbf{G}(\widetilde{\mathbf{S}})\rangle_{\mathcal{O}} = \mathbf{0}, \tag{2.18}$$

where we took $f = 1$, so that the grains cover the entire domain and the cracks have no volume. The assumption $\mathbf{S}^0 = \widetilde{\mathbf{S}}$ can be thought of as the construction of a hierarchical material with infinitely many scales, in the following way. Consider a material made of a homogeneous matrix containing widely-separated grains and cracks. Replace the embedding matrix by a set of grains and cracks at a much smaller length-scale, and repeat this operation until the matrix is entirely covered by grains and cracks. Now, in a polycrystal where cracks and grains have the same typical size, one may assume that each crack or grain is surrounded by many different, randomly-oriented cracks and grains. The approximation $\mathbf{S}^0 \approx \widetilde{\mathbf{S}}$ amounts to replace the surrounding medium around each inhomogeneity by a homogeneous effective material.

Rewrite now Equation (2.18) using (2.14), (2.15) and (2.17). We refer to [220] for amenable formula for the product and inverse of transversely-isotropic tensors. The means $\langle \mathbf{A} \rangle_{\mathcal{C},\mathcal{O}}$ of a transversely-isotropic stiffness tensor $\mathbf{A}$ with axis of symmetry parallel to e_3 is the isotropic tensor with bulk and shear moduli [142]:

$$K_A = \frac{2(A_{11}+A_{12}+2A_{13})+A_{33}}{9}, \quad G_A = \frac{3(2A_{44}+A_{66})+2(A_{11}-A_{13})+A_{33}-A_{12}}{15}, \tag{2.19}$$

respectively, where the A_{ij} refer to the Voigt notation (2.3). Denoting K_T and G_T the bulk and shear moduli associated to the compliance tensor of the l.h.s. of (2.18):

$$\mathbf{T} = \langle \mathbf{H}(\mathbf{S};\widetilde{\mathbf{S}}) \rangle_{\mathcal{C}} + \eta \langle \mathbf{G}(\widetilde{\mathbf{S}}) \rangle_{\mathcal{O}}, \tag{2.20}$$

one obtains the expressions below for the inverse moduli:

$$K_T^{-1} = \frac{2u_2+u_1-4u_3}{u_1u_2-2u_3^2} + \frac{8\eta(1-\widetilde{\nu})}{3\widetilde{G}}, \qquad \widetilde{\nu} = \frac{3\widetilde{K}-2\widetilde{G}}{2(3\widetilde{K}+\widetilde{G})}, \tag{2.21a}$$

$$G_T^{-1} = \frac{2u_2+4(u_1+2u_3)}{15(u_1u_2-2u_3^2)} + \frac{6}{15u_4} + \frac{6}{15u_5} + \frac{32\eta(5-6\widetilde{\nu}+\widetilde{\nu}^2)}{45\widetilde{G}(2-\widetilde{\nu})}, \tag{2.21b}$$

where $\widetilde{\nu}$ is the effective Poisson ratio and the u_i are a set of five independent components of the tensor $\mathbf{U} = \mathbf{H}^{-1}$ as follows:

$$u_1 = U_{1111}+U_{1122} = \left[18\widetilde{K}\widetilde{G} - 2(\widetilde{G}+3\widetilde{K})E_z\right]\frac{E_pE_z}{\Delta_u} + \frac{2\widetilde{G}(9+5\widetilde{\nu})}{15(1-\widetilde{\nu})}, \tag{2.22a}$$

$$u_2 = U_{3333} = \left[18\widetilde{K}\widetilde{G}(1-\nu_p) - (4\widetilde{G}+3\widetilde{K})E_p\right]\frac{E_z^2}{\Delta_u} + \frac{16\widetilde{G}}{15(1-\widetilde{\nu})}, \tag{2.22b}$$

$$u_3 = U_{1133} = \left[18\widetilde{K}\widetilde{G}\nu_{zp} + (2\widetilde{G}-3\widetilde{K})E_z\right]\frac{E_pE_z}{\Delta_u} + \frac{2\widetilde{G}(1+5\widetilde{\nu})}{15(1-\widetilde{\nu})}, \tag{2.22c}$$

$$u_4 = U_{1212} = \frac{\widetilde{G}E_p}{2\widetilde{G}(1+\nu_p)-E_p} + \frac{\widetilde{G}(7-5\widetilde{\nu})}{15(1-\widetilde{\nu})}, \tag{2.22d}$$

$$u_5 = U_{1313} = \frac{\widetilde{G}G_{zp}}{\widetilde{G}-G_{zp}} + \frac{\widetilde{G}(7-5\widetilde{\nu})}{15(1-\widetilde{\nu})}, \tag{2.22e}$$

$$\begin{aligned}\Delta_u = {} & [2(\nu_p-1)E_z + (8\nu_{zp}\widetilde{\nu}-1)E_p]\,(3\widetilde{K}+\widetilde{G})E_z \\ & +18(1-\nu_p)\widetilde{K}\widetilde{G}E_z + 3E_p\left[E_z^2 - (12\widetilde{K}\nu_{zp}^2+E_z)\widetilde{G}\right],\end{aligned} \tag{2.22f}$$

again, expressed in a basis where e_3 is the axis of transverse symmetry. The bulk and shear moduli K_T and G_T are, accordingly, rational functions of the bulk and shear moduli $\widetilde{K}$ and $\widetilde{G}$ and of all parameters of the problem. Condition (2.18) therefore can be rewritten as two polynomial equations in $\widetilde{K}$ and $\widetilde{G}$. The first one is of order 4 in $\widetilde{K}$ and 5 in $\widetilde{G}$, whereas the second one is of order 9 in $\widetilde{K}$ and 5 in $\widetilde{G}$. For an isotropic tensor $\mathbf{S}$ with bulk modulus K and shear modulus G, they reduce to a system of cubic equations:

$$\widetilde{G}\widetilde{K}\left[(9+16\eta)\widetilde{K}-9K\right] = 3\widetilde{G}^2(K-\widetilde{K})-12\eta\widetilde{K}^2K, \tag{2.23a}$$

$$\begin{aligned}27(75-32\eta)\widetilde{K}^2G &= 3\widetilde{G}\widetilde{K}\left[27(25+16\eta)\widetilde{K}+(704\eta-675)G\right]+(450+512\eta)\widetilde{G}^3\\ &\quad +3\widetilde{G}^2\left[9(75+64\eta)\widetilde{K}+2(128\eta-75)G\right].\end{aligned} \tag{2.23b}$$

Numerical solutions of the above are determined using the software “Mathematica” [262]. We obtained a unique set of real solutions in the domain $\widetilde{K}>0$, $\widetilde{G}>0$, for all elastic moduli $\widetilde{K}$ and $\widetilde{G}$ and crack-density parameter η considered in the present work. For arbitrary anisotropy, numerical solutions are readily obtained using the following fixed-point algorithm:

$$\begin{aligned}&\textit{Initialization:}\quad \text{set}\quad \widetilde{K}^{-1}=9\Delta/[2E_p+(1-\nu_p+4\nu_{pz})E_z],\\ &\qquad \widetilde{G}^{-1}=6\Delta/[E_p+2(1-\nu_p-2\nu_{pz})E_z],\quad \Delta=1-\nu_p-2\nu_{pz}\nu_{zp}.\end{aligned} \tag{2.24a}$$

$$\begin{aligned}&\textit{Iterations:}\quad \text{set}\quad \widetilde{K}^{-1}\leftarrow\widetilde{K}^{-1}+K_T^{-1}(\widetilde{K},\widetilde{G}),\quad \widetilde{G}^{-1}\leftarrow\widetilde{G}^{-1}+G_T^{-1}(\widetilde{K},\widetilde{G}),\\ &\qquad \text{until the absolute values of } \widetilde{K} \text{ and } \widetilde{G} \text{ change by less than } 10^{-10}.\end{aligned} \tag{2.24b}$$

In this algorithm, the effective moduli are initialized to the Voigt-Hill upper-bound given by $\langle\mathbf{S}^{-1}\rangle_C$ (step 2.24a) whereas iterations (2.24b) enforce infinite bulk and shear moduli $K_T=G_T=\infty$, i.e. the compliance tensor $\mathbf{T}$ vanishes. We emphasize that the value of $\widetilde{K}$ used to evaluate successively the functions K_T and G_T in step (2.24b) changes, as $\widetilde{K}$ is updated *before* $\widetilde{G}$. No convergence is observed, except at small cracks-density values, when the same value of $\widetilde{K}$ is used to evaluate K_T and G_T. With the above algorithm, nevertheless, we obtained fast convergence for arbitrary crack-density η and all sets of crystal anisotropy considered in the present study.

A general result states that the thermal expansion tensor of a homogeneous body is unchanged in the presence of pores [203], including cracks. Nevertheless, if the body is a polycrystal, or is in general heterogeneous, cracks do have an effect on the effective thermal expansion. This effect may be captured by homogenization techniques, such as the “generalized” self-consistent schemes relevant to multi-coated inclusion-reinforced composites [24]. In the present work, we rely on the exact relationship [23]:

$$\widetilde{\boldsymbol{\alpha}}:\langle\boldsymbol{\sigma}(\boldsymbol{x})\rangle=\langle\boldsymbol{\alpha}(\boldsymbol{x}):\boldsymbol{\sigma}(\boldsymbol{x})\rangle, \tag{2.25}$$

where $\boldsymbol{\sigma}(\boldsymbol{x})$ is the local stress field resulting from the macroscopic stress loading $\langle\boldsymbol{\sigma}(\boldsymbol{x})\rangle=\overline{\boldsymbol{\sigma}}$, with no thermal loading applied ($\Delta T=0$). Since the stress is distributed over all grains, the l.h.s. and r.h.s. may be rewritten as a mean over all crystallographic orientations i:

$$\widetilde{\boldsymbol{\alpha}}:\langle\boldsymbol{\sigma}^i\rangle_i=\langle\boldsymbol{\alpha}^i:\boldsymbol{\sigma}^i\rangle_i, \tag{2.26}$$

where $\boldsymbol{\sigma}^i$ is the constant stress field occurring in an isolated spherical inclusion of compliance tensor $\mathbf{S}^i$ and thermal expansion tensor $\boldsymbol{\alpha}^i$, oriented along direction i, and embedded in a medium with compliance tensor $\mathbf{S}^0$. Now, the macroscopic strain $\overline{\boldsymbol{\varepsilon}}$ in a large domain containing one single inclusion can be decomposed as:

$$\overline{\boldsymbol{\varepsilon}}=\mathbf{S}^0:(\overline{\boldsymbol{\sigma}}-f_i\boldsymbol{\sigma}^i)+f_i\mathbf{S}^i:\boldsymbol{\sigma}^i,$$

where f_i is the inclusion volume fraction. Comparing the above to (2.13), one obtains $\boldsymbol{\sigma}^i = \boldsymbol{\Gamma} : \overline{\boldsymbol{\sigma}}$ where the tensor $\boldsymbol{\Gamma} = \left[\mathbf{I} + \mathbf{Q} : (\mathbf{S} - \mathbf{S}^0)\right]^{-1}$ allows one to express the uniform field inside the inhomogeneity in terms of the prescribed field (see e.g. [220]). Equation (2.26) now reduces to:

$$\widetilde{\boldsymbol{\alpha}} : \langle \boldsymbol{\Gamma} \rangle_{\mathcal{C}} : \overline{\boldsymbol{\sigma}} = \langle \boldsymbol{\alpha} : \boldsymbol{\Gamma} \rangle_{\mathcal{C}} : \overline{\boldsymbol{\sigma}}, \tag{2.27}$$

and, taking $\overline{\sigma}_{ij} = \delta_{ij}$:

$$\widetilde{\alpha}_V = \frac{6\alpha_{11}(\Gamma_{1111} + \Gamma_{1122} + \Gamma_{1133}) + 3\alpha_{33}(\Gamma_{3333} + 2\Gamma_{3311})}{\Gamma_{3333} + 2(\Gamma_{1111} + \Gamma_{1122} + \Gamma_{1133} + \Gamma_{3311})}, \tag{2.28}$$

where the components of $\boldsymbol{\Gamma}$ are given in a basis with axis of symmetry e_3. Making use of (2.15) the effective thermal expansion coefficient reads:

$$\begin{aligned} \frac{\widetilde{\alpha}_V}{3} &= \frac{\alpha_{11}\gamma_z + \alpha_{33}\gamma_p}{\gamma_z + \gamma_p}, \qquad \Delta_\gamma = \frac{\widetilde{\nu}}{2\widetilde{G}(1+\widetilde{\nu})} - \frac{\nu_{zp}}{E_z}, && \text{(2.29a)} \\ \gamma_z &= (2u_3 - u_1)\Delta_\gamma + (u_2 - u_3)\left[\frac{1}{E_z} - \frac{1}{2\widetilde{G}(1+\widetilde{\nu})}\right], && \text{(2.29b)} \\ \gamma_p &= (u_3 - u_2)\Delta_\gamma + (u_1 - 2u_3)\left[\frac{1-\nu_p}{2E_p} - \frac{1-\widetilde{\nu}}{4\widetilde{G}(1+\widetilde{\nu})}\right], && \text{(2.29c)} \end{aligned}$$

where the u_i are given in Equation (2.22), and the effective bulk and shear moduli $\widetilde{K}$ and $\widetilde{G}$ are the solutions of (2.18).

In what follows, the self-consistent estimates (2.18) and (2.29) are denoted (SC$'$). When the polycrystal contains no crack ($\eta = 0$), the system (2.18) reduces to two polynomial equations, one of degree 2 in $\widetilde{K}$ and the other of degree 6 in $\widetilde{G}$ (not shown here). These two polynomial equations are equivalent to the self-consistent estimate of Berryman [26] or Willis [247] which is well suited to describe the overall behavior of cell materials [230] and polycrystalline media with moderate contrast [138, 137, 37]. It is useful also to consider the exact cross-property relation, due to Hashin [101], which relates the bulk and volumetric thermal expansion coefficient of isotropic polycrystalline aggregates containing hexagonal crystals such that $\mathbf{S}$ and $\boldsymbol{\alpha}$ share a common axis of symmetry:

$$\widetilde{\alpha}_V = \widetilde{\alpha}_{11} + \widetilde{\alpha}_{22} + \widetilde{\alpha}_{33} = \alpha_V + (\alpha_{33} - \alpha_{11})\frac{1/\widetilde{K} - S_{iikk}}{S_{ii33} - S_{ii11}}. \tag{2.30}$$

where e_3 is the axis of symmetry of the crystal and repeated indices are to be summed up. Hashin's result applies to the present problem when $\eta = 0$, and as expected estimates (2.18) and (2.29) satisfy (2.30) in that case. When $\eta \neq 0$ instead, (2.30) is not verified.

2.4 Percolating behavior

In porous and rigidly-reinforced materials, self-consistent estimates typically predict a percolation threshold. The results of these methods should be taken with care, especially with respect to percolating behavior, where the theory's predictions are sometimes unrealistic compared to real materials [100]. In linear elasticity, for instance, different percolation thresholds may be obtained for the bulk and shear moduli – whereas in real materials, the mechanical and geometrical percolation thresholds are expected to coincide (see [167, Chap. 10] for a discussion). This is because self-consistent estimates are realizable by very peculiar, hierarchical microstructures made of infinitely-many scales [12] and with no finite correlation length [132]. That being said, it is nevertheless a merit of the self-consistent theory that, in contrast with most other approximations and bounds, it does predict a percolation threshold (see e.g. [28] for a discussion).

For cracked media, the percolation thresholds is often expressed in terms of a critical crack-density threshold η_c, as, for instance, in the context of conductivity [212], permeability [211] or elastic wave propagation [210]. In the present problem of quasi-static elasticity, the percolation threshold is associated to the loss of connectivity of the matrix [204], at which point the effective elastic moduli vanish. For a Boolean set of uniformly-oriented disks, the geometrical percolation threshold of the complementary set of the disks has been estimated numerically in [264]. The authors give the threshold $(4/3)\pi\eta_c \approx 22.9$ i.e. $\eta_c \approx 5.5$ for the critical crack-density.

The zeros of the Euler-Poincaré characteristic (or connectivity number) has also been used to estimate the percolation thresholds of binary media [38]. Its expression reads, for a Boolean model of volume fraction $1-q$, intensity θ and primary grain A:

$$q\theta\left(1-\frac{\theta M_A S_A}{4\pi}+\frac{\pi\theta^2 S_A^3}{384}\right), \tag{2.31}$$

where S_A is the surface area of A and M_A the integral of the mean curvature along the boundary of A. For a disk of radius a, $S_A = 2\pi a^2$, $M_A = \pi^2 a$ so that, setting the above expression to zero provides us with the approximation $\eta_c = \theta a^3 = (4/\pi^2) \times (3 \pm \sqrt{6})$. The first value $\eta_c \approx 0.2231$ is close to the numerical estimate $\eta_c \approx 0.2230$ [265] for the percolation threshold of the disks. However the prediction using the connectivity number for the second threshold, $\eta_c \approx 2.21$, related to the loss of connectivity of the matrix, is significantly smaller than the estimate given in [264]. For linear elasticity, the self-consistent scheme of Budiansky and O'Conell [42] predicts the percolation threshold $\eta_c = 9/16 \approx 0.56$ for "dry cracks" embedded in an isotropic homogeneous body, whereas a different percolation threshold $\eta_c = 45/32 \approx 1.41$ is obtained for "wet" (fluid-saturated) cracks.

For the self-consistent estimates proposed in this work, the percolating behavior is obtained by expanding K_T^{-1} and G_T^{-1} (Equation 2.21) as a Taylor series of order 2 near the point $\eta \to \eta_c$ where η_c is unknown. The equations $K_T^{-1} = 0$ and $G_T^{-1} = 0$ provide a set of conditions on $\widetilde{K}$, $\widetilde{G}$ and η_c. We look for solutions of the form $\widetilde{K} \sim K_1(\eta_c - \eta)$, $\widetilde{G} \sim G_1(\eta_c - \eta)$ where the prefactors K_1 and G_1 are independent of η. These asymptotic forms will be confirmed later on in this study, using numerical results. We obtain the following condition on η_c:

$$135(225 + 1424\eta_c) = (64\eta_c)^2(64\eta_c - 28), \tag{2.32}$$

which provides the percolation threshold $\eta_c \approx 1.15752$. Furthermore, in the limit $\eta \to \eta_c$, the self-consistent estimates predicts constant thermal expansion coefficient and Poisson ratio, independently of the crystal's elastic moduli:

$$\widetilde{\alpha}_V \to \alpha_V = 2\alpha_{11} + \alpha_{33}, \qquad \widetilde{\nu} \to \frac{8704\eta_c^2 - 4608\eta_c - 6075}{512\eta_c^2 + 1800\eta_c} \approx 0.09144. \tag{2.33}$$

The limiting value for $\widetilde{\alpha}_V$ implies, in light of (2.25):

$$\langle \boldsymbol{\sigma}(\boldsymbol{x}) : \boldsymbol{\alpha}(\boldsymbol{x}) \rangle = \langle \boldsymbol{\sigma}(\boldsymbol{x}) \rangle : \langle \boldsymbol{\alpha}(\boldsymbol{x}) \rangle, \tag{2.34}$$

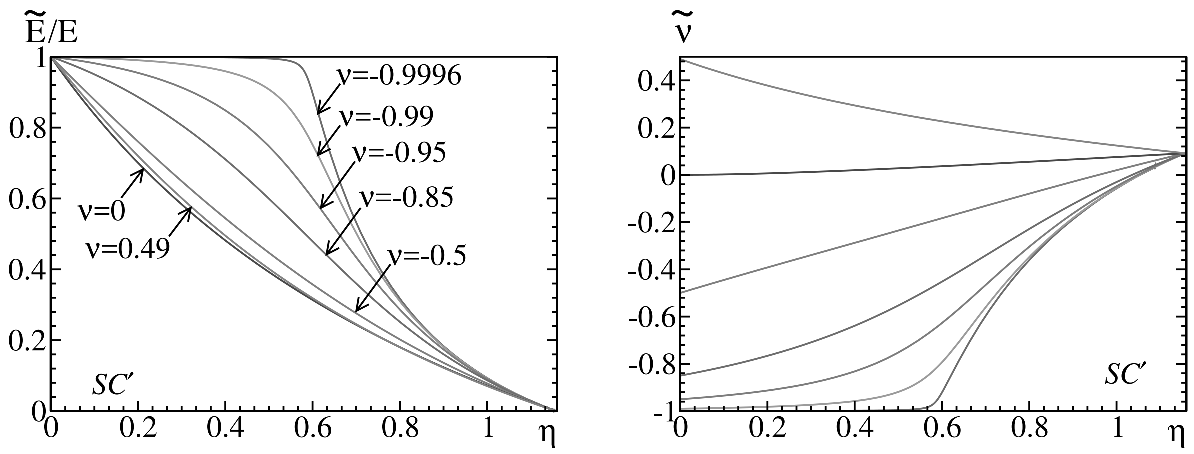

(a) (b)

Figure 2.1: Prediction of the self-consistent approximation (2.21) relevant to a homogeneous isotropic solid containing randomly-oriented cracks, for various Poisson ratios ν in the matrix. (a) Normalized effective Young modulus $\widetilde{E}/\widetilde{E}$ vs. crack density η, (b) Effective Poisson ratio $\widetilde{\nu}$.

where $\boldsymbol{\sigma}(\boldsymbol{x})$ is the local stress field occurring in the polycrystalline material subjected to stress loading, with no thermal loading. The above equality can be interpreted as a lack of correlation between the crystal's orientations and the stress field, as the percolation threshold is approached.

The considerations leading to (2.32) do not hold when some of the eigenvalues of $\mathbf{C}$ vanish. We first investigate the case $G_{zp} = 0$ with the moduli E_z and E_p strictly positive. Equation (2.21) yields the lower percolation threshold η'_c solution of:

$$4\left(2048\eta_c'^2 + 2448\eta'_c + 675\right) = (2176\eta'_c + 1125)\sqrt{16\eta'_c + 9}\,, \tag{2.35}$$

so that $\eta'_c \approx 0.373126$. Second, when $E_z = 0$, keeping $G_{zp} > 0$, $E_p > 0$, a third percolation threshold η''_c, in-between η'_c and η_c is obtained:

$$\eta''_c = \frac{32 + 13\sqrt{46}}{160} \approx 0.751064. \tag{2.36}$$

The predictions of estimates (2.23a) are represented in Figs. (2.1). The limiting value for the effective Poisson ratio at percolation (Equation 2.33, method SC′) is confirmed in Fig. (2.1b)

2.5 Isotropic body containing cracks

In the following, we compare the predictions of SC′ with three homogenization schemes developed in the literature: the self-consistent scheme of Budiansky and O'Connell [42] (denoted SC), the Mori-Tanaka method of Benveniste [22] (denoted MT) and the Hashin-Shtrikman-type bounds of Ponte Castañeda and Willis [194] (denoted HS). Scheme (MT) amounts to using an asymptotic expansion truncated to first-order in $\eta \ll 1$ for the inverse $1/\widetilde{E}$, and is equivalent to the "non-interacting approximation" presented in [222]. Method (HS) provides rigorous upper-bounds for classes of materials containing cracks embedded in uncracked regions ("security spheres"). In this

Figure 2.2: Random model of polycrystal containing a population of cracks: Poisson-Voronoï tessellation superimposed on a Boolean model of penny-shaped cracks (2D cut).

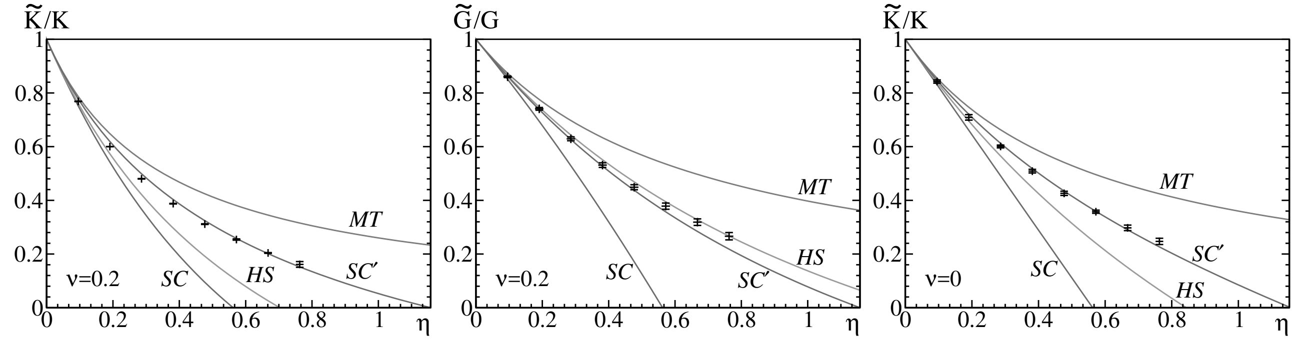

(a) (b)

Figure 2.3: Normalized bulk modulus $\widetilde{K}/K$ (a) and shear modulus $\widetilde{G}/G$ (b) vs. crack density η for a homogeneous isotropic body (Poisson ratio 0.2) containing cracks: comparison between analytical methods SC, SC′, HS, MT and FFT numerical results. (c) Bulk modulus $\widetilde{K}$ for a Poisson ratio $\nu = 0$ in the matrix.

construction, the cracks do not interpenetrate and the cracks-density parameter is constrained in the range $\eta \leqslant 3/(4\pi) \approx 0.239$.

We also carry out Fourier-based numerical computations using a Poisson-Voronoï tessellation as polycrystalline aggregate. This tesselation is parametrized by the density of germs, equal to n_g/V, the number of grains per unit volume. Assuming the volume Ω is a cube of dimension L, we choose to parametrize the tessellation by the grains typical size $\ell = [3/(4\pi/n_g)]^{1/3}L$, defined so that the mean grain volume equals that of a sphere of radius ℓ. We model the cracks by a Boolean model of equisized disks of radius a with homogeneous Poisson point process. The intensity of the Poisson point process is ηa^3. The Boolean model of disks is "superimposed" on the tessellation, so that the orientations of the grains and cracks, and their position compared to one another, are uncorrelated. In method SC′, no scale-separation hypothesis is made between the typical length scales of the cracks and that of the grains. Hereafter we choose $a = \ell$ so that the cracks and grains have similar size. A schematic view of the model is presented in Fig. (2.2). The Voronoï-Boolean model is not representative of real materials, but is useful nevertheless to draw comparisons between analytical estimates and exact numerical results.

Numerical Fourier-based computations are carried out on the random cracked-polycrystal model, using the backward-and-forward difference scheme [258, 249]. The domain Ω is discretized on grids of $L^3 = 128^3$, 256^3 and 512^3 voxels, the cylindrical cracks have a diameter of $D = 40$ or $D = 80$ voxels and the thickness is set to $w = 1.25$, 1.4, 1.5, 2, 3, 4 and 5 voxels. The diameter of the cracks in each configuration is adjusted so that the crack-density parameter stay the same. As described in another study [85], the effective elastic moduli are overestimated when $w \leqslant 1.4$, whereas a linear behavior is observed with respect to w in the region $w \geqslant 1.5$. Results for all data sets are extrapolated in the limit $w \to 0$. The mean absolute difference between the apparent moduli computed for the various data sets, i.e. different values of L and D, are used to estimate error bars. Data detailed in [85] show that the error on the bulk modulus is not more than 1% when $\eta \approx 0.38$. Nevertheless, the precision of the method deteriorates when the number of cracks increases, and hereafter we restrict ourselves to $\eta \leqslant 0.8$.

FFT predictions for the normalized bulk modulus $\widetilde{K}/K$ and normalized shear modulus $\widetilde{G}/G$ are shown in Fig. (2.3), and compared to the analytical estimates SC, SC′, MT and HS. The four methods SC, SC′, MT and HS are equivalent up to the first-order correction in η in the limit $\eta \to 0$. The stiffest estimate is provided by scheme MT which percolates at $\eta = \infty$, whereas method SC is the most compliant. This behavior is a consequence of the self-consistent assumption employed in method SC, which reads [105]:

$$\widetilde{\mathbf{S}} = \mathbf{S} + \eta\langle \mathbf{G}(\widetilde{\mathbf{S}})\rangle_{\mathcal{O}}.$$

This is in contrast with the present method, where both the matrix phase and the cracks are embedded in the equivalent medium. Similar observations hold when the Poisson ratio is $\nu = 0$ in the matrix (Fig. 2.3c).

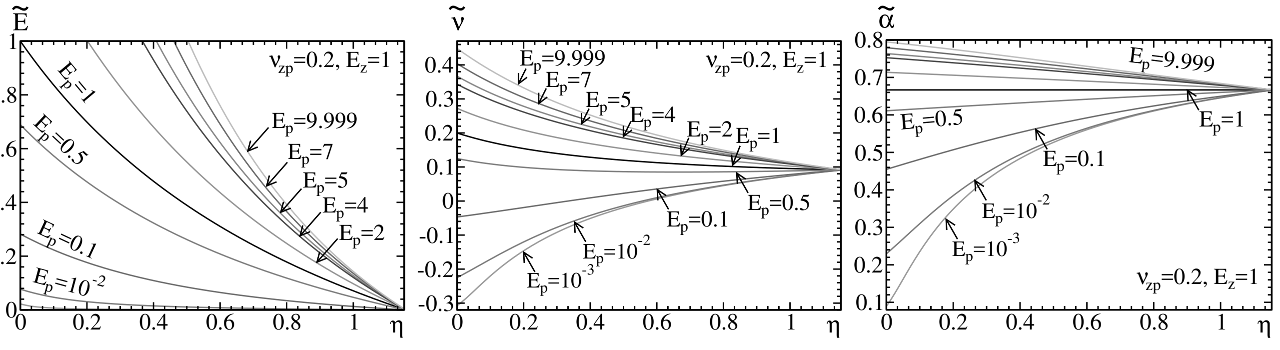

(a) (b) (c)

Figure 2.4: Self-consistent estimate SC′ for the effective response of a cracked polycrystal vs. crack density η, for varying in-plane Young modulus $E_p \leqslant 10$ with $\nu_{zp} = 0.2$, $E_z = 1$, $\alpha_{11} = 1$ and $\alpha_{33} = 0$. (a) Young modulus $\widetilde{E}$, (b) Poisson ratio $\widetilde{\nu}$, (c) bulk modulus $\widetilde{K}$, (d) shear modulus $\widetilde{G}$, (e) thermal expansion coefficient $\widetilde{\alpha} = \widetilde{\alpha}_V/3$.

At non-dilute crack density, the analytical estimates differ significantly. Numerical results for the Boolean microstructure considered here are very close to the predictions of methods SC′, up to about $\eta \approx 0.6$. At higher crack density ($\eta \geqslant 0.6$), the estimates provided by method SC′ are more compliant than numerical results. This behavior is not surprising since the percolation threshold for the loss of connectivity of the matrix, equal to 5.46 according to Yi and Esmail [264], is much higher than threshold $\eta_c \approx 1.16$ predicted by SC′ (Eq. 2.32). Note that this percolation threshold is independent of the elastic moduli, except in degenerate cases, as will be seen later on.

2.6 Cracked polycrystalline aggregates

Method SC′ is now applied to a polycrystal containing cracks. To illustrate the predictions of the method, we fix $E_z = 1$, $G_{zp} = 5/12$, $\nu_{zp} = \nu_p = 0.2$ and let E_p vary between 0 to its maximum value 10 (see Equation 2.6). Isotropic crystals are recovered when $E_p = E_z = 1$ (black solid line). The effective thermoelastic properties are represented as a function of the cracks density η in Fig. (2.4). The limiting value of $\widetilde{\nu} \approx 0.091$ (Equation 2.33) is recovered when $\eta \to \eta_c$, for all values of E_p, as well as $\widetilde{\alpha}_V = \alpha_V$.

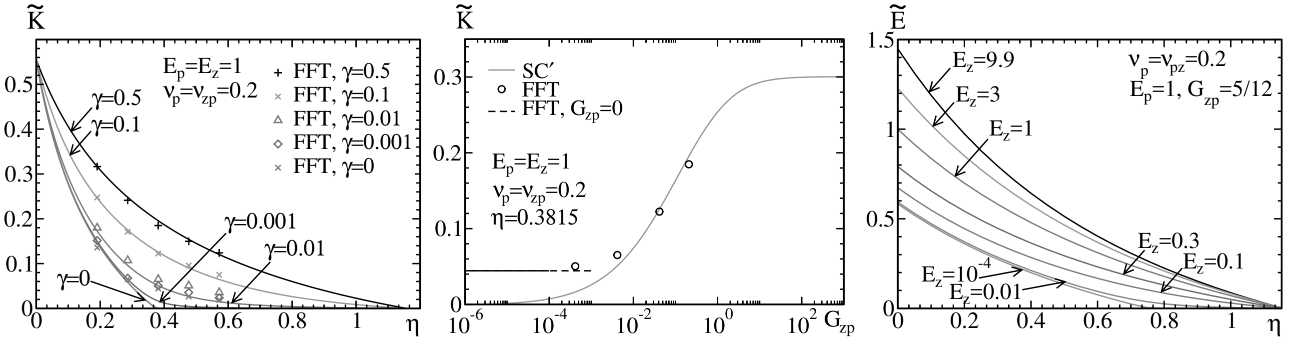

(a) (b) (c)

Figure 2.5: (a) Bulk modulus $\widetilde{K}$ vs. crack density η as the out-of-plane shear modulus G_{zp} tends to 0 ($G_{zp} = \gamma G_0$, $G_0 = 5/12$). Solid lines: SC′. Symbols: FFT results. (b) Bulk modulus $\widetilde{K}$ vs. G_{zp} when $\eta = 0.3815$, in lin-log plot. Symbols and dashed line: FFT results. (c) Effective Young modulus $\widetilde{E}$ vs. crack-density η as $E_z \to 0$.

The onset of an "advanced" percolation threshold when $G_{zp} \to 0$ (Equation 2.35) is confirmed in Figs. (2.5a,b), where the effective bulk modulus $\widetilde{K}$ is represented as a function of η for decreasing

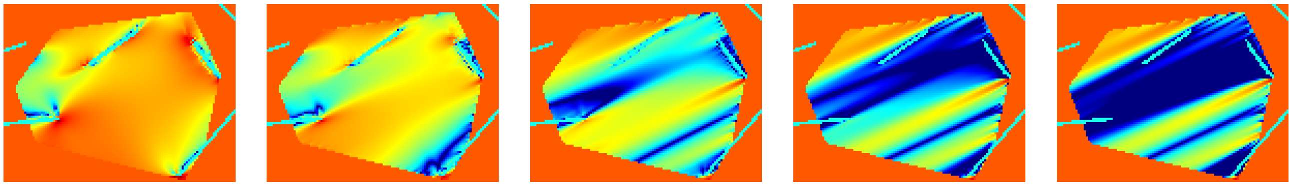

(a) (b) (c) (d) (e)

Figure 2.6: Map of the quantity $\log|\sigma_{33}|$ in a grain, thresholded in the range $[-22; 0.5]$ so that $\sigma_{33} \in [10^{-2}; 3.16]$. The axis of symmetry e_3 of the crystal is nearly-parallel to the plane of the 2D cut. Lowest values are indicated in blue, highest in red, and intermediate values in green-yellow. The same color scale is used for all maps (a-e). Cracks in cyan. The out-of-plane shear modulus is $G_{zp} = 0.21$ (a), 0.04 (b), $4\,10^{-3}$ (c), $4\,10^{-4}$ (d) and 0 (e).

values of G_{zp} monitored by the parameter $\gamma = G_{zp}/(5/12) = 0.50$, 0.1, 0.01, 10^{-3} and 0. At $G_{zp} = 0$, SC′ predicts vanishing bulk and shear moduli when $\eta \geqslant \eta'_c \approx 0.37$. Likewise, in the limit $E_z \to 0$ a percolation threshold $\eta''_c \approx 0.75$ (Equation 2.36) is obtained (Fig. 2.5c).

Additionally, we have carried out numerical FFT computations for varying values of $G_{zp} \ll 1$ (Fig. 2.5a). They lie very close to the predictions of SC′ when the anisotropy is moderate ($G_{zp} > 0.1$) or when η is smaller than η'_c. This is not the case when the crack density is high ($\eta > \eta'_c$) and the out-of-plane shear modulus is very small ($G_{zp} \leqslant 0.01$). On the one hand, FFT results indicate a finite limit for the effective elastic moduli of the cracked polycrystals, even when $G_{zp} = 0$. This is confirmed in Fig. (2.5b) which represents the effective bulk modulus as a function of G_{zp}, in semi-log plot, when $\eta = 0.3815$ is fixed. In this plot, the dotted line is the FFT prediction when G_{zp} is strictly zero. On the other hand, although no advanced percolation threshold is observed according to FFT results, a strong decrease of the effective moduli with respect to η is observed up to about 0.4, followed by a slower decrease in the range $\eta > 0.4$.

These results suggest a mechanism is responsible for the strong weakening of the moduli at moderate crack density, visible on the local stress fields. The stress component σ_{33} occurring in a crystal is represented in Fig. (2.6), with cracks shown in white. The crystal has been chosen so that its axis of symmetry, e_3, lies almost exactly in the same plane as the 2D cut where the fields are represented. Accordingly, σ_{33} corresponds to the traction component in the out-of-plane direction, and is oriented about 45 degrees from the horizontal in Fig. (2.6). Maps (a) to (e) show the fields at decreasing values of G_{zp}. When the shear modulus G_{zp} approaches zero, the material is weakened by large regions where the stress field σ_{33} is close to zero (Fig. 2.6e, regions colored in blue). These regions organize through large bands parallel to direction e_3. Indeed, $G_{zp} = 0$ implies in the crystal $\sigma_{31} = \sigma_{32} \equiv 0$. Accordingly, using stress equilibrium, $\partial_3 \sigma_{33} \equiv 0$. Along cracks embedded in the crystal, however, $\boldsymbol{\sigma} \cdot \boldsymbol{n} = 0$ implies $\sigma_{33} n_3 = 0$. These two results explain the development of weakening bands parallel to direction e_3, enclosing cracks. The weakening zones however do not cross the grain boundary (not shown). When the crystals are not covered by such bands, an increase of η has a strong weakening effect as each crack will weaken large regions in the surrounding crystals. Conversely, when most of the material is covered by weakening bands, an increase of η has a smaller weakening effect on the macroscopic properties.

This behavior may be compared to the effect of cracks on tension-field elastic sheets which are stiff in traction but very soft in compression. The sheets sustain tension only if a set of regions surrounding the cracks, free of stress, do not form a percolating phase connecting boundaries where a load is applied [144]. Weakening bands have also been observed in periodic structures subjected to plane strain and made of pores embedded in a strongly-anisotropic elastic matrix [260]. Specifically, the authors of [259] consider a transversely-isotropic, incompressible crystal with, referring to (2.4), $\nu_p = \nu_{pz} = \nu_{zp} = 1/2$, $E_p = E_z$ and $G_{zp} = kE_p$ where $k \ll 1$ monitors the anisotropy. The material is subjected to strain shear loading, resulting in a macroscopic strain $\overline{\varepsilon}_{11} = -\overline{\varepsilon}_{33} > 0$ and $\overline{\varepsilon}_{13} = 0$. The crystal contains a cylindrical void with axis of symmetry parallel to e_2. The authors have observed the presence of localized shear bands that develop from the void as the porosity increases. The length of the band scales as $\xi \sim a_p/\sqrt{k}$ where a_p is the pore radius. In the limit $k \to 0$ where the stiffness tensor is not positive and the governing partial derivative equations become hyperbolic, two regimes have been identified. The "dilute regime" (porosity $f \ll f_r$) occurs when the length of the localized shear bands are smaller than the size of the elementary cell, whereas a "strongly anisotropic regime" (porosity $f \gg f_r$) holds when the shear bands span the periodic array of pores (see Fig. 2.7). At the crossover between the two regimes, the porosity equals the critical value

(a) (b) (c)

Figure 2.7: FFT map of the strain shear component $\varepsilon_{11} - \varepsilon_{33}$, parallel to the applied load, in the plane (e$_1$; e$_3$), in the elementary cell of a periodic material with strong anisotropy ratio $k = 10^{-3}$ (see text). Porosities from left to right: $f = f_r/10$ (a, regular "dilute" regime); $f = f_r$ (b, crossover regime); $f = 10 f_r$ (c, "strongly anisotropic" regime), where $f_r \sim k/\pi$ is the crossover porosity. Incompressible matrix. Black represents the lowest field values, highest in white.

$f_r \sim k/\pi$. In the present problem, one may expect the development of similar shear bands as $G_{zp} \to 0$, with the size of the bands increasing as G_{zp} decreases. However, recall that the bands surrounding cracks are, according to FFT maps, constrained to lie within the grains the crack is embedded in, and have therefore a limited impact. This explains why, according to the predictions of SC′, the polycrystal sustains macroscopic loads in the domain $\eta < \eta'_c$, even when G_{zp} is strictly zero.

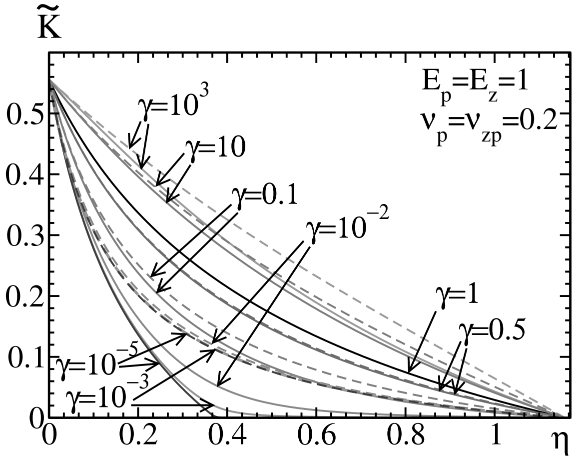

Figure 2.8: Effect of scale separation on the elastic response of a cracked polycrystal as a function of η: effective bulk modulus $\widetilde{K}$ at increasing values of the out-of-plane shear modulus G_{zp}, monitored by the anisotropy ratio $\gamma = G_{zp}/G_0$ ($G_0 = 5/12$). Solid lines: cracks and grains of similar size. Dotted lines: cracks much larger than the grains. A different gray color is used for each value of γ.

The effect of scale separation is illustrated in Fig. (2.8), which shows the effective bulk modulus

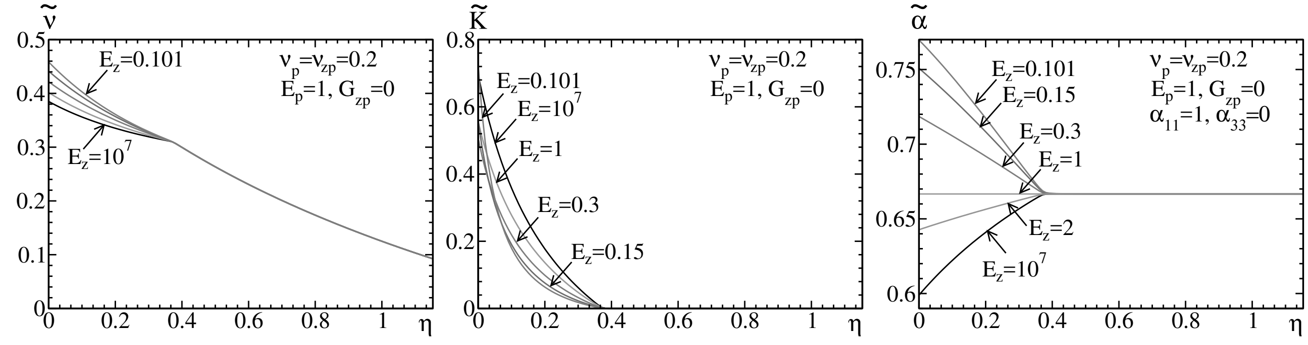

(a) (b) (c)

Figure 2.9: Effective response of a polycrystalline aggregate with out-of-plane shear modulus $G_{zp} = 0$ as a function of the crack density parameter η, for various out-of-plane Young modulus E_z. (a) Poisson coefficient $\widetilde{\nu}$, (b) bulk modulus $\widetilde{K}$, (c) thermal expansion coefficient $\widetilde{\alpha} = \widetilde{\alpha}_V/3$.

of cracked polycrystals as a function of the crack density η, for various values of the anisotropy ratio $\gamma = G_{zp}/G_0$. The value $\gamma = 1$ corresponds to an isotropic tensor $\mathbf{C}$ with Young moulus 1 and Poisson ratio 0.2. Two configurations are considered. In the first one, modeled using SC$'$, the cracks and grains have similar size, as previously considered (solid lines). In the second one, the size of the cracks is much larger than that of the grains (dotted lines). This latter case is modeled using method SC$'$ two times. The matrix surrounding the crack is first replaced by an effective medium by applying SC$'$ to an uncracked polycrystal (in this case the method is equivalent to Berryman's). Second, the cracks are accounted for using method SC$'$ specialized to a homogeneous body containing cracks (Eq. 2.23a). The two estimates coincide only when the crystals are isotropic ($\gamma = 1$, black line). In all other cases, the elastic response is stiffer when the cracks are larger than the grains. If scale separation is assumed, no advanced percolation threshold develops when $\gamma \to 0$. In that case percolation occurs when $\eta \approx 1.158$ independently of γ. Accordingly, a homogenization approach where grains and cracks are treated separately, using e.g. Berryman's method for the polycrystal and an homogenization scheme for the cracks (e.g. MT, HS or SC), would give incorrect results, in the case where the cracks and grains have similar size and the grains have strong anisotropy. Such situation occurs in TATB polycrystals, as investigated in e.g. [86].

To illustrate the predictions of SC$'$ when $G_{zp} = 0$, two effective elastic moduli and the thermal expansion coefficient are represented in Fig. (2.9) for various values of E_z, with $G_{zp} = 0$, $E_p = 1$, $\nu_p = \nu_{zp} = 0.2$, $\alpha_{11} = 1$ and $\alpha_{33} = 0$. At $\eta = \eta'_c$, method SC$'$ predicts $\widetilde{\nu} \approx 0.31$ independently of E_z whereas $\widetilde{\alpha} = 2/3$ as when $G_{zp} \neq 0$ (Fig. 2.4).

2.7 Conclusion

In the present chapter, we have derived explicit formula that approximate the effective thermal and elastic, response of a polycrystal with hexagonal symmetry containing randomly-oriented cracks. This model is not an extension of that developed by Huang and Hu [107] for cubic symmetry. In particular, the coupling between crystal anisotropy and cracks is much stronger in the present case.

The main results are the following. First, in the absence of crystal anisotropy, i.e. for a homogeneous cracked body, our self-consistent approach yields estimates that are very close to that of a Boolean model of disk-shaped cracks. Good agreement is observed up to a crack-density parameter $\eta \approx 0.7$. In this domain, most cracks intersect another crack, and the matrix's Young modulus is weakened by as much as 75% for a Poisson ratio in the embedding medium of 0.2. For general transversely-isotropic crystals, the self-consistent estimates predict a percolation threshold equal to about $\eta \approx 1.16$ for the crack density parameter.

Second, "advanced" percolation thresholds at $\eta = 0.37$ and 0.75 are predicted for crystals with vanishing out-of-plane shear or Young modulus. The low percolation threshold predicted by the self-consistent estimate in the former case can be related to the onset of "weakening" regions that surround the cracks and lie inside the grains. The existence of such regions has been confirmed by Fourier-based numerical computations carried out on a Voronoï-Boolean model. However, in contrast to the predictions of the self-consistent estimates, Fourier computations do not indicate a percolation threshold in highly-anisotropic crystals at low-crack density, but rather a strong weakening of the elastic moduli. The analytical estimates derived in the present approach fail to predict this mechanism.

Although the methodology presented herein has focused on cracked polycrystals, it is worth mentioning that such approach can be extended, in theory, to hexagonal polycrystals containing other types of inhomogeneities, including pores or rigid inclusions.

Chapter 3

Elastostatic field distributions: self-consistent estimates & Van Hove singularities

This chapter addresses the problem of the reconstruction of the local fields distribution occurring in heterogeneous linear elastic solids. The constitutive heterogeneities are crystals and cracks. Through comparisons with FFT computations, it is shown that self-consistent estimates together with an assumption of normal distribution at the phase scale provide an accurate description of the elastostatic field histograms in polycrystals without cracks. In the case of inter and transgranular cracks, full-field FFT simulations indicate that the field histograms present van Hove singularities. Their natures are determined analytically in the low-density regime, in the case of an homogeneous medium containing cracks.

3.1 Introduction

The probability distribution functions (or field histograms) of the local stress and strain fields in heterogeneous media are useful to gain insight on a material's mechanical response. On the one hand, distribution functions embody the material's macroscopic (homogenized) response, as well as statistics on the stress or strain extreme values (distribution tails). On the other hand, the information contained in probability distribution functions is highly condensed compared to the medium's full-field microscopic response. This property may be regarded as an advantage, since one-dimensional functions are easier to characterize and model than a material's full-field response, which requires an explicit description of the geometry.

Various works in micromechanics and in homogenization have investigated the distribution function of mechanical fields in heterogeneous media. Sevostianov [221] has modeled the distribution of the peak stresses occurring along the interface of porous inclusions in plane stress, using a Gumbel (double exponential) law. Idiart et al. [110] considered the fluctuations of mechanical fields in particulate viscoplastic composites, predicted by homogenization theories. Using FFT computations, they showed that the field distributions in the matrix are well approximated by Gaussian distributions in the linear case but strongly deviate from the latter when dealing with strong nonlinearities such as perfect plasticity. The distribution of elastic fields in polycrystals is considered in [128].

Probability distribution functions present, in general, Van Hove singularities, named after the work of Van Hove on the density of states of phonons in crystals [239]. Along Van Hove singularities, a distribution exhibits discontinuities, sharp peaks (blow-up and cusps) and non-differentiable points. These singularities occur whenever the field's spatial gradient vanishes [4, 161], typically extrema or saddle-points. Conversely, regions where the fields blow-up control the behavior of the distributions at infinity (distribution tails). Van Hove singularities occur in the probability distribution of the elastic fields in periodic media (see e.g. [260]), as well as in their electrical response [56]. Giordano [92] determined Van Hove singularities for the electric field surrounding an insulating crack. The local elastic response is dealt with in [93]. The effect of a crack on the field distributions has also been considered in [71] for dielectric breakdown. The case of a random dispersion of inclusions has been investigated by Cule & Torquato [56]. Comparing deterministic and random microstructures, the authors argue that, in random media, Van Hove singularities are smoothed out by disorder. Stokes flow in random porous media has also been investigated in [2].

The electrical (or dielectric) response has been considered in other works. Barthelemy and Orland [19] computed the local field distribution in random dielectric networks. The method makes use of the Lipmann-Schwinger equation and generalizes the classical self-consistent analytical treatment to field distributions. The method proposed by the authors show that the field distributions are well captured when taking into account first-neighbor interactions between bonds, and treating long-range interactions by an effective medium. Pellegrini [185] has modeled the field distributions in random dielectrics using Gaussian distributions to predict the response of "weakly nonlinear" media.

The present study aims at investigating up to which extent one may use homogenization theories to predict not only the mean (and second-order moments) of the fields but also the entire probability distribution functions of such fields, in linear elastic solids. The effect of a random dispersion of heterogeneities, made of crystals or cracks are examined. Self-consistent estimates and analytical results for the field surrounding an isolated crack are employed to model the elastic field distributions. Fourier-based computations are carried out to assess the validity of our approach, and to determine the presence of Van Hove singularities in random media. The asymptotics of the distribution tail for certain stress components, are determined as well in specific cases.

This chapter is organized as follows. The probability distribution functions of elastic fields occurring in 3D sound polycrystals are considered in Sec. (3.2). Sec. (3.3) deals with a homogeneous body containing an isolated crack, or a population of parallel, or randomly-oriented cracks, in plane strain, and investigates Van Hove singularities in the field distributions. Numerical and self-consistent results pertaining to the field histograms of cracked polycrystals in 3D are presented in Sec. (3.4).

3.2 Field histograms in sound polycrystals

3.2.1 Multivariate distributions of the elastostatic fields

A polycrystal made of elastically anisotropic grains can be considered as a composite material occupying a domain Ω whose constitutive phase (r) represents a given crystalline orientation.

Linear homogenization theories provide estimates for the intraphase first (i.e. mean) and second-order moments [30, 131, 193] of the strain field $\boldsymbol{\varepsilon}(\boldsymbol{x})$. For each phase (r), they read

$$\mathbf{M}^r_{\boldsymbol{\varepsilon}} = \langle \boldsymbol{\varepsilon} \rangle_{(r)} \quad \text{and} \quad \boldsymbol{\Sigma}^r_{\boldsymbol{\varepsilon}} = \langle \boldsymbol{\varepsilon} \otimes \boldsymbol{\varepsilon} \rangle_{(r)}, \quad \forall r = 1, \ldots, N. \tag{3.1}$$

The multivariate probability distribution function of the tensorial field $\boldsymbol{\varepsilon}(\boldsymbol{x})$ in phase (r) is defined as

$$P^r_{\boldsymbol{\varepsilon}}(\boldsymbol{t}) = \lim_{\zeta \to 0} \frac{1}{\zeta} P\left\{ ||\boldsymbol{\varepsilon} - \boldsymbol{t}|| < \zeta \right\} = \frac{1}{|\Omega_r|} \int_{\Omega_r} \delta(\boldsymbol{\varepsilon}(\boldsymbol{x}) - \boldsymbol{t})\, \mathrm{d}\boldsymbol{x}, \quad \boldsymbol{t} \in \mathcal{S}^2, \tag{3.2}$$

with δ the Dirac delta function, $|\Omega_r|$ the volume of phase r and $\mathcal{S}^2$ the space of symmetric second-order tensors in $\mathbb{R}^3$ equipped with norm $|| \bullet || = \sqrt{\bullet : \bullet}$. The intraphase first and second order moments of the strain field can thus be written

$$\mathbf{M}^r_{\boldsymbol{\varepsilon}} = \int_{\mathcal{S}^2} \boldsymbol{t}\, P^r_{\boldsymbol{\varepsilon}}(\boldsymbol{t})\, \mathrm{d}\boldsymbol{t} \quad \text{and} \quad \boldsymbol{\Sigma}^r_{\boldsymbol{\varepsilon}} = \int_{\mathcal{S}^2} (\boldsymbol{t} \otimes \boldsymbol{t})\, P^r_{\boldsymbol{\varepsilon}}(\boldsymbol{t})\, \mathrm{d}\boldsymbol{t}. \tag{3.3}$$

The overall distribution of the strain field $P_{\boldsymbol{\varepsilon}}$ in domain Ω reads

$$P_{\boldsymbol{\varepsilon}}(\boldsymbol{t}) = \frac{1}{|\Omega|} \int_{\Omega} \delta(\boldsymbol{\varepsilon}(\boldsymbol{x}) - \boldsymbol{t})\, \mathrm{d}\boldsymbol{x} = \sum_{r=1}^{N} f_r\, P^r_{\boldsymbol{\varepsilon}}(\boldsymbol{t}), \quad \boldsymbol{t} \in \mathcal{S}^2, \tag{3.4}$$

with $f_r = |\Omega_r|/|\Omega|$ the volume fraction of phase (r). Similar definitions hold for the intraphase stress moments $\mathbf{M}^r_{\boldsymbol{\sigma}}$ and $\boldsymbol{\Sigma}^r_{\boldsymbol{\sigma}}$ as well as the stress probability distributions $P^r_{\boldsymbol{\sigma}}$ and $P_{\boldsymbol{\sigma}}$.

In order to use estimates on $\mathbf{M}^r_{\boldsymbol{\varepsilon}}$ and $\boldsymbol{\Sigma}^r_{\boldsymbol{\varepsilon}}$ provided by mean-field homogenization models, it is natural to consider multivariate normal (i.e. Gaussian) distributions for random *tensor-valued* variables. However, a symmetric second-order tensor in $\mathbb{R}^3$ can also be seen as a vector in $\mathbb{R}^6$. Therefore, the well-known theory of *vector-valued* normal distributions can advantageously be used [9, 20, 120]. The probability distribution function for the strain field $\boldsymbol{\varepsilon}(\boldsymbol{x})$ then reads [20]

$$P^r_{\boldsymbol{\varepsilon}}(\boldsymbol{t}) = \frac{1}{\sqrt{|\mathbf{A}^r_{\boldsymbol{\varepsilon}}|(2\pi)^6}} \exp\left(-\frac{1}{2} (\boldsymbol{t} - \mathbf{M}^r_{\boldsymbol{\varepsilon}})^T \cdot (\mathbf{A}^r_{\boldsymbol{\varepsilon}})^{-1} \cdot (\boldsymbol{t} - \mathbf{M}^r_{\boldsymbol{\varepsilon}}) \right), \quad \boldsymbol{t} \in \mathcal{V}. \tag{3.5}$$

with $\mathcal{V}$ the vector space in $\mathbb{R}^6$. The covariance matrix $\mathbf{A}^r_{\boldsymbol{\varepsilon}}$ is defined by

$$\mathbf{A}^r_{\boldsymbol{\varepsilon}} = \langle (\boldsymbol{\varepsilon} - \mathbf{M}^r_{\boldsymbol{\varepsilon}}) \otimes (\boldsymbol{\varepsilon} - \mathbf{M}^r_{\boldsymbol{\varepsilon}}) \rangle_{(r)} = \boldsymbol{\Sigma}^r_{\boldsymbol{\varepsilon}} - \mathbf{M}^r_{\boldsymbol{\varepsilon}} \otimes \mathbf{M}^r_{\boldsymbol{\varepsilon}} \tag{3.6}$$

and $|\mathbf{A}^r_{\boldsymbol{\varepsilon}}| = \det(\mathbf{A}^r_{\boldsymbol{\varepsilon}})$. The inverse of the covariance matrix, which enters (3.5), is known as the precision matrix. Theorems available for vector-valued normal distributions [9] allow one to derive useful properties for the strain field distribution. In particular, any linear combination of the components of the strain field $\boldsymbol{\varepsilon}(\boldsymbol{x})$ follows a univariate Gaussian intraphase distribution. Since the constitutive law is linear elastic, it follows that each component of the stress field $\boldsymbol{\sigma}(\boldsymbol{x})$ is also normally-distributed in phase (r).

Let us diagonalize the covariance matrix $\mathbf{A}^r_{\boldsymbol{\varepsilon}}$ as:

$$\mathbf{A}^r_{\boldsymbol{\varepsilon}} = \mathbf{B}^r_{\boldsymbol{\varepsilon}} \cdot \mathbf{D}^r_{\boldsymbol{\varepsilon}} \cdot (\mathbf{B}^r_{\boldsymbol{\varepsilon}})^T. \tag{3.7}$$

The orthogonal matrix $\mathbf{B}^r_{\boldsymbol{\varepsilon}}$ is composed by the eigenvectors $\mathbf{b}^r_i$ $(i = 1, \ldots, 6)$ whereas the diagonal matrix $\mathbf{D}^r_{\boldsymbol{\varepsilon}}$ give the eigenvalues λ_i of the covariance matrix. Since the field $\boldsymbol{\varepsilon}$ follows a normal intraphase distribution, the eigenvectors $\mathbf{b}_i^r$ are independent normal random fields. This result allows one to obtain statistical realizations of the intraphase strain field by generating vectors $\hat{\boldsymbol{y}}$ whose components $\hat{y}_i$ $(i = 1, \ldots, 6)$ are independent normal random variables with mean $\mu = 0$ and variance $\sigma^2 = 1$ $(\hat{y}_i \sim \mathcal{N}(0,1))$. A particular realization $\widehat{\boldsymbol{\varepsilon}}^r$ of the strain field in phase (r) reads (see e.g. [120, Chap. 4]):

$$\widehat{\boldsymbol{\varepsilon}}^r = \mathbf{M}_{\boldsymbol{\varepsilon}}^r + \mathbf{B}_{\boldsymbol{\varepsilon}}^r \cdot \sqrt{\mathbf{D}_{\boldsymbol{\varepsilon}}^r} \cdot \hat{\boldsymbol{y}}. \tag{3.8}$$

Using the above, one may compute numerically the distribution of the equivalent von Mises strain $\varepsilon_{eq} = \sqrt{(2/3)\, \mathbf{e} : \mathbf{e}}$ with $\mathbf{e}$ the strain deviatoric tensor. More generally, Eqs. (3.7) and (3.8) allows one to compute the distribution of any function of the strain field components.

3.2.2 Self-consistent estimates

To get a statistical description of the local fields through mean-field homogenization, we adopt the self-consistent (SC) model (2.18) specialized to a sound polycrystal ($\eta = 0$). It can be written [247]:

$$\left\langle \left\{ \left[\mathbf{C}(\boldsymbol{x}) - \widetilde{\mathbf{C}} \right]^{-1} + \mathbf{P}(\widetilde{\mathbf{C}}) \right\}^{-1} \right\rangle = \mathbf{0} \tag{3.9}$$

with $\mathbf{C}$ (resp. $\widetilde{\mathbf{C}}$) the local (resp. effective) elastic tensors and $\mathbf{P}$ the Hill microstructural tensor (2.16) which depends on $\widetilde{\mathbf{C}}$ and on the spatial distribution of the phases. The elastic properties being uniform per phase (i.e. crystalline orientation), that is:

$$\mathbf{C}(\boldsymbol{x}) = \sum_{r=1}^{N} \chi_r(\boldsymbol{x})\, \mathbf{C}^r, \quad \forall \boldsymbol{x} \in \Omega, \tag{3.10}$$

with $\chi_r(\mathbf{x})$ the characteristic function of phase (r), relation (3.9) can be written

$$\sum_{r=1}^{N} f_r \left[(\mathbf{C}^r - \widetilde{\mathbf{C}})^{-1} + \mathbf{P}(\widetilde{\mathbf{C}}) \right]^{-1} = \mathbf{0}. \tag{3.11}$$

At the local scale, the self-consistent scheme provides information about the average fields for each crystalline orientation. For the strain field, for instance, the mean reads:

$$\mathbf{M}_{\boldsymbol{\varepsilon}}^r = \langle \boldsymbol{\varepsilon} \rangle_{(r)} = (\mathbf{C}^r + \mathbf{C}^*)^{-1} : \left(\widetilde{\mathbf{C}} + \mathbf{C}^* \right) : \overline{\boldsymbol{\varepsilon}}. \tag{3.12}$$

Besides, due to the quadratic dependence of the elastic energy on the strain field, the intraphase second moment of the strain field distribution can be obtained from the partial derivatives of the overall elastic energy $\widetilde{\omega}$ with respect to the local elastic tensors $\mathbf{C}^r$ [30, 131, 193]

$$\boldsymbol{\Sigma}_{\boldsymbol{\varepsilon}}^r = \langle \boldsymbol{\varepsilon} \otimes \boldsymbol{\varepsilon} \rangle_{(r)} = \frac{2}{f_r} \frac{\partial \widetilde{\omega}}{\partial \mathbf{C}^r} \quad \text{with} \quad \widetilde{\omega} = \frac{1}{2} \overline{\boldsymbol{\varepsilon}} : \widetilde{\mathbf{C}} : \overline{\boldsymbol{\varepsilon}}. \tag{3.13}$$

In a general context of anisotropy, the SC estimate of the intraphase second-moment is solution of a linear system which requires the numerical integration of the Hill microstructural tensor $\mathbf{P}$ and its derivative $\partial \mathbf{P} / \partial \widetilde{\mathbf{C}}$ [36, 37].

3.2.3 FFT-based computations

The distribution of the elastostatic fields in polycrystals can be addressed by considering unit-cell computations with different microstructure models. We consider the classical Poisson-Voronoi tessellation [160, 166] and, for comparison, a modified Poisson-Johnson-Mehl partition of the 3D space, with anisotropic distance functions [84] (see Fig. 3.1a). The latter has been optimized to model a TATB (triamino-trinitrobenzene, a molecular triclinic crystal) polycrystal material [8] and in particular contains much more grains with elongated and non-convex shapes than in the Voronoi tessellation. The TATB crystals are strongly anisotropic. Their elastic behavior displays a general triclinic symmetry [21] which may be approached by transverse isotropy. In this study, we adopt the approximation of the crystal elastic tensor used in [86]. For simplicity, the crystallographic orientations in the grains are independent and uniformly-distributed on the sphere, leading to an isotropic effective response.

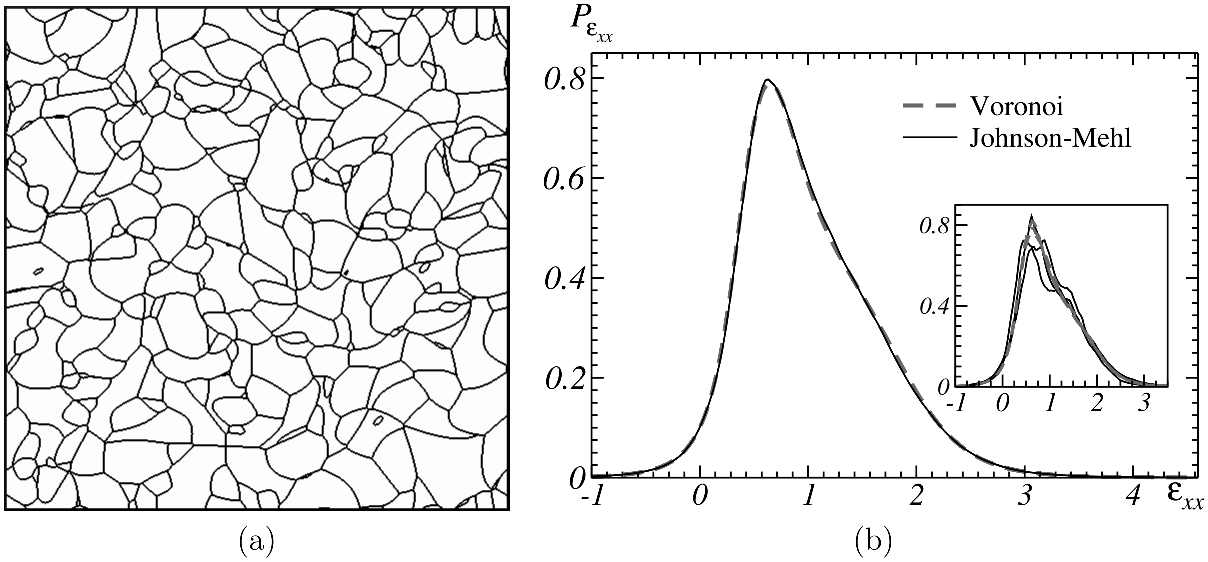

Figure 3.1: (a) Poisson-Johnson-Mehl tesselation of space made of elongated grains (2D cut). (b) Mean over three realizations of the distribution $P_{\varepsilon_{xx}}$ of the strain component ε_{xx} in Poisson-Voronoi (dashed gray line) and Poisson-Johnson-Mehl (black) polycrystals. Inset (bottom-right): individual distributions, computed in each one of the three realizations.

Numerical computations are carried out using a spectral Fourier method [174, 249] on voxel grids containing 1024^3 voxels and about 10^4 grains for the Voronoi model, and 256^3 voxels and about 200 grains for the Johnson-Mehl model. As an example, we apply a macroscopic hydrostatic strain, normalized so that $\langle \varepsilon_m \rangle = 1$. The field distributions $P_{\varepsilon_{xx}}$ are computed for three independent realizations of the Johnson-Mehl and Voronoi models (Fig. 3.1b). The overall distribution is nearly the same for all three realizations of the Voronoi model, except for small variations near the maximum $\varepsilon_{xx} \approx 0.6$ of the distribution (Fig. 3.1b, gray lines). As expected, the Johnson-Mehl model displays much higher variations with respect to the realizations (Fig. 3.1, inset). When averaged, however, the distributions for the Voronoi and Johnson-Mehl models nearly coincide (Fig. 3.1, black and gray solid lines). This result suggests that the histograms for the elastic fields are not very sensitive to the grains shape, at least for moderate anisotropy.

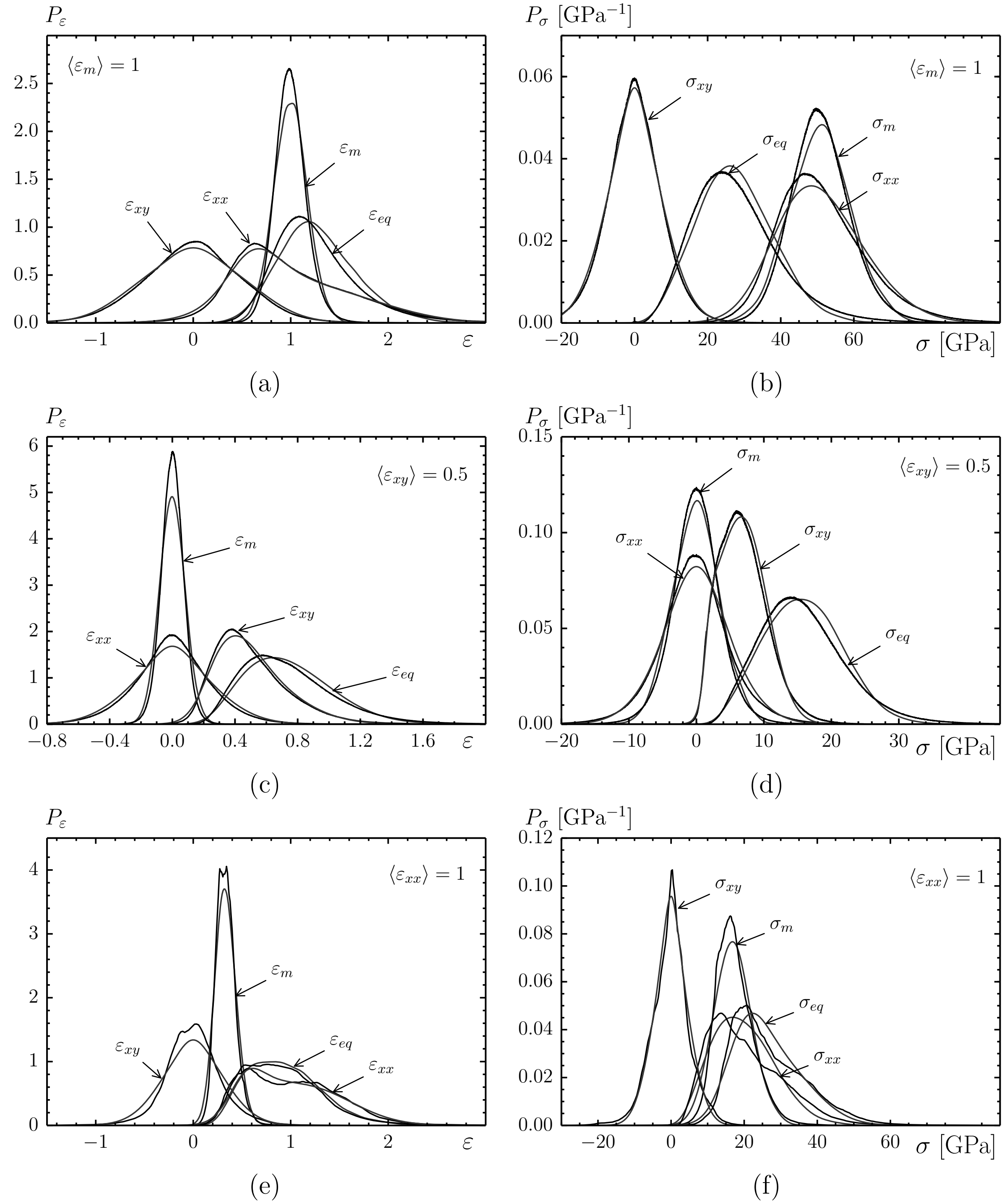

(a) (b)

(c) (d)

(e) (f)

Figure 3.2: (a,c,e) Probability distribution function $P_{\boldsymbol{\varepsilon}}$ for the mean and equivalent strains (ε_m, ε_{eq}) and strain components (ε_{xx}, ε_{xy}), (b,d,f) Probability distribution function $P_{\boldsymbol{\sigma}}$ for the mean and equivalent stress (σ_m, σ_{eq}) and stress components (σ_{xx}, σ_{xy}). Gray solid line: Self-consistent estimate; Black solid line: FFT computation. (a,b) Overall hydrostatic loading with $\langle\varepsilon_m\rangle = 1$. (c,d) Shear loading with $\langle\varepsilon_{xy}\rangle = 0.5$ (e,f) Uniaxial strain loading with $\langle\varepsilon_{xx}\rangle = 1$.

In the following, all computations are carried out using the Johnson-Mehl tessellation, discretized on a volume of 512^3 voxels and containing about $1,250$ grains. In the sequel, the full-field distributions are compared with the mean-field approximation based on the self-consistent model together with an assumption of intraphase normal distribution.

3.2.4 Elastic fields distribution: self-consistent estimates vs. FFT results

We evaluate the reconstruction of the fields distribution which is obtained by assuming a multivariate normal probability distribution within each phase (r) $(r = 1, \ldots, N)$. Each distribution is characterized by the intraphase mean and variance which are estimated with the SC model. These "mean-field" distributions are compared with reference FFT results for isotropic TATB-like polycrystals made of grains with hexagonal symmetry (transversely isotropic elastic behavior). The implicit SC equation (3.11) is solved by considering an isotropic distribution of the phases (i.e. spherical inclusion for the ancillary Eshelby inclusion problem) and a set of crystalline orientations. To approximate an isotropic crystallographic texture (i.e. uniform orientation distribution function), the space of orientations has been discretized by considering a division of the standard triangle, for hexagonal crystal symmetry, in equal area domains [209]. The isotropic texture is represented by a set of 2160 crystalline orientations (i.e phases) with equal volume fractions. Our numerical results on the overall bulk and shear moduli agree with the analytical result of the SC estimate for isotropic polycrystals made of hexagonal grains [26].

The probability distribution functions P_ε and P_σ, for field components and invariant quantities, have been computed for macroscopic hydrostatic $\langle \varepsilon_m \rangle = 1$, shear $\langle \varepsilon_{xy} \rangle = 0.5$ and uniaxial $\langle \varepsilon_{xx} \rangle = 1$ strain loadings. The comparisons with the FFT computations show an overall good agreement with a correct description of the distributions asymmetry (Fig. 3.2). These results on linear elastic polycrystalline aggregates are consistent with those reported for linear viscous two-phase particulate composites [110].

3.3 Field distributions in cracked media: homogeneous body under plane strain

This section focuses on the elastic field distributions in a homogeneous body containing cracks and subjected to plane strain. In Subsection 3.3.1, a model problem made of an isolated crack or a population of randomly-oriented non-interacting cracks is investigated analytically. Emphasis is put on Van Hove singularities and a methodology is proposed to reconstruct the field distributions in the case of a population of interacting cracks. In subsection 3.3.2, the method's predictions are compared to FFT-based computations.

3.3.1 Van Hove singularities

As previously stated, Van Hove singularities are non-differentiable points in the probability distribution function $P(t)$ of a spatial field. These singularities are contributions of regions where the spatial gradient of the field vanishes. The type of singularity depends on the eigenvalues of the Hessian (second-order spatial derivatives) matrix being of the same or opposite signs [161]. For a

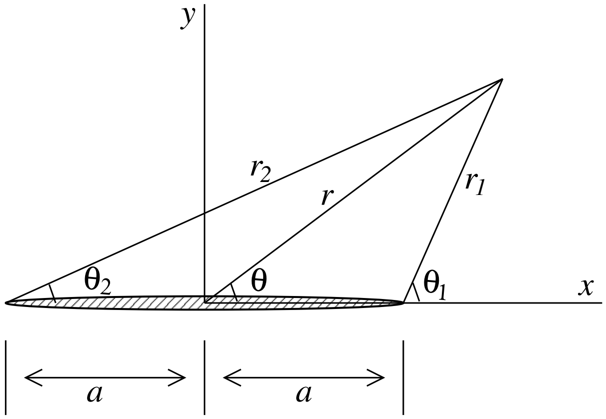

Figure 3.3: Coordinate systems around a crack (hashed area), in plane strain.

field in 2D space, a saddle-point generates a logarithmic singularity of the type $P(t) \sim -\log|t - t_0|$ where t_0 is the value of the field at the saddle-point. In 2D again, a local extremum generates a finite jump in $P(t)$ at $t = t_0$, where t_0 is the field extremal value. In 3D, saddle-points and local extrema induce powerlaw singularities with exponent 1/2, therefore the probability distribution $P(t)$ remains finite while its derivative is unbounded. "Extended" Van Hove singularities [4] may in addition occur if the Hessian matrix has one or more zero eigenvalues. In 2D, blow-ups of the probability distribution function as a powerlaw of exponent −1/2 [4] or −1/3 [260] have been reported.

Isolated crack We now examine histograms for the stress field surrounding an isolated crack. Vector and tensor components refer to a Cartesian coordinates system (e_x, e_y, e_z). The crack is modeled as an infinitely-thin cylinder of equation $|x| < a$, $y = 0$, that is, its length is $2a$ and its axis is parallel to e_z (see Fig. 3.3). The crack is subjected to plane strain in the (e_x, e_y) plane (i.e. $\varepsilon_{iz} \equiv 0$, $i = x, y, z$) and to remote biaxial stress loading, resulting in $\overline{\sigma}_{xx} = \overline{\sigma}_{yy} = \sigma_k > 0$, $\overline{\sigma}_{xy} = 0$ where $\overline{\boldsymbol{\sigma}} = \langle \boldsymbol{\sigma} \rangle_\Omega$ is the mean of the stress field over a very large domain Ω surrounding the crack.

In the vicinity of the crack tips, the stress components σ_{ij} become singular [246]. In the three polar coordinate systems (r, θ), (r_1, θ_1) and (r_2, θ_2) the stress around an isolated crack is expressed as [229]:

$$\sigma_{\substack{xx\\yy}} = \frac{\sigma_k r}{\sqrt{r_1 r_2}} \left[\cos\left(\theta - \frac{\theta_1 + \theta_2}{2}\right) \mp \frac{a^2}{r_1 r_2} \sin\theta \sin\frac{3}{2}(\theta_1 + \theta_2) \right], \tag{3.14a}$$

$$\sigma_{xy} = \frac{\sigma_k r a^2}{(r_1 r_2)^{3/2}} \sin\theta \cos\frac{3}{2}(\theta_1 + \theta_2). \tag{3.14b}$$

Variables $r_{1,2}$ and r denote the distances to the crack tips and to the mid-point along the crack, respectively, and $\theta_{1,2}$, θ are resp. the angles formed between the x-axis and the line joining the crack tips and the mid-point along the crack (see Fig. 3.3). The stress intensity factor "seen" by the crack is $\sigma_k/\sqrt{2\pi a}$ [229]. Maps of the three stress components are shown in Figs. (3.4a-c).

Consider now the probability distribution $P_{ij}(\sigma_k; t)$ of $\sigma_{ij} = t$, computed within a region Ω_k. We assume that Ω_k is a circular domain with radius D and surface fraction $f = \pi D^2/S$ and seek for the behavior of $P_{ij}(\sigma_k; t)$ when $t = 0$, or $t = \pm\infty$. Set $\theta_1 = \pi - \mathrm{d}\theta_1$ and $\theta_2 = \mathrm{d}\theta_2$ and expand
]

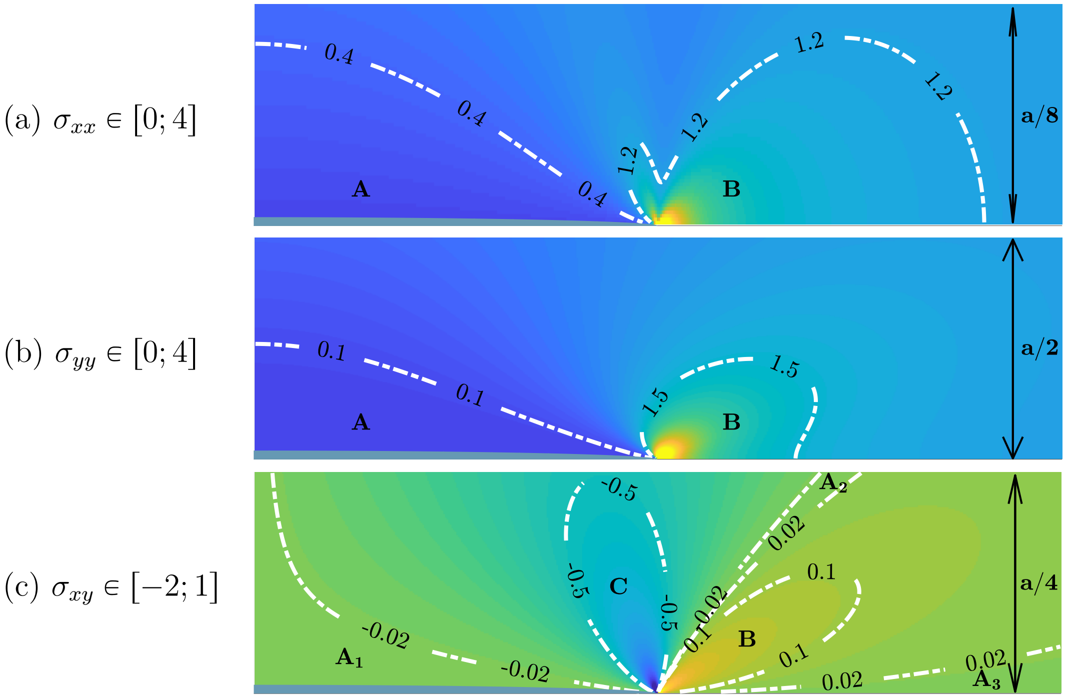

(a) $\sigma_{xx} \in [0; 4]$

(b) $\sigma_{yy} \in [0; 4]$

(c) $\sigma_{xy} \in [-2; 1]$

Figure 3.4: Maps of the stress components σ_{ij} around an isolated crack with $\sigma_k = 1$ GPa (Eqs. 3.14), in a domain $2a > x > 0$, $y > 0$ (see Fig. 3.3). Annotated regions enclosed by contour lines determine the behavior of $P_{ij}(t)$ as $t \to 0, \pm\infty$. Regions A, A_1, A_2, A_3: $t \to 0$. Region B: $t \to \infty$. Region C: $t \to -\infty$. To highlight the field patterns, values lower than a minimum and higher than a maximum are thresholded out (see legend, units are GPa). Lowest values are shown in blue and highest values in yellow. Intermediate values in green and orange.

(3.14) in the limit $\mathrm{d}\theta_1 \to 0$, $\mathrm{d}\theta_2 \to 0$. One obtains:

$$\sigma_{yy} = \sigma_k \frac{1 + 4(x/a)^2}{[1 - (x/a)^2]^{7/2}} \left(\frac{y}{a}\right)^3 + O(y^5). \tag{3.15}$$

When t is small, the region where $0 < \sigma_{yy} < t$ is accordingly delimited by the curves of equation:

$$y = \pm a \frac{[1 - (x/a)^2]^{7/6}}{[1 + 4(x/a)^2]^{1/3}} \frac{t^{1/3}}{\sigma_k^{1/3}}, \qquad -a < x < a \tag{3.16}$$

(region A, Fig. 3.4b). Integrating the above function leads to the extended Van Hove singularity:

$$P\{\sigma_{yy}(\boldsymbol{x}) < t;\ \boldsymbol{x} \in \Omega_k\} = \frac{4a^2 t^{1/3}}{\sigma_k^{1/3} |\Omega_i|} \int_0^1 \frac{\mathrm{d}u (1 - u^2)^{7/6}}{(1 + 4u^2)^{1/3}} + O(t) \approx 0.701 \frac{a^2 t^{1/3}}{D^2 \sigma_k^{1/3}}, \tag{3.17a}$$

$$P_{yy}(\sigma_k; t) \approx 0.234 \frac{a^2}{D^2 \sigma_k^{1/3} t^{2/3}} h(t), \qquad t \to 0, \tag{3.17b}$$

where $h(\bullet) = \max(\mathrm{sign}(\bullet), 0)$ denotes the Heaviside function.

Component σ_{xx} vanishes along the crack lips (region A, Fig. 3.4a), and its probability distribution function P_{xx} presents a jump at $t = 0$:

$$\sigma_{xx} = \frac{2\sigma_k}{\left[1-(x/a)^2\right]^{3/2}}\frac{y}{a} + O(y^2), \qquad P_{xx}(\sigma_k; t) = \frac{3a^2}{8D^2\sigma_k}h(t), \qquad t \to 0. \tag{3.18}$$

Component σ_{xy} is zero along the two lines $y = 0$, $x = 0$ (regions A_1 and A_3, Fig. 3.4c) and along four curves starting from the crack tip at angles $\theta_1 = \pm\pi/3$, $\theta_2 = \pm 2\pi/3$ (region A_2, Fig. 3.4c). The gradient of the field σ_{xy} is zero along the segment $y = 0$, $-a < x < a$ (region A_1), and is non-zero in regions A_2 and A_3. The contributions to $P_{xy}(t)$ ($t \ll 1$) of regions A_2 and A_3 are accordingly finite, so that only the contribution of region A_1 matters. A Taylor expansion provides in the right-upper quadrant $x > 0$, $y > 0$:

$$\sigma_{xy} = -\frac{3\sigma_k x/a(y/a)^2}{\left[1-(x/a)^2\right]^{5/2}}, \quad P_{xy} = -\frac{a^2\Gamma(-3/4)\Gamma(9/4)}{2\sqrt{3}D^2\pi^{3/2}\sqrt{\sigma_k|t|}} \approx \frac{0.2839a^2}{D^2\sqrt{\sigma_k|t|}}, \quad t \to 0, \tag{3.19}$$

where $\Gamma(\bullet)$ is the extended factorial function, or Gamma function.

The tails of the distributions are now derived using the asymptotic near-tip expansions [229] (see regions B and C in Figs. 3.4a-c):

$$\sigma_{\substack{xx\\yy}} = \frac{\sigma_k\sqrt{a}}{\sqrt{2r_1}}\cos\frac{\theta_1}{2}\left(1 \mp \sin\frac{\theta_1}{2}\sin\frac{3\theta_1}{2}\right), \quad \sigma_{xy} = \frac{\sigma_k\sqrt{a}}{\sqrt{2r_1}}\sin\frac{\theta_1}{2}\cos\frac{\theta_1}{2}\cos\frac{3\theta_1}{2}. \tag{3.20}$$

We solve the three equations $\sigma_{ij} = t$ for $t \to \pm\infty$ and obtain r_1 as a function of θ_1 and t. The probability distributions $P_{xx}(\sigma_k; t)$ and $P_{yy}(\sigma_k; t)$ are obtained by integration of $-(4/\pi D^2)r_1\partial_t r_1$ over θ_1 in the range $[-\pi; \pi]$. The distribution $P_{xy}(\sigma_k; t)$ is derived by integration of the same quantity over the domain $[-\pi; -\pi/3] \cup [0; \pi/3]$ (when $t \to \infty$, see region B, Fig. 3.4c) and $[-\pi/3; 0] \cup [\pi/3; \pi]$ (when $t \to -\infty$, see region C, Fig. 3.4c). This yields, to leading order-term in t:

$$P_{xx}(\sigma_k; t) \sim \frac{177a^2\sigma_k^4}{512D^2t^5}, \qquad t \to +\infty, \tag{3.21a}$$

$$P_{yy}(\sigma_k; t) \sim \frac{1089a^2\sigma_k^4}{512D^2t^5}, \qquad t \to +\infty, \tag{3.21b}$$

$$P_{xy}(\sigma_k; t) \sim \frac{9a^2\sigma_k^4}{1024D^2|t|^5}, \qquad t \to \pm\infty. \tag{3.21c}$$

The various probability distribution functions $\overline{P}_{ij}(t) = P_{ij}(\sigma_k = 1; t)$, computed numerically from (3.14) on grids of 5000^2 voxels, are shown in Fig. (3.5a). They present Van Hove singularities not only at $t = 0, \pm\infty$ but also at various finite values of t. For reasons that will be clear later on, we do not investigate the later.

Randomly-oriented non-interacting cracks Assume now that the material is made up of widely-separated cracks with uniformly-distributed orientations in the (e_x, e_y) plane. Apply as previously a biaxial remote stress $\overline{\sigma}_{xx} = \overline{\sigma}_{yy} = \sigma_k > 0$, $\overline{\sigma}_{xy} = 0$ in plane strain. Consider a crack oriented along a direction $0 \leqslant \beta \leqslant \pi$ with respect to the x-axis. The stress components σ_{ij}^{β} are obtained by a rotation of angle β in the plane (e_x, e_y) of the stress tensor given in (3.14). For instance σ_{xx}^{β} reads:

$$\sigma_{xx}^{\beta} = \sigma_{xx}\cos^2\beta + \sigma_{yy}\sin^2\beta - \sigma_{xy}\sin(2\beta). \tag{3.22}$$

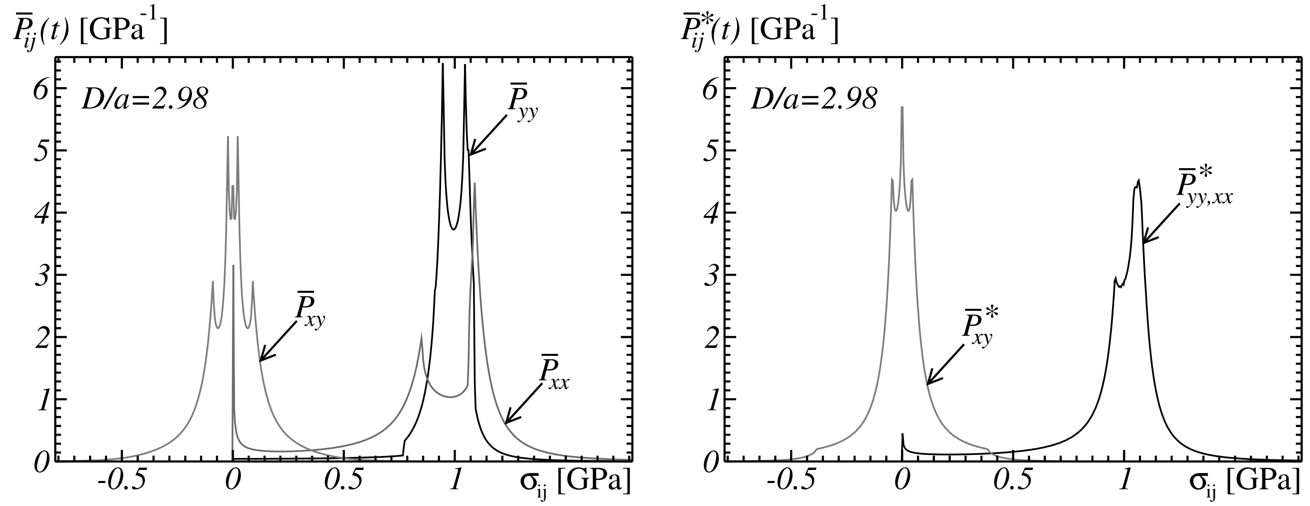

(a) (b)

Figure 3.5: (a) Probability distribution functions $\overline{P}_{ij}(t)$ for the stress component σ_{ij} around an isolated crack of length a, in a disk-shaped domain of radius D centered around the crack. (b) Probability distribution functions $\overline{P}^*_{ij}(t)$ for the stress component σ_{ij} around a set of isolated cracks of length a with uniform orientations, in disk-shaped domains of radius D centered around each crack.

The stress component σ^{β}_{xx} vanishes along the crack tips and a Taylor expansion provides:

$$\sigma^{\beta}_{xx} = 2\cos^2\beta\sigma_k(y/a)/[1-(x/a)^2]^{3/2}, \qquad y \to 0, \quad -a < x < a. \tag{3.23}$$

Accordingly, the corresponding distribution presents a jump and:

$$P^{\beta}_{xx}(\sigma_k; t=0) \approx \frac{3a^2}{8D^2\sigma_k\cos^2\beta}h(t), \qquad t \to 0. \tag{3.24}$$

The above equation reduces to (3.18) in the special case $\beta = 0$. The jump in (3.24) also blows up when $\beta = \pi/2$, at which point P^{β}_{xx} develops the singularity given in (3.17b).

Consider now the p.d.f. $P^*_{xx}(\sigma_k; t) = \langle P^{\beta}_{xx}(\sigma_k; t)\rangle_{\beta}$ of the stress fields surrounding cracks with stress factor σ_k, averaged over all orientations β. The smallest values of σ_k are concentrated in a region near the crack tips. Furthermore, the size of this region is much more important for cracks oriented with an angle $\beta \approx \pi/2$. Let us first examine the contribution of the values located along the line $x = 0$. Set $r = y$, $\theta = \pi/2$, $\theta_1 + \theta_2 = \pi$, $r_1 = r_2$ in (3.14) and (3.22). We obtain:

$$\sigma^{\beta}_{xx}(0, y) = \frac{\sigma_k y\left(a^2\cos(2\beta) + a^2 + y^2\right)}{\left(a^2 + y^2\right)^{3/2}}. \tag{3.25}$$

We solve $\sigma^{\beta}_{xx} = t$ for β and determine the interval $\beta \in [\beta_1(y,t); \pi/2]$ that contributes to values of σ^{β}_{xx} in the range $[0; t]$. This interval is not empty whenever $y < y_{\max} = at^{1/3}/\sqrt{\sigma_k^{2/3} - t^{2/3}}$. The region of interest, where the r.h.s. of (3.24) blows up, is $y \approx y_{\max}$ (as also confirmed by Eq. 3.16), therefore we make use of the variable change $y = y't^{1/3}$ in the following integral and obtain to leading-order in t:

$$\int_0^{y_{\max}(t)} \mathrm{d}y\ [\pi/2 - \beta_1(y,t)] \ \propto\ \frac{at^{2/3}}{\sigma_k^{2/3}}, \qquad t \to 0^+. \tag{3.26}$$

Accordingly, the contribution of the line $x = 0$ to P^*_{xx} scales as $\sim t^{-1/3}$. The analytical computation of the contribution of the entire domain Ω proves cumbersome and we resort to numerical computations. The distribution P^β_{xx} is computed by discretization of the field σ^β_{xx} on a grid of $10,000^2$ pixels, and P^*_{xx} is computed by averaging over 100 regularly-spaced values of the angle β. A fit of the numerical data, gives, with excellent agreement over two decades (see Fig. 3.6a):

$$P^*_{xx}(\sigma_k;t) \sim 0.44\frac{a^2\sigma_k^{1/3}}{D^2}t^{-0.33}, \qquad t \to 0^+, \tag{3.27}$$

which suggests an extended Van Hove singularity $P^*_{xx} = P^*_{yy} \sim t^{-1/3}$, as hinted by (3.26). This is a less singular behavior at the origin than that of the probability distribution P_{yy} obtained for parallel cracks (Eq. 3.17b), which blows up as $\sim t^{-2/3}$.

Regarding component σ_{xy}, numerical computations also provide the following fit:

$$P^*_{xy}(\sigma_k;t) \approx -0.91\frac{a^2}{D^2}\log\frac{|t|}{\sigma_k}, \qquad t \to 0, \tag{3.28}$$

with good agreement ranging over two and a half decades (see Fig. 3.6b). A powerlaw with small exponent $P^*_{xy} \sim t^{-0.1}$ instead of a logarithm can not be ruled out (Fig. 3.6b, inset) but appears less consistent with the data available. The logarithmic blow-up (3.28) is a weaker singularity than that obtained for the traction components σ_{xx} or σ_{yy} (Eq. 3.27).

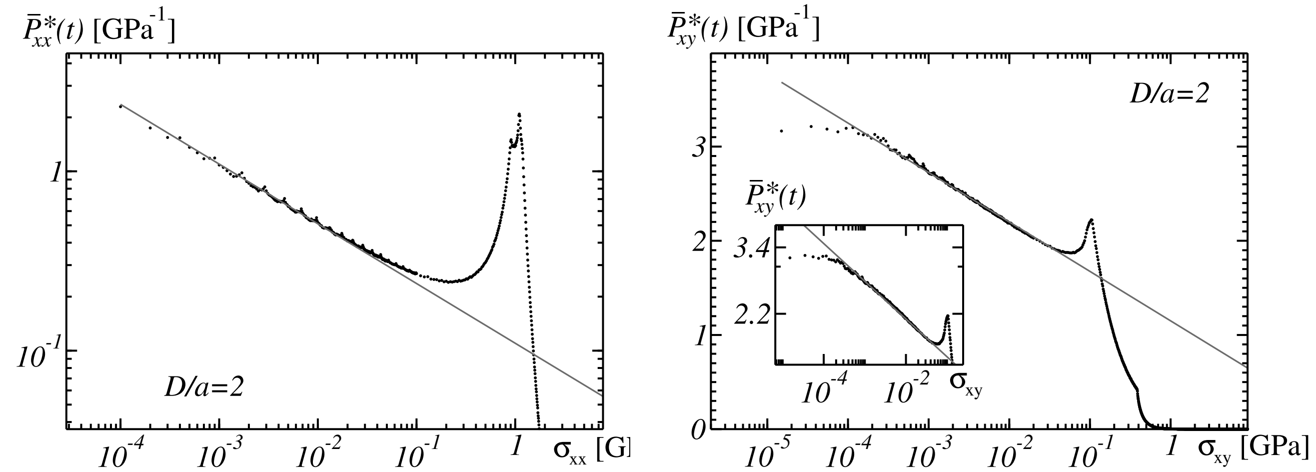

(a) (b)

Figure 3.6: Numerical fit of the probability distribution functions $\overline{P}^*_{xx}$, in log-log plot (a) and $\overline{P}^*_{xy}$, in semi-log plot (b) for components σ_{xx} and σ_{xy}, in media with randomly-oriented cracks. Solid line in (a): fit (3.27); in (b): fit (3.28), up to a constant term. Inset in (b): log-log plot of the data with fit $\overline{P}^*_{xy} = 5.5(a/D)^2(t/\sigma_k)^{-0.1}$.

Finally, the behavior at $t = \pm\infty$ is computed analytically in the same manner as in Sec. (3.3.1). We obtain, the x- and y-axis being statistically equivalent directions:

$$P^*_{\substack{xx\\yy}}(\sigma_k;t) \sim \frac{585a^2\sigma_k^4}{512D^2t^5}, \qquad t \to +\infty, \tag{3.29a}$$

$$P^*_{xy}(\sigma_k;t) \sim \frac{9a^2\sigma_k^4}{1024D^2|t|^5}, \qquad t \to \pm\infty. \tag{3.29b}$$

Observe that the prefactor for P^*_{xx} (or P^*_{yy}) lies in-between that of P_{xx} and P_{yy}, while it is unchanged for the shear component xy (Eq. 3.21c).

The probability distribution functions $\overline{P}^*_{ij}(t)$, are shown in Fig. (3.5b). They are computed numerically from (3.14) and (3.22) on grids of 5000^2 voxels. The parameter β is discretized along 200 values. Note that, as for the distribution functions $\overline{P}_{ij}$, they present Van Hove singularities at finite values of t, not investigated in the present work.

Parallel and randomly-oriented interacting cracks Consider now a population of interacting identical cracks, either parallel to one another or randomly-oriented. To take into account crack interactions, we assume that the overall distribution of the stress field around the cracks is the same as that of a set of isolated cracks subjected to random stress intensity factors, with a probability law for the stress intensity factors to be determined. As in the previous sections, the material is subjected to plane strain and in-plane biaxial stress loading. The cracks density is monitored by the non-dimensional parameter $\eta = N_c/Sa^2$ where $S = |\Omega|$ is the surface area of the domain Ω and N_c the number of cracks within the domain.

Consider a particular component σ_{ij} in a domain Ω_k containing a crack with remote stress σ_k, and with field distribution P_{ij}. Clearly:

$$P_{ij}(\sigma_k; t) = \frac{1}{|\sigma_k|}\overline{P}_{ij}\left(\frac{t}{\sigma_k}\right), \tag{3.30}$$

where $\overline{P}_{ij}(t) = P_{ij}(1; t)$ is the distribution obtained when taking $\sigma_k = 1$. For a continuous distribution $q(s)$ of stress intensity factors in domains Ω_k ($k = 1, ..., N_c$) with N_c very large, the probability distribution of σ_{ij} over Ω, is given by the convolution product:

$$\widetilde{P}_{ij}(t) = \int_{-\infty}^{+\infty} \mathrm{d}s \frac{q(s)}{|s|}\overline{P}_{ij}\left(\frac{t}{s}\right) = \int_{-\infty}^{+\infty} \mathrm{d}u \frac{\overline{P}_{ij}(u)}{|u|} q\left(\frac{t}{u}\right), \qquad \int_{-\infty}^{\infty} \mathrm{d}s\, q(s) = 1. \tag{3.31}$$

We also denote $\widetilde{P}^*_{ij}(t)$ the orientation-averaged distribution $\widetilde{P}_{ij}(t)$, equal to:

$$\widetilde{P}^*_{ij}(t) = \int_{-\infty}^{+\infty} \mathrm{d}s \frac{q^*(s)}{|s|}\overline{P}^*_{ij}\left(\frac{t}{s}\right), \qquad \int_{-\infty}^{\infty} \mathrm{d}s\, q^*(s) = 1, \tag{3.32}$$

where $\overline{P}^*_{ij}(t) = P^*_{ij}(\sigma_k = 1; t)$. The fields moments ($n = 1, 2, ...$) read:

$$\langle t^n \rangle_{\widetilde{P}_{ij}} = \langle t^n \rangle_{\overline{P}_{ij}} \langle t^n \rangle_q, \qquad \langle t^n \rangle_{\widetilde{P}^*_{ij}} = \langle t^n \rangle_{\overline{P}^*_{ij}} \langle t^n \rangle_{q^*}. \tag{3.33}$$

In principle, these formula can be used to reconstruct q knowing $\widetilde{P}_{ij}$ and $\overline{P}_{ij}$, under some conditions [224]. In practice, the problem is ill-posed and efficient numerical algorithms must be implemented [119]. In the present situation, our knowledge of the two moments in (3.33) leads to the natural assumption that q and q^* are Gaussian kernels:

$$q(s) = \frac{1}{\sqrt{2\pi v_q}}\exp\left(-\frac{(s-\mu_q)^2}{2v_q}\right), \qquad q^*(s) = \frac{1}{\sqrt{2\pi v^*_q}}\exp\left(-\frac{(s-\mu^*_q)^2}{2v^*_q}\right), \tag{3.34}$$

where we assume $\mu_q > 0$, $\mu^*_q > 0$. In doing so, we smooth out singularities that may be present in distributions $\overline{P}_{ij}$ and $\overline{P}^*_{ij}$ except possibly at $t = 0$ and $t = +\infty$, which are fixed under the transformation $t \mapsto t/s$. We emphasize that other choices are possible. Kushch et al. [133], notably, modeled the distribution of stress intensity factors in similar heterogeneous media using a Gumbel (double exponential) law.

Let us examine the possible Van Hove singularities of $\widetilde{P}_{ij}$ and $\widetilde{P}^*_{ij}$ as $t \to \pm\infty$. Using Eqs. (3.21) we obtain:

$$\widetilde{P}_{\substack{xx\\yy}}(t) \sim p_{\substack{xx\\yy}}|t|^{-5} \int_0^\infty \mathrm{d}s\, s^4 q(\mathrm{sign}(t)s), \qquad t \to \pm\infty, \tag{3.35a}$$

$$\widetilde{P}_{xy}(t) \sim p_{xy}|t|^{-5} \int_0^\infty \mathrm{d}s\, s^4 \left[q(s) + q(-s)\right], \qquad t \to \pm\infty, \tag{3.35b}$$

where $p_{ij}(t/\sigma_k)^{-5}$ is the asymptotic behavior of $P_{ij}(\sigma_k; t)$ as $t \to \infty$ provided by Eqs. (3.21). The same relations are obtained for $\widetilde{P}^*_{ij}$ with prefactors p_{ij} given by (3.29a) instead. Note that $\widetilde{P}_{xx}$, $\widetilde{P}_{yy}$, $\widetilde{P}^*_{xx}$ and $\widetilde{P}^*_{yy}$ possess distribution tails as $t \to -\infty$, unlike distributions $\overline{P}_{xx}$ and $\overline{P}_{yy}$. The tails are asymmetric: the prefactor at $t = -\infty$ is lower than that obtained in the $t = +\infty$ limit.

The behavior of $\widetilde{P}_{yy}$ as $t \to 0$ is determined as:

$$\widetilde{P}_{yy}(t) \sim p'_{yy}|t|^{-\nu} \int_0^\infty \mathrm{d}s\, s^{\nu-1} q(\mathrm{sign}(t)s), \qquad t \to 0^\pm, \tag{3.36}$$

where $p'_{yy}t^{-\nu}$ ($\nu = 2/3$) is the asymptotic behavior of $P^k_{yy}(\sigma_k; t)$ as $t \to 0^+$ (see Eq. 3.26). The behavior of $\widetilde{P}^*_{xx} = \widetilde{P}^*_{yy}$ as $t \to 0$ is obtained by taking $\nu = 1/3$ and by replacing prefactor p'_{yy} by that provided by Eq. (3.27). The behavior of $\widetilde{P}_{xy}$ as $t \to 0$ is obtained as:

$$\widetilde{P}_{xy}(t) \sim p'_{xy}|t|^{-1/2} \int_0^\infty \mathrm{d}s\, s^{-1/2} \left[q(s) + q(-s)\right], \qquad t \to 0. \tag{3.37}$$

where $p'_{xy}|t|^{-1/2}$ is the asymptotic behavior of P^k_{xy} given in (3.19).

We finally consider distribution $\widetilde{P}_{xx}$ which takes a finite value when $t = 0^+$ and is zero when $t < 0$ (3.18). The integral in (3.32) is splitted into two intervals $[0; t/t_0]$ and $[t/t_0; \infty]$. Assuming $0 < t \ll t_0 \ll 1$:

$$\int_0^{t/t_0} \frac{\mathrm{d}s}{s} q\left(\frac{t}{s}\right) \overline{P}_{xx}(s) \approx -q(t_0)\overline{P}_{xx}(0)\log(t_0), \tag{3.38a}$$

$$\int_{t/t_0}^\infty \frac{\mathrm{d}s}{s} q\left(\frac{t}{s}\right) \overline{P}_{xx}(s) \approx -q(t_0)\overline{P}_{xx}(0)\log\frac{t}{t_0}. \tag{3.38b}$$

A similar behavior is obtained when $t \to 0^-$ so that:

$$\widetilde{P}_{xx}(t) \sim -q(0)\overline{P}_{xx}(0^+)\log|t|, \qquad t \to 0^\pm. \tag{3.39}$$

This singularity, a logarithmic blow-up, is generated by regions around cracks subjected to nearly zero remote stress, consistently with (3.32). Notice that $\overline{P}_{xx}$ displays a finite jump at $t = 0$ (Eq. 3.18), unlike $\widetilde{P}_{xx}$. A similar treatment, carried out on distribution $\overline{P}^*_{xy}$ (Eq. 3.28), leads to:

$$\widetilde{P}^*_{xy}(t) \sim \frac{q(0)}{2}\log^2|t|, \qquad t \to 0^\pm. \tag{3.40}$$

	σ_{ij}	$\overline{P}_{ij}$	$\widetilde{P}_{ij}$	$\overline{P}^*_{ij}$	$\widetilde{P}^*_{ij}$
$t = 0^\pm$	σ_{xx}	$h(t)$	$-\log\|t\|$	$h(t)\|t\|^{-0.33}$	$h_\bullet(t)\|t\|^{-0.33}$
	σ_{yy}	$h(t)\|t\|^{-2/3}$	$h_\bullet(t)\|t\|^{-2/3}$		
	σ_{xy}	$\|t\|^{-1/2}$	$\|t\|^{-1/2}$	$-\log\|t\|$	$\log^2\|t\|$
$t = \pm\infty$	σ_{xx}, σ_{yy}	$h(t)\|t\|^{-5}$	$h_\bullet(t)\|t\|^{-5}$	$h(t)\|t\|^{-5}$	$h_\bullet(t)\|t\|^{-5}$
	σ_{xy}	$\|t\|^{-5}$			

Table 3.1: Van Hove singularities of the probability distribution functions of the stress components σ_{ij} in the non-interacting model of parallel ($\overline{P}_{ij}$) or randomly-oriented ($\overline{P}^*_{ij}$) cracks, and in the respective interacting models ($\widetilde{P}_{ij}$ and $\widetilde{P}^*_{ij}$). Prefactors are omitted for clarity. The term $h_\bullet(t)$ designates a function with a finite jump at $t = 0$, of the type $1 + bh(t)$ with $b > 0$.

Again, the nature of the singularity is different from the logarithmic blow-up found for $\overline{P}^*_{xy}$ in (3.28).

The Van Hove singularities at $t = 0$ and $t = \pm\infty$ of the distribution functions $\overline{P}_{ij}$, $\widetilde{P}_{ij}$, $\overline{P}^*_{ij}$ and $\widetilde{P}^*_{ij}$ are summarized in Tab. (3.1). As previously noted, the singularities of $\widetilde{P}_{ij}$ are different from that of $\overline{P}_{ij}$. For instance $\widetilde{P}_{yy}$ develops powerlaw singularities when $t \to 0^-$ or $t \to -\infty$, contrarily to $\overline{P}_{yy}$ which has support on $[0; \infty[$. Likewise, $\widetilde{P}_{xx}$ develops a logarithmic singularity when $t \to 0^-$, contrarily to $\overline{P}_{xx}$. Also, as will be seen later on, distributions $\widetilde{P}_{ij}(t)$ and $\widetilde{P}^*_{ij}(t)$ do not present singularities at finite (non-zero) values of t.

3.3.2 FFT-based computations

Reconstruction of the overall stress distribution vs. FFT data We compute numerically the stress distributions occurring in the solid phase of a 2D Boolean set [216] of cracks subjected to plane strain. The cracks are parallel to one another. Again, we use the FFT scheme with "backward-forward" finite difference [258], appropriate to the presence of discretized cracks [85], and computations are carried out on two independent realizations of the Boolean model, discretized on a 2048^2-pixels grid. We follow [85] and discretize the cracks as thin rectangles of width $w = 1.5$ voxel. In all computations hereafter, the overall applied stress is by convention equal to 1 GPa so that $\langle\sigma_{xx}\rangle = \langle\sigma_{yy}\rangle = 1$. The cracks have a finite thickness, therefore the mean of the stress field in the solid phase is slightly above 1 GPa.

The probability distribution function $\widetilde{P}_{xx}(t)$ is compared with FFT results in Fig. (3.7a). The first and second moments of the distribution of the stress intensity factor q, used to compute $\widetilde{P}_{xx}(t)$, are adjusted so that the moments of $\widetilde{P}_{xx}(t)$ fit the corresponding FFT data (see 3.33). The values of a and D are chosen so that the crack density parameter η is the same in the FFT computations and in each domain Ω_k, i.e.

$$\eta = \frac{N_c a^2}{S} = \frac{a^2}{\pi D^2}, \tag{3.41}$$

where $N_c = 60$ is the number of cracks in FFT computations, $S = 2048^2$ is the surface of the unit cell, $a = 25$ pixels, and so $\eta \approx 0.035$, $D \approx 75$ pixels. It is emphasized that FFT numerical results have been used, in the present work, to tailor the first and second-order moments of $\widetilde{P}_{xx}$. In principle, however, such moments could be determined using self-consistent estimates. For a cracked body in plane strain, these estimates, which include the case of an anisotropic embedding

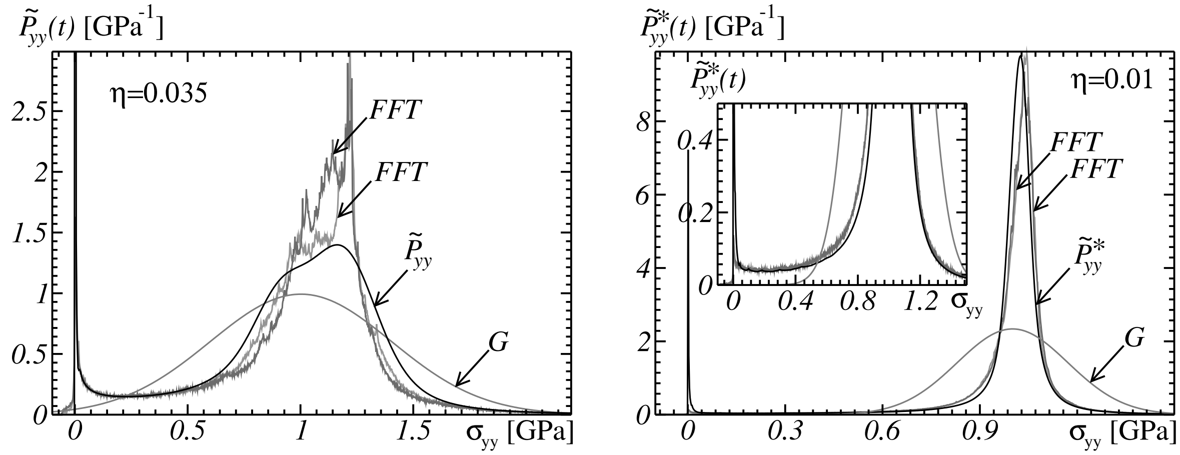

(a) (b)

Figure 3.7: Probability distribution functions $\widetilde{P}_{yy}(t)$ and $\widetilde{P}^*_{yy}(t)$ (solid black lines) for the stress component σ_{yy}, in a matrix containing a set of (a) parallel and (b) randomly-oriented cracks, resp., under plane strain. Gray solid lines: FFT results obtained on two random realizations. Solid line marked G: Gaussian distribution. Inset: enlargement in the region $\widetilde{P}^*_{yy}(t) < 0.5$.

medium, have been derived analytically by Nemat-Nasser & Horri [105].

A similar procedure is used in the random case. Consider the low crack-density regime $\eta \ll 1$. Eq. (3.33) gives the first and second-moments of q^*, given that of $\widetilde{P}^*_{ij}$. The latter are provided by FFT computations, carried out on a 8192^2 pixels grid. We use $a = 25$ pixels, $N_c = 20$, $D = 129$ and $\eta = 0.011$. The mean and second-order moments of $\widetilde{P}^*_{yy}$, given by FFT computations, are 1.0007 and 1.0279 resp. and the mean and variances of q are 1.0103 and $3\,10^{-4}$ resp. Results are shown in Fig. (3.7b).

The method however breaks down when η is larger than about 0.05, at which point (3.33) predicts a negative variance for q, so that this constraint can not be satisfied anymore. Indeed, our method assumes that all cracks are loaded in mode-I. In random media, in reality, the regions in which cracks are embedded are subjected to varying loadings, combining several modes. Furthermore, in the present method, the distribution q entering (3.33) does not depend on the stress component considered, hence, one can not simultaneously satisfy all set of constraints on the first and second moments of the stress components. Taking into account other modes would, in theory, provide additional degrees of freedom, at the expense of a more analytically-involved treatment.

Van Hove singularities We now focus on the singularities of the probability distribution functions $P^{*,FFT}_{ij}$, predicted by numerical FFT computations. All computations are carried out on two independent realizations of a Boolean model of cracks, discretized on a 8192^2 pixel grid containing $N_c = 200$ cracks. To highlight possible Van Hove singularities, we choose a crack density equal to $\eta = 0.12$ with $a = 25$ pixels. The following powerlaw behaviors are observed. When $t \to \pm\infty$:

$$P^{*,FFT}_{xx,yy} \approx |t|^{-5} \times \begin{cases} 1.8, & t \to +\infty, \\ 0.03, & t \to -\infty, \end{cases} \tag{3.42a}$$

$$P^{*,FFT}_{xy} \approx 0.02|t|^{-5}, \qquad t \to \pm\infty \tag{3.42b}$$

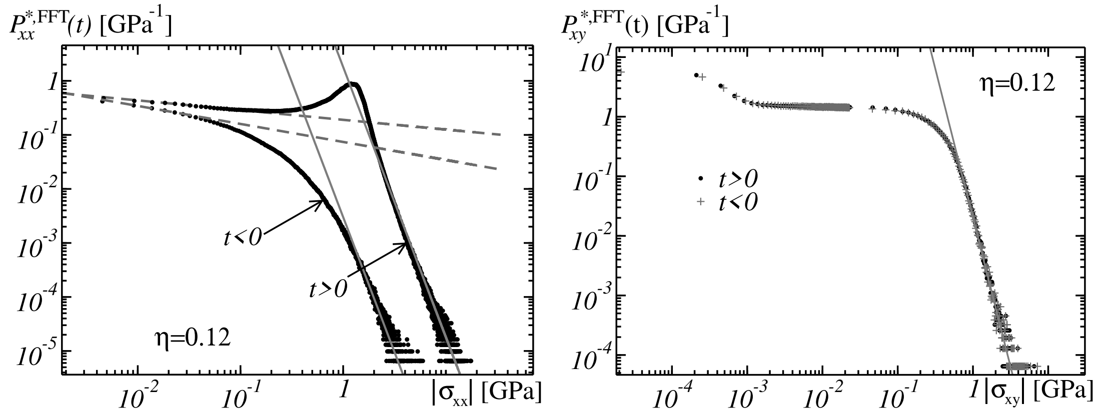

(a) (b)

Figure 3.8: Probability distribution functions $P_{yy}^{*,FFT}$ and $P_{xy}^{*,FFT}$ for the stress components σ_{yy} (a) and σ_{xy} (b) in randomly-oriented cracks, in log-log plot, as predicted by FFT computations. Solid and dotted lines: powerlaw fit (3.42) and (3.43) in the domains $|t| \ll 1$ and $|t| \gg 1$.

(see Figs. 3.8a-b). When $t \to 0$:

$$P_{xx,yy}^{*,FFT} \approx \begin{cases} 0.19t^{-0.18}, & t \to 0^+, \\ 0.074|t|^{-0.33}, & t \to 0^-. \end{cases} \tag{3.43}$$

Fits (3.43) should be taken with care as the two powerlaw regimes are observed on two decades only, or less (see Fig. 3.8a). The behavior of $P_{xy}^{*,FFT}$ as $t \to 0$ is not provided here, as FFT results are inconclusive.

FFT data for the distribution $P_{xx,yy}^{*,FFT}$ are shown in Fig. (3.9) for varying values of the crack

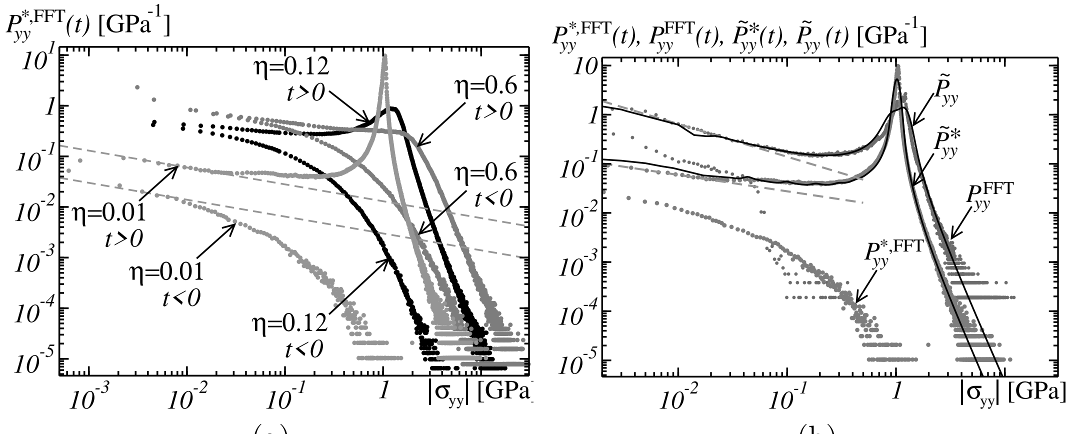

(a) (b)

Figure 3.9: (a) Log-log plot of the probability distribution function $P_{yy}^{*,FFT}$ for the stress components σ_{yy} in media with randomly-oriented cracks, as predicted by FFT computations. Dots: FFT data for $\eta = 0.01$, 0.12 and 0.6. Dashed lines: powerlaws $\sim t^{-1/3}$ (see text). (b) Comparison between the probability distribution functions P_{yy}^{FFT}, $P_{yy}^{*,FFT}$, predicted by FFT (dots) and models $\widetilde{P}_{yy}$ and $\widetilde{P}_{yy}^{*}$ (solid black lines), in log-log plot.

density parameter η. For $\eta = 0.01$, the data is consistent with the prediction $\widetilde{P}^*_{yy}(t) \sim |t|^{-0.33}$ (Tab. 3.1) in the region $t \gtrapprox 0$ (see dashed lines with slope $-1/3$).

Fig. (3.9b) shows, in log-log scale, the distribution functions P^{FFT}_{yy} and $P^{*,FFT}_{yy}$ for the stress component σ_{yy} in media with parallel ($\eta = 0.035$) and randomly-oriented ($\eta = 0.01$) cracks, as computed by FFT (black dots). This data is compared to the estimates $\widetilde{P}_{yy}$ and $\widetilde{P}^*_{yy}$ given by Eq. (3.31) (solid lines). The Van Hove powerlaw singularities for the distribution tails ($t \to \infty$) and near zero ($t \to 0^+$) are accurately reproduced. Dashed lines are powerlaw fits of the FFT data with exponent $-1/3$ and $-2/3$. When $t < 0$ however, estimates $\widetilde{P}_{yy}$ and $\widetilde{P}^*_{yy}$ greatly underestimate the true distributions $P^{FFT}_{yy}(t)$ and $P^{*,FFT}_{yy}(t)$. Indeed, for negative values of t, the distributions $\widetilde{P}_{yy}$ and $\widetilde{P}^*_{yy}$ fall outside of the graph in Fig. (3.9b) and are not represented. But again, the present approach does not take into account mixed-mode loadings and all cracks are supposed open so that high negative values of the stress components are presumably induced by regions around crack tips subjected to compression or mixed-mode loadings, which are not taken into account in the present approach.

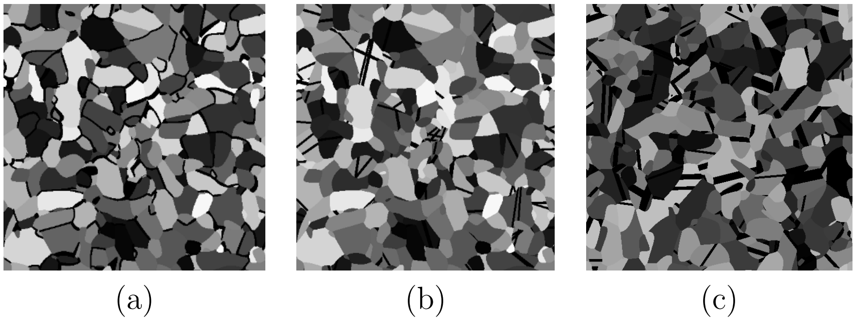
(a) (b) (c)

Figure 3.10: (a) Polycrystal model JM-I with integranular cracks. (b) Model JM-T with transgranular cracks. Cracks orientation uncorrelated to the crystal symmetry axis. (c) Model JM-TW with "weak-plane" transgranular cracks. Cracks oriented parallel to the basal plane in each crystal.

3.4 Field distributions in cracked polycrystals

This section is concerned with various models of cracked polycrystals based on the Johnson-Mehl model and introduced in [86]. The first one is a polycrystal with intergranular cracks, denoted JM-I and represented in Fig. (3.10a). Three transgranular cracks models are also considered. In the first one, denoted (JM-T), crystals and cracks orientations are uncorrelated and uniformly-distributed on the sphere (Fig. 3.10b). In the other two transgranular crack models, the cracks orientation are correlated to the crystal directions. In the "weak-plane" transgranular model, denoted (JM-TW), cracks are oriented parallel to the crystal basal plane (Fig. 3.10c). In the stiff-plane model, denoted (JM-TS), the cracks are oriented perpendicular to the basal plane. Finally, for comparison purposes, we also consider a homogeneous body containing cracks, denoted (JM-IB), obtained by replacing the grains in model (JM-I) by a homogeneous isotropic medium with the same elastic properties as those of the sound polycrystal. The density of cracks is fixed to $\eta = 0.24$ in all models.

The distributions of the equivalent strain $\varepsilon_{\mathrm{eq}}$, mean strain ε_{m} and shear strain ε_{xy} are shown in Figs. (3.11a-f), for hydrostatic strain loading $\langle\varepsilon_{\mathrm{m}}\rangle = 1$ and shear strain $\langle\varepsilon_{xy}\rangle = 0.5$. Solid lines

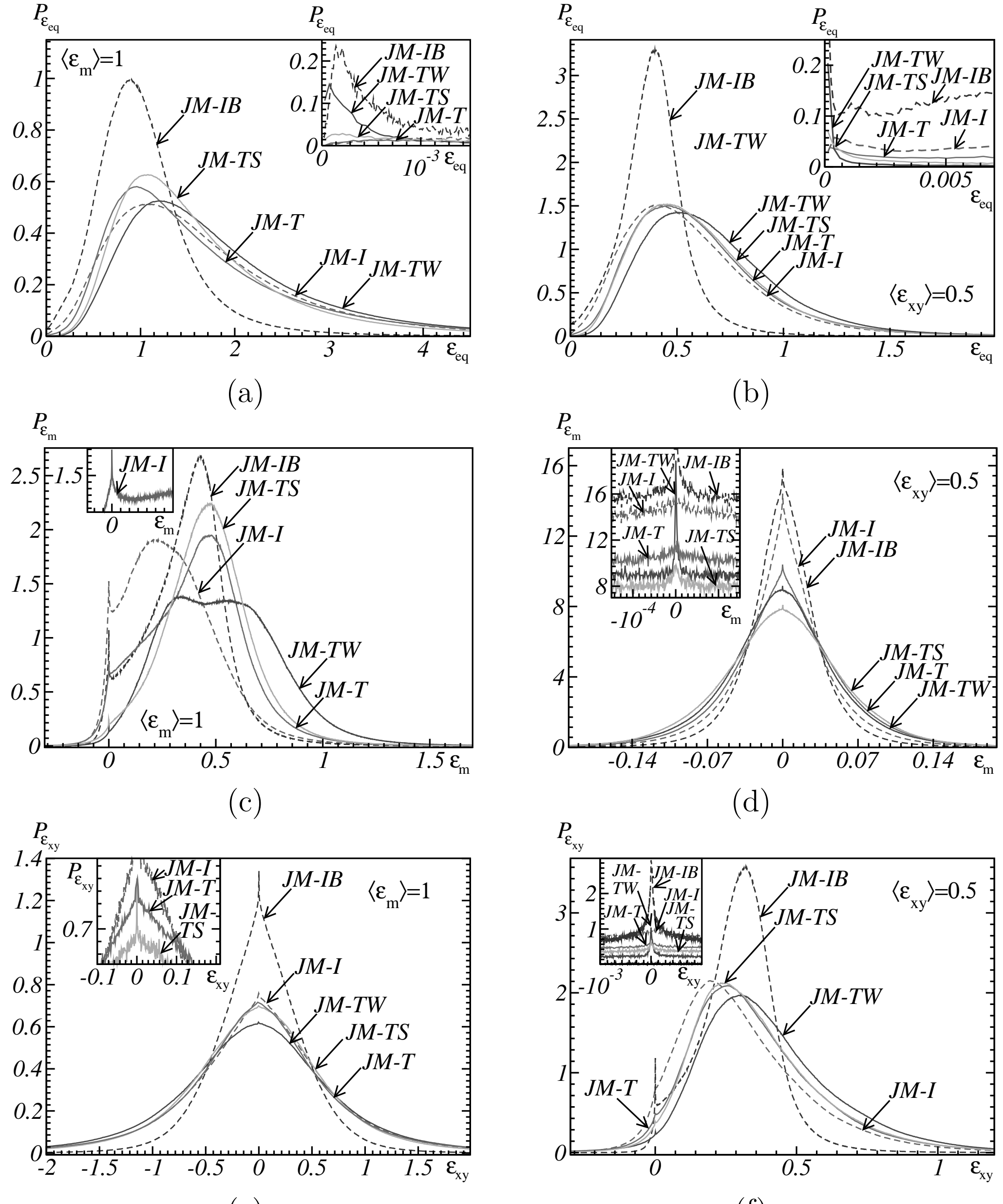

(a) (b)

(c) (d)

(e) (f)

Figure 3.11: Histograms of the strain field components ε_{eq} (a,b), ε_{m} (c,d), ε_{xy} (e,f) in various cracked media, subjected to hydrostatic strain loading (a,c,e) or shear (b,d,f). JM-I: polycrystal with intergranular cracks. JM-T: transgranular cracks. JM-TW: "weak-plane" transgranular cracks. JM-TS: "stiff-plane" transgranular cracks. JM-IB: homogeneous cracked body. Embedded graphs: strain distribution in the region $\boldsymbol{\varepsilon} \approx 0$.

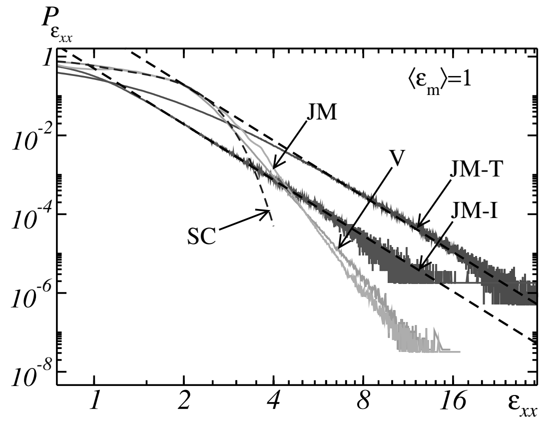

Figure 3.12: Tail of the distributions $P_{\varepsilon_{xx}}(t)$ $(t \gg 1)$ of the strain field ε_{xx} in media subjected to hydrostatic strain loading: comparison between sound Voronoi (V) and Johnson-Mehl (JM) polycrystals and cracked models JM-I (intergranular cracks) and JM-T (uncorrelated transgranular cracks), represented in log-log plot. Black dashed lines: powerlaw fits $P_{\varepsilon_{xx}}(t) = 0.5t^{-4.7}$ and $P_{\varepsilon_{xx}}(t) = 10t^{-4.7}$. Gray dashed line marked SC: self-consistent estimate for a sound polycrystal.

represent polycrystals with transgranular cracks. Dashed lines refer to the integranular model (JM-I) and homogeneous cracked medium (JM-IB). Overall, the field distributions differ significantly depending on the microstructure. In models with transgranular cracks, the correlation between the cracks orientation and the grains basal plane has a strong effect on the field distribution ε_{m}, for hydrostatic strain loading (Figs. 3.11c).

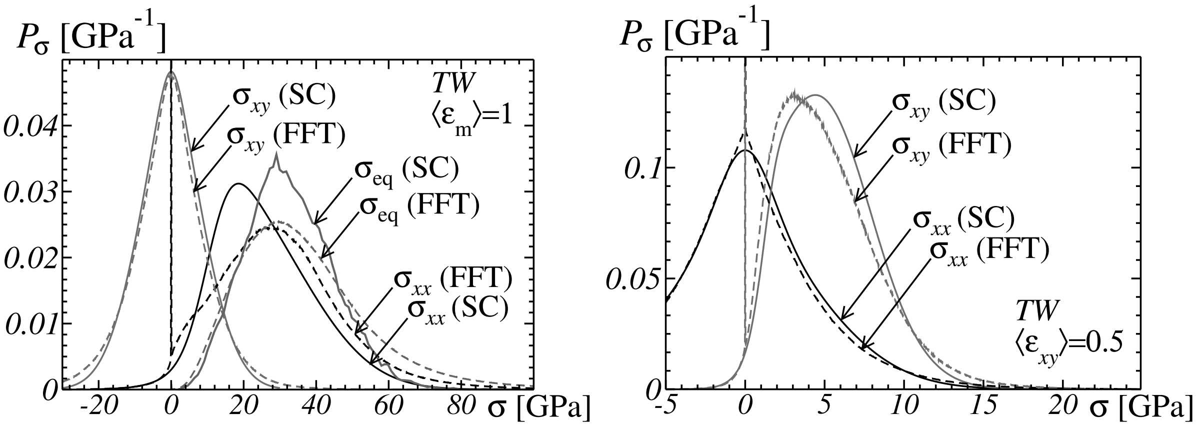

(a) (b)

Figure 3.13: Distribution of stress components σ_{xx}, σ_{eq} and σ_{xy} in a polycrystal with transgranular cracks oriented along basal planes (model "TW"). Solid lines: self-consistent estimates; dashed lines: FFT computations. (a): Hydrostatic strain loading. (b) Shear strain loading.

All field distributions exhibit a singularity, or accumulation point at $\varepsilon = 0$. For the von Mises equivalent deviatoric part $\varepsilon_{\mathrm{eq}}$, a local peak appears near $\varepsilon = 0$, in all models, whereas the distributions for $\varepsilon_{\mathrm{eq}}$ and ε_{xy} blow up at $\varepsilon = 0$. The peak appears to be more important for model with intergranular cracks than for models with transgranular cracks.

The decay of the distribution tails for the strain component ε_{xx} is shown in Fig. (3.12), for various models subjected to hydrostatic loading. The transgranular model (JM-T) and intergranular model (JM-I) as well as a sound polycrystal model, with Johnson-Mehl (JM) or Voronoi (V) tessellation are considered. Models (JM-T) and (JM-I) exhibit powerlaw decays $P_{\varepsilon_{xx}}(t) \sim t^{-\nu}$ as $t \to \infty$ with $\nu \approx 4.7 \approx 5$. This exponent is close to that obtained in plane strain (Sec. 3.3). As shown by Fig. (3.12), the distribution of the field ε_{xx} decays at a much faster rate in sound polycrystal models (light gray curves) than in cracked polycrystal models (dark gray curves). For Jonsohn-Mehl and Voronoi sound polycrystals, the rate of decay for the distribution $P_{\varepsilon_{xx}}(t)$ as $t \to \infty$ is close to that of a powerlaw. The exponent of the powerlaw is about -8. It varies greatly with the realization of the model (not shown) but is nevertheless much lower than -5. In any case, such powerlaw decay may result from the blow-up of the elastic fields at multimaterial corners, which has been studied, notably, in plane strain and plane stress problems [18, 17, 146, 16, 147]. The powerlaw decay is not predicted by the self-consistent method described in Sec. (3.2), which assumes a Gaussian intraphase field distribution (dashed line, Fig. 3.12).

We close this section by further considerations regarding a particular model, the one containing weak-plane transgranular cracks (JM-TW). We make use of a self-consistent estimate, proposed in [86] for this model, which assumes separation of scales between the cracks and grains. In this method, the elastic moduli of each grain is weakened by the presence of micro-cracks. Thus, the same methodology as proposed in Sec. (3.2) may be applied to model (JM-TW), provided that the grains are replaced by weakened grains. Our results for the distribution of the stress components σ_{eq}, σ_{xx} and σ_{xy} are shown in Fig. (3.13) and compared to FFT predictions. As previously, hydrostatic or shear loading is applied, and the FFT histograms are computed in the matrix only, as for the strain. In FFT computations, Van Hove singularities appear at $\boldsymbol{\sigma} = 0$. As expected, the reconstruction making use of the self-consistent estimates are unable to reproduce such singularities.

3.5 Conclusion

To investigate how one may use homogenization theories to predict the field probability distribution functions in linear elastic solids, the present contribution has examined two model problems in mechanics, that of a polycrystal and that of cracked media. Two different methods have been followed, based on an ansatz for the field distributions in grains or in regions surrounding a crack. Our main results are as follows.

The probability distribution function of the local elastic fields in sound polycrystals, with highly anisotropic grains and Johnson-Mehl or Voronoi tessellation microstructures, is accurately predicted by the self-consistent model and an hypothesis of multivariate Gaussian distribution of the intraphase strain and stress fields, except for the distribution tails. The method is not sufficient, however, when dealing with media containing cracks. The elastic fields in this case exhibit extended Van Hove singularities at $\boldsymbol{\varepsilon} = 0$ or $\boldsymbol{\sigma} = 0$, even when the cracks are randomly-distributed and randomly-oriented.

For the model problem of a homogeneous body containing a population of cracks and subjected to plane strain, in particular, the probability distribution for the stress field exhibits a powerlaw decay $\sim |\sigma_{ij}|^{-5}$ as $\sigma_{ij} \to \pm\infty$, resulting from the singularity of the elastic field at the crack tip. A method has been proposed to reconstruct the probability distribution function of the stress fields, based on the assumption that the field surrounding each crack is governed by a stress intensity factor which follows a Gaussian probability distribution. The method gives accurate predictions for the probability distribution when the density of cracks is small, except for negative field values. Finally, numerical Fourier-based computations carried out in cracked media in 2D and 3D suggest a powerlaw decay $\sim |\sigma_{ij}|^{-5}$. In 3D cracked polycrystals, FFT data confirm the existence of Van Hove singularities at $\sigma_{ij} = 0$.

Acknowledgements I am indebted to R. Brenner for the reconstruction of the fields distribution in Fig. 3.2 and for the text in Sec. 3.2.2.

Part II

Perfectly-plastic media

Chapter 4

Minimal paths in random media

In this chapter, we develop a method for computing upper-bounds on the length of geodesics spanning random sets in two, three (or more) dimensions, with emphasis on Boolean models containing a vanishingly small surface or volume fraction of inclusions $f \ll 1$. The distance function is zero inside the grains and equal to the Euclidean distance outside of them, and the geodesics are shortest paths connecting two points far from each other. The asymptotic behavior of the upper-bounds is derived in the limit $f \to 0$. The scalings involve powerlaws with fractional exponents $\sim f^{2/3}$ for Boolean sets of disks and $\sim f^{1/2}$ for the Boolean set of spheres. These results are extended to models of hyperspheres in arbitrary dimension and, in two and three dimensions, to a more general problem where the distance function is non-zero in the inclusions. Finally, other fractional exponents are derived for geodesics spanning multiscale (Cox) Boolean sets, based on inhomogeneous Poisson point processes, in two and three dimensions.

4.1 Introduction

The present chapter deals with various types of random sets representing microstructures, which are made of particles embedded in a matrix. We focus on Boolean sets [158], studied in G. Matheron's seminal works [153, 155], for both theoretical and practical reasons. On the theoretical side, a key property of these models is that of "infinite divisibility" [217]. Boolean models are obtained as the limit of unions of non-Boolean models such as tessellations [217]. This property is regarded as analogous, in the context of random sets, to that of the central limit theorem [217, 55] and suggest that, from a theoretical point of view, Boolean sets play the same role with respect to unions as the Gaussian distribution with respect to summation. On the practical side, Boolean models are straightforward to simulate, and are arguably the most commonly-used for representing random structures of the matrix-inclusion type (for a few examples among many, see e.g. [97, 240, 31]).

4.2 Boolean set of disks in two dimensions

This section details how to construct an upper-bound for the length of minimal paths spanning random media in the continuum. Out attention is restricted to particulate materials with dilute concentration of heterogeneities. We compare the bound with numerical results for the length of geodesics in finite-size systems. We also investigate the “rugosity” of the path used to construct the bound and that of the minimal path.

Hereafter, a Boolean set [156, 217] of disks in $\mathbb{R}^2$, of surface fraction $0 \leqslant f \leqslant 1$ is considered. The disks have constant diameter $D > 0$ and may interpenetrate. Their centers follow a homogeneous Poisson point process. Disks are crossed at no cost whereas the embedding medium is crossed at a unit cost. The distance between two points $\boldsymbol{A}$ and $\boldsymbol{B}$ therefore reads:

$$\begin{aligned} d(\boldsymbol{A},\boldsymbol{B}) &= \inf_{\boldsymbol{p}\in\mathcal{K}} \int_0^1 \mathrm{d}t\ \chi(\boldsymbol{p}(t))\,||\partial_t \boldsymbol{p}(t)||\,, \qquad (4.1)\\ \chi(\boldsymbol{M}) &= \begin{cases} 0 & \text{if } \boldsymbol{M} \text{ lies inside a disk,}\\ 1 & \text{otherwise,}\end{cases}\end{aligned}$$

where χ is the indicator function of the embedding medium, $||\cdot||$ is the Euclidean norm and:

$$\mathcal{K} = \left\{\boldsymbol{p} \in \mathcal{C}\left([0;1],\mathbb{R}^2\right), \quad \boldsymbol{p}(0) = \boldsymbol{A}, \quad \boldsymbol{p}(1) = \boldsymbol{B}\right\} \tag{4.2}$$

is the set of continuous curves from $\boldsymbol{A}$ to $\boldsymbol{B}$. Some immediate properties of the function $d(\cdot,\cdot)$ follow from (4.1). For all points $\boldsymbol{A}$, $\boldsymbol{B}$ and $\boldsymbol{C}$:

$$\begin{aligned} d(\boldsymbol{A},\boldsymbol{A}) &= 0, \qquad d(\boldsymbol{A},\boldsymbol{B}) = d(\boldsymbol{B},\boldsymbol{A}) \geqslant 0, &(4.3\text{a})\\ d(\boldsymbol{A},\boldsymbol{B}) &\leqslant d(\boldsymbol{A},\boldsymbol{C}) + d(\boldsymbol{B},\boldsymbol{C}), \qquad d(\boldsymbol{A},\boldsymbol{B}) \leqslant ||\boldsymbol{B}-\boldsymbol{A}||, &(4.3\text{b})\end{aligned}$$

so that d is a pseudo-distance. Also from (4.1), it is clear that any continuous portion $\boldsymbol{p}'$ of the path $\boldsymbol{p}$ is a minimal path between its extremal points. Accordingly, if the path $\boldsymbol{p}'$ lies entirely in the embedding medium ($\chi(\boldsymbol{p}'(t)) \equiv 1$), it is necessarily straight. Therefore, minimal paths are unions of segments joining disk centers. Assume, for convenience, that the end points of the line segments are $(\boldsymbol{A};\boldsymbol{C}^1;...;\boldsymbol{C}^N;\boldsymbol{B})$ ($N \geqslant 0$) where the $\boldsymbol{C}^i$ are disk centers of coordinates $(C_1^i;C_2^i)$.

We now focus on the limiting behavior of the normalized distance:

$$\xi = \frac{d(\boldsymbol{A},\boldsymbol{B})}{L}, \qquad L = ||\boldsymbol{A}-\boldsymbol{B}|| \to \infty. \tag{4.4}$$

Without loss of generality, we assume that $\boldsymbol{A}$ is the center of a disk at the origin of a Cartesian coordinate system $(\mathbf{e}_1;\mathbf{e}_2)$ and that the line joining $\boldsymbol{A}$ and $\boldsymbol{B}$ is parallel to $\mathbf{e}_1$. When $\boldsymbol{A}$ is fixed and $L \to \infty$, the computation of ξ amounts to study the limit shape of the set:

$$S_t = \left\{\frac{1}{t}\boldsymbol{B}; \quad d(\boldsymbol{A},\boldsymbol{B}) \leqslant t\right\}, \qquad \frac{1}{t}\boldsymbol{B} = \left(\frac{B_1}{t};\frac{B_2}{t}\right), \tag{4.5}$$

as $t \to \infty$. The above can be regarded as a growth process in the continuum [106, 59]. In the present work, an isotropic Boolean set of disks is considered, and so the limiting shape S_∞ of S_t is a disk with radius $\lim_{L\to\infty}(1/\xi)$.

In the rest of this work, we study the behavior of $\lim_{L\to\infty}\xi$ in the dilute limit $f \to 0$, and more exactly its leading-order correction in f. In effect, this amount to take the double limit:

$$\lim_{f\to 0}\lim_{L\to\infty}\xi. \tag{4.6}$$

The two limits are not interchangeable, for if $\boldsymbol{A}$ and $\boldsymbol{B}$ are fixed and $f \to 0$, the minimal path between $\boldsymbol{A}$ and $\boldsymbol{B}$ is almost surely a straight line and $\xi = 1$. Therefore, in the rest of this work $f \ll 1$ is fixed and $L \gg D$ is chosen sufficiently large that the minimal path between $\boldsymbol{A}$ and $\boldsymbol{B}$ passes through a very large number of disks ($N \gg 1$).

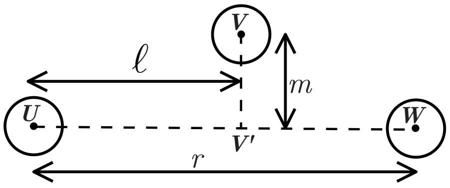

Figure 4.1: Three disks with centers $\boldsymbol{U}$, $\boldsymbol{V}$ and $\boldsymbol{W}$.

4.2.1 Three discs

Consider three non-intersecting discs, identified by their centers $\boldsymbol{U}$, $\boldsymbol{V}$ and $\boldsymbol{W}$. We denote by $\boldsymbol{V}'$ the projection of $\boldsymbol{V}$ onto the line $(\boldsymbol{UW})$ and set $\ell = ||\boldsymbol{U} - \boldsymbol{V}'||$, $m = ||\boldsymbol{V} - \boldsymbol{V}'||$ and $r = ||\boldsymbol{U} - \boldsymbol{W}||$ (see Fig. 4.1). We are interested in the condition under which a path of minimal length joining $\boldsymbol{U}$ to $\boldsymbol{W}$ must pass through $\boldsymbol{V}$. Inequality:

$$||\boldsymbol{U} - \boldsymbol{V}|| - D + ||\boldsymbol{V} - \boldsymbol{W}|| - D \leqslant ||\boldsymbol{U} - \boldsymbol{W}|| - D$$

yields:

$$m \leqslant \frac{\sqrt{D(D+2r)(D+2r-2\ell)(D+2\ell)}}{2(D+r)}. \tag{4.7}$$

In the dilute limit $f \to 0$, taking $r \gg D$ and $\ell \gg D$, (4.7) reduces to:

$$m \leqslant \sqrt{2D\ell(1-\ell/r)}. \tag{4.8}$$

Assuming that $\boldsymbol{U}$ and $\boldsymbol{W}$ are fixed, equation (4.7) defines a domain of interest where disks may be looked for, in order to construct paths with small length. The surface of domain (4.8), scales as:

$$S = 2\int_0^r \sqrt{2D\ell(1-\ell/r)}\mathrm{d}\ell = \frac{\pi r\sqrt{Dr}}{\sqrt{8}}. \tag{4.9}$$

The width of this domain grows as $\sim \sqrt{r}$, which suggests a power-law behavior for the length of minimal paths in the dilute limit, in the continuum, following the argument of Roux & François [205]. This is detailed hereafter by the derivation of an upper-bound on ξ.

4.2.2 Upper-bound in the dilute limit

We identify $\boldsymbol{U}$ with the center $\boldsymbol{C}^i$ of the i^{th} disk on a path $(\boldsymbol{C}^1; ...; \boldsymbol{C}^N)$ and $\boldsymbol{W}$ as the "first" disk encountered in the direction $\mathbf{e}_1$ starting from $\boldsymbol{U}$, if the path was straight. The choice $\boldsymbol{C}^{i+1} = \boldsymbol{W}$ amounts to follow closely direction $\mathbf{e}_1$ and is not advantageous, unless there exists no disk $\boldsymbol{V}$ satisfying (4.7), an event that has a low probability. Hence, we consider instead the disk $\boldsymbol{V}$ satisfying (4.8) with minimal value of ℓ. Clearly, $\ell \ll r$ and condition (4.8) becomes:

$$m \leqslant \sqrt{2D\ell}. \tag{4.10}$$

The above property suggests the following iterative procedure for constructing a path $(\boldsymbol{C}^0; \boldsymbol{C}^1; ...; \boldsymbol{C}^N)$ starting with the point $\boldsymbol{C}^0$. Knowing $\boldsymbol{C}^i$, $\boldsymbol{C}^{i+1}$ is the disk in the domain delimited by two

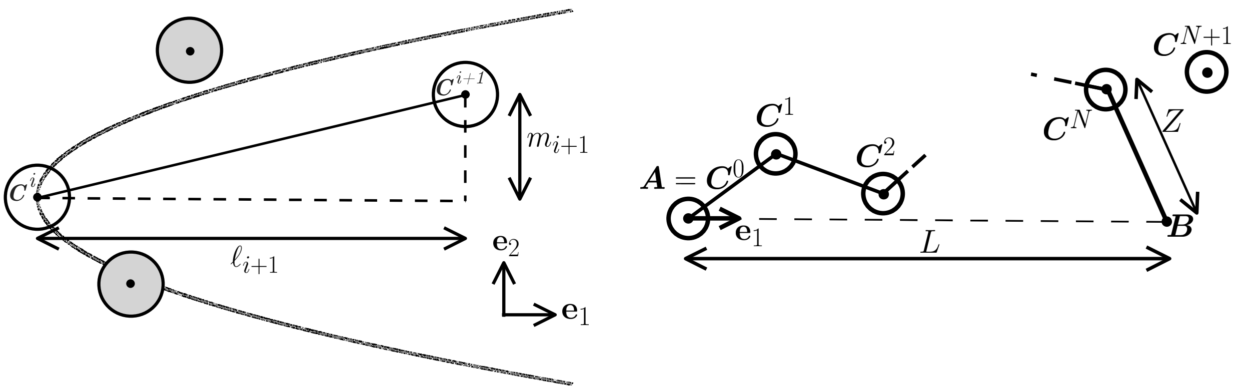

(a) (b)

Figure 4.2: (a) Method for choosing the disk $\boldsymbol{C}^{i+1}$, knowing $\boldsymbol{C}^i$. (b) Path $(\boldsymbol{A};\boldsymbol{C}^1;...;\boldsymbol{C}^N;\boldsymbol{B})$ defined by (4.12) and used to deliver an upper-bound on the length of geodesics.

curves of equation $x_2 = C_2^i \pm \sqrt{2D|x_1 - C_1^i|}$, with minimal coordinate x_1 along $\mathbf{e}_1$ (see Fig. 4.2a):

$$\begin{aligned} \boldsymbol{C}^{i+1} &= \mathrm{arginf}_{\boldsymbol{C}\in\mathcal{K}'} C_1, \\ \mathcal{K}' &= \left\{ \boldsymbol{C} \text{ a disk center; } C_1 > C_1^i,\ |C_2 - C_2^i| \leqslant \sqrt{2D|C_1 - C_1^i|} \right\}. \end{aligned} \tag{4.11}$$

This procedure may be compared to that used by Lee [140] who derived a bound on the minimal length of self-avoiding paths in random lattices by selecting a series of points which move "as directly as possible" from one vertex to another. In the present method, however, we consider a continuum medium and the geodesics must follow a privileged direction.

Let us first replace condition (4.11) by:

$$\begin{aligned} \boldsymbol{C}^{i+1} &= \mathrm{arginf}_{\boldsymbol{C}\in\mathcal{K}''} C_1, \\ \mathcal{K}'' &= \left\{ \boldsymbol{C} \text{ a disk center; } C_1 > C_1^i + D,\ |C_2 - C_2^i| \leqslant \alpha\sqrt{D|C_1 - C_1^i|} \right\}, \end{aligned} \tag{4.12}$$

where $\alpha > 0$ is a constant to be optimized on. We also request that $C_1^i > C_1 + D$ so that the disks do not overlap. This technical assumption simplifies the analytical treatment, and has no effect in the dilute limit where disks are "almost always" far from each other. Starting from $\boldsymbol{C}^0 = \boldsymbol{A}$, we construct the path $(\boldsymbol{A};\boldsymbol{C}^1;...;\boldsymbol{C}^N;\boldsymbol{B})$ where the number N is chosen so that $\boldsymbol{C}^{N+1}$ is the first disk center with coordinate along $\mathbf{e}_1$ larger than B_1, i.e. $C_1^{N+1} > B_1$ and $C_1^N \leqslant B_1$. As in Sec. 4.2.1, we set $\ell_i = |C_1^i - C_1^{i-1}|$, $m_i = C_2^i - C_2^{i-1}$ ($i \geqslant 1$). The path (4.12) provides the following upper bound on $\xi = d(\boldsymbol{A},\boldsymbol{B})/L$:

$$\xi \leqslant \frac{\sum_{i=1}^N \left(\sqrt{\ell_i^2 + m_i^2} - D\right) + Z}{\sum_{i=1}^N \ell_i}, \tag{4.13}$$

where $Z = ||\boldsymbol{C}^N - \boldsymbol{B}||$ is the Euclidean distance from $\boldsymbol{C}^N$ to $\boldsymbol{B}$ (see Fig. 4.2b). Rewrite (4.13) as:

$$1 - \xi \geqslant \frac{\sum\limits_{i=1}^N \left(D + \ell_i - \sqrt{\ell_i^2 + m_i^2}\right) - Z}{\sum_{i=1}^N \ell_i} \approx \frac{\sum\limits_{i=1}^N [D - m_i^2/(2\ell_i)] - Z}{\sum_{i=1}^N \ell_i}. \tag{4.14}$$

To evaluate the above, we determine the mean of the ℓ_i and of m_i^2/ℓ_i. The m_i are uniform random variables in the interval $[-\alpha\sqrt{\ell_i D}; \alpha\sqrt{\ell_i D}]$. The probability $P\left\{\ell_i > \ell\right\}$ is the probability that the domain delimited by the two curves in Fig. (4.2a) and enclosed by the lines $x_1 = C_1^{i-1} + D$ and $x_1 = C_1^{i-1} + \ell_i$ contains no disk center. This probability is given by the Choquet capacity of a Poisson point process [155] as $\exp(-\theta V)$ where V is the size of the domain and $\theta = -4\log(1-f)/(\pi D^2)$ is the intensity of the Poisson point process (i.e. the disks centers) used to build the Boolean set. We compute V and obtain:

$$P\left\{\ell_i \leqslant \ell\right\} = 1 - (1-f)^{16\alpha/(3\pi)\left[(\ell/D)^{3/2}-1\right]}, \tag{4.15}$$

as the cumulative probability function of the random variable ℓ_i in $[D; \infty)$. The above yields, for the average of the ℓ_i, using the variable change $\eta = (D/\ell)^{3/2}$:

$$\begin{aligned} \frac{1}{DN}\sum_{i=1}^{N}\ell_i &\approx \frac{1}{D}\int_{\ell\geqslant D} \ell\, P\left\{\ell \leqslant \ell_i \leqslant \ell + \mathrm{d}\ell\right\} \\ &= 1 + \frac{2}{3}(1-f)^{-\frac{16\alpha}{3\pi}} E_{1/3}\!\left(\frac{-16\alpha\log(1-f)}{3\pi}\right) = \left(\frac{\pi}{4\alpha\sqrt{6f}}\right)^{2/3}\Gamma\left(\frac{2}{3}\right) + o(1), \end{aligned} \tag{4.16}$$

where $E_{1/3}(t) = \int_0^1 \mathrm{d}\eta \mathbf{e}^{-t/\eta}\eta^{-5/3}$ is the exponential integral function of parameter 1/3. Furthermore:

$$\frac{1}{N}\sum_{i=1}^{N}\frac{m_i^2}{\ell_i} \approx \int_{\ell\geqslant D}\int_{m=0}^{\alpha\sqrt{\ell D}} \frac{m^2}{\ell}\, P\left\{\ell \leqslant \ell_i \leqslant \ell + \mathrm{d}\ell\right\} \frac{\mathrm{d}m}{\alpha\sqrt{\ell D}} = \frac{D\alpha^2}{3}. \tag{4.17}$$

At lowest order in f:

$$\xi \leqslant 1 - \frac{2\alpha^{2/3}\left(6-\alpha^2\right)}{3\Gamma\left(\frac{5}{3}\right)}\left(\frac{2}{3\pi}\right)^{2/3} f^{2/3} + O(f^{4/3}) + \frac{Z}{\sum_{i=1}^{N}\ell_i}, \tag{4.18}$$

where Γ is the Gamma (or extended factorial) function. Furthermore, (4.16) entails $m_i \sim f^{-1/3}$ and:

$$Z = \left|\sum_{i=1}^{N} m_i\right| \sim \sqrt{N} f^{-1/3} \sim \sqrt{L}. \tag{4.19}$$

Accordingly the term $Z/\sum_{i=1}^{N}\ell_i \sim 1/\sqrt{L}$ in (4.18) is negligible when L is large. The choice $\alpha = \sqrt{3/2}$ in (4.18) then yields:

$$\xi \leqslant 1 - \frac{3}{\Gamma\left(\frac{2}{3}\right)}\left(\frac{3f}{2\pi}\right)^{2/3} + O(f^{4/3}) \approx 1 - 1.3534 f^{2/3}. \tag{4.20}$$

4.2.3 Comparison between the length of the minimal path and its upper-bound

Hereafter, we compare the dilute limit expansion (4.20) to numerical results, obtained using the algorithm in Appendix (4.A). The paths used to construct bound (4.20) and the minimal path are represented in Fig. (4.5). The two paths join two opposite corners of a realization of a Boolean set in a square domain. Our numerical computations are carried out on random configurations containing on average 10,000 disks at increasing surface fractions $f = 10^{-7}$, ..., 10^{-1}. For each value of f, 20 random configurations are averaged. We also compute numerically the bound (4.13). Results, indicated in Fig. (4.3a), show an excellent agreement between bound (4.13) and expansion (4.20) (solid lines and black dots). A power-law fit on the numerical data for the exact minimal path length provides $\xi \sim 1 - 1.85 f^{0.67}$.

The upper-bound (4.13) is generalized for non-dilute surface fraction of grains as:

$$\xi \leqslant \lim_{N\to\infty} \frac{\sum_{i=1}^{N} \max\left\{0; \sqrt{\ell_i^2 + m_i^2} - D\right\}}{\sum_{i=1}^{N} \ell_i}, \tag{4.21}$$

The above bound is now computed for the full range of porosity $0 \leqslant f \leqslant 1$ using (4.16) and:

$$\begin{aligned} \frac{1}{DN}\sum_{i=1}^{N} \max\left\{0; \sqrt{\ell_i^2 + m_i^2} - D\right\} \quad \approx \quad & \int_{x\geqslant 1} \frac{2\mathrm{d}x}{\pi}(1-f)^{\frac{16\alpha x^{3/2}}{3\pi}} \log(1-f) \\ & \times \left[4\alpha\sqrt{x} - 2\alpha x\sqrt{\alpha^2 + x} - x^2 \log\left(1 + \frac{2\alpha}{x}\left(\alpha + \sqrt{\alpha^2 + x}\right)\right)\right] \\ & + \int_{x=\sqrt{1+\frac{\alpha^4}{4}}-\frac{\alpha^2}{2}}^{1} \frac{-4\mathrm{d}x}{\pi}(1-f)^{\frac{16\alpha x^{3/2}}{3\pi}} \log(1-f) \\ & \times \left[\alpha x\sqrt{\alpha^2 + x} + \sqrt{1-x^2} - 2\alpha\sqrt{x} + x^2 \log\left(\sqrt{x}\frac{\alpha + \sqrt{\alpha^2 + x}}{1 + \sqrt{1-x^2}}\right)\right]. \end{aligned} \tag{4.22}$$

The two integrals in the above are computed numerically. Numerical experiments indicate that $\alpha = \sqrt{3/2}$ is optimal, i.e. produces the sharpest bounds, for all values of f. The bound is compared to numerical estimates of ξ in Fig. (4.3b). Results are represented in Fig. (4.3b), with error bars that indicate statistical fluctuations. As expected, the upper-bound (4.21) is significantly higher than the exact result when the surface fraction f of the disks is not small. For small values of f, however, the bound becomes a good estimate of the geodesics. As expected, the upper-bound percolates at $f = 1$, a value larger than the actual percolation threshold, which is about $f = f_p^{\mathrm{2D}} \approx 0.68$ [196].

4.2.4 Rugosity exponent

We close this section by a discussion of the rugosity of the minimal path and that of the path used to derive bound (4.20). The m_i are independent variables with zero mean and finite variance:

$$\langle m_i^2 \rangle = \left(\frac{\pi}{12f}\right)^{2/3} \Gamma\left(\frac{2}{3}\right)\frac{D^2}{2} = \langle \ell_i \rangle \frac{D}{2} = \frac{LD}{2N}, \tag{4.23}$$

hence, by the Central Limit theorem, $(1/N)\sum_i m_i$ is Gaussian for N large. Accordingly, Z follows the probability distribution function:

$$P\{z < Z < z + \mathrm{d}z\}\frac{1}{\mathrm{d}z} = \frac{2}{\sqrt{LD\pi}}\mathrm{e}^{-z^2/(LD)}. \tag{4.24}$$

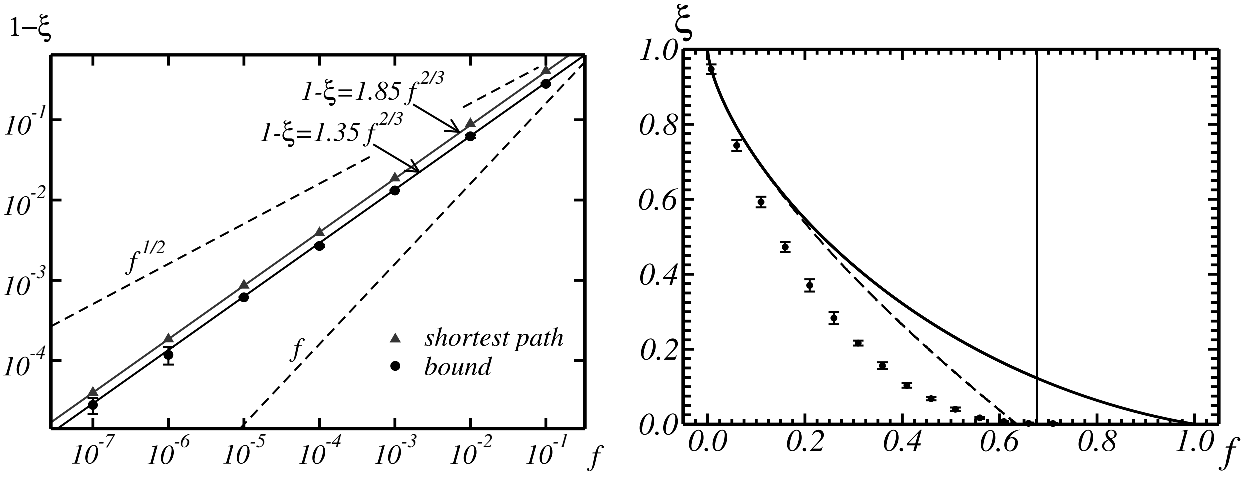

(a) (b)

Figure 4.3: (a) Leading-order correction to the length of geodesics ξ vs. disk concentration f, in log-log plot. Black dots: numerical computation of bound (4.13); black solid line: analytical estimate (4.20); triangles: numerical computation of ξ using the exact shortest path on finite-size systems; gray solid line: power-law fit of the latter; dotted lines: power-law corrections $\sim f$ and $\sim f^{1/2}$. (b) Upper-bound (4.21) (solid line) vs. numerical estimates for ξ (circles with error bars) for increasing values of the disks surface fraction f. Dashed line: asymptotic expansion (4.20). Vertical solid line: percolation threshold $f_c \approx 0.68$.

We have simulated the probability distribution function for Z on $40,000$ configurations each containing $15,000$ disks, with $f = 0.01$ fixed. The value of Z is estimated at various values of L/D and compared with that obtained for the shortest path (Fig. 4.4). For the later, Z is defined to be the deviation along the direction transverse to propagation, i.e. it is equal to $|x_2|$ where $\boldsymbol{x}$ lies on the shortest path such that $x_1 = L$, the origin of the shortest path being 0 by convention. The data points for the numerical estimates of Z are in excellent agreement with (4.24). We also observe that the distribution of the variable Z for the exact shortest path, at given value of L/D, is much wider than that of the bound (triangles in Fig. 4.4a). We study the width of the distribution of Z hereafter.

Consider the path transverse fluctuations $w = (\langle Z^2 \rangle - \langle Z \rangle^2)^{1/2}$ as a function of L, for fixed value of $f = 10^{-2}$, 10^{-3} and 10^{-4}. It has been shown [108, 123] that the minimal path is very rough with scaling law $w \sim L^{-2/3}$ as L becomes large (see numerical computations, Fig. 4.4b). As expected, this is not so for the path used to derive bound (4.20) which exhibits a much more common scaling law $\sim L^{-1/2}$ (black line, Fig. 4.4b). Thus, the exponent 2/3 obtained in bound (4.20) is not directly linked to the "roughness exponent" related to the scaling law for w.

4.3 Other Boolean and Cox-Boolean sets in two dimensions

In this section, we extend result (4.20) obtained for a Boolean set of discs to other random sets. The discs are replaced by an arbitrary compact, *non-random*, fully connected grain in Sec. (4.3.1).

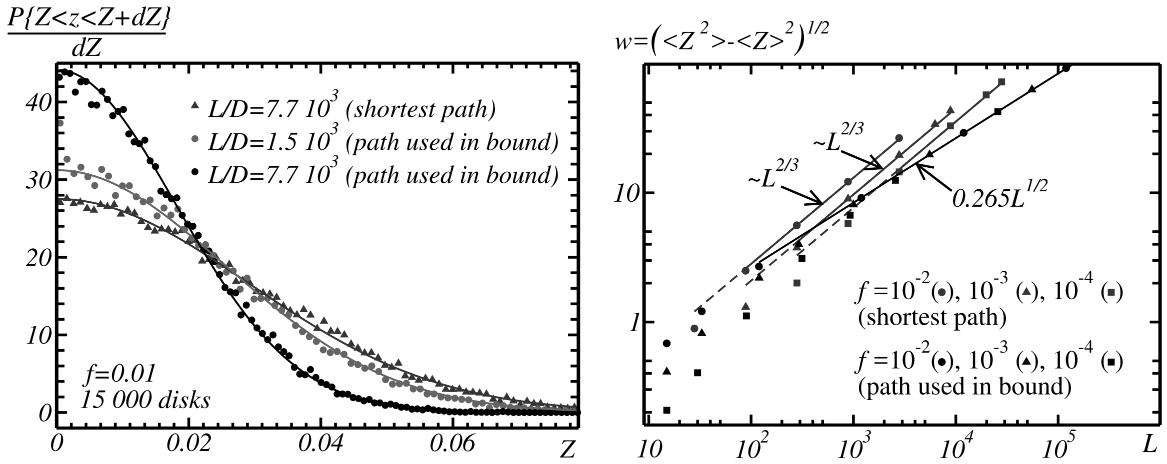

(a) (b)

Figure 4.4: (a) Probability distribution function for the random variable Z, representing the deviation transverse to the direction of propagation, computed numerically (symbols) and analytically (solid lines). Black dots and triangles: path used in bound (4.20). Gray dots: shortest path fitted with a folded Gaussian distribution (4.24). (b) Transverse fluctuations w as a function of the path length L in log-log plot, for various values of f. Gray symbols: shortest path. Black symbols: path used in bound (4.20). Solid lines: power-law fit of the data.

In Sec. (4.3.2) we let the distance function be non-zero inside the inclusions. Finally, we consider two-scales random media in Sec. (4.3.3).

4.3.1 Boolean set of compact grains

Let us first suppose that the inclusions are aligned squares of side D and that points $\boldsymbol{A}$ and $\boldsymbol{B}$ are aligned with one of the direction of the squares. The path $(\boldsymbol{A}; \boldsymbol{C}^1; ...; \boldsymbol{C}^N; \boldsymbol{B})$ is defined by:

$$\begin{aligned}|C_1^{i+1} - C_1^i| \quad = \quad & \inf\Big\{|C_1 - C_1^i|;\ \boldsymbol{C} \text{ a square center};\\ & C_1 > C_1^i + D,\ |C_2 - C_2^i| \leqslant \alpha\sqrt{D|C_1 - C_1^i|}\Big\}.\end{aligned} \tag{4.25}$$

Note that compared to Eq. (4.12), the $\boldsymbol{C}^i$ are now square centers and we have added the condition $C_1 > C_1^i + D$. Like in Sec. (4.2.2), we set $\ell_i = C_1^i - C_1^{i-1}$, $m_i = C_2^i - C_2^{i-1}$ with $\ell_i \geqslant D$, $|m_i| \leqslant \alpha\sqrt{\ell_i D}$. Again, α is a constant to be optimized on and we denote $f \ll 1$ the surface fraction of the squares. The distance function d_{sq} is defined as in (4.1) with χ replaced by the indicator function of the Boolean set of squares. Note that:

$$d_{\mathrm{sq}}(\boldsymbol{C}^{i-1}, \boldsymbol{C}^i) \leqslant \sqrt{(\ell_i - D)^2 + (m_i - D)^2},$$

which yields for the normalized geodesic distance:

$$\xi_{\mathrm{sq}} = \frac{d_{\mathrm{sq}}(\boldsymbol{A}, \boldsymbol{B})}{L} \leqslant \frac{Z + \sum_{i=1}^{N} \sqrt{(\ell_i - D)^2 + (m_i - D)^2}}{\sum_{i=1}^{N} \ell_i}, \tag{4.26}$$

with $Z = |\boldsymbol{C}^N\boldsymbol{B}|$, $L = |\boldsymbol{AB}|$. For squares, Eq. (4.15) now takes the form:

$$P\left\{\ell_i \leqslant \ell\right\} = 1 - (1-f)^{\frac{4\alpha}{3}\left[(\ell/D)^{3/2}-1\right]},$$

and the average of the ℓ_i reads:

$$\frac{1}{N}\sum_{i=1}^{N}\frac{\ell_i}{D} \approx 1 + \frac{2}{3}(1-f)^{-\frac{4\alpha}{3}}E_{1/3}\left(\frac{-4\alpha\log(1-f)}{3}\right) \tag{4.27}$$

$$= \frac{\Gamma\left(\frac{2}{3}\right)}{(\sqrt{6}\alpha f)^{2/3}} + O(f^{1/3}), \qquad f \to 0. \tag{4.28}$$

The mean of the term $\sqrt{(\ell_i - D)^2 + (m_i - D)^2}$ occurring in (4.26) is expressed as a double integral like in Sec. (4.2.2). We develop it for $\ell_i \gg D$ and integrate over ℓ_i and m_i:

$$\frac{1}{DN}\sum_{i=1}^{N}\sqrt{(\ell_i - D)^2 + (m_i - D)^2} = \frac{\Gamma\left(\frac{2}{3}\right)}{\left(\sqrt{6}\alpha f\right)^{2/3}} + \left(\frac{\alpha^2}{6} - 1\right) + O(f^{1/3}). \tag{4.29}$$

We neglect Z and choose $\alpha = \sqrt{3/2}$:

$$\xi_{\mathrm{sq}} \leqslant 1 - \frac{3^{5/3}}{4\Gamma\left(\frac{2}{3}\right)}f^{2/3} + o(f^{2/3}) \approx 1 - 1.1521 f^{2/3}. \tag{4.30}$$

This correction is smaller than that derived for the disks model. We emphasize that this model is anisotropic and that the geodesics are directed parallel to the sides of the squares.

More generally, it is clear that, in a Boolean model with non-random connected compact grain, the minimal path used in the present bound depends, to leading-order term in the dilute limit, solely on the width of the grain, in the direction of propagation of the geodesics. The "width" of a shape is the distance between parallel lines (transverse to the direction of propagation) bounding it. The mean width, taken over all orientations, is the perimeter of the convex hull of the grain divided by π [214].

For instance, consider a Boolean model made of grains of surface A_g and width w_g in the direction of propagation of the geodesics. The width w_g is the highest difference between the coordinates of two points in the grain, measured along the direction of propagation. The upper-bound in the dilute limit reads:

$$\xi_{\mathrm{c}} \leqslant 1 - \frac{3^{5/3}}{4\Gamma\left(\frac{2}{3}\right)}\left(\frac{w_g^2 f}{A_g}\right)^{2/3} + o(f^{2/3}), \tag{4.31}$$

where f/A_g is the density of grains (number of grains per unit surface). This result holds for arbitrary compact, *non-random* grain. Note that since the convex hull of a shape has the same width in all directions, bound (4.31) is unchanged when a grain is replaced by its convex hull. In the case of a set of parallel segments (modeling, e.g., cracks), (4.31) reduces to $1 - \xi_{\mathrm{c}} \geqslant g_0\eta^{2/3}$ where η is the crack density parameter (2.12) and g_0 depends on the orientation of the crack with respect to the direction of propagation of the geodesics.

The homogenized metric in bound (4.31) is isotropic for particles of constant width [96, Chap. 6.7], such as a Reuleaux triangle. By Barbier's theorem [244], the bound then reduces to:

$$\xi_{\mathrm{c}} \leqslant 1 - \frac{3^{5/3}}{4\Gamma\left(\frac{2}{3}\right)}\left(\frac{p_g^2 f}{A_g \pi^2}\right)^{2/3} + o(f^{2/3}), \tag{4.32}$$

where p_g is the perimeter of the grain. The shape of given constant width with smallest area is the Reuleaux triangle [46]. Therefore, for a given surface fraction f, the Reuleaux triangle is also the shape minimizing bound (4.32) among particles of constant width. The shape of constant width maximizing the same bound is the disk, for fixed surface fraction f.

4.3.2 Boolean set of disks with non-zero distance function inside the disks

In this section, we consider a Boolean model of disks with the following modified distance function:

$$\begin{aligned} d_p(\boldsymbol{A},\boldsymbol{B}) &= \inf_{\boldsymbol{p}\in\mathcal{K}} \int_0^1 \mathrm{d}t\ \chi_p(\boldsymbol{p}(t))\,||\partial_t \boldsymbol{p}(t)||\,, \\ \chi_p(\boldsymbol{M}) &= \begin{cases} \mathrm{p} & \text{if } \boldsymbol{M} \text{ lies inside a disk,} \\ 1 & \text{otherwise,} \end{cases} \end{aligned} \tag{4.33}$$

where $0 \leqslant p < 1$ is the cost associated to the distance in the disks. The distance function d in (4.1) is recovered when $p = 0$. We consider a similar path $(\boldsymbol{A};\boldsymbol{C}^1;...;\boldsymbol{C}^N;\boldsymbol{B})$ as in Sec. (4.2.2), defined by:

$$\begin{aligned} |C_1^{i+1} - C_1^i| &= \inf\Big\{|C_1 - C_1^i|;\ \boldsymbol{C} \text{ a disk center;} \\ &\qquad C_1 > C_1^i + D,\ |C_2 - C_2^i| \leqslant \alpha\sqrt{D|C_1 - C_1^i|}\Big\}. \end{aligned} \tag{4.34}$$

with the extra condition $C_1 > C_1^i + D$. It provides a bound on $d_p(\boldsymbol{A},\boldsymbol{B})$:

$$\xi_p = \frac{d_p(\boldsymbol{A},\boldsymbol{B})}{L} \leqslant \frac{\sum_{i=1}^N \left[\sqrt{\ell_i^2 + m_i^2} - (1-p)D\right]}{\sum_{i=1}^N \ell_i}, \tag{4.35}$$

with $Z = |\boldsymbol{C}^N\boldsymbol{B}|$, $\ell_i = C_1^i - C_1^{i-1}$, $m_i = C_2^i - C_2^{i-1}$, $\ell_i \geqslant D$, $|m_i| \leqslant \alpha\sqrt{\ell_i D}$ and $\alpha > 0$. Note that the path $(\boldsymbol{A};\boldsymbol{C}^1;...;\boldsymbol{C}^N;\boldsymbol{B})$ used to derive bound (4.35) consists in a set of segments joining the disks centers. Most geodesics will not pass through disk centers when $p > 0$. Nevertheless, in the dilute regime considered here we expect $|m_i| \ll \ell_i$ so that bound (4.35) should be a very good estimate of the length of the path $(\boldsymbol{A};\boldsymbol{C}^1;...;\boldsymbol{C}^N;\boldsymbol{B})$. The asymptotic expansions for the means of the ℓ_i and of the quantity m_i^2/ℓ_i are the same as in (4.16) and (4.17). This yields:

$$\begin{aligned} \xi_{\mathrm{p}} &\leqslant 1 - \left(\frac{2\alpha}{3\pi}\right)^{2/3} \frac{6(1-p) - \alpha^2}{\Gamma\left(\frac{2}{3}\right)} f^{2/3} + o(f^{2/3}), & (4.36) \\ &= 1 - \frac{3(1-p)^{4/3}}{\Gamma\left(\frac{2}{3}\right)}\left(\frac{3}{2\pi}\right)^{2/3} f^{2/3} + o(f^{2/3}) \approx 1.3534(1-p)^{4/3} f^{2/3}, & (4.37) \end{aligned}$$

with $\alpha = \sqrt{3(1-p)/2}$. The upper-bound above is sharper than the trivial bound $\xi_{\mathrm{p}} \leqslant 1-(1-p)f$ in the domain $f \ll 1-p$.

4.3.3 Multiscale Boolean set of disks

Consider first two Boolean sets of disks with constant diameter, denoted $\mathcal{M}_1$ and $\mathcal{M}_2$. The disks of set $\mathcal{M}_1$ have constant diameter D_1 and that of set $\mathcal{M}_2$ have diameter $D_2 \ll D_1$. The centers of the disks in the Boolean sets $\mathcal{M}_1$ and $\mathcal{M}_2$ follow a homogeneous Poisson point process. We denote by f_1 and f_2 the surface fractions of sets $\mathcal{M}_1$ and $\mathcal{M}_2$ respectively and assume $f_1 \ll 1$, $f_2 \ll 1$. Hereafter we consider the intersection of the two sets $\mathcal{M} = \mathcal{M}_1 \cap \mathcal{M}_2$ which is a two-scales random set with surface fraction $f = f_1 f_2$. The model is assumed "symmetric" so that $f_1 = f_2 = \sqrt{f}$ and the distance function defined as in (4.1).

Accordingly to (4.20), the distance $d(\boldsymbol{A'}, \boldsymbol{B'})$ between two points $\boldsymbol{A'}$ and $\boldsymbol{B'}$ that lie in a disk contained in $\mathcal{M}_1$ admits the following upper bound:

$$\frac{d(\boldsymbol{A'}, \boldsymbol{B'})}{L'} \leqslant 1 - \frac{3}{\Gamma\left(\frac{2}{3}\right)} \left(\frac{3}{2\pi}\right)^{2/3} f_2^{2/3} + o(f_2^{2/3}),$$

when $L' = |\boldsymbol{A'B'}| \gg D_2$. In the limit $D_2 \ll D_1$ the distance function in $\mathcal{M}$ is well approximated by that considered in Sec. (4.3.2) with $p = 1 - \left[3/\Gamma\left(\frac{2}{3}\right)\right]\left[3f_2/(2\pi)\right]^{2/3}$. Eq. (4.37) then provides the following bound, for two points $\boldsymbol{A}$ and $\boldsymbol{B}$ sufficiently far away from each other:

$$\xi_{\mathrm{ms}} = \frac{d(\boldsymbol{A}, \boldsymbol{B})}{L} \leqslant 1 - \frac{3^{35/9}}{(2\pi)^{14/9}\Gamma\left(\frac{2}{3}\right)^{7/3}} f^{7/9} + o(f^{7/9}) \approx 1 - 2.0261 f^{7/9}. \tag{4.38}$$

This correction is smaller than that derived in the one-scale model (4.20) and indicates that clustering tend to "constraint" the shortest paths and increase their lengths. Similarly, the 2D periodic model, which has a very homogeneous spatial distribution of voids, has an exponent 1/2 and its geodesics are shorter than in the one-scale Boolean set of disks.

4.4 Boolean sets in three dimensions or more

4.4.1 Boolean set of spheres

In this section, we study a Boolean set of spheres of volume fraction f. The distance function $d^{3\mathrm{D}}$ is defined in 3D as in (4.1):

$$d^{3\mathrm{D}}(\boldsymbol{A}, \boldsymbol{B}) = \inf_{\boldsymbol{p} \in \mathcal{K}} \int_0^1 \mathrm{d}t \; \chi^{3\mathrm{D}}(\boldsymbol{p}(t)) \, ||\partial_t \boldsymbol{p}(t)|| \,, \tag{4.39}$$

with $1 - \chi^{3\mathrm{D}}$ is the indicator of the Boolean set of spheres and $\mathcal{K}$ is given by (4.2). We define the path $(\boldsymbol{C}^0 = \boldsymbol{A}; \boldsymbol{C}^1; ...; \boldsymbol{C}^N; \boldsymbol{C}^{N+1} = \boldsymbol{B})$ by:

$$\begin{aligned} |C_1^{i+1} - C_1^i| \;&=\; \inf\Big\{|C_1 - C_1^i|;\; \boldsymbol{C} \text{ a sphere center;} \\ &\qquad C_1 > C_1^i + D,\; |\boldsymbol{C} - \boldsymbol{C'}| \leqslant \alpha\sqrt{D|C_1 - C_1^i|}\Big\}, \end{aligned} \tag{4.40}$$

where $\boldsymbol{C'}$ is the orthogonal projection of $\boldsymbol{C}$ onto the line $(\boldsymbol{C}^i; \boldsymbol{C}^i + \mathbf{e}_1)$ and α is a constant to be optimized on. As in Sec. (4.2), the axis $\mathbf{e}_1$ is aligned with the line passing by $\boldsymbol{A}$ and $\boldsymbol{B}$. We set

$\ell_i = C_1^i - C_1^{i-1}$ and $m_i = |\boldsymbol{C}^i \boldsymbol{C}^{i'}|$ so that $|\boldsymbol{C}^{i-1}\boldsymbol{C}^i|^2 = \ell_i^2 + m_i^2$. The path (4.40) leads to the bound:

$$\xi^{3\mathrm{D}} = \frac{d^{3\mathrm{D}}(\boldsymbol{A}, \boldsymbol{B})}{L} \leqslant \frac{\sum_{i=1}^N \left(\sqrt{\ell_i^2 + m_i^2} - D \right) + Z}{\sum_{i=1}^N \ell_i}, \tag{4.41}$$

with $Z = |\boldsymbol{C}^N \boldsymbol{B}|$. Using the Choquet capacity [155], the variables $\ell_i \in [D; \infty)$ follow the cumulative probability function according t:

$$P\left\{ \ell_i \leqslant \ell \right\} = 1 - (1-f)^{3\alpha^2\left[(\ell/D)^2 - 1\right]}. \tag{4.42}$$

and so, for the mean of the ℓ_i:

$$\begin{aligned} \frac{1}{DN} \sum_{i=1}^N \ell_i &\approx 1 + \frac{(1-f)^{-3\alpha^2}}{2\alpha} \sqrt{\frac{\pi}{-3\log(1-f)}} \operatorname{erfc}\left(\alpha\sqrt{-3\log(1-f)} \right) \\ &= \frac{1}{2\alpha}\sqrt{\frac{\pi}{3f}} + O(\sqrt{f}), \qquad f \to 0, \end{aligned} \tag{4.43}$$

where $\operatorname{erfc}(z) = 2/\sqrt{\pi} \int_z^\infty \mathrm{d}t\, \mathbf{e}^{-t^2}$ is the complementary error function. The mean of the quantity $\sqrt{\ell_i^2 + m_i^2}$ reads:

$$\begin{aligned} \frac{1}{N} \sum_{i=1}^N \frac{\sqrt{\ell_i^2 + m_i^2}}{D} &\approx \int_{\ell=D}^\infty \int_{m=0}^{\alpha\sqrt{\ell D}} \sqrt{\ell^2 + m^2}\; P\left\{ \ell \leqslant \ell_i \leqslant \ell + \mathrm{d}\ell \right\} \frac{2m\mathrm{d}m}{\alpha^2 \ell D^2} \\ &= -\int_{x=1}^\infty \mathrm{d}x\, 4x^{3/2} \log(1-f)(1-f)^{3\alpha^2(x^2-1)} \left[(x+\alpha^2)^{3/2} - x^{3/2} \right] \\ &= \frac{1}{2\alpha}\sqrt{\frac{\pi}{3f}} + \frac{\alpha^2}{4} + O(\sqrt{f}), \end{aligned} \tag{4.44}$$

where the expression behind the integral has been expanded for $x \to \infty$. With $\alpha = 2/\sqrt{3}$ and $Z \ll 1$:

$$\xi^{3\mathrm{D}} \leqslant 1 - \frac{8}{3\sqrt{\pi}}\sqrt{f} + o(\sqrt{f}) \approx 1 - 1.5045\sqrt{f}, \qquad f \to 0. \tag{4.45}$$

The number of "possible choices" for picking $\boldsymbol{C}^{i+1}$ knowing $\boldsymbol{C}^i$ is greater in 3D than in 2D and results in a lower exponent in 3D.

4.4.2 Non-zero distance function in spheres

The reasoning above extends to a distance function $d_{\mathrm{p}}^{3\mathrm{D}}$ which is non-zero in the spheres. Define the distance $d_{\mathrm{p}}^{3\mathrm{D}}$ as in (4.39) with $\chi^{3\mathrm{D}}$ replaced by:

$$\chi_{\mathrm{p}}^{3\mathrm{D}}(\boldsymbol{M}) = \begin{cases} \mathrm{p} & \text{if } \boldsymbol{M} \text{ lies inside a sphere,} \\ 1 & \text{otherwise,} \end{cases} \tag{4.46}$$

where $0 \leqslant p < 1$ is a parameter. The following upper-bound on the normalized shortest paths is derived:

$$\xi_{\mathrm{p}}^{3\mathrm{D}} = \frac{d_{\mathrm{p}}^{3\mathrm{D}}(\boldsymbol{A}, \boldsymbol{B})}{|\boldsymbol{AB}|} \leqslant 1 - \frac{8(1-p)^{3/2}}{3\sqrt{\pi}}\sqrt{f} + o(\sqrt{f}), \qquad f \to 0. \tag{4.47}$$

Again, this bound is non-trivial when $f \ll 1 - p$.

4.4.3 Multiscale Boolean set of spheres

The two-scales "symmetric" Boolean set of spheres is constructed similarly as in Sec. (4.3.3). The latter is the intersection of two Boolean models of spheres with scale separation. The indicator function $\chi_{\text{ms}}^{\text{3D}}$ of the two-scales Boolean model is used to define the distance $d_{\text{ms}}^{\text{3D}}$ as in (4.39). The normalized shortest path is expanded in the dilute limit as:

$$\xi_{\text{ms}}^{\text{3D}} = \frac{d_{\text{ms}}^{\text{3D}}(\boldsymbol{A}, \boldsymbol{B})}{|\boldsymbol{AB}|} \leqslant 1 - \left(\frac{8}{3\sqrt{\pi}} \right)^{5/2} f^{5/8} + o(f^{5/8}) \approx 1 - 2.7764 f^{5/8}, \quad f \to 0. \tag{4.48}$$

Our conclusions are the same as that given in 2D. At fixed volume fraction of pores, geodesics are higher in the two-scales symmetric model than in the one-scale Boolean model. The shortest geodesics are found for the 3D periodic model, in which the spatial distribution of voids is very homogeneous and the voids well-separated.

4.4.4 Boolean model of hyperspheres

In this section we consider a Boolean model of hyperspheres in dimension $d \geqslant 2$. The geodesic distance d^{dD} and path $(\boldsymbol{A}; \boldsymbol{C}^1; ...; \boldsymbol{C}^N; \boldsymbol{B})$ are defined as in (4.39) and (4.40) with spheres replaced by hyperspheres. A bound for the geodesic is given by the path from $\boldsymbol{A}$ to $\boldsymbol{B}$. With $\ell_i = C_1^i - C_1^{i-1}$, $m_i = |\boldsymbol{C}^i \boldsymbol{C}^{i\prime}|$, $Z = |\boldsymbol{C}^N \boldsymbol{B}|$ and $\boldsymbol{C}'$ the orthogonal projection of $\boldsymbol{C}$ onto the line $(\boldsymbol{C}^i; \boldsymbol{C}^i + \mathbf{e}_1)$, we have:

$$\xi^{\text{dD}} = \frac{d^{\text{dD}}(\boldsymbol{A}, \boldsymbol{B})}{L} \leqslant \frac{\sum_{i=1}^N \left(\sqrt{\ell_i^2 + m_i^2} - D \right) + Z}{\sum_{i=1}^N \ell_i} \approx 1 - \frac{-Z + \sum_{i=1}^N \left(D - \frac{m_i^2}{2\ell_i} \right)}{\sum_{i=1}^N \ell_i}. \tag{4.49}$$

Denote by $\pi_d(D)$ the volume of the hyperdimensional ball of diameter D and V_ℓ that of the domain:

$$\left\{ \boldsymbol{C}; \quad D \leqslant C_1 \leqslant \ell, \quad 0 \leqslant |\boldsymbol{C}'| \leqslant \alpha \sqrt{\ell D} \right\}.$$

The probability law for the $\ell_i \in [D, \infty($ depends on V_ℓ by:

$$P\left\{ \ell_i \leqslant \ell \right\} = 1 - (1-f)^{\frac{V_\ell}{\pi_d(D)}} = 1 - (1-f)^{\frac{2^{d+1}\alpha^{d-1}\Gamma\left(1+\frac{d}{2}\right)}{(d+1)\sqrt{\pi}\,\Gamma\left(\frac{1+d}{2}\right)} \left[\left(\frac{\ell}{D} \right)^{\frac{d+1}{2}} - 1 \right]}, \tag{4.50}$$

which provides the sum:

$$\frac{1}{DN} \sum_{i=1}^N \frac{m_i^2}{\ell_i} \approx \int_{\substack{\ell \geqslant D, \\ m \leqslant \alpha\sqrt{\ell D}}} P\left\{ \ell \leqslant \ell_i \leqslant \ell + \mathrm{d}\ell \right\} \frac{(d-1) m^d \mathrm{d}m}{\alpha^{d-1} (D\ell)^{\frac{d+1}{2}}} = \alpha^2 \frac{d-1}{d+1}. \tag{4.51}$$

The mean of the ℓ_i, approximated by $\int_{\ell \geqslant D} \ell P\left\{ \ell \leqslant \ell_i \leqslant \ell + \mathrm{d}\ell \right\}$, is determined using the symbolic solver Mathematica [262]. The expression involves the function Γ as well as incomplete Γ functions (not shown). Carrying out a Taylor expansion of the latter and optimizing on α yield $\alpha = \sqrt{(1+d)/d}$. Finally:

$$\xi^{\text{dD}} \leqslant 1 - \frac{(d+1)^{\frac{1+3d}{1+d}}}{\Gamma\left(\frac{2}{1+d}\right)} \left[\frac{\Gamma\left(1+\frac{d}{2}\right)}{2\sqrt{\pi} d^d \Gamma\left(\frac{3+d}{2}\right)} \right]^{\frac{2}{1+d}} f^{\frac{2}{1+d}} + o(f^{\frac{2}{1+d}}), \qquad f \to 0. \tag{4.52}$$

The above generalizes (4.20) and (4.45). Taking successively the limits $f \to 0$ and $d \to \infty$:

$$\xi^{\mathrm{dD}} \leqslant 1 - 2\left[1 - \frac{\log(2d\pi) - 2(1+\gamma)}{d}\right] f^{\frac{2}{1+d}} \sim 1 - \left(\frac{f}{\sqrt{f_p}}\right)^{2/d} \tag{4.53}$$

where $\gamma \approx 0.5772$ is Euler's constant and $f_p \sim 2^{-d}$ is the asymptotic percolation threshold in dimension $d \gg 1$ [237].

4.5 Conclusion

Powerlaws with fractional exponents 2/3 and 1/2 have been derived for the lowest-order corrections to the lengths of geodesics in 2D and 3D Boolean models of discs and spheres, respectively. The method is general and provides an upper-bound with lowest-order correction $\sim f^{\frac{2}{d-1}}$ in dimension $d \geqslant 2$.

The bounds obtained for multiscale models, which scale as $\sim f^{7/9}$ in 2D and $\sim f^{5/8}$ indicate lower variations of the geodesics near the point $f = 0$. These results underline that the the singularities for the geodesics are small for highly-heterogeneous dispersion of particles, and high when the dispersion is homogeneous. This phenomenon will be investigated in more details in Chap. (6).

4.A Algorithm for computing minimal paths in porous media

Our numerical algorithm for computing shortest paths in a model of disks is described here. Assume domain Ω contains N disks of centers $\boldsymbol{C}_i$ and radii R_i ($i = 1, ..., N$). Set $d_{ij} = \max(0; |\boldsymbol{C}^i - \boldsymbol{C}^j| - R_i - R_j)$ where $|\bullet|$ is the Euclidean distance. The distances $d_i = d(\boldsymbol{A}, \boldsymbol{C}_i)$ between a given point $\boldsymbol{A}$ and any disk is computed by the following algorithm, described hereafter.

(i) Set $d_i := \max(0; |\boldsymbol{C}_i - \boldsymbol{A}| - R_i)$.

(ii) For all i, j, set $d_i := \min(d_i, d_j + d_{ij})$.

(iii) If any value of d_i has been changed in step (ii) GOTO (ii), otherwise STOP.

Note that distances d_{ij} are computed on the fly and need not be saved in memory, and that only the distances d_i are saved. This algorithm nevertheless requires $O(N^2)$ computations at each step and becomes impractical for certain Boolean sets with inhomogeneous Poisson point process, such as multiscale random sets. To increase its speed, disk centers are sorted beforehand with respect to the distance of propagation $|\boldsymbol{C}_i - \boldsymbol{A}|$, and the distance d_i is updated by checking disks $\boldsymbol{C}_j$ in an interval $i - N_0 \leqslant j \leqslant i + N_0$, while we let N_0 increases, until $N_0 = N$. The justification rests on the fact that the distance function usually increases with $|\boldsymbol{C}_i - \boldsymbol{A}|$ and that d_i is not usually updated when a disk far from $\boldsymbol{C}_i$ is checked. The new algorithm reads:

(i) Label each disk with a number so that $|\boldsymbol{C}_i - \boldsymbol{A}|$ increases with the index i.

(ii) Set $d_i := \max\left(0; |\boldsymbol{C}_i - \boldsymbol{A}| - R_i\right)$ and $N_0 = 5\sqrt{N}$.

(iii) For $i = 1, ..., N$, and for $j = \max(1, i - N_0), ..., \min(N, i + N_0)$, set $d_i := \min\left(d_i, d_j + d_{ij}\right)$.

(iv) If any value of d_i has been changed in step (iii) GOTO (iii), otherwise continue to next step.

(v) if $N_0 < N$ set $N_0 := 2M$ and GOTO (iii), otherwise STOP.

The initial value of N_0 is so that, for a homogeneous distribution of inclusions, on average the 5 disks closest to each disk are checked. The results given by the algorithm is illustrated Fig. (4.5).

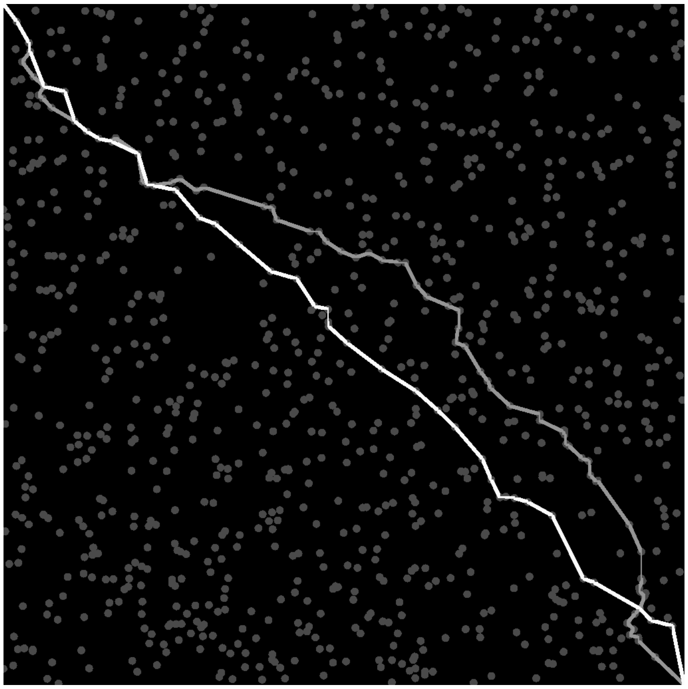

Figure 4.5: Boolean set of discs with surface fraction $f = 10\%$ and 10^3 disks. Gray line: minimal path joining two opposite corners. White line: path used to derive bound (4.13).

Chapter 5

Effective behavior and geodesics: lattice vs. continuum

In this chapter, we investigate the effective conductivity of strongly nonlinear media in two dimensions. The nonlinear behavior is characterized by a threshold value for the maximal absolute current. Our main focus is on random media containing an infinitesimal proportion $f \ll 1$ of insulating phase. We first consider a random conducting network on a square grid and establish a relationship between the length of minimal paths spanning the network and the network's effective response. In the dilute limit $f \ll 1$, the network's effective conductivity scales, to leading-order correction in f, as $\sim f^{\nu}$ with $\nu = 1$ or $\nu = 1/2$, depending on the direction of the applied field with respect to the grid. Second, we introduce coupling between local bonds, and observe an exponent $\nu \approx 2/3$, in agreement with the upper-bound for the length of geodesics spanning random media in the continuum. We argue that $\nu = 2/3$ for random composites in the continuum with homogeneously-distributed, monodisperse particles, in two dimensions.

Outline The present chapter is articulated around three main sections. A model problem in a random square lattice is formulated in Sec. (5.1). In Sec. (5.2), a scaling law is established for the effective conductivity with respect to f, the proportion of broken bonds, in the limiting case $f \to 0$. In Sec. (5.3), we introduce local coupling between the bonds and draw comparisons with the problem in the continuum. We conclude in Sec. 5.4.

5.1 Nonlinear resistor network

Consider a resistor network on a square grid (Fig. 5.1b) with nodes $\boldsymbol{x} = (x_1, x_2) \in \mathbb{Z}^2$. Each node is linked to its four closest neighbours by bonds oriented along $\mathbf{e}_1$ and $\mathbf{e}_2$ (see Fig. 5.1a). At each node $\boldsymbol{x}$ lies a potential $\phi(\boldsymbol{x})$, and along each bond $(\boldsymbol{x}, \boldsymbol{x} + \mathbf{e}_i)$ lies component $J_i(\boldsymbol{x})$ of the current and component $E_i(\boldsymbol{x})$ of the electric field. Following Kirchhoff's law:

$$\sum_{i=1}^{2} \left[J_i(\boldsymbol{x}) - J_i(\boldsymbol{x} - \mathbf{e}_i) \right] = 0, \qquad E_i(\boldsymbol{x}) = -\left[\phi(\boldsymbol{x} + \mathbf{e}_i) - \phi(\boldsymbol{x}) \right], \tag{5.1}$$

for all $\boldsymbol{x}$ and $i = 1, 2$. Each bond in the resistor network is either insulating, in which case $J_i(\boldsymbol{x}) = 0$, or conducting. The conducting bonds follow the nonlinear constitutive law:

$$J_i(\boldsymbol{x}) = \begin{cases} \sigma E_i(\boldsymbol{x}) & \text{if } \sigma|E_i| \leqslant J_0, \\ J_0 \text{sign}(E_i(\boldsymbol{x})) & \text{if } \sigma|E_i| > J_0, \end{cases} \tag{5.2}$$

where $\text{sign}(\bullet) = \bullet/|\bullet|$ is the sign function, $J_0 > 0$ is the yield current and $\sigma > 0$ is a parameter used for numerical regularization (see Fig. 5.1c). In the limit $\sigma \to \infty$, Eq. (5.2) reads:

$$J_i = J_0 \quad \text{if} \quad E_i > 0, \tag{5.3a}$$

$$J_i = -J_0 \quad \text{if} \quad E_i < 0, \tag{5.3b}$$

$$|J_i| < J_0 \quad \text{if} \quad E_i = 0. \tag{5.3c}$$

This constitutive law is obtained as the limiting behavior of "power-law materials". This class of materials, extensively studied in the context of nonlinear homogenization theories [192], is characterized by local potentials which are power-law of the electric or current fields. In the present case, referred to as "strongly nonlinear", the potential corresponding to the constitutive law (5.3) is not strictly convex, and fields may localize along critical paths [70].

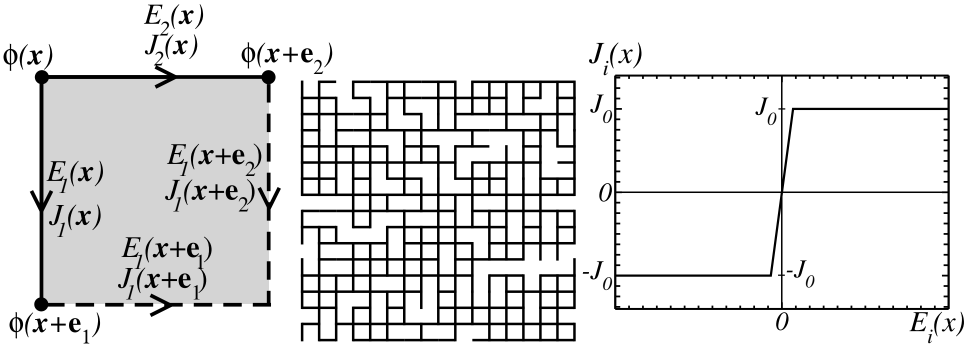

(a) (b) (c)

Figure 5.1: (a) Two bonds originating from a node at point $\boldsymbol{x}$ and joining nodes at $\boldsymbol{x} + \mathrm{e}_{1,2}$ (solid lines); other nearby bonds are represented as dotted lines. (b) 16×16-nodes random conducting network. Conducting bonds shown in black, insulating bonds omitted. (c) Nonlinear constitutive law (5.2) satisfied along each conducting bond.

For numerical purposes, we assume that the medium is periodic in the two directions and is given by its elementary cell $\Omega = [0; M-1]^2$ made of M^2 bonds. A random configuration of Ω is depicted in Fig. 5.1b for $M = 16$. In domain Ω, the network is made up of two phases, the phase label following a Bernouilli distribution, that is, a bond has constitutive law (5.2) with probability $1 - f$ and is insulating with probability f. The vector fields $\boldsymbol{E}$ and $\boldsymbol{J}$ are Ω-periodic whereas the potential is the sum of a periodic and linear function:

$$\phi(\boldsymbol{x}) = -\overline{\boldsymbol{E}} \cdot \boldsymbol{x} + \phi^*(\boldsymbol{x}), \qquad \phi^* \#, \tag{5.4}$$

where $\overline{\boldsymbol{E}}$ is a remote field applied at infinity and # denotes doubly-periodic fields. Problem (5.1)-(5.2)-(5.4) is solved *exactly* on the finite domain Ω using the Fourier-based method with "discrete"

Green operator appropriate to resistor networks [254]. As for the iterative algorithm, we make use of the so-called "augmented Lagrangian" scheme [163]. When applied to materials with nonlinear threshold law (5.2), this scheme requires one to solve the equation in $\boldsymbol{E}$:

$$\sigma_0 \boldsymbol{E} + \boldsymbol{J}(\boldsymbol{E}) = \boldsymbol{P}, \tag{5.5}$$

for arbitrary $\boldsymbol{P}$. Making use of (5.2), the solution to this problem is straightforward. In the above, σ_0 is the reference conductivity of the homogeneous medium, which we choose equal to 1. We also choose $J_0 = 1$ and restrict ourselves to $|\overline{\boldsymbol{E}}| = 1$, so that the problem depends on σ, f, M and the direction of the applied field $\overline{\boldsymbol{E}}$. Convergence is obtained when current conservation is observed at all nodes (Eq. 5.1). Our convergence criterion is the L_2-norm of the divergence of the current field:

$$|\mathrm{div}\boldsymbol{J}| = \left(\sum_{\boldsymbol{x}\in\Omega} \sum_{i=1}^{2} |J_i(\boldsymbol{x}) - J_i(\boldsymbol{x} - \mathbf{e}_i)|^2 \right)^{1/2} < \eta, \tag{5.6}$$

with $\eta = 10^{-10}$. Convergence is somehow erratic but nevertheless obtained (Fig. 5.2a).

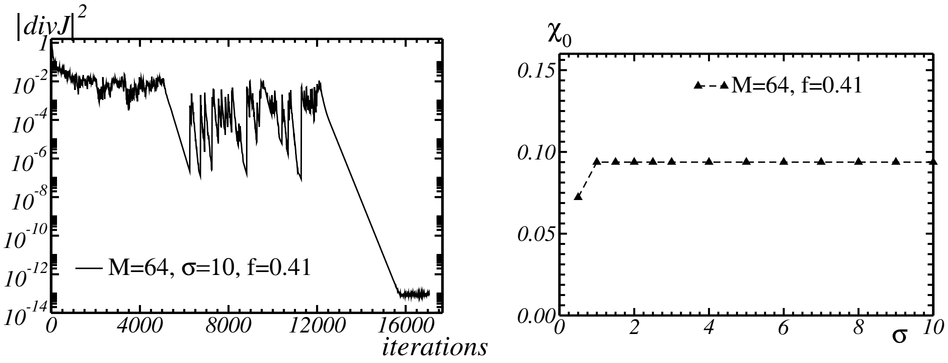

Figure 5.2: Random network in a 64×64 grid. (a) Convergence criterion (5.6) vs. number of iterations. (b) Effective conductivity χ_0 vs. slope σ, with $\overline{\boldsymbol{E}} = \mathbf{e}_1$.

Define the effective conductivity tensor as:

$$\overline{\boldsymbol{J}} = \langle \boldsymbol{J}(\boldsymbol{x}) \rangle_\Omega = \overline{\boldsymbol{\chi}} \cdot \overline{\boldsymbol{E}}, \tag{5.7}$$

where $\langle \bullet \rangle_\Omega$ denotes a spatial mean over Ω. We also define the scalar effective conductivity, that depends on the orientation of the applied field:

$$\chi_0 = \frac{\overline{\boldsymbol{J}} \cdot \overline{\boldsymbol{E}}}{|\overline{\boldsymbol{E}}|^2}. \tag{5.8}$$

We seek for high values of the slope at origin σ so that χ_0 represents the effective yield current. In the rest of this work, we set $\sigma = 10$, so that the effective behavior has reached its yield value when $\langle \boldsymbol{E} \rangle = \overline{\boldsymbol{E}}$ (Fig. 5.2b, with $\boldsymbol{E} = \mathbf{e}_1$).

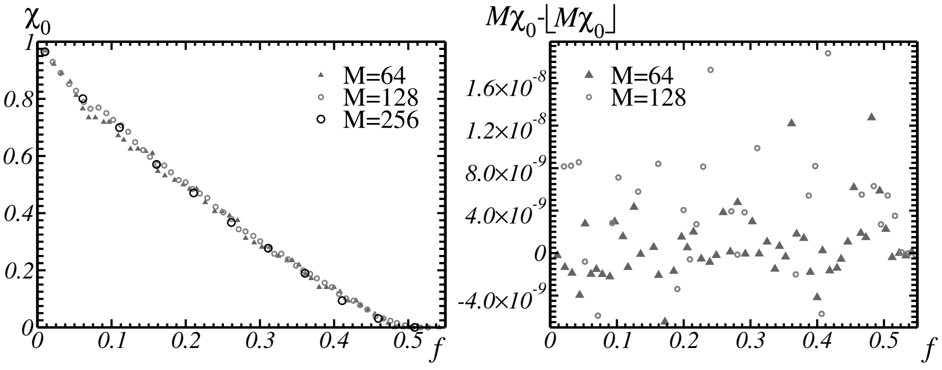

(a) (b)

Figure 5.3: (a) Effective scalar conductivity χ_0 vs. insulator fraction f, for various grid sizes, with applied electric $\overline{\boldsymbol{E}} = \mathbf{e}_1$. (b) Fractional part of $M\chi_0$ showing that $M\chi_0$ is an integer.

5.2 Fourier-base numerical results

Using $\sigma = 10$, the effective conductivity is computed on grids of increasing size along each dimension $M = 64$, 128 and 256 and insulator fraction f in the range $[0; f_c]$ where $f_c = 1/2$ is the bond-percolation threshold for square lattices (Fig. 5.3a). We observe that the effective conductivity χ_0 for all FFT data point on this graph is of the form k/M where $0 \leqslant k \leqslant M$ is an integer, up to an error of less than 10^{-7} (Fig. 5.3b). A connection may be established between this property and the onset of a minimal path (of integer length) along which the electric field localizes. This is illustrated in Figs. (5.4) which shows component E_1 of the electric field, represented as an image (Fig. 5.4a), as well as the grid itself (Fig. 5.4b). On the dual graph, there exists two paths of minimal length (Fig. 5.4b) that span the medium in the direction $\mathbf{e}_2$ transverse to the applied field (horizontal on the image). The length of a path is defined by counting a unit cost for crossing a conducting bond and 0 for an insulating bond, thereby minimizing the number of conducting bonds crossed by the path. Using this definition, the two minimal paths shown in Fig. (5.4b) have normalized length $\xi = 17/M$ and we notice that $\chi_0 = \xi J_0$. It is obvious that ξJ_0 is an upper-bound of χ_0. Conversely, the existence of a divergence-free current field with mean ξJ_0 is a consequence of the "max-flow min-cut" theorem [57]. Hence, $\xi = \chi_0 / J_0$.

The non-unicity of the electric field is a consequence, in general, of the non-unicity of minimal paths. Assume that there is a closed loop in the set of minimal paths on the dual graph such as, for instance, two minimal paths joining at infinity. Along the bonds crossing the loop, the current field is J_0 and the electric field is larger than, or equal to, J_0/σ. Therefore, if the electric component along any of these bonds is larger than $J_0/\sigma + \delta E$ with $\delta E > 0$, a solution of the problem may be defined by adding a quantity smaller than δE to the potential $\phi(\boldsymbol{x})$ at each node $\boldsymbol{x}$ located in the interior of the loop. The electric fields $\boldsymbol{E}$ should be different in each solution, while the current field $\boldsymbol{J}$, and the overall energy $(1/2)\sum_{\Omega} \boldsymbol{E} \cdot \boldsymbol{J}$, is unique.

The length of minimal paths in random lattices is closely related to the "time constant" in first-passage percolation theory [124]. In this problem, domain that grows with respect to a discrete time t is considered. Growth at each time step is controlled by the value along each bond at the frontier of the domain. After a long time ($t \to \infty$), the region asymptotically defines a limiting shape [104] which in general, is not a ball [69], due to the anisotropy of the lattice. Thus, if $s(\boldsymbol{x}, \boldsymbol{x}')$ is the minimal length between two points $\boldsymbol{x}$ and $\boldsymbol{x}'$, we expect $s(\boldsymbol{x}, \boldsymbol{x}')/|\boldsymbol{x} - \boldsymbol{x}'|$ to converge to a finite value when $|\boldsymbol{x} - \boldsymbol{x}'| \to \infty$, which depends on the direction of $\boldsymbol{x} - \boldsymbol{x}'$. Equivalently, χ_0 depends on the loading direction $\overline{\boldsymbol{E}}$ in the square lattice, as expected.

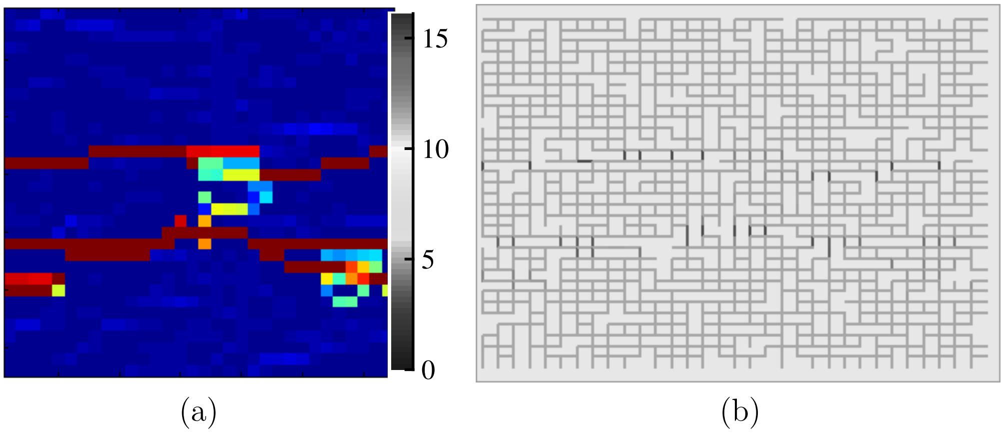

(a) (b)

Figure 5.4: FFT results obtained on a grid Ω of 32×32 nodes, with $f = 0.2$ and $\overline{\boldsymbol{E}} = \mathbf{e}_1$ where $\mathbf{e}_1$ is oriented top to bottom. (a) Component E_1 of the electric field, each bond being represented by a voxel. (b) Square grid. Missing bonds are insulating, the gray-level color in other bonds represents the value of the electric field: highest values in black, lowest in light gray.

We now perform FFT computations of the effective conductivity χ_0 for small values of f, equal to 10^{-4}, 10^{-3}, 10^{-2} and 10^{-1} (Fig. 5.5). A fit of the data provides $\chi_0 \approx 1 - \sqrt{f}$, with nearly unit prefactor, when $\overline{\boldsymbol{E}}$ is oriented along direction $\mathbf{e}_1 + \mathbf{e}_2$ (light gray symbols). FFT results obtained for a macroscopic field oriented along $\mathbf{e}_1$, are less conclusive (black symbols) but point nevertheless to a linear correction $\chi_0 \approx 1 - 2.7f$.

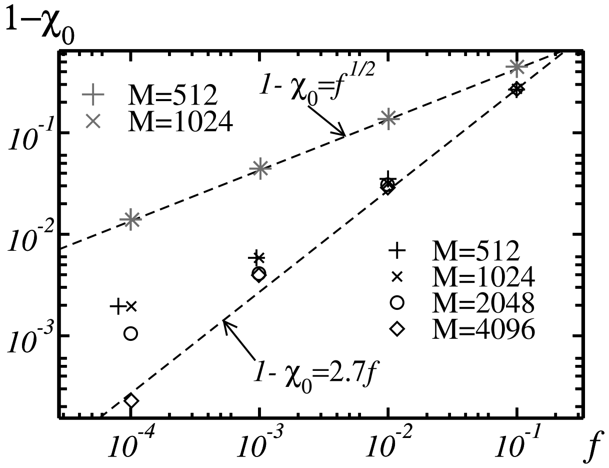

Figure 5.5: FFT results for the effective conductivity in the random resistor network. Gray symbols: loading in the $(1, 1)$ direction $\overline{\boldsymbol{E}} = \mathbf{e}_1 + \mathbf{e}_2$. Black symbols: loading in the $(1, 0)$ direction $\overline{\boldsymbol{E}} = \mathbf{e}_1$.

As pointed out by Roux & François [205], the scaling law correction $\sim f^{1/2}$ in the $(1, 1)$ direction is related to the rugosity (width in the transverse direction) of minimal paths. Suppose that a path of minimal length passes through two points $\boldsymbol{x}$ and $\boldsymbol{x}'$ far from each other with $\boldsymbol{x}-\boldsymbol{x}'$ parallel to $\mathbf{e}_1+\mathbf{e}_2$ (Fig. 5.6). In the absence of broken bonds, the length of the two gray paths are the same. Therefore, if any broken bond appears inside the square $[x_1;x_1']\times[x_2;x_2']$ the length of the path will be reduced by 1. Accordingly, the length of the minimal path normalized by $|\boldsymbol{x}'-\boldsymbol{x}|$ will be reduced by $1/(\sqrt{2}|x_1'-x_1|)$ whereas f increases by about $1/L^2$, thus the normalized length of the minimal path change by a factor $\sim\sqrt{f}$. In the $(1,0)$ direction, minimal paths are mostly flat [61, 205], therefore, the leading-order correction to χ_0 is expected to be linear ($\sim f$), as would be obtained for a straight line.

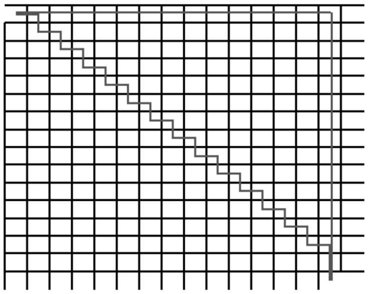

Figure 5.6: Two minimal paths (in light gray) joining two broken bonds (top-left and bottom-right) in the square lattice.

5.3 Network with local coupling between bonds

Hereafter we consider a resistor network that may be used as a model for a material in the continuum. The elementary cell Ω is now made of a set of $M\times M$ pixels, rather than nodes. The electric and current field $\boldsymbol{E}(\boldsymbol{x})$ and $\boldsymbol{J}(\boldsymbol{x})$, and the potential field $\phi(\boldsymbol{x})$ are defined in each pixel. We keep the conservation and admissibility equations (5.1) and (5.4), i.e., we use finite differences, but consider instead of (5.2) the constitutive law:

$$J_i(\boldsymbol{x})=\begin{cases}\sigma E_i(\boldsymbol{x}) & \text{if } \sigma|\boldsymbol{E}(\boldsymbol{x})|\leqslant J_0,\\ J_0E_i(\boldsymbol{x})/|\boldsymbol{E}(\boldsymbol{x})| & \text{if } \sigma|\boldsymbol{E}(\boldsymbol{x})|>J_0,\end{cases}\tag{5.9}$$

where $|\boldsymbol{E}(\boldsymbol{x})|^2=E_1(\boldsymbol{x})^2+E_2(\boldsymbol{x})^2$. Problem (5.1)-(5.4)-(5.9) is that of a random resistor network with local coupling between bonds pointing from the same node. As previously we solve this problem numerically using FFT computations, carried out using $\sigma=10$, this time on grids of 2048^2 and 4096^2 voxels. The augmented Lagrangian scheme is found to be somehow slow to deal with this problem, and we turn to the “accelerated scheme” [77] with “discrete” Green operator [254]. The accelerated scheme was originally devised for linear behavior. However, it is straightforward to extend it to nonlinear behavior, provided one is able to invert an equation of the type (5.5). We choose $\sigma_0=0.01$ for the conductivity of the reference medium. The effective conductivity χ_0 is again defined by (5.8).

We consider the limiting case of a dilute concentration of insulators. FFT results for the effective behavior are represented in Fig. (5.7) as a function of the concentration of insulators, in

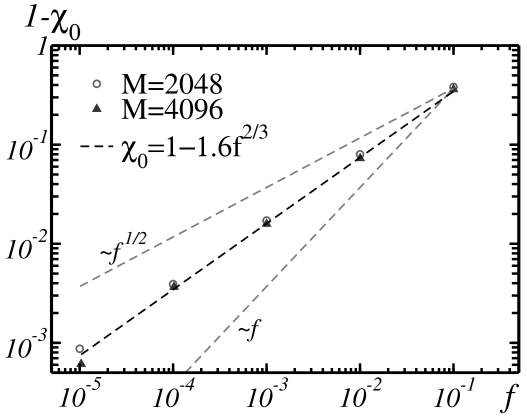

Figure 5.7: Log-log plot of $1 - \chi_0$ vs. fraction of insulating bonds f, in the dilute limit $f \to 0$. Data points: FFT results. Black dashed line: power-law fit with 2/3 exponent of FFT data points. Gray dashed lines: power-law f and $f^{1/2}$.

log-log plot. The leading-order term in f exhibits a power-law scaling with exponent $\approx 2/3$. This scaling law is consistent with the interpretation of the effective conductivity in terms of minimal path, and the bound (4.20) obtained in the continuum.

Assume now that the constitutive law in each phase is of type (5.9) with yield current J_0 in the matrix and J_1 in inclusions, i.e.:

$$\boldsymbol{J} = \min(\sigma|\boldsymbol{E}|, J_c)\frac{\boldsymbol{E}}{|\boldsymbol{E}|}, \tag{5.10}$$

with $J_c = 1$ in the matrix and $J_c = J_1$ $(0 \leqslant J_1 \leqslant 1)$ in inclusions. The effective conductivity of such material may be compared to bound (4.37) appropriate to a Boolean model in the continuum with finite contrast, i.e.:

$$\xi \leqslant 1 - \frac{3(1-J_1)^{4/3}}{\Gamma\left(\frac{2}{3}\right)}\left(\frac{3f}{2\pi}\right)^{2/3} + O(f^{4/3}) \approx 1 - 1.3534(1-J_1)^{4/3} f^{2/3}, \tag{5.11}$$

in the dilute limit $f \to 0$.

We carry out FFT computations of the effective conductivity of a random network containing two nonlinear phases obeying (5.9). Results, shown in Fig. (5.8), are compared to the analytical bound (5.11). The estimate $\xi \approx 1 - 1.6(1-J_1)^{4/3} f^{2/3}$ is also represented as a dashed line in Fig. (5.8). The bound (5.11) appears meaningful as it displays the same concavity as the FFT data, although FFT results are quite sensitive to the size of the elementary cell Ω.

5.4 Conclusion

The present chapter examined how one may characterize the effective behavior of a binary mixture made of an insulating phase embedded in a conducting nonlinear phase characterized by a yield current. The problem is addressed in the context of a random resistor network in two dimensions.

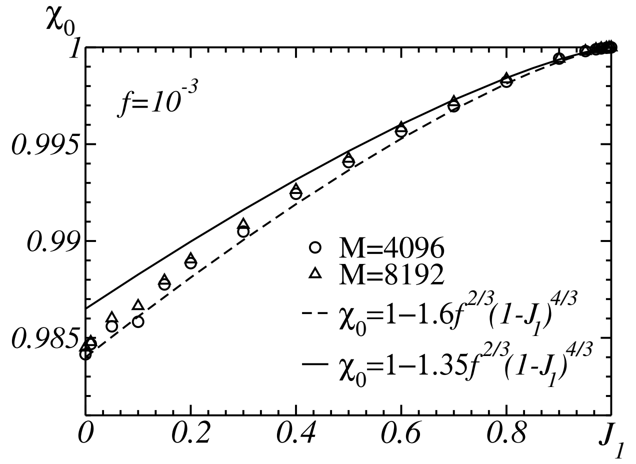

Figure 5.8: Effective conductivity χ_0 of a binary resistor network with yield currents $J_0 = 1$ and $0 \leqslant J_1 \leqslant 1$, as a function of J_1. Black solid line: bound (5.11). Dashed line: estimate $\chi_0 \approx 1 - 1.6(1 - J_1)^{4/3} f^{2/3}$ (see text).

We observe that the network's effective conductivity is given by the length of the minimal path defined on the dual lattice. The path spans the network in the direction transverse to the applied field and its length is weighted by the yield current along each bond.

For a dilute concentration of insulating phase, the effective conductivity exhibits singular power-law behavior when the applied macroscopic field is oriented transverse to the directions of the lattice, or if local coupling, that mimic an isotropic law, is introduced between the nodes and the applied field is parallel to the lattice directions. In these two cases, the responses are characterized by a correction $\sim f^{\nu}$ with exponent ν equal to 1/2 and 2/3 respectively. Furthermore, we derive an upper-bound for the length of geodesics spanning a composite in the continuum, a Boolean set of disks. This bound exhibits an exponent 2/3 in the dilute limit, consistently with numerical data. These results suggest a leading-order correction $\sim f^{2/3}$ for the effective conductivity of nonlinear composite materials containing a dilute concentration f of homogeneously-distributed, monodisperse, insulating particles. Other problems of interest include hierarchical microgeometries, some of which are exactly solvable [111].

In the dual problem of an ideally-plastic media reinforced by rigid particles, strong connections have also been reported between geodesics and shear bands [117], highlighting the links between effective flow stress, geodesics and the localization patterns of the shear bands [189].

Chapter 6

Homogenized metrics in planar, multiscale random sets

In this chapter, we investigate homogenized metrics in planar, multiscale random sets. The length of geodesics (minimal paths) spanning a stationary random sets of grains is considered. The pseudometric is zero in “pores” and infinite in “rigid obstacles”, and equals the Euclidean distance in the embedding matrix. Accordingly, minimal paths tend to cross porous grains while avoiding rigid particles. Multiscale random structures based on Boolean sets of disk-shaped grains are considered, as well as random sequential adsorption models of squares, and we focus on the asymptotic limit of an infinitesimal density of grains. Our approach relies on numerical computations on the one hand, and on upper-bounds on the other hand.

This work is motivated by the connection between geodesics and effective conducting behavior, outlined in the previous chapter for nonlinear resistor networks. Our results, of a purely-geometric nature, are compared to the predictions of nonlinear homogenization theories for the effective yield stress of particulate composites subjected to anti-plane shear, and to rigorous bounds established for the same problem.

Outline This chapter is organized as follows. In Sec. (6.1) we define various “porous” random models of disks in 2D, with emphasis on multiscale structures. In Sec. (6.2), the minimal path problem is defined, and numerical results are obtained for the porous case. Sec. (6.3) deals specifically with the dilute porosity limit. Sec. (6.4) is concerned by the dual problem of minimal paths spanning a medium containing a population of “rigid” grains. Analytical results related to nonlinear homogenization problems are discussed in (6.4.4). We conclude in Sec. (6.5).

6.1 Multiscale random structures

Our starting point is a Boolean model of equisized disks, denoted $\mathcal{B}_E$, with homogeneous Poisson intensity in the plane [226, 169]. A realization of $\mathcal{B}_E$ is the union of translations $\boldsymbol{G}_i$ of a primary grain $\boldsymbol{G}$ implanted along a set of germs g_i which are Poisson-distributed in the plane [165]:

$$\mathcal{B}_E = \bigcup_{i=1}^{\infty} \boldsymbol{G}_i, \qquad \boldsymbol{G}_i = \{\boldsymbol{x} + g_i ; \boldsymbol{x} \in \boldsymbol{G}\}, \tag{6.1}$$

where, for simplicity, we denote $\mathcal{B}_E$ both the probabilistic model and one of its realization. The random Poisson point process $(g_i)_{i>0}$ is defined by its intensity $\theta(\boldsymbol{x})$, also known as a a regionalized density, which depends on the space variable $\boldsymbol{x} \in \mathbb{R}^2$. The quantity $\theta(\boldsymbol{x})\mathrm{d}S$ is the expectation (mean over realizations) of the number of germs g_i contained in a domain of infinitesimal surface area $\mathrm{d}S$ centered around $\boldsymbol{x}$. Additionally, the number of germs in two disjoint domains are independent random variables. These two properties completely define a Poisson point process [226]. Furthermore, the Poisson point process is called "homogeneous" if $\theta(\boldsymbol{x})$ is uniform in space ($\theta(\boldsymbol{x}) \equiv cst$).

In the present work, the primary grain $\boldsymbol{G}$ is a disk of radius R. The mean surface fraction $0 \leqslant f \leqslant 1$ of the disks, averaged over the plane, is given by:

$$f = 1 - \mathrm{e}^{-\theta\pi R^2}. \tag{6.2}$$

The above is a consequence of a more general result, known as the Choquet-Matheron-Kendall theorem [226] which gives an explicit form of the capacity functional, i.e. the probability that a compact set K hits $\mathcal{B}_E$. The theorem, which involves morphological transforms of the primary grain with structuring element K (e.g. dilation, erosion), reduces to (6.2) when the convex K is a point, and is the basis of many other analytical results related to Boolean media. However the simple formula (6.2) may also be derived by elementary means (see "Avrami equation" [13]).

Consider now a square domain Ω of surface area S containing a realization of the set $\mathcal{B}_E \cap \Omega$, and denote n the number of germs (or disk centers) lying in Ω. The number n is a random variable which follows the *discrete* Poisson distribution law of mean θS:

$$n \sim P(\theta S). \tag{6.3}$$

In the dilute limit $\theta \ll 1$ (or $f \ll 1$), Eq. (6.2) entails the obvious result $f \approx \theta\pi R^2 \approx n\pi R^2/S$. The "representativity" of realizations of the model in Ω for estimating a statistical quantity may be defined by the asymptotic behavior of the variance of that quantity as $S \to \infty$. For instance, the surface fraction of disks in domain Ω scales asymptotically as $\sim 1/S$ when $S \to \infty$ [170, 135].

A realization of $\mathcal{B}_E$ in a domain Ω is represented in Fig. (6.1a). The model parameters θ and R have been chosen so as to enforce, on average, $n = 500$ and $f = 30\%$, referring to (6.2) and (6.3).

The Boolean model $\mathcal{B}_E(\theta(\boldsymbol{x}), R)$ made of disks of constant radius R and based on a homogeneous or inhomogeneous intensity $\theta(\boldsymbol{x})$ serves as an ingredient to define the following "two-scale" models:

$$\mathcal{B}_P = \mathcal{B}_1 \cup \mathcal{B}_2, \quad \mathcal{B}_C \sim \mathcal{B}_E(\theta_2 \mathbf{1}_{\mathcal{B}_1}(\boldsymbol{x}), R_2) \quad \text{with} \quad \mathcal{B}_1 \sim \mathcal{B}_E(\theta_1, R_1), \quad \mathcal{B}_2 \sim \mathcal{B}_E(\theta_2, R_2), \tag{6.4}$$

where θ_1, $\theta_2 > 0$ and $R_1 > R_2 > 0$ are parameters, $\mathbf{1}_{\mathcal{B}_1}(\boldsymbol{x})$ is the characteristic function of the Boolean set $\mathcal{B}_1$, and $\mathcal{B}_i \sim \mathcal{B}_E(\theta_i, R_i)$ ($i = 1, 2$) designates independent random realizations of Boolean models of equisized discs.

The "polydisperse" model $\mathcal{B}_P$ is according to (6.4) the union of two Boolean models of disks of radii R_1 and R_2. It is also a Boolean model of randomly-sized grains with intensity $\theta_1 + \theta_2$ (see Fig. 6.1b for an example). The "Cox-Boolean" model $\mathcal{B}_C$ is built in two steps. In the first step, a realization of a Boolean set $\mathcal{B}_1$ of disks of radius R_1 and homogeneous intensity θ_1 is simulated. In the second step, smaller-sized disks of radius $R_2 < R_1$ are homogeneously implanted in domain $\mathcal{B}_1$. At the end of the process, the largest disks, of radius R_2, are discarded. The point process for the disk centers in this later model is known as a Cox point process [171]. This procedure allows one to generate a set of grains aggregated into clusters (Fig. 6.1c, clusters shown in the embedded image).

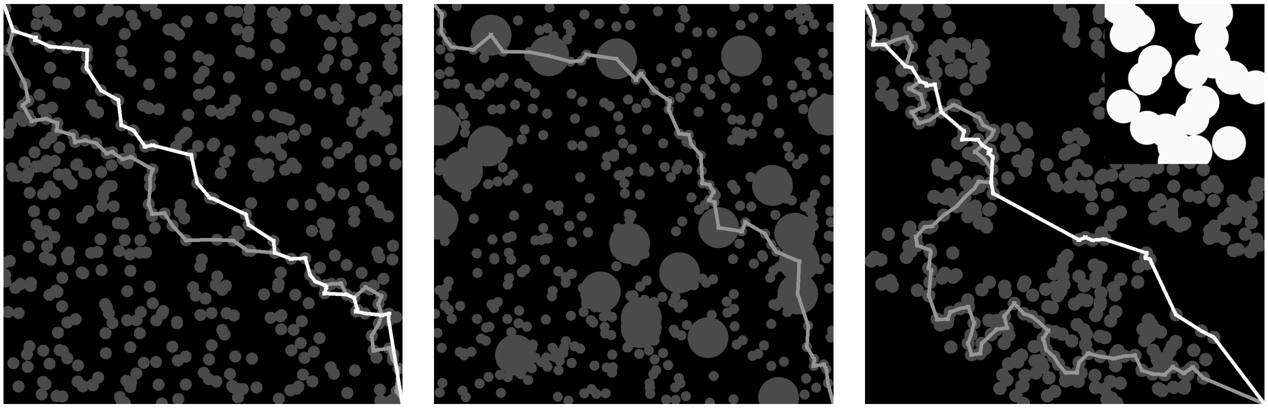

(a) (b) (c)

Figure 6.1: Random realizations of three Boolean random sets containing about 500 disks with surface fraction $f \approx 30\%$. (a) Equisized disks (Boolean model $\mathcal{B}_E$). (b) Polydisperse model $\mathcal{B}_P$. (c) Symmetric Cox-Boolean model $\mathcal{B}_S$ (top-right: model $\mathcal{B}_1$ used to generate the structures). Gray lines: path of minimal length joining two opposite corners. White line: paths used to compute bounds (6.12) and (6.18) for the distance between the two corners.

When $R_2 \ll R_1$, i.e. for widely-separated disk radii, models $\mathcal{B}_P$ and $\mathcal{B}_C$ can be described as two-scale random structures. The length scales R_1 and R_2 are related to the granulometry of the grains (model $\mathcal{B}_P$) or to the typical sizes of grains and of grains aggregates (model $\mathcal{B}_C$). The two models nevertheless depend on four parameters R_1, R_2, θ_1 and θ_2. In the following, we specialize and parametrize them using quantities relevant to homogenization theories, in particular the mean disk surface fraction. Denote f_1 and f_2 the surface fractions of the sets $\mathcal{B}_1$ and $\mathcal{B}_2$. The surface fractions f_P and f_C of models $\mathcal{B}_P$ and $\mathcal{B}_C$ read:

$$f_P = f_1 + f_2 - f_1 f_2, \qquad f_C \approx f_1 f_2. \tag{6.5}$$

In the above, the second equation is only an approximation. Equality between f_C and $f_1 f_2$ would hold if $\mathcal{B}_C$ had been defined as the intersection $\mathcal{B}_C = \mathcal{B}_1 \cap \mathcal{B}_2$. This choice has not been made here because $\mathcal{B}_1 \cap \mathcal{B}_2$ is not a union of disks, and minimal paths in this set are much more complex to study analytically and numerically. Nevertheless, relation $f_C = f_1 f_2$ is asymptotically exact in the limiting case of scale separation $R_1/R_2 \to \infty$.

Standard relations (Eq. 6.2) entail:

$$\theta_1 = \frac{-\log(1 - f_1)}{\pi R_1^2} = \frac{n_1}{S}, \qquad \theta_2 = \frac{-\log(1 - f_2)}{\pi R_2^2} = \frac{n_2}{S}, \tag{6.6}$$

where n_1 and n_2 are the number of germs implanted in domain Ω for models $\mathcal{B}_1$ and for $\mathcal{B}_2$. Consider the polydisperse model $\mathcal{B}_P$. A proportion of disks of radius R_2 which are entirely contained in $\mathcal{B}_1$ are not observable from a realization of $\mathcal{B}_P$, once the largest disks are implanted. When f_1 and f_2 are small and $R_1 \ll R_2$, the total number of observable disks n is about:

$$n = n_1' + n_2', \qquad n_1' \approx n_1, \quad n_2' \approx n_2(1 - f_1), \tag{6.7}$$

where n_1' and n_2' are the number of observable disks of radius R_1 and R_2. In the following, we choose the parameters θ_1, θ_2, R_1 and R_2 for model $\mathcal{B}_P$ so as to impose $f_1 \approx f_2$ and $n_1' \approx \sqrt{n}$.

The first condition aims to enforce equal effect of the two population of disks in terms of surface fraction of disks, which is the most important parameter in homogenization theories. The second condition is a compromise between two opposite goals: (i) achieving representativity of realizations of $\mathcal{B}_1$ in Ω, and (ii) scale separation $R_2 \ll R_1$. Accordingly, we set:

$$R_1^2 = \frac{-\log(1-f_P)}{2\pi\sqrt{n}}S, \quad R_2^2 = R_1^2\frac{\sqrt{1-f_P}}{\sqrt{n}-1}, \quad \theta_1 \sim P\left(\frac{\sqrt{n}}{S}\right), \quad \theta_2 \sim P\left(\frac{\sqrt{n}R_1^2}{SR_2^2}\right). \tag{6.8}$$

Model $\mathcal{B}_P$ is now parametrized by the two variables f_P and n, which approximate the surface fraction and mean number of observable disks in the domain, respectively. Scale separation $R_1/R_2 \gg 1$ is achieved when $n \to \infty$. The realization of model $\mathcal{B}_P$ shown in Fig. (6.1b) has been generated by setting $f_P = 30\%$ and $n = 500$ and using (6.8).

Consider now model $\mathcal{B}_C$, which contains disks of radius R_2. When $f_2 \to 0$ and $R_2 \ll R_1$, the number of disks in Ω is $n \approx f_1 n_2$. To simulate representative configurations of the set of aggregates $\mathcal{B}_1$ in Ω while approaching scale separation ($R_1/R_2 \gg 1$), we choose, as for model $\mathcal{B}_P$, $n_1 = \sqrt{n}$. The parameters θ_1, θ_2, R_1 and R_2 are accordingly set to:

$$R_1^2 = \frac{-\log(1-f_1)}{\pi\sqrt{n}}S, \quad R_2^2 = \frac{-\log(1-f_C/f_1)}{\pi n}f_1 S, \quad \theta_1 \sim P\left(\frac{\sqrt{n}}{S}\right), \quad \theta_2 \sim P\left(\frac{n}{f_1 S}\right). \tag{6.9}$$

Model $\mathcal{B}_C$ is now parametrized by three variables which represent the surface fraction of the disks (f_C), the surface fraction of clusters ($f_1 > f_C$) and the mean number of disks (n).

We also introduce a "symmetric" Cox-Boolean model, denoted $\mathcal{B}_S$, corresponding to model $\mathcal{B}_C$ (Eq. 6.9) with the choice $f_1 = f_2 = \sqrt{f_C}$. This model depends on two parameters, $0 \leqslant f_C \leqslant 1$ and n. A realization of model $\mathcal{B}_S$ is represented in Fig. (6.1c) with $f_C = 30\%$, $n = 500$.

The critical disk surface fraction at the percolation threshold is, for the Boolean model $\mathcal{B}_E$, $f_c \approx 0.6763$ [195]. Regarding model $\mathcal{B}_P$, it is clear that the disk percolate whenever $\max(f_1, f_2) \geqslant f_c$. The inverse proposition holds at scale separation, assuming R_2 is infinitesimal. Indeed, if $f_2 < f_c$, no connected path of length $\sim R_1$ exists in the complementary set of $\mathcal{B}_1$, hence percolation of the disks imply percolation of the largest disks. Accordingly, the percolation threshold for $\mathcal{B}_P$ must be $f_c^P = 2f_c - f_c^2 \approx 0.8952$. Similarly, disk percolation in model $\mathcal{B}_C$ occurs if and only if $\min(f_1, f_2) \geqslant f_c$, assuming scale separation, hence, $f_c^S = f_c^2 \approx 0.4574$ for the disk percolation threshold in model $\mathcal{B}_S$.

6.2 Geodesics and homogenized distance

In the following, the length of a path is defined as the Euclidean length of the parts of the path located in the complementary set of the union of disks. The distance $d(A, B)$ between two points A and B is the minimal length of a path joining the two points, and we call geodesics such paths of minimal length.

The distance function in a stationary random (or periodic) medium may be homogenized, in the sense that it behaves, at sufficiently large scales, as the distance function of a homogeneous medium [181]. If the medium is isotropic, as is the case for the models defined in Sec. (6.1), the homogenized distance function is necessarily isotropic. We denote ξ the limit distance rate $\lim_{t\to\infty} d(A, A + t\boldsymbol{v})/t$ where A is any fixed point and $\boldsymbol{v}$ a unit vector.

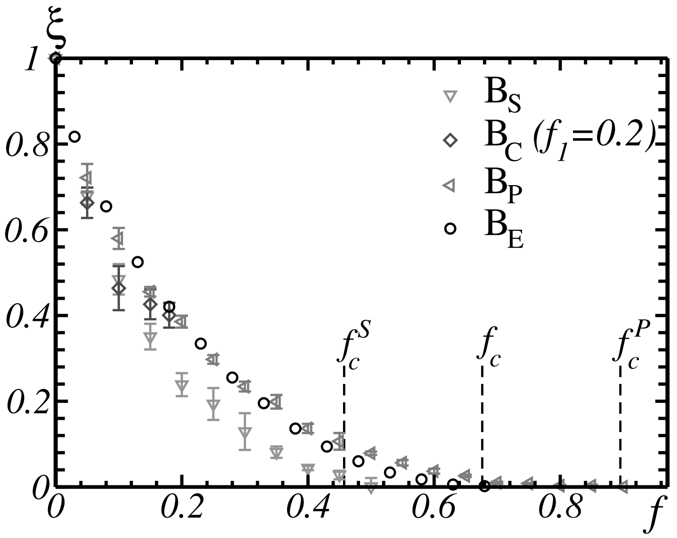

Figure 6.2: Length of minimal paths in the Boolean model $\mathcal{B}_E$ (black circles) and in various two-scale Boolean models: $\mathcal{B}_P$ (left triangles), $\mathcal{B}_C$ (diamonds) and $\mathcal{B}_S$ (bottom triangles).

More generally, we also make use of the homogenized distance function ξ' of models with "finite contrast p". As previously, the length of a path contained in the complementary set of the union of disks is its Euclidean length. However, when the path is inside disks, its length is p times its Euclidean length, instead of 0. When $p = 0$, $\xi' = \xi$, and, trivially, $\xi' = 1$ when $p = 1$. For any stationary (translation invariant) random material, a straight line provides the bound:

$$\xi' \leqslant 1 + (p-1)f. \tag{6.10}$$

In the rest of this work, we denote ξ_E, ξ_P, ξ_C and ξ_S the homogenized distance for models $\mathcal{B}_E$, $\mathcal{B}_P$, $\mathcal{B}_C$ and $\mathcal{B}_S$, respectively. The homogenized distance function relevant to model $\mathcal{B}_E$ with "cost" $p > 0$ in the disk is denoted ξ'_E.

We compute numerically distance ξ for various models of disks. Our algorithm, summarized in Appendix (4.A), does not rely on the discretization of sets of grains on a regular grid, as in fast marching [219] or fast sweeping [266] methods. Instead, the geodesics and the distance function are computed exactly, for a given realization, using the disk centers and radii as input. The geodesics shown as gray lines in Fig. (6.1) have been obtained using this method.

Remark that as a consequence of scale separation $R_1/R_2 = \infty$, distance ξ_P is obtained from ξ_E as:

$$\xi_P(f) = \left[\xi_E\left(1 - \sqrt{1-f}\right)\right]^2, \tag{6.11}$$

where $1 - \sqrt{1-f}$ represents the surface fractions $f_1 = f_2$ in Eq. (6.5).

Estimates of ξ vs. f, the overall disk surface fraction, are shown in Fig. (6.2) for models $\mathcal{B}_E$, $\mathcal{B}_P$, $\mathcal{B}_C$ (with $f_2 = 20\%$) and $\mathcal{B}_S$. The data has been obtained using two random realizations made of $n = 10^5$ disks. This value was deemed sufficient for a rough estimate, indeed estimates for $n = 10^4$ disks are similar while displaying larger fluctuations (not shown). Error bars, corresponding to standard deviation, are shown for all models except for $\mathcal{B}_E$, for clarity. The variances of ξ were found to be very small for this model and need not be represented. The percolation thresholds f_c, f_c^P and f_c^S are indicated in the figure as dotted lines.

Distance ξ_P (model $\mathcal{B}_P$) is similar to that of the one-scale model $\mathcal{B}_E$ (Fig. 6.2, left triangles). However, $\xi_P > \xi$ for $f > 0.3$, consistently with a higher percolation threshold $f_c^P > f_c$, whereas $\xi_P < \xi$ at small surface fraction $f < 0.1$. The numerical data for ξ_P can as well be computed using the data for ξ_E together with Eq. (6.11). For the sake of clarity, this second estimate has not been represented in Fig. (6.2), although it is probably more accurate. Nevertheless, the two sets of data are similar.

The distance function ξ_S in model $\mathcal{B}_S$ (Fig. 6.2, down triangles), is significantly lower than that of the one-scale model $\mathcal{B}_E$, for all values of f simulated. This is consistent with a lower percolation threshold $f_c^S < f_c$. As expected, the distance function ξ_C (Fig. 6.2, diamonds), defined in the range $0 \leqslant f \leqslant f_1$ ($f_1 = 0.2$), reduces to ξ_E when $f = f_2$. Although not visible in the figure, the curves for ξ_C and ξ_S also cross each other when $f = f_1^2 = 0.04$.

6.3 Porous media in the dilute limit

6.3.1 Two-scale random microstructures

In the limit of a vanishing surface fraction of disks $f \to 0$, the distance function ξ_E in the one-scale model decays at a rate at least as high as $\sim f^{2/3}$. Indeed, according to (4.20):

$$\xi_E \leqslant 1 - \alpha f^{2/3}, \qquad \alpha \approx 1.3534. \tag{6.12}$$

The relevance of this bound is confirmed by numerical results in Sec. (4.2.3) which indicate a powerlaw behavior with a similar exponent and slightly higher prefactor:

$$\xi_E = 1 - \gamma f^{\nu} + o(f^{\nu}), \qquad \gamma \approx 1.85, \quad \nu \approx 0.67. \tag{6.13}$$

Consider now the two-scale model $\mathcal{B}_C$ containing clusters of pores with total porosity $f = f_1 f_2$, f_1 being the volume fraction of clusters and f_2 the volume fraction of pores relative to clusters. At the largest scale, minimal paths in $\mathcal{B}_C$ join clusters to one another. Assuming separation of length scales, we identify these minimal paths as that occurring in a one-scale Boolean model $\mathcal{B}_E$ of equisized disks (the clusters) with finite contrast p (Sec. 6.2) where p is a positive "cost" associated to paths crossing the disks. The bound (4.37) extending (6.12) for such a model reads:

$$\xi_E' \leqslant 1 - \alpha(1-p)^{4/3} f_1^{2/3}, \tag{6.14}$$

where $0 \leqslant p \leqslant 1$. Bound (6.14) as well as (6.12) has been obtained by constructing a path and computing its length explicitly (see Chap. 4). These paths are represented by white lines in Figs. (6.1a,c). Observe that, depending on the value of p, bound (6.14) may be higher or lower than that in (6.10). Therefore, combining the two bounds, we obtain:

$$\xi_E' \leqslant 1 - \max\left\{(1-p)f_1;\, \alpha(1-p)^{4/3} f_1^{2/3}\right\}. \tag{6.15}$$

Accordingly, bound (6.10) improves on bound (6.14) in the low-contrast case $\alpha^3(1-p) \leqslant f_1$. This is because bound (6.14) assumes that the minimal path is made of segment of lines joining disk centers. This condition becomes too restrictive in the low contrast case. To show this, let us consider the simple configuration of Fig. (6.3) in which two paths join two disks of centers A and

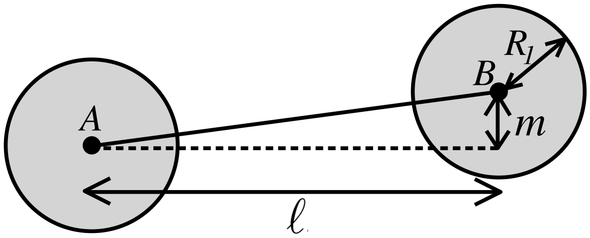

Figure 6.3: Path (solid line) crossing two disks of centers A and B.

B. One path, shown as a solid line, joins the two disk centers whereas the other, represented by a dashed line, is oriented along the horizontal direction, which we assume is the direction along which a minimal path is sought for. The first segment of line mimic a part of the path considered in bound (6.14) in the low-contrast case $p \approx 1$. The second is part of the path used to derive bound (6.10). It is straightforward to compute the length of each segment of line, which we expand as $\ell \to \infty$. Finally, we find that the segment of line joining the disk centers has a lower length than the horizontal segment if $(1-p) \leqslant R_1/\ell$. The term R_1/ℓ is of the same order as the fraction of the disk along a line, i.e. f_1, hence $1-p \sim f_1$.

We now make use of (6.15) to compute a bound for minimal paths spanning $\mathcal{B}_C$. Assume separation of length scales and replace p with the r.h.s. expression in (6.12):

$$\xi_C \leqslant 1 - \max\left\{\alpha f_2^{2/3} f_1;\ \alpha^{7/3} f_2^{8/9} f_1^{2/3}\right\}. \tag{6.16}$$

When specialized to $f_1 = cste \ll 1$, one obtains, replacing f_2 with f/f_1:

$$\xi_C \leqslant \begin{cases} 1-\alpha f_1^{1/3} f^{2/3} & \text{if} \quad f \leqslant f_1^{5/2}\alpha^{-6}, \\ 1-\alpha^{7/3} f_1^{-2/9} f^{8/9} & \text{if} \quad f \geqslant f_1^{5/2}\alpha^{-6}, \end{cases} \tag{6.17}$$

with $\alpha^{-6} \approx 0.16$ ($\gamma^{-6} \approx 0.025$). The above holds when the surface fraction of pores in clusters decreases at a much faster rate than the surface fraction of clusters. The scaling law (6.17a) is obtained when the minimal path is flat at the largest scale and "rough" inside clusters (Fig. 6.4a). In contrast, bound (6.17b) is obtained when the minimal path is rough both at the largest scale and inside clusters (Fig. 6.4b).

When specialized to model $\mathcal{B}_S$, bound (6.10) becomes irrelevant, since $f_1 = \sqrt{f}$ is always smaller than $\alpha^3(1-p) = \alpha^4 f^{1/3}$. We thus obtain:

$$\xi_S \leqslant 1 - \alpha^{7/3} f^{7/9}, \tag{6.18}$$

a result identical to (4.38).

The numerical data obtained in Sec. (4.2.3) suggests the same scaling law as in (6.14), with prefactor γ instead of α:, i.e.

$$\xi_E' \approx 1 - \gamma(1-p)^{4/3} f^{2/3}, \qquad f \to 0. \tag{6.19}$$

This entails the following expressions for the dilute limit expansions of ξ_C and ξ_S, similar to (6.17)

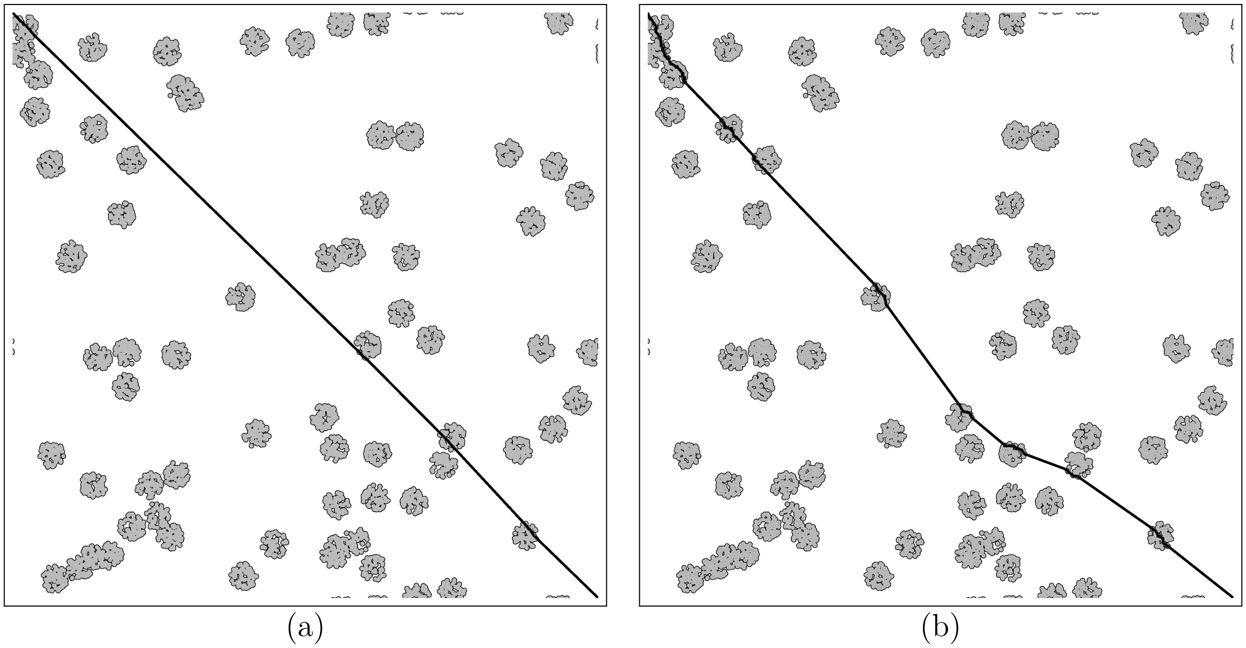

Figure 6.4: Minimal path (black line) in two realizations of model $\mathcal{B}_C$ containing $n = 5000$ disks, with the same surface fraction of clusters $f_1 = 10\%$. The surface fraction of disks inside is clusters $f_2 = 7\,10^{-4}$ (a) and $f_2 = 5\,10^{-2}$ (b). The disks displayed in (a) and (b) have been enlarged so that they are visible. In the real microstructures, their radii is 70 times and 8 times smaller, for (a) and (b) resp.

and (6.18):

$$\xi_C \approx \begin{cases} 1 - \gamma f_1^{1/3} f^{2/3} & \text{if} \quad f \leqslant f_1^{5/2}\gamma^{-6} \\ 1 - \gamma^{7/3} f_1^{-2/9} f^{8/9} & \text{if} \quad f \geqslant f_1^{5/2}\gamma^{-6} \end{cases} \tag{6.20a}$$

$$\xi_S \approx 1 - \gamma^{7/3} f^{7/9}, \tag{6.20c}$$

with $f \to 0$. Finally, for the polydisperse model $\mathcal{B}_P$, Eqs. (6.11) and (6.13) require that:

$$\xi_P \approx 1 - 2^{1/3}\gamma f^{2/3}, \qquad f \to 0. \tag{6.21}$$

The lowest-order correction in this asymptotic expansion is higher than that in (6.13). This is consistent with the data in Fig. 6.2 (Sec. 6.2) which suggests that $\xi_P < \xi_E$ for $f < 0.1$.

In the following, we carry out numerical computations of the lengths ξ_P, ξ_C and ξ_S of minimal paths spanning models $\mathcal{B}_P$, $\mathcal{B}_C$ and $\mathcal{B}_S$. We focus on small surface fractions of disks, ranging from $f = 10^{-6}$ to $f = 10^{-1}$. The number of inclusion is set to $n = 10^6$, and use is made of two random realizations for each data point. Our results are represented in Figs. 6.5a (polydisperse model, ξ_P), 6.5b (symmetric Cox-Boolean model, ξ_S) and 6.6 (Cox-Boolean model, ξ_C).

The numerical data for ξ_P is in good agreement with the scaling law predicted by expansion (6.21) (see Fig. 6.5a, triangles). The data for ξ_S, related to the cluster model $\mathcal{B}_S$ is close to a powerlaw (Fig. 6.5b, triangles) with slope clearly in-between 2/3 and 1. A fit of the data points in the region $f \in [10^{-6}; 10^{-2}]$ provides $\xi_S \approx 4.16 f^{0.79}$ (Fig. 6.5a, solid black line) in excellent agreement with expansion (6.20c), shown as a light-gray solid line.

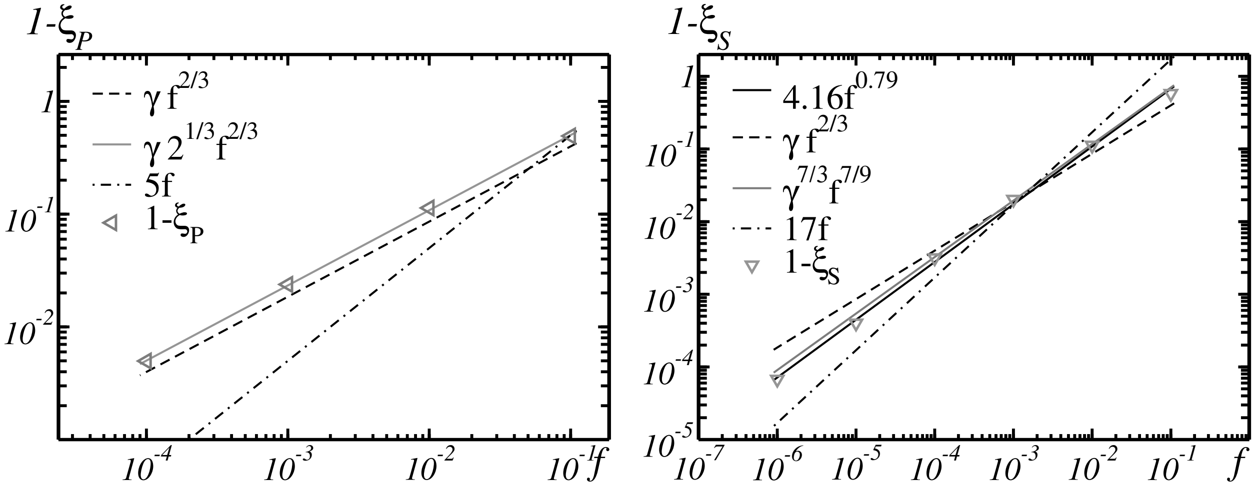

(a) (b)

Figure 6.5: (a) Normalized distance ξ_P in the polydisperse model $\mathcal{B}_P$. Solid gray line: scaling law (6.21). Dashed lines: scaling law (6.13) and linear correction $\sim f$. (b): Distance ξ_S in the symmetric Cox-Boolean model $\mathcal{B}_S$. Triangles: numerical results. Gray solid line: scaling law (6.20c). Black solid line: powerlaw fit of the numerical data. Dashed lines, for comparison: scaling law (6.13) and linear correction $\sim f$.

The numerical data relevant to ξ_C is represented in Fig. (6.6). The surface fraction of the clusters take on values $f_1 = 0.01$ (+ signs) and $f_1 = 0.02$ (diamond symbols). The predictions of Eq. (6.20a) are shown as solid lines. Numerical data points exhibit a powerlaw behavior with exponent close to 8/9, as predicted by (6.20a$_2$), in the range $f \geqslant f_1^{5/2}/\gamma^6$. In the highly-dilute regime $f \ll f_1^{5/2}/\gamma^6$, numerical computations have been carried out using two configurations of $n = 3\,10^6$ disks, for each value of $f = 10^{-7}$ and $f = 10^{-8}$. Results are less conclusive, because, the representativity of the simulated realizations, is insufficient in this case. Nevertheless, we observe that the correction $1 - \xi_C$ is higher when $f_1 = 0.02$ (diamonds) compared to that obtained when $f_1 = 0.01$ (plus signs). The opposite tendency holds when $f \leqslant 10^{-6}$.

6.3.2 “Second-order” nonlinear homogenization theory

In this section, the results of the bounds on geodesics are compared to the predictions of the “non symmetric fully-optimized second-order” method, with strain potential, denoted SO here, and reported in [83, Annex B]. Closed-form expressions are given, in this reference, in the ideally plastic limit. It is straightforward to expand these in the dilute limit $f \to 0$. We obtain, for a 2D medium:

$$\xi_E^{\prime(SO)} \approx 1 - \max\left\{\alpha'(1-p)^{4/3} f^{2/3};\, (1-p)f\right\}, \qquad \alpha' = 3 \times 2^{-5/3} \approx 0.94, \tag{6.22}$$

as $f \to 0$, where $\xi_E^{\prime(SO)} < 1$ is the effective yield stress, normalized by the yield stress in the inclusions, and p is the yield stress in the inclusions divided by that in the matrix. Formula (6.22) is the same as (6.15), save for a prefactor. The second-order theory accordingly entails the same

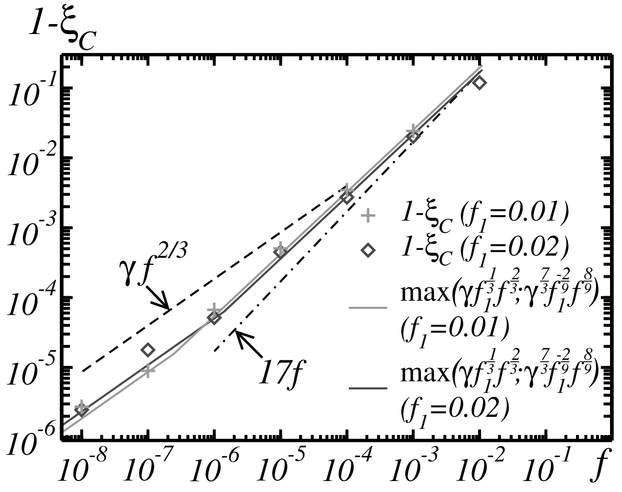

Figure 6.6: Normalized distance ξ_C in the Cox-Boolean model $\mathcal{B}_C$. Symbols: numerical results ($f_1 = 0.01$ for + signs, $f = 0.02$ for diamonds). Black and gray solid lines: scaling law (6.20a). Dashed lines, for comparison: scaling law (6.12) and linear correction $\sim f$.

expressions as in (6.17) and (6.18), with α replaced by α':

$$\xi_C^{(SO)} \approx \begin{cases} 1-\alpha' f_1^{1/3} f^{2/3} & \text{if} \quad f \leqslant f_1^{5/2}\alpha'^{-6} \\ 1-\alpha'^{7/3} f_1^{-2/9} f^{8/9} & \text{if} \quad f \geqslant f_1^{5/2}\alpha'^{-6} \end{cases} \tag{6.23a}$$

$$\xi_S^{(SO)} \approx 1-\alpha'^{7/3} f^{7/9}, \tag{6.23c}$$

with f, $f_1 \to 0$. The predictions of the second-order theory, computed numerically for model ξ_C in the dilute limit, are shown in Fig. (6.7) as symbols. The data is very close to the asymptotic formula (6.23a) (not shown), and also to bound (6.17), shown as solid lines in Fig. (6.7). The lower envelope of the curves, i.e. the set of points where the regime change occurs (see 6.17), is the curve of equation $\xi_C = \alpha^{9/5} f^{4/5}$, represented as a dotted grey line in Fig. (6.7). Along this curve, the effect of the pores is minimal, for a given porosity f.

6.3.3 Multiscale random microstructures

Eq. (6.20a) relevant to model $\mathcal{B}_C$ assumes that f_1 is constant but very small. This limit is obtained by letting f_1 decrease with respect to f in a much slower way than f_2, for instance by enforcing $f_1 = f^\beta$, $f_2 = f^{1-\beta}$ with $\beta \ll 1$. Said otherwise, the dilute limit is obtained when, as f goes to 0, pores are replaced by the solid phase uniformly in each cluster. This is in contrast with the dilute limit of model $\mathcal{B}_S$, where both pores and entire clusters are removed as $f \to 0$, according to $f_1 = f_2 = \sqrt{f}$.

Other dilute limits arise when, more generally, $f_1 = f^\beta$ and $f_2 = f^{1-\beta}$, with $0 \leqslant \beta \leqslant 1$. Eq. (6.16) then leads to:

$$1-\xi_C \sim f^\nu, \qquad \nu = \min\left\{\frac{2+\beta}{3}, \frac{8-2\beta}{9}\right\}, \tag{6.24}$$

where constant prefactors on the r.h.s. have been omitted for simplicity. When $\nu = (2+\beta)/3$, the geodesics are “flat” at the scale of the clusters, and display rugosity when $\nu = (8-2\beta)/9$. The

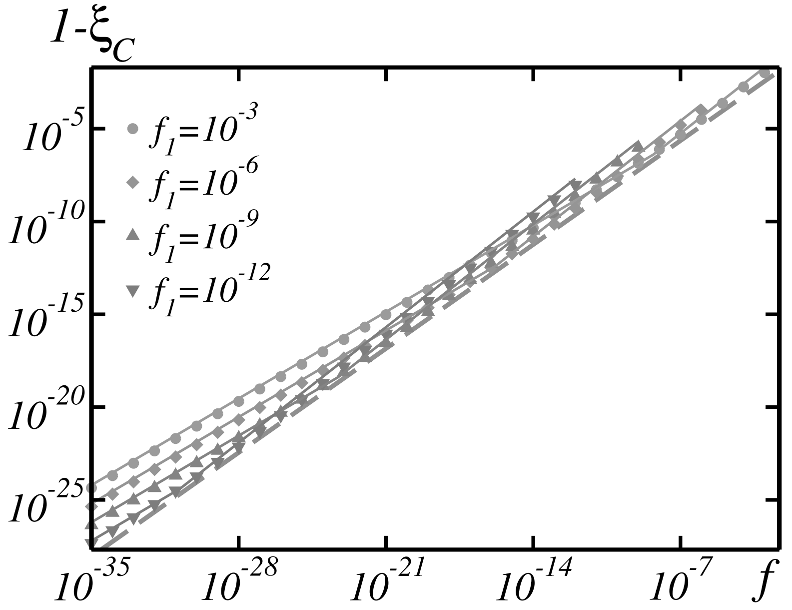

Figure 6.7: Normalized effective yield stress in the two-scale model $\mathcal{B}_C$ as a function of the porosity f, for various values of cluster volume fraction f_1. Symbols: prediction of the second-order theory. Solid gray lines: bound (6.17). Each gray-level refers to the same value of f_1.

maximum value of ν is obtained when the two expressions for ν coincide, that is $\beta = 2/5$, $\nu = 4/5$. Also observe that $\nu \geqslant 2/3$ with equality when $\beta = 0, 1$.

Let us now examine the prediction of the upper-bounds on geodesics for multiscale microstructures with more than two scales. Consider a N-scale Boolean microstructure analogous to $\mathcal{B}_C$. For instance, when $N = 3$, the microstructure is made of grains, aggregated into clusters, and the clusters themselves are aggregated into super-clusters. We denote f_1 the surface fraction of the clusters at the largest scale, f_2 at the next-to-largest scale etc. and f_n the porosity inside the smallest clusters. Assume further that $f_1 = f^{\beta_1}$, ..., $f_N = f^{\beta_N}$, with $f = f_1 ... f_N$ the overall porosity and $\beta_1 + ... + \beta_N = 1$. Making use of (6.15) one obtains the recurrence relation:

$$1 - \xi_C^{(NS)} \sim f^{\nu_1}, \qquad \nu_N = 2\beta_N/3, \quad \nu_i = \nu_{i+1} + \frac{2}{3}\beta_i + \frac{1}{3}\min\left\{\beta_i; \nu_{i+1}\right\}, \quad 1 \leqslant i < N. \tag{6.25}$$

for the leading-order correction to the geodesic length $\xi_C^{(NS)}$. We have that:

$$\nu_1 = \frac{2}{3} + \min(\beta_1, \nu_2) + ... + \min(\beta_{N-1}, \nu_N),$$

hence $\nu_1 \geqslant 2/3$, this value being attained when $\beta_1 = 1^-$ or $\beta_N = 1^-$. It is also clear that $\nu_1 < 1$. The maximum value is obtained by taking $\beta_i = \nu_{i+1}$ $(i < N)$ and choosing β_N so that $\sum_i \beta_i = 1$. We find that $\beta_N = 3/(1 + 2^N)$ and $\nu_1 = 1/(1 + 2^{-N})$, a value that approaches 1 as $N \to \infty$. For the "symmetric" model corresponding to $\beta_1 = ... = \beta_N = 1/N$, it is straightforward to show that $\nu_1 = 1 - 4/(9N)$, which again tends to 1 as $N \to \infty$. A linear correction is accordingly recovered for these various media with infinitely-many scales.

6.4 Rigid grains in the dilute and highly-packed limit

In this section, we consider the dual problem of geodesics spanning a medium containing a set of "rigid" obstacles. The distance function is now infinite inside particles and geodesics are entirely contained in the complementary set of the inclusions. To simplify the analysis and numerical computations, we assume that the inclusions are a set of non-overlapping squares. Indeed, in such model, the minimal path in-between two points outside the squares consists in a continuous line made of a set of segments joining square corners, which are known a priori (Fig. 6.10a). We emphasize that the squares are aligned and not randomly-oriented, and so the model is anisotropic. Furthermore, the direction of propagation of the minimal paths are parallel to one of the axis of symmetry of the squares. The results in this section are therefore restricted to this particular direction. We mention nevertheless, that a study of a similar medium, the random checkerboard, suggests that the metric of that set is in fact isotropic [181].

6.4.1 Random checkerboard

Square-shaped obstacles

Consider an infinite checkerboard, made of randomly-occupied cells, as depicted in Fig. (6.8a). Each cell is occupied, with probability f, by a square-shaped grain with side length D made of two closed and two open boundaries. More precisely, the grain are translations of the set $]0; D[\times[0; D]$.

We define a path spanning the complementary set of the squares as shown in Fig. (6.8). In the figure, the frontiers of the squares are open along the vertical sides and closed along the horizontal ones. We seek for a minimal path oriented along the horizontal direction.

The "visibility" ℓ_i from the corner of a square may be defined as the length of the longest ray starting from that point and oriented in the horizontal direction, which does not intersect a square or the frontier of a square. At its end, the ray necessarily hits two adjacent cells (right of Fig. 6.8). Around the end of the ray, we define a region of maximal size ℓ_i' containing no occupied cells and made of two rows of cells on each side of the ray (Fig. 6.8a). Furthermore, we denote m_i the length of the path, oriented in the vertical direction, which follows the frontier of the obstacle at the end of the ray. This length is the minimal in the up and down direction.

Let us now define a path that we will use to construct a bound. The path follows the ray along a distance $\ell_i - \ell_i'$, then follows an oblique direction along a distance $\sqrt{\ell_i'^2 + D^2}$, and finally circumvent the obstacle following a path of length $m_i - D$. The square open boundaries in the transverse direction allow for configurations where $\ell_i = D$ or $\ell_i' = 0$ and guarantee that the path is still in the complementary set of the squares.

The path normalized length reads:

$$\overline{\xi} = \frac{\sum_{k=1}^{N} \left(\ell_i - \ell_i' + \sqrt{\ell_i'^2 + D^2} + m_i - D \right)}{\sum_{k=1}^{N} \ell_i} = 1 + \frac{\left\langle \sqrt{\ell_i'^2 + D^2} - \ell_i' \right\rangle_i + \langle m_i \rangle_i - D}{\langle \ell_i \rangle_i}. \tag{6.26}$$

Since the cells are occupied independently of each other, one has:

$$P\{\ell_i = kD\} = f^2(1-f^2)^{k-1}, \qquad \langle \ell_i \rangle_i = D/f^2, \tag{6.27a}$$

$$P\{m_i = kD\} = f^{2(k-1)}(1-f^2), \qquad \langle m_i \rangle_i = D/(1-f^2), \tag{6.27b}$$

for $k \geqslant 1$. For ℓ'_i, one obtains the conditional probability:

$$P\{\ell'_i = jD | \ell_i = kD\} = \begin{cases} 2f(1-f)^{2j+1}(1-f^2)^{-j-1}, & j = 0, ..., k-2, \\ (1-f)^{2(k-1)}(1-f^2)^{1-k}, & j = k-1. \end{cases} \tag{6.28}$$

and so, making use of (6.27a):

$$P_j = P\{\ell'_i = jD\} = f^2(1-f)^{2j} + 2f(1-f)^{2j+1}, \qquad j \geqslant 0, \tag{6.29}$$

$$\frac{1}{D}\left\langle \sqrt{\ell_i'^2 + D^2} - \ell'_i \right\rangle_i = \sum_{j\geqslant 0} P_j \left(\sqrt{j^2+1} - j\right) = P_0 + (\sqrt{2}-1)P_1 + \sum_{j\geqslant 2} P_j \left(\sqrt{j^2+1} - j\right). \tag{6.30}$$

Let us replace the term $\sqrt{j^2+1}$ in the r.h.s. by its Taylor expansion as $j \to \infty$. The symbolic calculator [262] provides an exact summation of each term of the Taylor expansion up to order 20, involving "polylogarithmic" special functions [241] (not explicited here). The resulting expressions for the r.h.s. of (6.30) admit, in the dilute limit $f \to 0$, the following expansion:

$$(C_0 - \log f)f + O(-f^2 \log f), \tag{6.31}$$

where C_0 is a constant approaching $C_0 \approx 1.0888$ as the number of terms in the Taylor expansion increases. Thus:

$$\overline{\xi} = 1 + (C_0 - \log f)f^3 + O(-f^4 \log f). \tag{6.32}$$

To make sure that the path considered here may be used as a bound, we compute its transverse deviation. Denote $n_i = \pm m_i$ the transverse distance, counted positive if the "next" point is "up" (as in Fig. 6.8) and negative otherwise. The transverse deviation of the path is $\sum_{i=0}^{N} n_i$. By the central limit theorem:

$$\frac{1}{\sqrt{N}}\sum_{i=0}^{N} n_i = \mathcal{N}\left(0, \langle m_i^2 \rangle_i\right), \qquad \langle m_i^2 \rangle_i = D^2(1+f^2)(1-f^2)^{-2}. \tag{6.33}$$

where $\mathcal{N}$ denotes a normal distribution. The normalized deviation reads:

$$\frac{|\sum_{i=0}^{N} n_i|}{\sum_{i=0}^{N} \ell_i} \sim f^2 \sqrt{\frac{2}{N\pi}} \frac{\sqrt{1+f^2}}{1-f^2} \to 0, \qquad N \to \infty. \tag{6.34}$$

Thus $\xi \leqslant \overline{\xi}$ where $\overline{\xi}$ admits the asymptotic expansion (6.32).

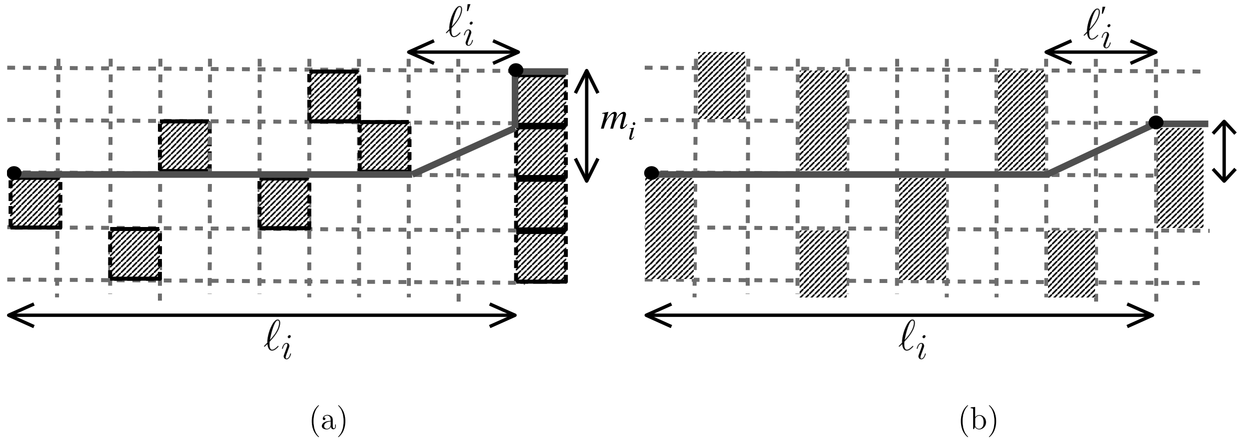

(a) (b)

Figure 6.8: Checkerboard containing randomly-occupied cells. (a) Square model. (b) Model of rectangles. Gray solid lines: path used to obtain a bound on geodesics.

Multiscale random checkerboards

Consider a two-scale random checkerboard which appears as in Fig. (6.8a) at the largest scale. Each occupied cell is itself a random checkerboard at much smaller scale. The occupied cells at the largest scale are therefore clusters, of surface fraction f_1, whereas the surface fraction of cells at the smallest scale in each cluster is f_2. The total surface fraction of the grains is therefore $f_1 f_2$. Applying the above construction at the largest scale, one may consider a path that avoids completely all clusters, and therefore:

$$\xi \leqslant 1 + (-\log f_1) f_1^3, \qquad f_1 \to 0. \tag{6.35}$$

Now, one may consider a nearly straight path at the largest scale (bound 6.10), and make use of bound (6.32) within each cluster:

$$\xi \leqslant 1 + (-\log f_2) f_2^3 f_1, \qquad f_2 \to 0. \tag{6.36}$$

Assume that the surface fractions f_1 and f_2 tends to 0 as $f_1 \sim f^{\beta}$, $f_2 \sim f^{1-\beta}$. Making use of the two previous bounds, one obtains:

$$\xi - 1 \leqslant cst(-\log f) f^{\nu}, \quad \nu = \max(3\beta, 3 - 2\beta), \qquad f_1,\, f_2 \to 0. \tag{6.37}$$

The exponent ν varies between 9/5 and 1. Bound (6.35) is lower than (6.36) when $3/5 < \beta < 1$. Conversely, (6.36) gives a lower bound when $\beta < 3/5$. Similar regime changes have been observed in the periodic checkerboard for which exact analytical results are available [7].

For a medium with N iterated scales, and surface fraction $f = f_1 ... f_N$, with $f_i = f^{\beta_i}$ ($0 < \beta_i < 1$, $\sum_i \beta_i = 1$), one obtains, more generally:

$$\xi - 1 \leqslant cst(-\log f) f^{\nu}, \quad \nu = \beta_1 + \max(2\beta_1, \beta_2 + \max(2\beta_2, \beta_3 + ... + \max(2\beta_{N-1}, 3\beta_N)...)), \tag{6.38}$$

as $f \to 0$. The exponent ν is less than 3, this value being attained when $\beta_1 = 1^-$ or $\beta_N = 1^-$. The minimal value of the exponent ν is obtained when $3\beta_N = 2\beta_{N-1}$, $3\beta_{N-1} = 2\beta_{N-2}$, ..., $2\beta_1 = 3\beta_2$, i.e. $\beta_i = (2/3)^{i-1}\beta_1$. Since $\beta_1 + ... + \beta_N = 1$, this entails $\nu = [1 - (2/3)^N]^{-1}$ which approaches 1 (i.e. a quasi-linear correction) as $N \to \infty$, for such a medium containing infinitely-many scales.

Rectangular obstacles

Consider, as previously, a 2D checkerboard made of a square-shaped cells. Each bond parallel to the horizontal direction is either occupied with probability η or free with probability $1 - \eta$. Furthermore, we assume that the state of a bond (occupied or free) is independent from the state of other horizontal bonds. We define the rigid obstacles in the plane by the set of rectangles made of the two adjacent cells that are either "above" or "below" each occupied bond (see Fig. 6.8b, hashed areas). Again, in order to derive rigorous bound, we assume that the rectangles are open sets, i.e. the matrix-rectangles boundaries are in the matrix. Accordingly, vertical lines in the lattice are free of obstacles, whereas in the horizontal direction, straight geodesics are prohibited by the presence of occupied bonds (Fig. 6.8b).

As previously, we construct a path that spans the checkerboard in the horizontal direction while avoiding the set of rectangular obstacles. The method is defined in much the same way as in Sec. (6.4.1). The path is broken into a set of subpaths comprising three segments, one horizontal of length $\ell_i - \ell'_i$, one oblique, of length ℓ'_i in the horizontal direction and D in the vertical direction, and the third vertical of length $m_i - D$ (see gray line, Fig. 6.8b). As previously, the variable ℓ_i denotes the visibility in the horizontal direction from the initial point. As a consequence, the length of such a path is given by Eq. (6.26). However, the variables ℓ_i, m_i and ℓ'_i now follows different probability laws. We obtain, for ℓ_i and m_i ($k \geqslant 1$):

$$P\{\ell_i = kD\} = \eta(1-\eta)^{k-1}, \qquad \langle \ell_i \rangle_i = D/\eta, \tag{6.39a}$$

$$P\{m_i = kD\} = \eta^{2(k-1)}(1-\eta^2), \qquad \langle m_i \rangle_i = D/(1-\eta^2). \tag{6.39b}$$

The conditional probability of ℓ'_i reads:

$$P\{\ell'_i = jD | \ell_i = kD\} = \begin{cases} \eta(2-\eta)(1-\eta)^{2j}, & j = 0, ..., k-2, \\ (1-\eta)^{2(k-1)}, & j = k-1, \end{cases} \tag{6.40}$$

which entails, making use of (6.39a):

$$P_j = P\{\ell'_i = jD\} = \eta(1-\eta)^{3j}\left[\eta^2 + 3(1-\eta)\right], \qquad j \geqslant 0. \tag{6.41}$$

Inserting this expression in (6.30) and expanding the term $\sqrt{j^2+1}$ as $j \to \infty$:

$$\frac{1}{D}\left\langle \sqrt{\ell_i'^2 + D^2} - \ell'_i \right\rangle_i \approx \left(C'_0 - \frac{3}{2}\log\eta\right)\eta + O(-\eta^2\log\eta), \tag{6.42}$$

where the constant $C'_0 \approx 1.025$ is given by the symbolic calculator [262] as an expression involving the Riemann Zeta function. Again, the number of terms in the expression increases with the order of the Taylor expansion. The first ten digits however are unchanged when $\sqrt{j^2+1}$ is expanded to order 20 or more in j.

Inserting expressions (6.42) and (6.39a) into (6.26), one obtains:

$$\overline{\xi} = 1 + \left(C'_0 - \frac{3}{2}\log\eta\right)\eta^2 + O(-\eta^3\log\eta), \qquad \eta \to 0. \tag{6.43}$$

The surface fraction of the rectangles is $f = \eta(2-\eta)$ and so, in terms of f:

$$\overline{\xi} = 1 + \left(C'_1 - \frac{3}{8}\log f\right)f^2 + O(-f^3\log f), \qquad C'_1 \approx 0.513, \qquad f \to 0. \tag{6.44}$$

As in the previous model, the expression for $\overline{\xi}$ is an upper-bound of the length of the geodesic. This bound exhibits a power 2 of f and is significantly higher that that in (6.32). Indeed, in the square model relevant to (6.32), the presence of an obstacle at the end of a ray is much less likely than in the model of rectangles.

For a medium with N iterated scales of surface fraction $f_i = f^{\beta_i}$ ($0 < \beta_i < 1$, $\sum_i \beta_i = 1$), and total surface fraction $f = f_1 ... f_N$, with f_1 the concentration of clusters at the largest scale and f_N the concentration of obstacles at the smallest scale, we derive, more generally:

$$\xi - 1 \leqslant cst(-\log f)f^\nu, \quad \nu = \beta_1 + \max(\beta_1, \beta_2 + \max(\beta_2, \beta_3 + ... + \max(\beta_{N-1}, 2\beta_N)...)), \tag{6.45}$$

as $f \to 0$. This may be interpreted in a similar way as the model of squares. The exponent ν is less than 2, this value being attained when $\beta_1 = 1^-$ or $\beta_N = 1^-$. The minimal value for ν is obtained when $2\beta_N = \beta_{N-1}$, $2\beta_{N-1} = \beta_{N-2}$, ..., $\beta_1 = 2\beta_2$, i.e. $\beta_i = 2^{1-i}\beta_1$. Since $\beta_1 + ... + \beta_N = 1$, this entails $\nu = [1 - 2^{-N}]^{-1}$ which approaches 1 as $N \to \infty$.

6.4.2 High-packing limit

Let us extend the results of Sec. (6.4.1) and construct an upper-bound for the length of the minimal path in the checkerboard with square-shaped obstacles appropriate to the high-packing limit $f \to 1$. The same microstructure as in Sec. (6.4.1) is considered. Furthermore, we assume that the cost for crossing an occupied cell is equal to pD with $p \geqslant 1$. Compared to Sec. (6.4.1), a slightly simpler path is considered. The path is made of N subpaths each of them consisting of a segment of length $m_i D$ oriented along direction e_2 (transverse to the macroscopic direction of the minimal path) followed by a segment of line of length D, oriented along direction e_1. If $p = \infty$, we follow the same procedure as in Sec. (6.4.1), so that m_i is chosen to be the minimal length of segments oriented along e_2 that reach a non-occupied cell (see Fig. 6.9). If the segments of minimal length in the upward and downward directions have the same length, one of them is chosen at random. When p is finite, the same value of m_i is picked, except if the cost $(m_i + 1)D$ is larger than pD, in which case we set $m_i = 0$. In the latter case only, an occupied cell is crossed with cost pD at the end of the subpath.

Let us denote m'_i the value of m_i when $p = \infty$. We obtain:

$$P\{m'_i = kD\} = f^{2k}(1 - f^2), \tag{6.46a}$$

$$P\{m_i = kD\} = \begin{cases} 0 & \text{if} \quad k \geqslant \lfloor p \rfloor, \\ P\{m'_i = kD\} & \text{if} \quad 1 \leqslant k \leqslant \lfloor p \rfloor - 1, \\ P\{m'_i = 0\} + \sum_{j \geqslant \lfloor p \rfloor} P\{m'_i = jD\} & \text{if} \quad k = 0, \end{cases} \tag{6.46b}$$

where $k \geqslant 0$ and $\lfloor \cdot \rfloor$ is the integer part (or “floor”) function. The mean length of the subpath is then:

$$D \sum_{k=0}^{\lfloor p \rfloor - 1} (k + 1) P\{m'_i = kD\} + pD \sum_{k=\lfloor p \rfloor}^{\infty} P\{m'_i = kD\}, \tag{6.47}$$

which provides the bound:

$$\xi \leqslant \overline{\xi}(p, f) = \frac{1 - f^{2\lfloor p \rfloor}}{1 - f^2} + (p - \lfloor p \rfloor)\, f^{2\lfloor p \rfloor}. \tag{6.48}$$

Consider now a n-scales microstructure consisting of a sequential iteration of n random checkerboards with widely-separated length scales. At the smallest scale, the microgeometry is made of a (one-scale) random checkerboard, characterized by a concentration f_1 of obstacles and a contrast p. The i^{th} scale is obtained by replacing each occupied cell in a random checkerboard with concentration of occupied cells f_i by the microgeometry at the $(i-1)^{\text{th}}$ scale. A bound for such n-scale iterated material read:

$$\xi_n(f) = \xi(\xi_{n-1}(f/f_n), f_n), \tag{6.49}$$

where ξ_i is a bound for the iterated microstructure at scale i. Suppose that occupied cells are highly-packed at each scale ($f_i \approx 1$) and that $f_1 = ... = f_n$. The overall concentration of obstacles is $f = f_1 ... f_n$ with $f_i = f^{1/n}$. We have, when $n \to \infty$:

$$\xi_{n-1}(f/f_n) \approx \xi_{n-1}(f - (f/n)\log f) = \xi_{n-1}(f) - \xi'_{n-1}(f)\frac{f}{n}\log f. \tag{6.50}$$

Insert the above into (6.49) and make use of (6.48). For simplicity, we assume that p is an integer. After some algebra:

$$1-(1-f^{2/n})\xi_n(f) \approx 1+\frac{2}{n}\left[\xi_{n-1}(f)-\xi'_{n-1}(f)\frac{f}{n}\log f\right]\log f+\frac{2}{n^2}\xi_{n-1}^2\log^2 f. \tag{6.51}$$

Simplifying this expression further, all terms cancel up to order $\mathcal{O}(1/n)$ whereas setting to zero the term of order $\mathcal{O}(1/n^2)$ provides us with the ordinary differential equation:

$$\xi_n-\xi_n^2+f\xi_n'=0, \qquad n\to\infty. \tag{6.52}$$

Its solution reads:

$$\xi_n=\frac{1}{1-(1-1/p)f}, \qquad n\to\infty. \tag{6.53}$$

In the high-packing limit $f\to 1$ Eq. (6.53) coincides with (6.48) up to $\mathcal{O}(1-f)$:

$$\xi_n=\overline{\xi}=p-p(p-1)(1-f)+\mathcal{O}(1-f)^2, \qquad n=\infty, \quad p<\infty, \quad f\to 1. \tag{6.54}$$

This is not so when $p=\infty$, in which case:

$$\xi_n=(1-f)^{-1}, \qquad \overline{\xi}=\frac{1}{2}(1-f)^{-1}+\mathcal{O}(1), \qquad n=\infty, \quad p=\infty, \quad f\to 1. \tag{6.55}$$

Accordingly, if bounds are to be interpreted as approximations of the exact behavior, the sequential microstructure is stiffer than the one-scale checkerboard in the high-packing limit.

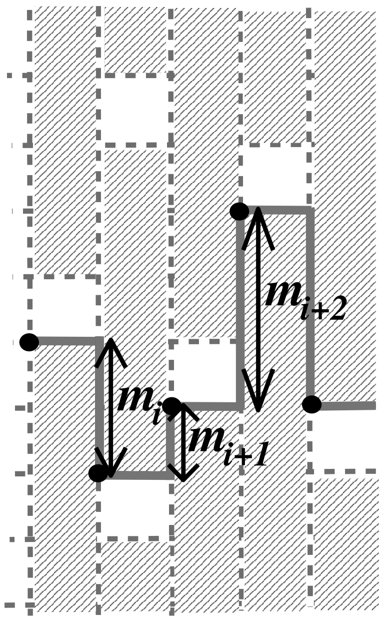

Figure 6.9: Path used to compute bound (6.48) in the random checkerboard.

6.4.3 Random sequential adsorption model of rigid squares

Hereafter, we consider the “random sequential adsorption” model [231] made of squares in the plane. In this model, trial grains are added sequentially in a 2D domain at random position, with uniform regionalized density. When a grain overlaps a previously inserted grain, it is rejected, otherwise, it is implanted. Random sequential adsorption is one among many models of non-overlapping grains [145]. For dilute surface fraction of grains, the position of the grains in random sequential adsorption models is asymptotically equivalent to that of a Poisson point process [145]. Realizations of the model are generated in a domain Ω of surface S. The model is parametrized by the surface fraction of squares $f = nb^2/S$ where n is the number of disks in Ω and b^2 the surface of a square.

Inspired by the algorithm relevant to a union of disks (Appendix 4.A), we devise an algorithm for computing the minimal path between two points in a model of rigid squares, again without discretizing the medium. The task is significantly more demanding, because of the important computational cost involved in determining whether a given segment intersects a square. The algorithm is described in Sec. (6.A).

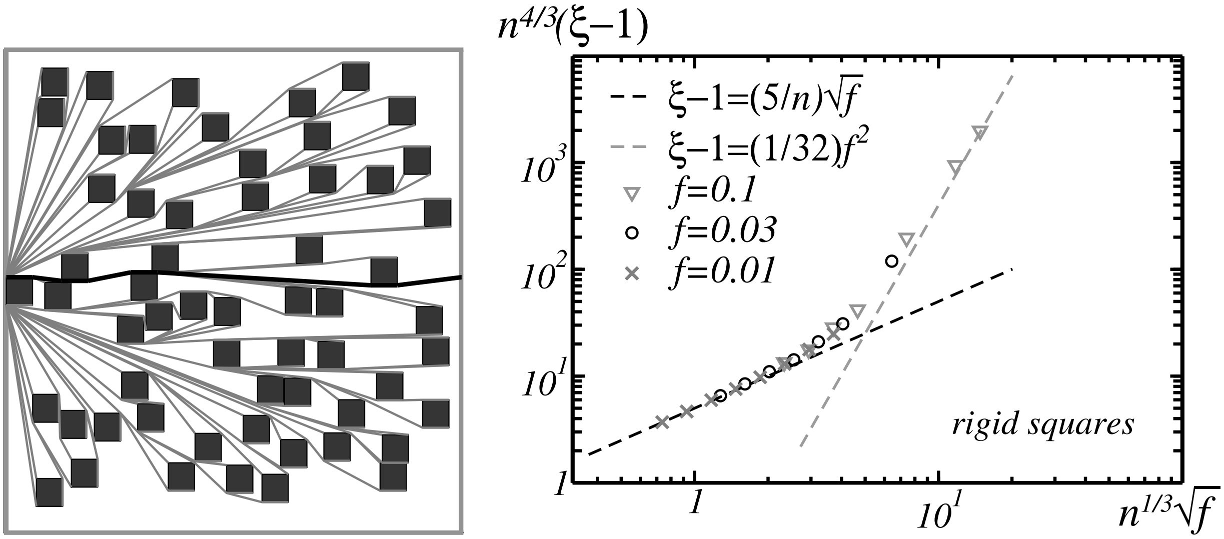

(a) (b)

Figure 6.10: (a) Model of non-interpenetrable squares (in dark gray). Light gray lines: geodesics joining the mid-point on the left side of the domain with all square corners, forming a tree. Black solid line: minimal path joining the two mid-points on the left and right sides. (b) Rigid squares in the RSA model. Numerical data for the quantity $n^{4/3}(\xi - 1)$ vs. $n^{1/3}\sqrt{f}$, in log-log plot.

We now compute the minimal path joining two mid-points on the “right” and “left” sides of Ω, as shown in Fig. (6.10a). In this figure, the direction of propagation is horizontal. We let $f = 0.1$, 0.03 and 0.01. For each value of f, the number of disks takes on values $n = 400$, 800, 1600, ..., 102400. In the dilute regime $f \to 0$, we expect very “flat” minimal paths. Hence, we consider rectangular domains Ω of dimension 1 (a.u.) along the direction of propagation and $h \ll 1$ along the transverse direction. We let $h = 100/n$. With this choice, all minimal paths are constrained in a narrow strip of width at most 24% of the domain. Note that if the value chosen for h is too small, the minimal path predicted by the algorithm is close to the border of the domain and “avoids” the entire set of squares. This can be detected a posteriori. In that case, a new computation would be carried out with a larger value of h.

Numerical results for the quantity $n^{4/3}(\xi - 1)$ are represented in Figs. (6.10b) as a function of $n^{1/3}\sqrt{f}$ in log-log plot. This graph shows the existence of two regimes, one where $\xi - 1 \approx (5/n)\sqrt{f}$, when $n \leqslant n_c = 125 f^{-3/2}$, and the other in which:

$$\xi \approx 1 + \alpha_0 f^2, \qquad \alpha_0 \approx 0.04, \tag{6.56}$$

which holds when $n > n_c$ (Fig. 6.10b). Behavior (6.56) may be interpreted as follows. Let us write the length of the minimal path as:

$$\xi = \frac{\sum_{i=1}^{N} \sqrt{\ell_i^2 + m_i^2}}{\sum_{i=1}^{N} \ell_i} = \frac{\langle \sqrt{m_i^2 + \ell_i^2} \rangle_i}{\langle \ell_i \rangle_i}, \tag{6.57}$$

where the square root term is the length of the i-th segment in the path, ℓ_i and m_i are the length of the projection of the segment along the direction of propagation and transverse to it, and $N \gg 1$ is the number of segments. Averages $\langle \bullet \rangle_i$ are to be taken over all segments in the minimal path. Now, most segments are expected to be nearly horizontal in the dilute limit so that $m_i \ll \ell_i$. A Taylor expansion of (6.57) in $\ell/m \to \infty$ gives, neglecting the contribution of small values of the ℓ_i:

$$\xi \approx 1 + \frac{\langle m_i^2/\ell_i \rangle_i}{2\langle \ell_i \rangle_i}. \tag{6.58}$$

As an approximation, one may identify ℓ_i as the length of the "visibility" in the direction of propagation, which is the longest distance from a given point in that direction that does not intersect a grain (see [44] from some exact results of related quantities in Boolean models). We expect ℓ_i to be of order $\sim b/f$, since the fraction of a line intersected by the squares is, on average, f, and $m_i \sim b/4$. One accordingly expects $\xi - 1 \sim f^2/32 \approx 0.03 f^2$. We emphasize that, unlike in Sec. (6.3), this reasoning is not rigorous, because no explicit (nor admissible) path has been considered.

6.4.4 Comparison with non-linear homogenization theories

The problem of a rigidly-reinforced, perfectly plastic material in anti-plane shear has been considered in [94] and [95]. The author derives an upper-bound for the effective yield stress Y of such a medium. The inclusions are much stiffer than the matrix, and the bound depends on the perimeter and area of the inclusions. The latter reads, for a dilute concentration of squares:

$$Y \leqslant Y_m \left(1 + \frac{7}{2} f \right), \tag{6.59}$$

where Y_m is the yield stress in the matrix. This result is consistent with (6.56), yet in the dilute limit, the bound's prediction, i.e. a leading-order term $\sim f$, is significantly higher than our numerical result, which is of order $\sim f^2$ (6.56). Note however that bound (6.59) holds for an arbitrary distribution of squares. Specifically, consider a N-scale arrangement of square-shaped particles similar to the iterated model $\mathcal{B}_C$, with particle surface fraction $f = f_1 \ldots f_N$ where f_1 is the concentration of clusters at the largest scale and f_N that of particles in the smallest clusters. Making use of (6.56) and following a similar treatment as in Sec. (6.4.1) we obtain:

$$\xi \leqslant 1 + \alpha_0 \min\left(f_1^2; f_1 f_2^2; f_1 f_2 f_3^2; ...; f_1 ... f_{N-1} f_N^2\right). \tag{6.60}$$

To maximize this quantity, we choose:

$$f_1 = f^{(1/2)[1-2^{-N}]^{-1}}, \quad f_2 = \sqrt{f_1}, \quad ..., \quad f_N = \sqrt{f_{N-1}}, \tag{6.61}$$

so that $f_1^2 = f_1 f_2^2 = ... = f_1 ... f_{N-1} f_N^2$. Taking now $N \to \infty$:

$$\xi \leqslant 1 + \alpha_0 f. \tag{6.62}$$

The latter expansion explains the scaling law $\sim f$ in (6.59), assuming the r.h.s. of (6.62) is a good approximation of the length of the exact minimal path in a RSA model of squares with infinitely-many separated scales following (6.61).

In this section, we also consider, as in the porous case, the "non symmetric fully-optimized second-order" (SO) method [83, Annex B]. In the dilute limit $f \to 0$, the (SO) theory predicts, asymptotically:

$$\xi_E^{\prime(SO)} \approx 1 + \min\left\{\frac{f^2}{8}; \, (p-1)f\right\}, \tag{6.63}$$

where $\xi_E^{\prime(SO)} > 1$ is the effective yield stress, normalized by the yield stress in the inclusions, and p is the yield stress in the inclusions divided by that in the matrix. When specialized to $p = \infty$, this formula is close to (6.56). Since bound (6.56) also holds for arbitrary value of p, and given (6.10), it is clear that:

$$\xi_E' \leqslant 1 + \min\left\{\alpha_0 f^2; \, (p-1)f\right\}, \qquad f \to 0, \tag{6.64}$$

which is very similar to (6.63).

We remark that the (SO) theory also predicts that, when $p \geqslant p^*$ (where p^* is a function depending on f only), then $\xi = \sqrt{1 + f^2/4}$ becomes independent of p. This prediction may be interpreted by the fact that, when inclusions are sufficiently stiff, shear bands span the matrix only. Thus, the effective response is unchanged when the inclusions yield stress is increased.

6.5 Conclusion

In this chapter, we have examined the effect of a multiscale distribution of rigid obstacles on the length of minimal paths spanning the media. The dual problem of a multiscale distribution of porous inclusions has also been considered. In the porous case, we have extended bounds on the minimal paths spanning Boolean random media to multiscale materials. In Cox-Boolean models, obtained as the intersection of Boolean models with widely-separated length scales, the length of minimal paths increase with the number of scales, at small surface fraction of particles f. In the limit of infinitely-many scales, the bound predict a linear correction in f at leading-order term. In the rigid case, a small effect of the particles is observed in the dilute limit, resulting in a leading-order correction $\sim f^2$, according to numerical data. Bounds obtained for a random checkerboard geometry confirm a behavior which is essentially quadratic in f. A multiscale distribution of obstacles, where particles are organized as clusters, increase the minimal path length, according to the bounds. For infinitely-many scales, a linear correction in f is predicted. The numerical results obtained in the present chapter, as well as the predictions of nonlinear homogenization theories for the effective yield stress of media in antiplane shear suggest that the present bounds are sharp.

Acknowledgements I thank P. Suquet for pointing to me Refs. [94, 95].

6.A Algorithm for computing shortest paths in a model of squares

In general, geodesics bypassing an obstacle are made of two straight-line segments and of a segment of a curve inbetween, that follows the frontier of the obstacle's convex hull [11, Chap. 13]. Furthermore, the two straight-line segments are tangent to the frontier of the obstacle. Accordingly, in the case of polyhedral obstacles, geodesics are made of segments of lines joining the corners of polyhedra. Lozano-Pérez & Wesley have proposed a numerical algorithm to compute geodesics in such systems of polyhedra [143]. Indeed, for polyhedral shapes, the problem in the continuum can be reformulated as that of a minimal path problem in the "visibility graph", which can be solved using Djikstra's efficient algorithm for graphs [62]. The nodes in the visibility graph are the vertices of the obstacles, and the bonds between nodes are segments joining two of the obstacles vertices, that do not intersect an obstacle. The size of the visibility graph, and so the number of steps to compute the shortest path between two points, however increases rapidly with the number of obstacles [183]. Faster algorithms have been proposed for L_1-metrics [168] of for special geometries, requiring only a subgraph of the visibility graph, such as a set of parallel barriers [139]. The latter can not be used in the present work and we follow the visibility graph approach. Our algorithm is summarized hereafter.

Consider a model of non-interpenetrable squares in two dimensions with infinite distance function inside the squares, i.e. the geodesics are located in the complementary set of the union of squares. Since the geodesics are locally straight lines, they reduce to a set of segments joined by square corners. Two square corners are said to be "visible" from one another if the segment joining the two corners is included in the matrix (if it lies exactly along the matrix-square frontier, the two corners are visible to one another). Thus, for instance a square corner is visible by two of the other other corners in the same square, but not by the third.

In theory, algorithm (4.A) may be used to compute a solution provided one determines the pairs of square corners that are visible to one another. A brute-force approach requires one to determine, for every pair of corners, if a square intersects the segment joining the two corners. This has complexity $O(N^3)$ where N is the number of squares and is prohibitively expensive. Instead, we rely on a different approach, described below.

Assume the domain is divided into subdomains of rectangular shapes whose dimensions are larger than the squares. We are interested in a square corner C located in a subdomain. We first determine the square corners in the same subdomain that are visible from C, using a "brute-force" technique. We then determine the set of "forbidden" angular sectors which are obstructed by the neighboring squares, located in the same subdomain. We then consider a larger set of 8 (or less) subdomains around the square and determine visible square corners in that domain. If a corner is located in a direction included in the forbidden angular sectors, it is discarded, otherwise we determine if it is obstructed by another square. We update the set of obstructed angular sectors, and consider an even larger set of subdomains. This process continues until obstructed angular sectors entirely cover the rest of the (unchecked) domain.

Chapter 7

Cross-over behavior in periodic composites under plane strain and anti-plane shear

The previous chapters have investigated how certain parameters of the microstructure may influence the effective response of materials using a combination of geometrical bounds for the homogenized distance function and FFT numerical results. The results are relevant to nonlinear conductivity with a non-strictly convex potential and to the yield stress of materials subjected to anti-plane shear. This study aims, in contrast with the previous ones, to understand how localization bands may develop, in a setting where the matrix phase follow a strictly convex, powerlaw potential. The problem is investigated in simple, periodic configurations in two dimensions, using limit analysis.

7.1 Conductivity problem

Consider a periodic medium in two dimensions made of a square-shaped elementary cell Ω containing a single disc of radius a (Fig. 7.1a). We assume that the size L of the domain Ω is the length unit, i.e. $L = 1$. The quantity a may alternatively be considered as a non-dimensional parameter that monitors the disc surface fraction f, with $a = \sqrt{f/\pi}$. Points in Ω are referred to in a Cartesian coordinates system ($\mathbf{e}_1$, $\mathbf{e}_2$) so that $\Omega = [-1/2; 1/2]^2$ and the disc center is at the origin.

We are looking for the solution to the problem:

$$\begin{aligned} W(\overline{\boldsymbol{E}}) &= \widetilde{\chi}\frac{\overline{\boldsymbol{E}}^{n+1}}{n+1} = \inf_{\boldsymbol{E}\in\mathcal{K}}\left\{\frac{1}{\Omega}\int_{\Omega}\mathrm{d}\,\boldsymbol{x}\chi(\boldsymbol{x})\frac{|E(\boldsymbol{x})|^{n+1}}{n+1}\right\}, \\ \mathcal{K} &= \left\{\boldsymbol{E},\ \exists\phi : \boldsymbol{E} = -\nabla\phi, \langle\boldsymbol{E}\rangle = \overline{\boldsymbol{E}}\right\}, \end{aligned} \tag{7.1}$$

where $0 \leqslant n \leqslant 1$ is the nonlinearity exponent, $\boldsymbol{E}$ the electric field, $\overline{\boldsymbol{E}}$ the mean applied field, ϕ the electric potential, $\chi(\boldsymbol{x})$ the conductivity at point $\boldsymbol{x}$, $W(\overline{\boldsymbol{E}})$ the macroscopic energy density and $\widetilde{\chi}$ the effective conductivity. In the following, we assume the inclusions is insulating and embedded in a conducting matrix, accordingly $\chi(\boldsymbol{x}) = 0$ in the disc and $\chi(\boldsymbol{x}) = \chi_m > 0$ outside of the disc. The applied field is oriented along the x_1-axis, so that $\boldsymbol{E} = |\boldsymbol{E}|\mathbf{e}_1$.

Consider a trial electrical field $\boldsymbol{E}_\psi$ with components of the form $E_{\psi_2}(\boldsymbol{x}) \equiv 0$, $E_{\psi_1}(\boldsymbol{x}) = \psi(\boldsymbol{x}\cdot\mathbf{e}_1)$ where the function ψ is to be optimized on, under the constraint $\int_0^1 \psi = 1$.

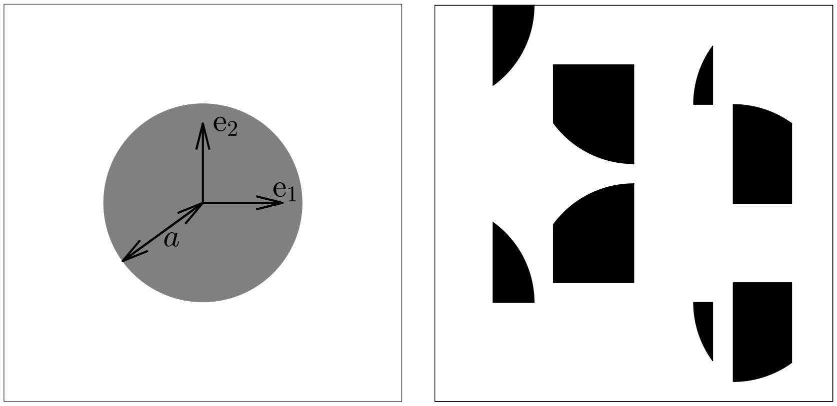

(a) (b)

Figure 7.1: (a) Elementary cell Ω of a periodic microstructure, containing a single disk. (b): "scrambled disk".

$$W(\overline{\boldsymbol{E}}) \leqslant W_\psi = \frac{2\chi_m}{n+1}\left[\int_a^{1/2} \mathrm{d}x|\psi(x)|^{n+1} + \int_0^a \mathrm{d}x|\psi(x)|^{n+1}(1-2\sqrt{a^2-x^2})\right]. \tag{7.2}$$

Set $\partial W_\psi^*/\partial\psi(z) = 0$ where $W_\psi^* = W_\psi + \theta\left(1-\int_0^1\psi\right)$ and solve for ψ:

$$\boldsymbol{E}_\psi(\boldsymbol{x}) = \frac{\overline{\boldsymbol{E}}}{\chi_\psi^{-1/n}} \times \begin{cases} 1 & \text{if } |x_1| > a, \\ \left(1-2\sqrt{a^2-x_1^2}\right)^{-1/n} & \text{if } |x_1| \leqslant a, \end{cases} \tag{7.3a}$$

$$\frac{\widetilde{\chi}}{\chi_m} \leqslant \chi_\psi = \left[1-2a+2a\int_0^1 \mathrm{d}u\,\left(1-2a\sqrt{1-u^2}\right)^{-1/n}\right]^{-n}. \tag{7.3b}$$

A Taylor expansion of the integrand in (7.3b) in the limit $a \to 0$ (n fixed) provides, upon integration:

$$\chi_\psi = 1-\pi a^2 - \frac{8(n+1)}{3n}a^3 + O(a^4). \tag{7.4}$$

The previous expansion is a good approximation of χ_ψ when the integrand in (7.3b) stays close to $1+2a/n\sqrt{1-u^2}$, hence when $a \ll a_c = n/2$ or equivalently $n \gg n_c = 2a$. However, when $n \to 0$ (a fixed), the integral in (7.3b) is governed by the values of its integrand around $u \approx 0$. Let us expand the term $\sqrt{1-u^2}$ to second-order in u in (7.3b). Using the variable change $u \to u\sqrt{n}$ and integrating, we obtain:

$$\int_0^1 \mathrm{d}u\,\left(1-2a\sqrt{1-u^2}\right)^{-1/n} = (1-2a)^{-1/n}\left[\sqrt{\frac{n\pi(1-2a)}{4a}} + o(n)\right], \tag{7.5}$$

so that:

$$\chi_\psi = (1-2a)\left[1-\frac{n}{2}\log(n\pi a(1-2a)) + O(n\log(n))\right]. \tag{7.6}$$

We expect this expansion to hold when the logarithmic term in the r.h.s. is much smaller than $2a$. Solving for $2a = -(n/2)\log(\pi n a)$ entails $a \gg a_c'$ with $a_c' = (n/4)W(4/(\pi n^2))$, where $W(\bullet)$ is the special Lambert function, inverse of $W \mapsto W\mathrm{e}^W$. As $n \to 0$, a_c' is equivalent to:

$$a_c' \sim -\frac{n}{2}\log n. \tag{7.7}$$

We also define n_c' so that $a_c'(n_c') = n_c'$ which is close to

$$n_c' \sim \frac{2a}{-\log a}, \tag{7.8}$$

as $a \ll 1$. Notice that expansions (7.4) and (7.6) do not hold in the interval $a \in [a_c; a_c']$, and in particular when $1 \ll 2a/n \ll -\log n$. The behavior of χ_ψ in this intermediate regime is obtained by approximating the integrand in χ_ψ as follows:

$$\left(1 - 2a\sqrt{1-u^2}\right)^{-1/n} \approx \mathrm{e}^{2a/n}\mathrm{e}^{-au^2/n}.$$

Integrating the above yields:

$$\chi_\psi \approx \left[1 - 2a + \sqrt{\pi a n}\,\mathrm{erf}\left(\sqrt{\frac{a}{n}}\right)\mathrm{e}^{2a/n}\right]^{-n} \tag{7.9}$$

where "erf" is the "error function" $\mathrm{erf}(z) = (2/\sqrt{\pi})\int_0^z \exp(-t^2)\mathrm{d}t$. When $t \to 0$, $\mathrm{erf}(t) \approx 2t/\sqrt{\pi}$ and one obtains:

$$\chi_\psi \approx 1 + 3an - \mathrm{e}^{2a/n}\sqrt{\pi a}n^{3/2} + n^2, \tag{7.10}$$

which is a good approximation of χ_ψ in the region $a_c \ll a \ll a_c'$ (Fig. 7.2a).

The shape of the local electrical field in the band surrounding the inclusion, given by (7.3a), is plotted in Fig. (7.2b), after normalization between 0 and 1. Various values of the exponent n are used. The profile $E_{\psi 1}(x_1, 0)$ for the trial electric field changes in the interval $n \in [n_c'; n_c]$. A concave shape at $n = n_c$ is replaced by a curve exhibiting an inflection point when $n = n_c'$, highlighting the electric field localization. The coordinate of the inflection point is obtained as the root of a polynomial equation of degree 3, given by the second derivative of $E_{\psi 1}(x_1, 0)$ with respect to coordinate x_1 (not shown). The typical width ℓ_b of the localization band then reads:

$$\ell_b = \sqrt{\frac{2n}{a}} + \frac{n}{2a} + o(n), \qquad n \to 0. \tag{7.11}$$

It is clear that when $n = 0$, the electric field is localized along a one-dimensional path that passes through the disc center, with minimum length $1 - 2a$. When n is small but not zero, the field is localized over a band of finite width.

Observe that the present analysis would hold if the disc had been cut along lines parallel to e_1 and e_2 into pieces and each piece moved at a different location, in such a way that points located along a line $x_1 = cst$ stay along a line $x_1 = cst$ (Fig. 7.1b). Obviously, the distribution of the pore fractions along lines parallel to axis e_2 is the same in the original microstructure and in the elementary cell with "scrambled disk". In such a configuration, the localization band are spread into many vertical paths, of suboptimal length, smaller than $1 - 2a + n/(4a^2)$. Such solution bears

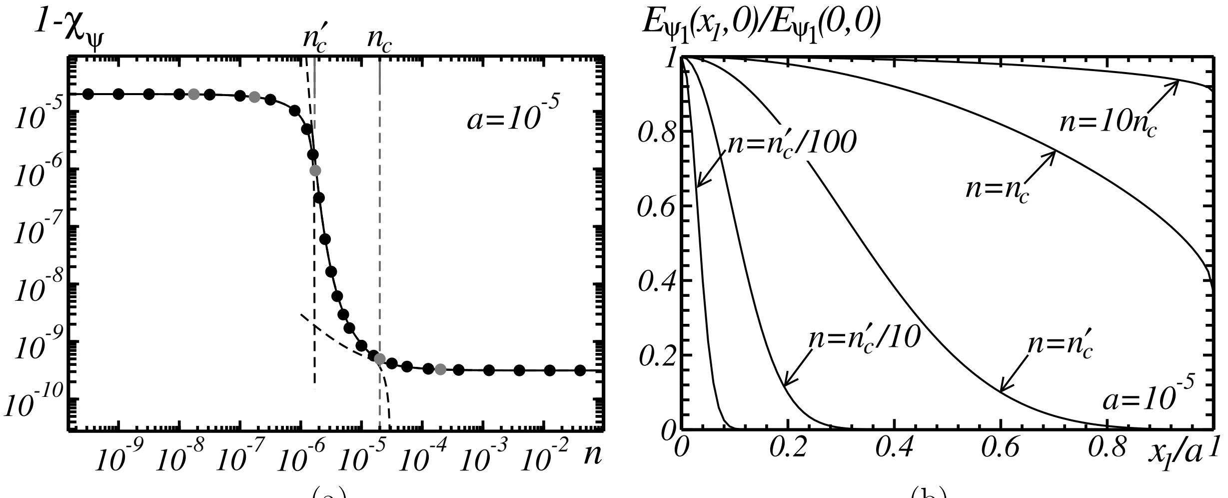

(a) (b)

Figure 7.2: (a) Quantity $1 - \chi_\psi$ vs. exponent n in log-log scale, with $a = 10^{-5}$ fixed (data points). Solid and dashed lines (left to right): expansions (7.6), (7.10) and (7.4), respectively. Gray vertical lines: exponents n_c and n'_c. (b) Normalized profile of the local electrical field E_{ψ_1} within the band surrounding the inclusion, for various values of the nonlinearity exponent n, corresponding to the light gray points in (a).

similarity to localization bands *of varying intensity* that span elastic, perfectly-plastic media under plane strain (see e.g. [258]).

The effective behavior is represented in Fig. (7.3a). In the region $a \ll a_c$, the effective conductivity scales, to leading-order term, as $\sim a^2$, i.e. a linear correction in term of the volume fraction f. The field are not localized in this domain, corresponding to dilute regime (Fig. 7.3b). The electric field in the matrix, in particular, is close to the macroscopic field $\overline{E}$. In the intermediate regime $a_c \ll a \ll a'_c$, the electric field (and local energy density) in the matrix diminishes as a increases, and increases in the band surrounding the inclusion. The increase is maximum along the line of minimal path (Fig. 7.4). In the region $a \gg a'c$ (Fig. 7.3b), characterized as a "localized regime", the electric field takes on very high values within a thin band. The effective response χ_ψ scales as $\sim 1 - 2a$ or equivalently, as $\sim 1 - 2\sqrt{f/\pi}$.

7.2 Nonlinear elasticity

7.2.1 Local and effective behavior

This section is devoted to the analysis of the *plane strain, mechanical* response of a composite material with the same periodic geometry as considered in the previous section. In the matrix, the local infinitesimal deformation and stress tensors are related by:

$$\boldsymbol{\sigma} = \frac{\partial w}{\partial \boldsymbol{\varepsilon}}, \qquad w(\boldsymbol{\varepsilon}) = \frac{y_0 \varepsilon_0}{1+n} \left(\frac{\varepsilon_e}{\varepsilon_0} \right)^{1+n} + (\infty)\mathrm{tr}(\boldsymbol{\varepsilon}), \tag{7.12}$$

where y_0 and ε_0 are the flow stress and reference strain and $w = w(\varepsilon_e)$ is an isotropic strain potential depending on the Von-Mises equivalent strain $\varepsilon_e = \sqrt{(2/3)\boldsymbol{\varepsilon}' : \boldsymbol{\varepsilon}'}$, in which $\boldsymbol{\varepsilon}'$ denotes the

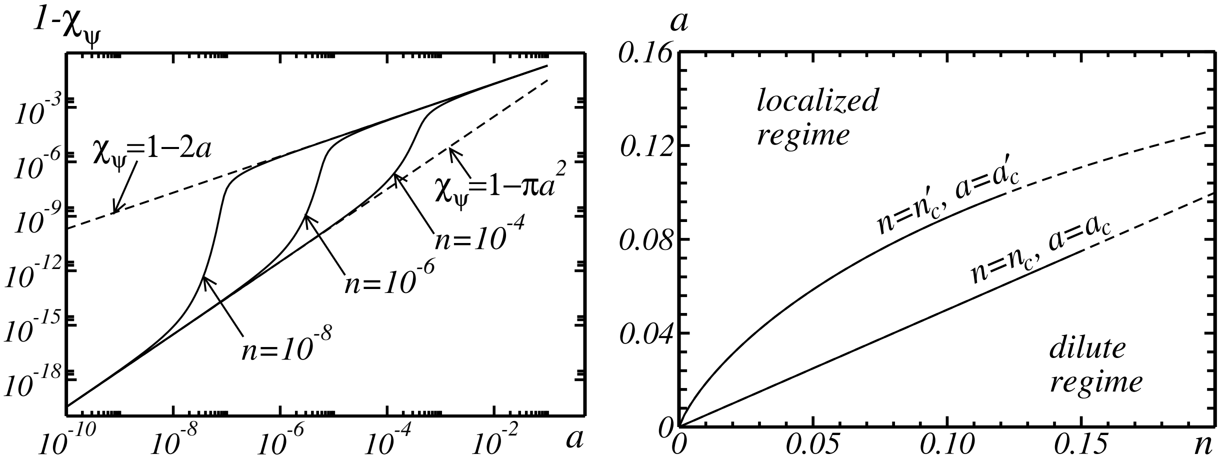

(a) (b)

Figure 7.3: Solid lines: leading-order correction to the effective conductivity upper-bound χ_ψ in the dilute limit $a \to 0$, for various values of the nonlinearity exponent n, in log-log plot. Dashed lines: "highly-dilute" and "localized" regimes described by Eqs. (7.4) and (7.6).

strain deviatoric part. The matrix is incompressible, the potential ω being infinite when $\mathrm{tr}(\boldsymbol{\varepsilon}) \neq 0$. The constitutive law's nonlinearity is monitored by the exponent $0 \leqslant n \leqslant 1$. The limiting values $n = 1$ and $n = 0$ accordingly characterize a linear and rigid-ideally plastic behavior, in the context of deformation theory.

In the following, periodic boundary conditions are applied along the frontiers $\partial\Omega$ of the elementary cell Ω. The medium is accordingly subjected to the macroscopic strain field $\overline{\boldsymbol{\varepsilon}} = \langle \boldsymbol{\varepsilon} \rangle_\Omega$, where $\langle \bullet \rangle_\Omega$ denotes a mean over Ω. The "effective" behavior is described by the effective potential:

$$\widetilde{w}(\overline{\boldsymbol{\varepsilon}}) = \inf_{\boldsymbol{\varepsilon} \in \mathcal{K}(\overline{\boldsymbol{\varepsilon}})} \langle w(\boldsymbol{x}, \boldsymbol{\varepsilon}) \rangle_\Omega, \tag{7.13}$$

where $\mathcal{K}(\overline{\boldsymbol{\varepsilon}})$ is the set of kinematically admissible strain fields:

$$\mathcal{K}(\overline{\boldsymbol{\varepsilon}}) = \left\{ \boldsymbol{\varepsilon};\ \exists \boldsymbol{u} : \boldsymbol{\varepsilon} = (\mathrm{grad}\boldsymbol{u})_{\mathrm{sym}},\ \ u = \overline{\boldsymbol{\varepsilon}} \cdot \boldsymbol{x} + u^*,\ \ u^*\#,\ \ \mathrm{tr}(\boldsymbol{\varepsilon}) = 0 \right\}. \tag{7.14}$$

Let us focus on the case of a 'simple shear' loading where the principal axes of $\overline{\boldsymbol{\varepsilon}}$ are aligned with $\mathrm{e}_1 \pm \mathrm{e}_2$, referring to the Cartesian axis of Fig. (7.1a). Accordingly, $\overline{\varepsilon}_{12} = \overline{\varepsilon}_{21}$ is the only non-zero component of $\overline{\boldsymbol{\varepsilon}}$. The effective potential $\widetilde{w}$ is then characterized by an effective flow stress $\widetilde{y}_0$ which may be rewritten as:

$$\widetilde{w}(\overline{\boldsymbol{\varepsilon}}) = \frac{\widetilde{y}_0 \varepsilon_0}{1+n} \left(\frac{\overline{\varepsilon}_e}{\varepsilon_0} \right)^{1+n}, \tag{7.15}$$

from which the macroscopic stress $\langle \boldsymbol{\sigma} \rangle_\Omega$ may be obtained. In both (7.12) and (7.15), due to the isochoric loading direction considered and the material incompressibility, the Von Mises strains read:

$$\varepsilon_e = \frac{2}{\sqrt{3}} \sqrt{\varepsilon_{12}^2 + \left(\frac{\varepsilon_{11} - \varepsilon_{22}}{2} \right)^2}, \qquad \overline{\varepsilon}_e = \frac{2|\overline{\varepsilon}_{12}|}{\sqrt{3}}. \tag{7.16}$$

In the rest of this chapter, the variational formulation (7.13) defining the homogenized behavior of the composite is used to derive bounds for the effective flow stress $\widetilde{y}_0$. Two cases of

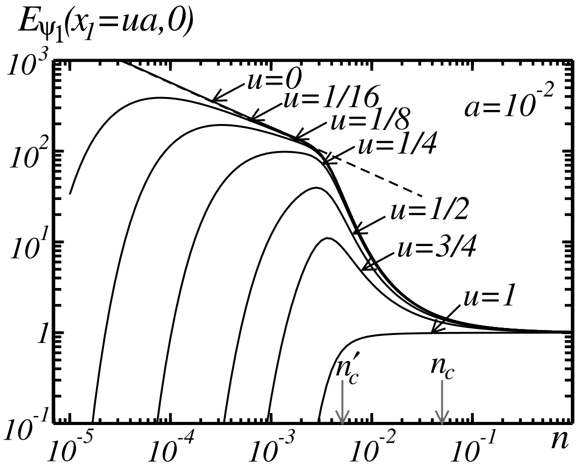

Figure 7.4: Local trial electric field $E_{\psi_1}(x_1, 0)$ at various points of coordinate $0 \leqslant x_1 \leqslant a$ as a function of the nonlinearity exponent n for fixed $a = 10^{-5}$, in log-log plot. Dotted line: scaling law $E_{\psi_1} = 1/\sqrt{n\pi a}$.

interest are considered, namely, a material containing an array of cylindrical pores and a composite reinforced by an array of rigid, cylindrical inclusions. To assess the domains of validity of the bounds, use is made of the nonlinear second-order homogenization theory, relevant to such periodic microstructures [112], and of Fourier numerical computations. The latter computations are carried out on grids of 1024^2 voxels, using the "augmented Lagrangian" method [162] with 'discrete' Green operator [258]. A regularized form of the constitutive law (7.12) is implemented in Fourier computations. Namely, the behavior is linear-elastic at small strain and the medium is compressible with bulk modulus κ:

$$\boldsymbol{\sigma}' = \begin{cases} 2\mu\boldsymbol{\varepsilon}' & \text{if } 3\mu\varepsilon_e < y_0\varepsilon_e^n, \\ (2/3)y_0\varepsilon_e^{n-1}\boldsymbol{\varepsilon}' & \text{otherwise,} \end{cases} \qquad \mathrm{tr}(\boldsymbol{\sigma}) = 3\kappa\,\mathrm{tr}(\boldsymbol{\varepsilon}), \tag{7.17}$$

so that the Von Mises equivalent stress $\sigma_e = \sqrt{(3/2)\sigma' : \sigma'}$ reads:

$$\sigma_e = \begin{cases} 3\mu\varepsilon_e & \text{if } 3\mu\varepsilon_e < y_0\varepsilon_e^n, \\ y_0\varepsilon_e^n & \text{otherwise.} \end{cases} \tag{7.18}$$

where σ' the stress deviatoric part. In the FFT computations, we set $y_0 = 1$ (a.u.), $\kappa = 1000$ (a.u.), $\mu = 1$ (a.u.) and apply a strain loading $\overline{\varepsilon}_{12} = 4$, using steps of $\Delta\overline{\varepsilon}_{12} = 0.1$. These values allow one to approach an incompressible behavior, and to recover the effective nonlinear response $\overline{\sigma}_e \approx \widetilde{y}_0\overline{\varepsilon}_e^n$ (see [112]). Note that the augmented Lagrangian method requires one to invert the equation

$$\mathbb{L}^0 : \boldsymbol{\varepsilon} + \boldsymbol{\sigma} = \tau$$

where τ is a given symmetric second-order tensor and $\boldsymbol{\sigma}$ is provided by (7.17). This inversion is carried out numerically by an iterative method, at each grid point. Newton's method fails when very small exponents are considered, therefore, we use the bisection method. More involved FFT schemes, such as the ones discussed in [213], have not been considered in this work.

In the porous case, we set $\sigma = 0$ in the cylindrical void. For the rigid inclusion, we use $\sigma = \mathbb{L} : \boldsymbol{\varepsilon}$ with isotropic stiffness tensor $\mathbb{L}$ with elastic moduli $\mu_2 = 1000$ and $\kappa_2 = \kappa$. For the porous medium, the fastest convergence rate offered by the Fourier algorithm, in term of the L_1-norm of the divergence of the stress field, is obtained with quite small values of the reference moduli, about 10^{-4}. The convergence rate is less sensitive to the reference medium for quasi-rigid inclusions. In that case, we use reference elastic moduli slightly stiffer than κ and μ.

In the rest of this chapter, we focus on the dilute-limit behavior for the effective flow stress, that is, we assume the cylindrical inclusion has a very small volume fraction $f \ll 1$. In this limit, the second-order nonlinear homogenization theory predicts the isotropic macroscopic behavior:

$$\frac{\widetilde{y}_0}{y_0} = \begin{cases} 1-(1+\sqrt{n})^2/(2\sqrt{n})f + O(f^2) & \text{(porous inclusion)}, \\ 1+\frac{1}{2}\sqrt{n}(1+\sqrt{n})^2 f + O(f^2) & \text{(rigid reinforcement)}, \end{cases} \tag{7.19}$$

as $f \to 0$. Note that scaling law (7.19_1) above has been obtained in the case of *incompressible* pores.

In the following, we focus on the 'strongly-nonlinear' case $n \ll 1$. Limit analysis bounds provide that, when $n = 0$ [68, 112]:

$$\widetilde{y}_0 = y_0\left(1-\alpha_0 f^{1/2}\right), \qquad 2/\sqrt{\pi} \leqslant \alpha_0 \leqslant 2\sqrt{2/\pi}, \tag{7.20}$$

in the porous case, to leading-order term in f. In effect, numerical results indicate [248]:

$$\widetilde{y}_0 \approx y_0\left(1-1.185 f^{1/2}\right). \tag{7.21}$$

In the rigid case, the upper-bound provides the exact result:

$$\widetilde{y}_0 = y_0, \tag{7.22}$$

in the interval $f < \pi/4$. The purpose of the next sections is twofold. First, we wish to assess the validity of the predictions (7.19). Our second goal is to clarify the regime change that (presumably) occurs between (7.19) and (7.20)-(7.22).

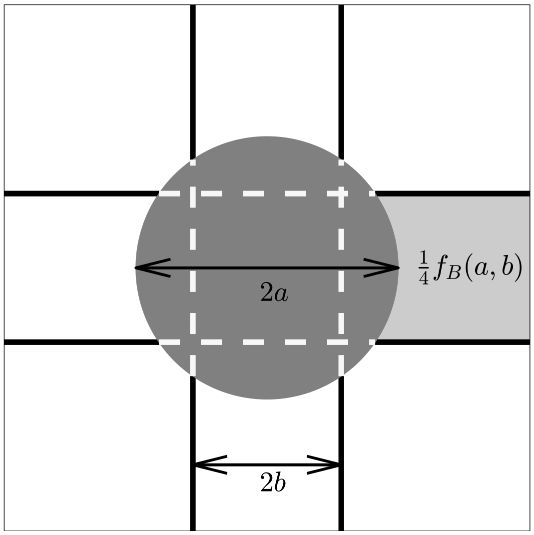

Figure 7.5: Field pattern for the limit analysis trial field in the unit cell.

7.2.2 Porous material

One can attempt to estimate the behavior of the crossover threshold f_c between the two regimes by equaling expressions (7.21) and (7.20_1) to find:

$$f_c = 4\alpha_0^2 n. \tag{7.23}$$

We will show that the actual regime change occurs at a much lower porosity. Inspired by the bounds obtained in conductivity, we approach the porous problem by means of a continuous trial field:

$$u_1(x_{1,2}) = \bar{\varepsilon}_{12} \begin{cases} r x_2, & |x_2| < b, \\ r b \operatorname{sign}(x_2) + (1-2rb)(1-2b)^{-1}\left[x_2 - \operatorname{sign}(x_2) b\right], & |x_2| < b, \end{cases} \tag{7.24}$$

and $u_2(x_1, x_2) = u_1(x_2, x_1)$, with $-1/2 \leqslant x_{1,2} \leqslant 1/2$. The parameter b monitors the unknown half-width of a band passing through the pore (see Fig. 7.5) and the parameter r the field intensity along that band. The two parameters are in the intervals $0 < b < a$ and $0 < r < 1/(2b)$. For convenience, we restrict ourselves to $b < a/\sqrt{2}$, so that the square intersection area of the bands remains within the pore. Denote $f_B(a, b)$ the area of the band that lie outside the void. Straightforward geometrical considerations lead to:

$$f_B(a, b) = 4\left(b - a^2 \sin^{-1}\frac{b}{a} - ab\sqrt{1 - b^2/a^2}\right). \tag{7.25}$$

We insert the trial field $\boldsymbol{\varepsilon}$ corresponding to the above displacement field into (7.13) which provides us with:

$$\frac{\widetilde{y}_0}{y_0} \leqslant \int_{\text{matrix}} \mathrm{d}^2\boldsymbol{x} \left(\frac{\varepsilon_{12}}{\bar{\varepsilon}_{12}}\right)^{n+1} = \frac{f_B}{2^{n+1}}\left(r + \frac{1-2rb}{1-2b}\right)^{n+1} + (1 - f - f_B)\left(\frac{1-2rb}{1-2b}\right)^{n+1}. \tag{7.26}$$

A simplified bound is obtained by taking $r = 1/(2b)$, i.e. $\varepsilon_{12} = 0$ outside the bands, in which case:

$$\frac{\widetilde{y}_0}{y_0} \leqslant \inf_{b \leqslant a/\sqrt{2}} f_B(a, b)(4b)^{-(n+1)}. \tag{7.27}$$

This choice is accurate in the regime where the strain field localizes, i.e. when n is very small. An optimal band width b^* is now sought for to minimize (7.27). The scaling law for b^* turns out to be $b^* \propto \sqrt{an}$ for $n \ll 1$. This is shown by replacing b by $k\sqrt{an}$ (k constant) in (7.27), expanding the latter as $n \to 0$ and optimizing on k. The optimal value of b^* ensues:

$$b^* = \min\left(\sqrt{(3/2)(1-2a)an}; a/\sqrt{2}\right), \tag{7.28}$$

where the restriction over b has been accounted for. The analytical upper-bound now reads:

$$\frac{\widetilde{y}_0}{y_0} \leqslant f_B(a, b^*)(4b^*)^{-(n+1)}. \tag{7.29}$$

In practice, curves drawn with this expression are indistinguishable from those obtained by a numerical minimization of (7.27). When $n \to 0$, bound (7.29) reduces to the upper-bound (7.20).

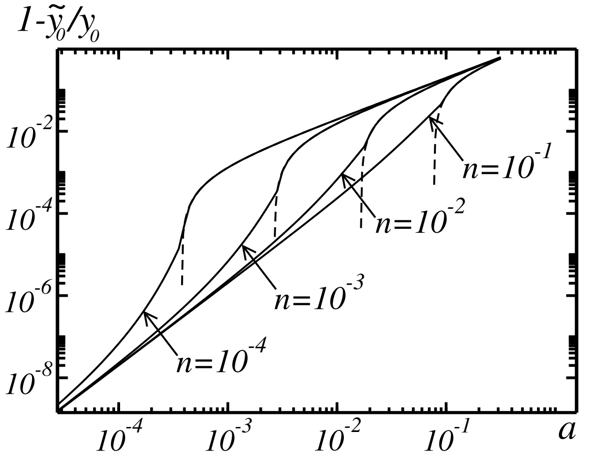

Figure 7.6: Upper-bound (7.31) for the normalized effective yield stress $\widetilde{y}_0/y_0$ vs. disk radius a in a periodic medium, in log-log plot, for various values of the nonlinear exponent n.

It should be noted that bound (7.29) becomes useless when $a \to 0$ with n fixed, as the bound will then be greater than 1. In this regime, the field pattern can not be approached by a straight, localized band that join pores. We find numerically with good precision that this occurs when $-2a/\log a \lesssim n$. Thus, to account for the dilute regime $a \ll n$, we take $b = a/\sqrt{2}$ in (7.26) and obtain the bound:

$$\frac{\widetilde{y}_0}{y_0} \leqslant \zeta(a,n) = \min_{ar\sqrt{2}<1} \left\{ \frac{f_B(a, a/\sqrt{2})}{2^{n+1}} \left(r + \frac{1 - ra\sqrt{2}}{1 - a\sqrt{2}} \right)^{n+1} + \left[1 - f - f_B\left(a, \frac{a}{\sqrt{2}}\right) \right] \left(\frac{1 - ra\sqrt{2}}{1 - a\sqrt{2}} \right)^{n+1} \right\}, \tag{7.30}$$

which is numerically estimated, by optimizing on r. Our upper-bound on the entire domain $0 < n < 1$, $0 < a < 1/2$ then reads:

$$\frac{\widetilde{y}_0}{y_0} \leqslant \min \left\{ \zeta(a,n), f_B(a, b^*)(4b^*)^{-(n+1)} \right\}. \tag{7.31}$$

The behavior of this upper-bound is similar to results obtained in conductivity (Sec. 7.1), see Fig. (7.6). The curves in Fig. (7.6) are not smooth at a single point where the minimum for the trial field switches from bound (7.30) to (7.29). The behavior in the regime $a \ll n$ is, as expected, inconsistent with (7.19_1). Although both analytical results predict a linear correction in f, the prefactor of that correction depends on n, contrary to the upper-bound (7.31). This is because, in the dilute limit, the simple trial field corresponding to our bound does not adequately describe the fields. Those fields are necessarily homogeneous except in the region surrounding the inclusion, unlike the trial field which always display a straight band. Nevertheless, bound (7.31) may capture some information regarding the regime change between the 'localized' and 'dilute' regime.

Since bound (7.30) is not meaningful, we restrict our attention to bound (7.29). This is compared to the dilute estimates (7.19) and to FFT computations in Fig. (7.7). The quantity $1 - \widetilde{y}_0/y_0$ is represented in log-log scale as a function of a, for various values of the exponent $n = 10^{-1}$, ..., 10^{-4}. Bound (7.30) ceases to be meaningful when $2a \sim -n \log a$, hence:

$$f_c \approx -(\pi/4) n^2 \log^2 n. \tag{7.32}$$

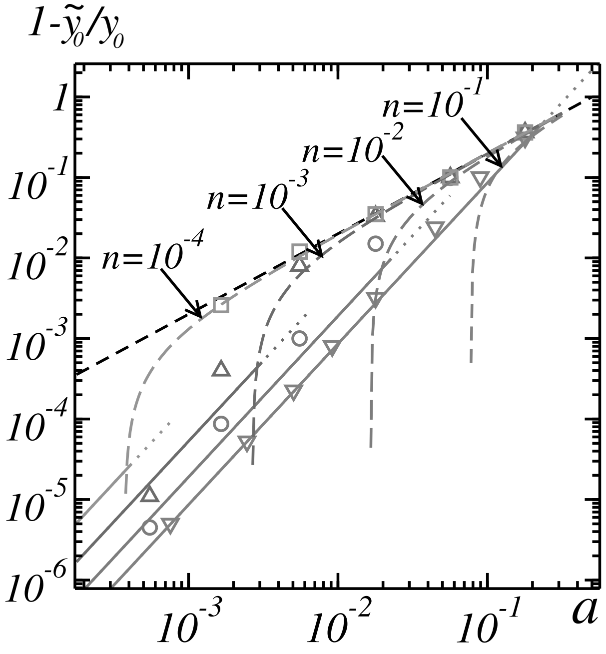

Figure 7.7: Normalized effective yield stress $\widetilde{y}_0/y_0$ vs. disk radius a in a periodic medium, in log-log plot, for various values of the nonlinear exponent n. Symbols: FFT computations. Solid and dotted lines: asymptotic dilute estimates (7.19) predicted by the nonlinear "second-order" homogenization theory [112]. Gray dashed lines: upper-bound (7.29). Black dashed line: expansion (7.21).

The scaling (7.21), corresponding to a localized strain field, is confirmed by FFT computations in the domain $n \lesssim -2a/\log a$. The dilute estimates (7.19) are also confirmed by FFT computations when $n = 10^{-1}$. For smaller values of n, FFT data is not conclusive, owing the difficulty of obtaining numerical results in highly-dilute, strongly-nonlinear cases. Nevertheless, the FFT data confirms that the scaling law $\widetilde{y}_0/y_0 \sim 1 - \alpha_0 a$ (Eq. 7.21) ceases to be valid at much smaller values than that predicted by (7.23) and in fact suggests a cross-over consistent with the much smaller threshold (7.32) provided by bound (7.29), although the numerical data can not conclusively confirm it.

7.2.3 Rigid inclusion

As in the porous case, the bound (7.22) is extended as a bound for rigidly-reinforced, powerlaw materials of rate-sensitivity exponent n, by considering a continuous regularization of the trial displacement field. Again, we limit ourselves to simple shear loading and strain fields. The situation is simpler than in the porous case, since we already know from FFT results that the relevant band width is $2a$ (see FFT maps in). A continuous trial field consistent with the rectangular patterns of [112, Tab. 2] on the unit cell $-1/2 \leqslant x, y \leqslant 1/2$ is:

$$u_1(x_{1,2}) = \frac{\overline{\varepsilon}_{12}}{2} \begin{cases} 0, & |x_2| < a, \\ \operatorname{sign}(x_2)(|x_2| - a)(1-2a)^{-1}, & |x_2| > a, \end{cases} \tag{7.33}$$

and $u_2(x_1, x_2) = u_1(x_2, x_1)$. Accordingly, ε_{12} is constant within each of a set of 9 rectangles, and vanishes in the square circumscribed to the rigid inclusion disk. The following upper bound is

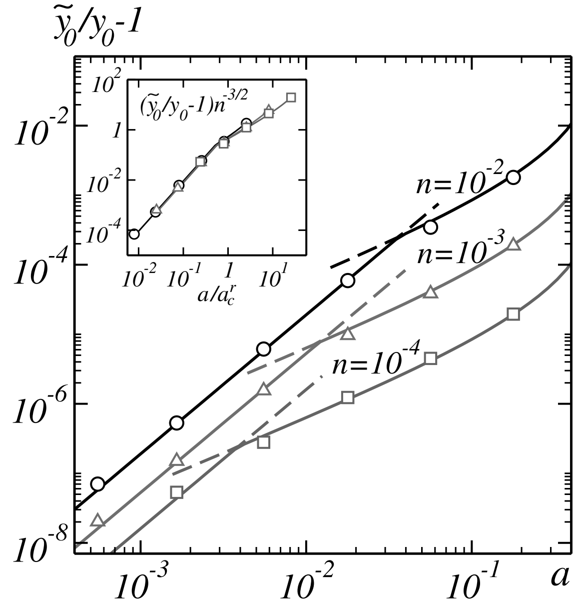

Figure 7.8: Normalized effective yield stress $\widetilde{y}_0/y_0 - 1$ vs. disk radius a in a periodic medium, in log-log plot, for various values of the nonlinear exponent n. Comparisons between limit analysis bounds (7.34) (solid lines), second-order dilute predictions (7.19_2) (solid lines) and FFT estimates (symbols).

readily obtained:

$$\frac{\widetilde{y}_0}{y_0} \leqslant (1-2a)^{-n}\left[1-2a(1-2^{-n})\right]. \tag{7.34}$$

Being valid for any $a \leqslant 1/2$ and always greater than one for $0 \leqslant n \leqslant 1$, it does not suffer the limitations encountered in the porous case. It moreover reduces to (7.22) when $n = 0$, and constitutes a good estimate as long as n is small enough for the rectangular field pattern to hold. In the dilute limit, Eq. (7.34) reads:

$$\frac{\widetilde{y}_0}{y_0} = 1 + 2\left(n + 2^{-n} - 1\right)a + O(a^2), \tag{7.35}$$

so that comparing to Eq. (7.19) the latter provides a crossover at $a_c^r(n) = (4/\pi)(1-\log 2)\sqrt{n}$. Both regimes can be encoded in the form:

$$\frac{\widetilde{y}_0}{y_0} = 1 + n^{3/2} G\left(a/a_c^r(n)\right), \tag{7.36}$$

where the scaling function is such that $G(t) \sim t^2$ (resp. $G(t) \sim t$) when $t \ll 1$ (resp. $t \gg 1$). To check these results, composite curves built from the infimum of expressions (7.19) and (7.34) are compared to FFT data in Fig. (7.8), where the inset shows the scaling function G. The agreement is excellent, and confirms that Eq. (7.34) and (7.19_2) hold when $a > a_c^r$ and $a < a_c^r$, respectively. In terms of the volume fraction, the regime change occurs when:

$$f = f_c^r(n) = \frac{16}{\pi}(1-\log 2)^2 n \approx 2.49n. \tag{7.37}$$

It would be useful to study this problem in the context of a random distribution of particles, such as the one investigated in Sec. (6.4.3).

7.3 Conclusion

This chapter presented an investigation of the effective response of powerlaw materials with decreasing nonlinearity (or strain-rate sensitivity) exponent n and dilute porosity f, or in the case of rigid reinforcements, small concentration of particles. Our attention has been restricted to periodic structures. Numerical FFT results, limit analysis bounds and the predictions of nonlinear homogenization theories have been used to investigate the material response. One of the main finding of this work is the observation of a crossover-type behavior for the porous case in the dilute concentration and small rate-sensitivity regime. As f goes to 0, the effective flow stress tends to the flow stress in the matrix with a correction proportional to f, consistently with a set of non-interacting inhomogeneities (Eq. 7.19_1). However, the prefactor blows up as $n^{-1/2}$ as $n \to 0$, suggesting that the range of validity of this expansion tends to zero in the the ideally plastic limit. In contrast to this result, a regime consistent with a collective-type behavior induced by strongly-interacting voids is obtained when taking the limit $n \to 0$, in which case the effective flow stress scales as $f^{1/2}$ as leading-order correction in f. The limit analysis study presented in this chapter suggests a cross-over in between the two regimes, at $f \sim n$. The bound obtained by limit analysis and FFT results also suggest a much more abrupt transition between the weakly and strongly-interacting regimes than in the corresponding linear problem with strongly anisotropic matrix [259], also discussed in Sec. (2.6).

For the rigidly-reinforced materials, the two asymptotic regimes were found to be consistent up to the first correction and a weaker crossover-type behavior was found, which could be completely elucidated. In this case, the strongly dilute regime is found to be linear in f (cf. 7.19_2) with a prefactor that tends to zero as $m \to 0$, while the strongly nonlinear regime has a vanishing correction for sufficiently small values of f (cf. 7.22). This result has implications also for random material, such as the “RSA” model of squares (Sec. 6.4.3).

Part III

Stokes flow in porous media

Chapter 8

Covariance of a Boolean set of anisotropic grains

This chapter focuses on the variance properties of isotropic Boolean random sets containing randomly-oriented cylinders with circular cross-section. Emphasis is put on cylinders with large aspect ratios, of the oblate and prolate types. A link is established between the powerlaw decay of the covariance function and the variance of the estimates of the volume fraction of cylinders. The covariance and integral range of the Boolean mixtures are expressed in terms of the orientation-averaged covariogram of cylinders, for which exact analytical formulas and approximate expressions are provided.

8.1 Introduction

The covariogram, originally introduced by G. Matheron [152], gives the volume of the intersection of a (convex) body with a translation of itself. The function is closely related to the distribution of the length of the chords of a body, and also a key ingredient in the theory of Boolean stochastic models based on Poisson point processes (see [153, 155, 156, 216, 226] and references therein). A key-theorem relates the covariance function of stationary Boolean sets in the Euclidean space to the Poisson intensity of the point process and to the covariogram of the primary grain. In turn, the covariance function itself governs basic features of the model, such as the specific surface area and the integral range. The integral range is linked to the estimates on finite-size volumes of the random set volume fraction.

Another property of interest concerns the probability that a segment is entirely contained in the complementary set of a Boolean model. This probability takes a simple form for convex primary grains, which depends on the derivative of the covariogram at 0 [216]. Linear erosion allows one to compute this probability numerically which is especially useful for model identification [187, 118].

An important subclass of Boolean models, commonly used in material science for modelling heterogeneous materials, concern isotropic random sets. In dimension 3, this model requires one to average the covariogram over all directions uniformly on the sphere. In the rest of this chapter, the orientation-averaged covariogram, also denoted “isotropized covariogram” in the literature, will be referred to as “mean covariogram”. The mean covariogram is a special case of so-called “kinematic” integrals (see [215], Chap. 5) of the form (in dimension d):

$$\int_{G^d} V_d\,(M \cap gA)\,\mu(\mathrm{d}g) \tag{8.1}$$

where a convex body A is moved into gA and the volume of the intersection of gA with a convex set M is averaged with respect to the measure μ over all transformations g in the motion group G^d. The measure μ is invariant in G^d. The mean covariogram required for describing isotropic Boolean models is obtained by taking translations at fixed distance uniformly distributed on the sphere for G^d and μ and $M = A$. Unfortunately, such kinematic covariogram is usually not known explicitly, especially in 3D. Some notable exceptions include the sphere, parallelepiped, cylinder [89, 91] and Poisson polyhedra [154]. The mean covariogram for cylinders is useful for identifying stochastic fibrous models from experimental 2D (e.g. SEM) or 3D (e.g. tomography) images of fibrous materials [202, 187, 198]. More generally, heterogeneous microstructures studied for various industrial applications can be approached by random models of cylinders. Examples include flakes in optics [54] or platelets in mesoporous materials [240].

This work focuses on the mean covariogram of 3D cylinders with circular cross-section and its applications to Boolean models. It is organized as follows: the covariogram of a cylinder is recalled in Sec. (8.2). The mean covariogram is derived in Sec. (8.3). Boolean models of cylinders are considered in Sec. (8.4). The integral range is given in Sec. (8.4.1). Variance properties are discussed in Secs. (8.4.2) and (8.4.3). We conclude in Sec. (8.5).

8.2 Covariogram of a cylinder

Consider a cylinder $\boldsymbol{C}$ of height h and circular cross-section of radius r, and a Cartesian coordinate system with origin O and axes $\mathbf{e}_x$, $\mathbf{e}_y$ and $\mathbf{e}_z$. We assume that O is at the center of one of the bases of $\boldsymbol{C}$ and that $\mathbf{e}_z$ is parallel to the cylinder main axis. Consider now the translation $\boldsymbol{C}'$ of the cylinder $\boldsymbol{C}$ by a vector $\boldsymbol{v}$. We parametrize $\boldsymbol{v}$ by its norm $t = |\boldsymbol{v}|$ and two angles $\phi \in [0; 2\pi]$ and $\theta \in [-\pi/2; \pi/2]$ in spherical coordinates. The azimuthal angle ϕ is the angle between $\mathbf{e}_x$ and the projection of $\boldsymbol{v}$ onto the plane $(0; \mathbf{e}_x, \mathbf{e}_y)$. The variable θ denotes the angle between $\boldsymbol{v}$ and the plane $(0; \mathbf{e}_x, \mathbf{e}_y)$ so that $\theta = \pi/2$ when $\boldsymbol{v}$ is parallel to $\mathbf{e}_z$ and $\theta = 0$ when $\boldsymbol{v}$ is contained in the plane $(0; \mathbf{e}_x, \mathbf{e}_y)$. Note that, using this convention, θ is the complementary of the polar angle.

The (oriented) covariogram of a cylinder $K(\theta, t)$ is defined as the volume of the intersection of $\boldsymbol{C}$ with $\boldsymbol{C}'$:

$$K(\theta, t) = L_3\left(\boldsymbol{C} \cap \boldsymbol{C}'\right), \tag{8.2}$$

where L_3 denotes the Lebesgue measures in $\mathbb{R}^3$. The covariogram K depends on r, h, t and θ, but not on ϕ. For conciseness, the dependence on r and h is omited in the notation for K and in the notations for other variables hereafter. Let us introduce the ratios:

$$x = \frac{t}{2r}, \qquad y = \frac{h}{t}. \tag{8.3}$$

The two variables x and y, not to be confounded with Cartesian coordinates, will be used preferentially to t, h and r. Furthermore, the variable t as argument of a function will be replaced indifferently by x or y. For instance $K(\theta, t)$ is also denoted $K(\theta, x)$.

The expression for the covariogram K is derived from the formula of a covariogram of a disk in the plane and reads [99]:

$$\begin{aligned} K(\theta,t) &= \widetilde{K}(\theta,x)H(\theta,t), && (8.4a)\\ \widetilde{K}(\theta,x) &= 4r^3\left(\frac{h}{2r} - x\sin\theta\right)\left[\cos^{-1}(x\cos\theta) - x\cos\theta\sqrt{1-x^2\cos^2\theta}\right], && (8.4b) \end{aligned}$$

where $H(\theta,t) = 1$ when θ and t are such that the two cylinders $\boldsymbol{C}$ and $\boldsymbol{C}'$ intersect, and 0 otherwise. More precisely:

$$H(\theta,t) = \begin{cases} 1 & \text{if } t \leqslant t_{\max}, \\ 0 & \text{otherwise}, \end{cases} \qquad t_{\max} = \begin{cases} \frac{2r}{\cos\theta} & \text{if } \theta \in [0; \tan^{-1}\frac{h}{2r}], \\ \frac{h}{\sin\theta} & \text{if } \theta \in [\tan^{-1}\frac{h}{2r}; \frac{\pi}{2}]. \end{cases} \tag{8.5}$$

The term $\cos^{-1}$ in Eq. (8.4) refers to the inverse cosine function, also denoted arccos and $\tan^{-1}$ in (8.5) denotes the inverse tangent function. Likewise, $\sin^{-1}$ hereafter is used to denote the inverse sine function.

The following section is concerned by the normalized mean covariogram:

$$k(t) = \frac{1}{4\pi}\int_0^{2\pi} \mathrm{d}\phi \int_{-\pi/2}^{\pi/2} \mathrm{d}\theta \frac{K(\theta,t)}{h\pi r^2}\cos\theta = \int_0^{\pi/2} \mathrm{d}\theta \frac{K(\theta,t)}{h\pi r^2}\cos\theta, \tag{8.6}$$

where the mean is taken over all directions on the sphere, assuming the distribution of orientations is uniform on the latter. Here, the covariogram K is normalized by the cylinder volume and surface area of the unit sphere so that the function $k(t) = 1$ when $t = 0$ and $k(t) = 0$ when $t = \infty$. Like K, the quantity k depends on $r \geqslant 0$ and $h \geqslant 0$.

8.3 Mean covariogram of a cylinder

In this section, the isotropized covariogram of a cylinder with circular cross-section is given. We refer to [89, 90, 91, 228] where this problem has been studied in details.

8.3.1 Prolate cylinders

In this section, we compute the limit $k_\infty(t)$ of $k(t)$ when $h \to \infty$ with r and t fixed. The condition $t \leqslant t_{\max}$ (Eq. 8.5) reduces to $x\cos\theta \leqslant 1$ which is satisfied for all θ when $x < 1$ and for $\theta > \cos^{-1}(1/x)$ when $x > 1$. Therefore the term K can be replaced by $\widetilde{K}$ in (8.6) provided the integration is carried out in the intervals $[0; \pi/2]$ ($x < 1$) and $[\cos^{-1}(1/x); \pi/2]$ ($x > 1$):

$$k_\infty(x) = \begin{cases} \lim_{h\to\infty} \frac{1}{h\pi r^2}\int_0^{\pi/2} \mathrm{d}\theta \widetilde{K}(\theta,x)\cos\theta, & \text{if } x < 1, \\ \lim_{h\to\infty} \frac{1}{h\pi r^2}\int_{\cos^{-1}(1/x)}^{\pi/2} \mathrm{d}\theta \widetilde{K}(\theta,x)\cos\theta, & \text{if } x > 1. \end{cases} \tag{8.7}$$

Observe however that, when $x > 1$, $\widetilde{K}(\theta,t)$ is purely imaginary in the domain $0 < \theta < \cos^{-1}(1/x)$. Accordingly, it is sufficient to integrate in the interval $[0; \pi/2]$ instead of $[\cos^{-1}(1/x); \pi/2]$, provided the imaginary part of the integral is discarded:

$$k_\infty(x) = \lim_{h\to\infty} \frac{1}{h\pi r^2} \operatorname{Re}\left\{\int_0^{\pi/2} \mathrm{d}\theta\, \widetilde{K}(\theta,x)\cos\theta\right\}, \tag{8.8}$$

where Re stands for the real part of complex numbers. Replacing K with its expression (8.4) and expanding the integrand at first order in $1/h$ yields:

$$k_\infty(x) = \frac{2}{\pi}\,\mathrm{Re}\left\{\int_0^{\pi/2} \mathrm{d}\theta \cos\theta \left[\cos^{-1}(x\cos\theta) - x\cos\theta\sqrt{1-x^2\cos^2\theta}\right]\right\}. \tag{8.9}$$

As seen above, k_∞ depends on t and r through $x = t/(2r)$ only. The integral in (8.9) is readily computed in the complex domain using a symbolic calculator [262]. The expression depends on the complete elliptic integrals of the first and second kind, denoted F and E respectively and defined by:

$$F(z) = \int_0^{\pi/2} \frac{\mathrm{d}u}{\sqrt{1 - z\sin^2 u}}, \qquad E(z) = \int_0^{\pi/2} \mathrm{d}u\,\sqrt{1 - z\sin^2 u}. \tag{8.10}$$

The above functions F and E are real-valued when $z \leqslant 1$ and complex with non-zero real and imaginary parts when $z > 1$. We refer to the online resources [242] (and references therein) for an overview of their properties. Note that the elliptic functions are usually defined by $z \to F(\sqrt{z})$, $E(\sqrt{z})$. In this work we follow the notation used in [262].

The elliptic functions F and E appear in the integration of both the square root and inverse cosine terms in (8.9). For instance, when $x < 1$, the $\cos^{-1}$ term is integrated by parts as follows:

$$\begin{aligned} \int_0^{\pi/2} \mathrm{d}\theta\, \cos^{-1}(x\cos\theta)\cos\theta &= \int_0^{\pi/2} \frac{x\sin^2\theta\,\mathrm{d}\theta}{\sqrt{1-x^2\cos^2\theta}} = \left(x - \frac{1}{x}\right)F(x^2) + \frac{E(x^2)}{x} \\ &= \frac{\sqrt{1-x^2}}{x}\,\mathrm{Im}\left\{E\left(\frac{1}{1-x^2}\right)\right\}, \end{aligned} \tag{8.11}$$

where Im denotes the imaginary part of complex numbers. The final formula for $k(x)$ reads, after simplification in the regions $x < 1$ and $x > 1$:

$$k_\infty(x) = \begin{cases} 1 - \frac{2\sqrt{1-x^2}}{\pi x}\left\{\mathrm{Im}\left[E\left(\frac{1}{1-x^2}\right)\right] + \frac{2x^2-1}{3}E\left(\frac{x^2}{x^2-1}\right) + \frac{1}{3}F\left(\frac{x^2}{x^2-1}\right)\right\}, & \text{if } x < 1, \\ 1 - \frac{2\sqrt{x^2-1}}{\pi x}\left\{E\left(\frac{1}{1-x^2}\right) + \mathrm{Im}\left[\frac{2x^2-1}{3}E\left(\frac{x^2}{x^2-1}\right) + \frac{1}{3}F\left(\frac{x^2}{x^2-1}\right)\right]\right\}, & \text{if } x > 1. \end{cases} \tag{8.12}$$

The function k_∞ is represented in Fig. 8.1a (top curve).

8.3.2 Cylinders of arbitrary aspect ratio

This section is devoted to the general case, i.e. finite h and r. The intervals of integration for θ are required for computing (8.6). Take first $h < 2r$ and examine the condition $t \leqslant t_{\max}$ in (8.5). The quantity K in (8.4) is non-zero in the following intervals for θ (recall that $y = h/t$):

$$\theta \in \begin{cases} [0; \pi/2] & \text{if } t < h, \\ [0, \sin^{-1}(y)] & \text{if } h < t < 2r, \\ [\cos^{-1}(1/x), \sin^{-1}(y)] & \text{if } 2r < t. \end{cases} \tag{8.13}$$

Whereas, when $h > 2r$, K is non-zero if:

$$\theta \in \begin{cases} [0; \pi/2] & \text{if } t < 2r, \\ [\cos^{-1}(1/x), \pi/2] & \text{if } 2r < t < h, \\ [\cos^{-1}(1/x), \sin^{-1}(y)] & \text{if } h < t. \end{cases} \tag{8.14}$$

As in Sec. (8.3.1), $\widetilde{K}$ is purely-imaginary when $\theta \in [0; \cos^{-1}(1/x)]$, so one may carry out the integration in (8.6) along intervals $[0; a]$ with $a = \pi/2$ or $a = \sin^{-1}(y)$ depending on conditions precised in (8.13) and (8.14). We are left with the evaluation of the following integral:

$$k(x,y) = \mathrm{Re}\left\{\int_0^a \mathrm{d}\theta \frac{\widetilde{K}(\theta,x)\cos\theta}{h\pi r^2}\right\}. \tag{8.15}$$

Now according to (8.13) and (8.14), $a = \pi/2$ when $y > 1$ ($t < h$) and $a = \sin^{-1} y$ when $y < 1$ ($t > h$). We first examine the case $a = \pi/2$, i.e. $y > 1$. Equation (8.15) takes the form:

$$\begin{aligned} k(x,y) &= k_{y>1}(x,y) = k_\infty(x) \qquad\qquad (8.16)\\ &-\frac{2}{\pi y}\mathrm{Re}\left\{\int_0^{\pi/2} \mathrm{d}\theta \cos(\theta)\sin(\theta)\left[\cos^{-1}(x\cos\theta) - x\cos\theta\sqrt{1-x^2\cos^2\theta}\right]\right\}, \end{aligned}$$

where we have identified $k_\infty(x)$, the covariogram for $h = \infty$ given in (8.12). The integral in (8.16) is computed using a software for symbolic computations, and, after rearranging the terms:

$$k_{y>1}(x,y) = k_\infty(x) - \frac{1}{8x^2 y} + \frac{H'(x)}{2y\pi}\left[\left(\frac{1}{2x} + x\right)\sqrt{1-x^2} + \left(\frac{1}{2x^2} - 2\right)\cos^{-1} x\right], \tag{8.17}$$

where H' is the step function:

$$H'(x) = \mathbb{1}_{[1;+\infty]} = \begin{cases} 1 & \text{if } x < 1, \\ 0 & \text{if } x > 1. \end{cases} \tag{8.18}$$

As expected, the quantity between square brackets in (8.17) is real when $x < 1$ and so is $k(x,y)$ for all x.

We now consider the case $y < 1$ ($t > h$) and the integral in (8.15) with $a = \sin^{-1} y$. The symbolic calculator [262] provides a lengthy formula for the solution. After simplification, the expression takes different forms for $x < 1$ and $x > 1$. For $x > 1$ and $y < 1$, the covariogram k reads:

$$\begin{aligned} k_{\substack{y<1\\x>1}}(x,y) &= \frac{4\sqrt{x^2-1}}{3\pi x}\mathrm{Im}\left[F\left(\sin^{-1} y\middle|\frac{x^2}{x^2-1}\right) - (1+x^2)E\left(\sin^{-1} y\middle|\frac{x^2}{x^2-1}\right)\right]\\ &+\left(\frac{y}{\pi} + \frac{4x^2-1}{4\pi y x^2}\right)\cos^{-1}\left(x\sqrt{1-y^2}\right)\\ &-\frac{1}{2\pi}\left(\frac{xy}{3} + \frac{1}{2xy} + \frac{x}{y}\right)\sqrt{1-y^2}\sqrt{1-x^2(1-y^2)}. \end{aligned} \tag{8.19}$$

The functions of two variables $F(\phi|z)$ and $E(\phi|z)$ are the *incomplete* elliptic integrals of the first and second kind, respectively, defined by [243]:

$$E\left(\phi\middle|z\right) = \int_0^\phi \mathrm{d}u\,\sqrt{1-z\sin^2 u}, \qquad F\left(\phi\middle|z\right) = \int_0^\phi \frac{\mathrm{d}u}{\sqrt{1-z\sin^2 u}}. \tag{8.20}$$

The complete elliptic integrals in (8.10) are special cases:

$$E(z) = E\left(\frac{\pi}{2}\middle|z\right), \qquad F(z) = F\left(\frac{\pi}{2}\middle|z\right). \tag{8.21}$$

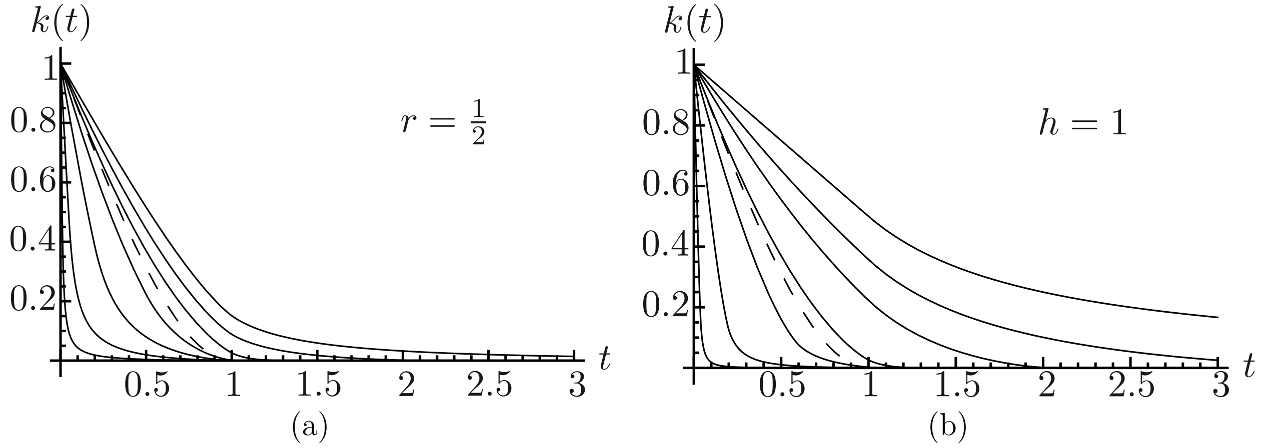

Figure 8.1: Normalized mean covariogram $k(t)$ as a function of t: **(a)** with $r = 1/2$ fixed and increasing height $h = 0.01$, 0.05, 0.2, 0.5, 1, 2, $+\infty$ (bottom to top, solide lines); **(b)** with $h = 1$ fixed and increasing radius $r = 0.02$, 0.1, 0.3, 0.5, 1, 2, $+\infty$ (bottom to top, solide lines). Dashed lines: covariogram of a sphere of diameter 1.

The incomplete elliptic integrals are real-valued if $z \sin^2 \phi < 1$. Note that this is never the case for the arguments of E and F in (8.19), so that the two functions have complex values. Note also that, owing to $t \leqslant \sqrt{h^2 + 4r^2}$:

$$x\sqrt{1-y^2} < 1, \qquad 1 - x^2(1-y^2) < 1, \tag{8.22}$$

and so $k_{\substack{y<1\\x>1}}(x, y)$ in (8.19) is real. Now, when x, $y < 1$, one finds for $k(x, y)$:

$$\begin{aligned}
k_{\substack{y<1\\x<1}}(x,y) \;\; = \;\; & \frac{4\sqrt{1-x^2}}{3\pi x}\left[F\left(\sin^{-1} y \middle| \frac{x^2}{x^2-1}\right) - (1+x^2)E\left(\sin^{-1} y \middle| \frac{x^2}{x^2-1}\right)\right] \\
& + \left(\frac{y}{\pi} + \frac{5x^2-2}{4\pi y x^2}\right)\cos^{-1}\left(x\sqrt{1-y^2}\right) + \frac{2-5x^2}{4\pi y x^2}\cos^{-1} x \\
& - \frac{1}{2\pi}\left(\frac{xy}{3} + \frac{1}{2xy} + \frac{x}{y}\right)\sqrt{1-y^2}\sqrt{1-x^2(1-y^2)} + \frac{1+2x^2}{4\pi y x}\sqrt{1-x^2} \\
& + \frac{1-x^2}{4\pi y x^2}\cos^{-1}\left(x^2\sqrt{1-y^2} + \sqrt{1-x^2}\sqrt{1-x^2(1-y^2)}\right).
\end{aligned} \tag{8.23}$$

Note the similarities with the formula for $x > 1$ in (8.19). Also, all three expressions inside $\cos^{-1}$ in the above are comprised between 0 and 1 and so $k(x, y)$ is real.

To summarize, the exact expression for $k(x, y)$ is given by (8.17) and (8.12) when $y > 1$, by (8.19) when $y < 1 < x$, and by (8.23) when $x < 1$ and $y < 1$. The covariogram is plotted as a function of t in Fig. (8.1a) and (8.1b) for various values of r and h (solid lines), and compared with that of a sphere (dotted lines).

An asymptotic expansion of $k(t)$ when $t \to 0$ is now carried out. Use the expansion ($m \to 0$):

$$F\left(\phi \middle| m\right) = \phi + \frac{\sin(2\psi) - 2\psi}{8} m + O(m^2), \qquad E\left(\phi \middle| m\right) = \phi + \frac{\sin(2\psi) - 2\psi}{8} m + O(m^2), \tag{8.24}$$

to find:

$$k_\infty(t) = 1 - \frac{t}{2r} + O(t^3), \qquad k(t) = 1 - \frac{1}{2}\left(\frac{1}{r} + \frac{1}{h}\right) t + \frac{2}{3\pi h r} t^2 + O(t^3), \quad t \to 0. \tag{8.25}$$

As expected the derivative of $k(t)$ at $t = 0$ is equal (up to the sign) to the surface/volume ratio of the cylinder.

The second-order derivative of $k(t)$ becomes infinite at the point $t = h$ [89]. Connections between the second-order derivative of the covariogram of a compact set and and its singular points have been previously noticed in the plane [74].

8.3.3 Oblate cylinders

Consider now the limit $r \to \infty$ with h fixed so that $x \to 0$ and y remains finite. We take the limit in the formula (8.23) when $y < 1$ and (8.17) when $y > 1$. The covariogram k depends of y only and reads:

$$k_0(y) = \begin{cases} 1 - \frac{1}{2y}, & \text{if } y > 1, \\ \frac{y}{2}, & \text{if } y < 1. \end{cases} \tag{8.26}$$

Note that, in the limit $r \to \infty$ the cylinders amount to infinite layers enclosed between two planes. The same asymptotic limit would accordingly be recovered when considering cylinders with other non-circular cross-section. This is in contrast to the prolate case (Sec. 8.3.1), where the covariogram depends on the shape of the cylinders cross-section.

8.3.4 Approximate formulas

We now give approximate expressions of the exact solutions which do not involve Elliptic functions. Such simpler expressions are useful for material applications, in particular for identifying random models, when a high accuracy is not required.

We first consider the domain $r \gg h$. The exact solution is given by (8.26) when $r = \infty$ and by (8.17) and (8.23) when $r < \infty$. We first let $r \to \infty$ and $t \to \infty$ with h and the ratio t/r fixed, and expand (8.23) to order $O(r^{-3})$. In the region $t < h$, i.e. $y > 1$, we let $t \to 0$ and compute an expansion to $O(t^3)$ with r, h fixed. In the region $t > 2r$, we set $k \approx 0$. One obtains:

$$k(t) \approx k_{r \gg h}(t) = \begin{cases} 1 - \frac{1}{2}\left(\frac{1}{h} + \frac{1}{r}\right) t + \frac{2t^2}{3\pi r h} + \frac{t^3}{64 r^3}, & \text{if } t < h, \\ \frac{h}{\pi t} \cos^{-1}\left(\frac{t}{2r}\right) + \left(\frac{h^2}{6t^2} - 1\right) \frac{h}{2\pi r} \sqrt{1 - \frac{t^2}{4r^2}}, & \text{if } h < t < 2r, \\ 0 & \text{if } t > 2r. \end{cases} \tag{8.27}$$

The expansion above is continuous except at points $t = h$, and is exact in the limit $r = \infty$ only. It turns out, however, that formula (8.27) is a very good approximation of the exact covariogram for $r > h$. The maximal error $\sup_t |k(t) - k_{r \gg h}(t)|$ between (8.27) and the exact result is attained when $t \lessapprox h$ whenever $r > h$. As expected, this error decreases and tends to 0 when $r/h \to \infty$. It is about 0.5% for $r = h$ and 0.1% for $r = 4h$ (Fig. 8.2). The error is much smaller at points $t \not\approx h$: for instance, the mean error $\langle |k(t) - k_{r \gg h}(t)| \rangle_t$ is 0.1% and 0.004% when $r = h$ and $r = 4h$

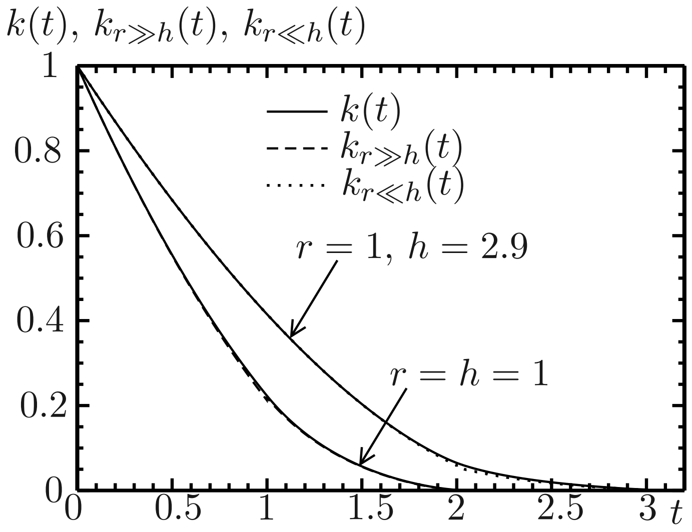

Figure 8.2: Mean normalized covariogram k of a cylinder: comparison between the exact result (solid line) and approximations (8.27) and (8.28) (dotted lines) when $r = h = 1$ and $r = 1$, $h = 2.9$, respectively.

respectively. Approximation (8.27) is good in the region $h/2 < r < h$. The errors are about $\sup_t |k - k_{r\gg h}| = 2.6\%$ and $\langle |k - k_{r\gg h}| \rangle_t = 0.6\%$ when $r = h/2$.

We now consider the domain $h \gg r$ and compute an approximation of $k(t)$ valid in the region $h \gg r$. This task is more difficult than in the oblate case $h \ll r$ because the exact result for $h = \infty$ involves elliptic functions. In the domain $2r < t < h$, we let h and $t \to \infty$ with r and the ratio h/t fixed and expand (8.17) to $O(h^{-4})$. We use the same expression in the domain $t > h$, as long as the latter is positive and 0 otherwise. In the domain $t < 2r$, we expand (8.19) when h, $t \to \infty$ with r and the ratio h/t fixed, to $O(h^{-4})$. One finds:

$$k(t) \approx k_{r\ll h}(t) = \begin{cases} 1 - \dfrac{t}{2r}\left[1 - \dfrac{1}{2}\left(\dfrac{t}{4r}\right)^2 - \dfrac{1}{4}\left(\dfrac{t}{4r}\right)^4\right] - \dfrac{t}{2h} + \dfrac{2t^2}{3\pi h r}\left(1 - \dfrac{t^2}{40r^2}\right), & t < 2r, \\ \max\left\{0; \dfrac{r^2}{2t^2}\left(1 - \dfrac{t}{h} + \dfrac{r^2}{2t^2}\right)\right\}, & t > 2r. \end{cases} \tag{8.28}$$

We emphasize that, contrary to (8.27), the expressions above are not asymptotically correct in the limit $h \to \infty$. Also, approximation $k_{r\ll h}(t)$ is discontinuous at $t = 2r$. The maximal error $\sup_t |k(t) - k_{r\ll h}(t)|$ is attained at $t \gtrsim 2r$, is constant and equal to about 1.1% for $h > 2r$. In the domain $1.6r < h < 2r$, the maximal error is less than 1.4% (Fig. 8.2).

To summarize, a good approximation of the covariogram is given by (8.27) when $h < 1.6r$ and by (8.28) when $h > 1.6r$ with a maximal absolute error of 1.8%.

8.4 Boolean model of cylinders

In this section, we consider a Boolean model [156] of cylinders with radius r and height h. The Boolean model is defined by an homogeneous Poisson point process of intensity ψ (average number of points per unit area). A cylinder $\boldsymbol{C}$ oriented in a random direction, uniformly distributed on the sphere, is implanted on each Poisson point. The cylinder volume fraction, denoted p, is linked to the Poisson intensity through [155]:

$$\log(p) = -\psi\pi h r^2. \tag{8.29}$$

Hereafter, we examine the integral range of Boolean random sets made of cylinders. The Boolean model, denoted $\mathbf{B}$ is the union of all cylinders $\boldsymbol{C}$, implanted at Poisson points so that cylinders may interpenetrate. Its characteristic function is denoted $\chi_{\mathbf{B}}$.

8.4.1 Integral range

The covariance $C(t)$ of the Boolean model of cylinders $\mathbf{B}$ reads:

$$C(t) = \{z \in \mathbf{B}, z + \mathbf{t} \in \mathbf{B}, |\mathbf{t}| = t\} = 2p - 1 + (1-p)^{2-k(t)}. \tag{8.30}$$

Its integral range is defined by [156]:

$$A_3 = \frac{1}{p(1-p)} \int_0^\infty \mathrm{d}t \, 4\pi t^2 \left[C(t) - p^2\right] = \frac{4\pi(1-p)}{p} \int_0^\infty \mathrm{d}t \, t^2 \left[\mathbf{e}^{-k(t)\log(1-p)} - 1\right], \tag{8.31}$$

where the integrand $C(t) - p^2$ is the centered covariance. For cylinders the centered covariance is identically zero for $t \geqslant t_c$ where $t_c = \sqrt{4r^2 + h^2}$ is the maximum length of a chord in the cylinder. The integral range is useful to quantify the representative volume element for the set $\mathbf{B}$. Using the exact expression derived in Sec. (8.3.2), we compute the normalized covariogram:

$$\widetilde{A}_3 = \frac{A_3}{\pi h r^2}, \tag{8.32}$$

for $r = 1/2$ (Fig. 8.3). The latter is equal to 1 when $p = 0$. Remark that the integral range is very close, but not equal, to that of a Boolean model of sphere of diameter 1:

$$\widetilde{A}_3^{\text{sphere}} = \frac{6}{\pi p} \int_0^1 \mathrm{d}t \, \left[(1-p)^{3t/2 - t^3/2} - 1 + p\right]. \tag{8.33}$$

When $p = 1/2$, the maximum value of A_3 is found to occur for h very slightly smaller than 1 (Fig. 8.4). This value is still smaller than $\widetilde{A}_3^{\text{sphere}}$. Furthermore, numerical computations show that the normalized integral range A_3 is almost unchanged when h is changed to $1/h$ (Fig. 8.3).

8.4.2 Variances and representative volume element: prolate and oblate cylinders

Assume p_W is the measure of the volume fraction of cylinders over a domain W of volume V:

$$p_W = \frac{L_3(\mathbf{B} \cap V)}{V} = \int_W \mathrm{d}u \, \chi_{\mathbf{B}}(u). \tag{8.34}$$

Denote $\overline{p}_W$ the mean of the estimates p_{W_i} taken over N independent realizations $W = W_1$, ..., W_N of volume V. The variance $D^2_{\mathbf{B}}(V)$ of the estimates p_{W_i} is given by:

$$D^2_{\mathbf{B}}(V) = \frac{1}{N} \sum_{i=1}^N \left[\frac{1}{V} \int_{W_i} \mathrm{d}u \, \chi_{\mathbf{B}}(u) - \overline{p}_W\right]^2 = \frac{1}{N} \sum_{i=1}^N \left[\left(\frac{1}{V} \int_{W_i} \mathrm{d}u \, \chi_{\mathbf{B}}(u)\right)^2 - \overline{p}_W^2\right]. \tag{8.35}$$

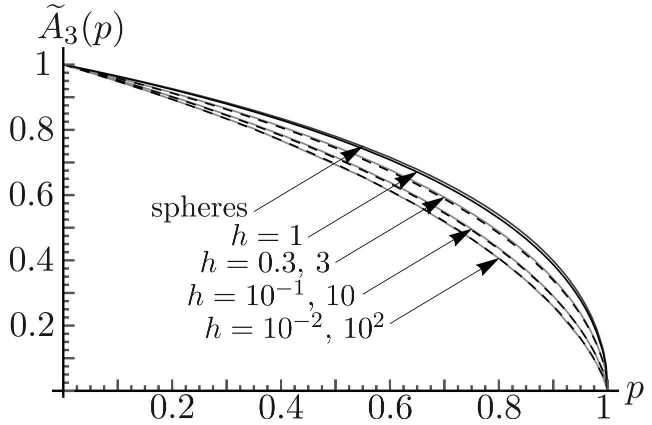

Figure 8.3: Normalized integral range $\widetilde{A}_3(p)$ in a Boolean model of cylinders with radius $r = 1/2$ as a function of the volume fraction p of cylinders, with varying cylinder heights $h = 3,\ 10,\ 10^2$ (solid grey lines, top to bottom), $1/3,\ 10^{-1},\ 10^{-2}$, (dotted black lines, top to bottom) and $h = 1$ (solid black line). Dark-grey solid line on top: normalized integral range for a Boolean model of spheres of diameter 1.

Taking N large and $\overline{p}_W \approx p$ in the above:

$$D^2_{\mathbf{B}}(V) = \frac{1}{NV^2} \sum_{i=1}^{N} \iint_{u,v \in W_i} \mathrm{d}u\mathrm{d}v \, \left[\chi_{\mathbf{B}}(u)\chi_{\mathbf{B}}(v) - p^2\right]. \tag{8.36}$$

Take $W_i \to \mathbb{R}^3$ and make use of the variable change $t = v - u$. The double integral amounts to an integral of the centered covariance function and so:

$$D^2_{\mathbf{B}}(V) = \frac{1}{V} \int_{\mathbf{R}^3} \mathrm{d}t \left[C(t) - p^2\right] = p(1-p)\frac{A_3}{V}, \tag{8.37}$$

a result first derived by Matheron [156]. The asymptotic expansion (8.37) is actually valid for volumes V much larger than A_3 and so requires that A_3 (and t_c) is finite. The latter shows that, when $V \gg A_3$, the volume W acts as n independent domains of volume A_3 with $n = W/A_3$. Thus the volume A_3 is said to be "representative" of the Boolean model $\mathbf{B}$. Note however that the variance $D^2_{\mathbf{B}}(V)$ also depends on the point variance $p(1-p)$.

When A_3 is infinite, a scaling law different from (8.37) is expected [135]. For prolate and oblate cylinders, the theory respectively predicts [116]:

$$D^2_{\mathbf{B}}(W) \sim \frac{\alpha}{V^{2/3}}, \qquad D^2_{\mathbf{B}}(W) \sim \frac{\alpha'}{V^{1/3}}, \qquad V \gg A_3, \tag{8.38}$$

where α, α' are prefactors. The scaling laws above indicate a slower decrease of the variance with respect to the volume than in (8.37), due to *infinite* correlation lengths.

For prolate and oblate cylinders, the behavior of $D^2_{\mathbf{B}}(W)$ should be linked to that of the integral of the covariance $C(t)$ when $t \to \infty$. Consider first the asymptotic behavior of $k(t)$ when $t \to \infty$ in the cases $h = \infty$ and $r = \infty$. Making use of the expansions for $\phi \to 0$:

$$F\left(\phi \middle| m\right) = \phi + \frac{m\phi^3}{6} + \frac{m(9m-4)\phi^5}{120} + O(\phi^7), \tag{8.39a}$$

$$E\left(\phi \middle| m\right) = \phi - \frac{m\phi^3}{6} + \frac{m(4-3m)\phi^5}{120} + O(\phi^7), \tag{8.39b}$$

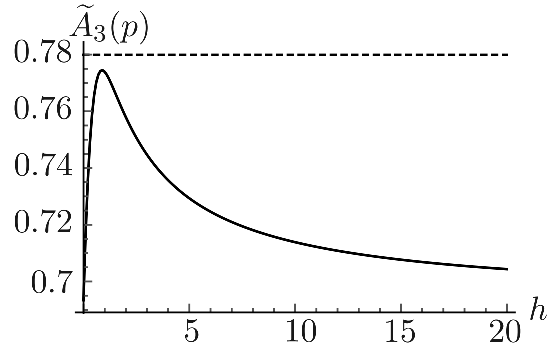

Figure 8.4: Normalized integral range $\widetilde{A}_3(p)$ in a Boolean model of cylinders with radius $r = 1/2$ and volume fraction $p = 1/2$ as a function of the cylinders height h (solid line). Dashed line: normalized integral range for a Boolean model of spheres of diameter 1.

one finds, when $t \to \infty$:

$$k_\infty(t) = \frac{r^2}{2t^2} + O\left(\frac{1}{t^4}\right), \quad (\text{if } h = +\infty), \qquad k_0(t) = \frac{h}{2t} + O\left(\frac{1}{t^2}\right), \quad (\text{if } r = +\infty). \tag{8.40}$$

For prolate and oblate cylinders, the integral of the centered covariance on a spherical domain of radius ℓ diverges as:

$$A_3(\ell) = \int_{t \leqslant \ell} (4\pi t^2)\mathrm{d}t \left[C(t) - p^2\right] \sim \begin{cases} -\frac{2\pi(1-p)}{p} r^2 \log(1-p)\ell, & \text{if } h \to \infty, \\ -\frac{\pi(1-p)}{p} h \log(1-p)\ell^2, & \text{if } r \to \infty. \end{cases} \tag{8.41}$$

We remark that $A_3(\ell)/\ell^3$ behave as $\sim V^{-2/3}$ and $\sim V^{-1/3}$ respectively for prolate and oblate cylinders, where V is the sphere of radius ℓ. This qualitatively explains the expansions (8.38).

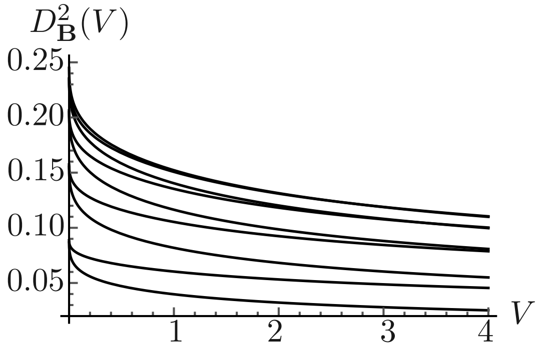

Figure 8.5: Variance $D^2_{\mathbf{B}}(V)$ of the estimate of the volume fraction measured in a spherical domain W vs. volume size V of the domain for oblate cylinders ($r = +\infty$). The cylinders height is fixed to $h = 1$. Top to bottom: volume fraction of cylinders $p = 0.5$, 0.4, 0.6, 0.3, 0.7, 0.2, 0.8, 0.1, 0.9.

However, the variable change $t = v - u$ leading to (8.37) can not be directly carried out for finite domains W_i and infinite integral range. We derive it here for spherical domains W_i of radius ℓ. One needs to compute the probability $\mathrm{d}P(t, \ell)$ that two points A and B in a sphere are separated from a distance in the interval $[t; t + \mathrm{d}t]$. We first fix A, a point at a distance $0 < a < \ell$ of the sphere center. The volume of points at a distance in the interval $[t; t + \mathrm{d}t]$ from A is given by:

$$\mathrm{d}V_t = \begin{cases} 4\pi t^2 \mathrm{d}t, & \text{if } t < \ell - a, \\ 2\pi t \mathrm{d}t \left(t - \frac{a}{2} + \frac{\ell^2 - t^2}{2a} \right), & \text{if } \ell - a < t < \ell + a. \end{cases} \tag{8.42}$$

Integrating over a, one finds the required probability:

$$\mathrm{d}P(t, \ell) = \frac{3\mathrm{d}t}{\ell} \frac{t^2}{\ell^2} \left(1 - \frac{t}{2\ell}\right)^2 \left(1 + \frac{t}{4\ell}\right), \qquad 0 \leqslant t \leqslant 2\ell. \tag{8.43}$$

Replace now the term $\chi_{\mathbf{B}}(u)\chi_{\mathbf{B}}(v)$ in (8.36) by $C(t)$ and integrate over t:

$$D^2_{\mathbf{B}}(V) = \frac{1}{N} \sum_{i=1}^{N} \frac{1}{V^2} \iint_{u,v \in W_i} \mathrm{d}u\mathrm{d}v \left[\chi_{\mathbf{B}}(u)\chi_{\mathbf{B}}(v) - p^2\right] \approx \int_{t \leqslant 2\ell} \mathrm{d}P(t, \ell) \left[C(t) - p^2\right]. \tag{8.44}$$

The integral above is analytically solvable as a closed-form expression, for oblate cylinders ($r = \infty$). When $2\ell > h$, the solution involves the exponential integral function $E_i(z) = -\int_{-z}^{\infty} \mathbf{e}^{-s}/s \mathrm{d}s$. The exact solution is a lengthy expression, which, for conciseness, is not given here. It is provided by the software *Mathematica* [262]. The variance $D^2_{\mathbf{B}}(V)$ is plotted as a function of V for various volume fraction of cylinders in Fig. (8.5).

Taking the limit $\ell \to \infty$ and using the expansion (8.40) yields:

$$D^2_{\mathbf{B}}(V) \sim \frac{-9(1-p)^2 r^2 \log(1-p)}{8\ell^2} + O(1/\ell)^3, \qquad (h = +\infty), \tag{8.45a}$$

$$D^2_{\mathbf{B}}(V) \sim \frac{-3h(1-p)^2 \log(1-p)}{5\ell} + \frac{9h^2(1-p)^2 \left[\log(1-p)\right]^2}{32\ell^2} + O(1/\ell)^3, \qquad (r = +\infty). \tag{8.45b}$$

when $\ell \to \infty$, with $V = (4/3)\pi\ell^3$. Note that the results above are identical up to a constant factor to those obtained by replacing A_3 in (8.37) by $A_3(\ell)$ from (8.41).

8.4.3 Variances and representative volume element: cylinders with finite height and radius

This section is concerned with the behavior of $D^2_{\mathbf{B}}(V)$ for r or h large but not infinite. We first examine h large. The integral in Eq. (8.44) is computed numerically for increasing values of $h = 10$, 10^2, ..., 10^4 with $r = 1/2$ fixed (Fig. 8.6a). The data is compared to $h = \infty$ (solid line, top) and to the expansion (8.45) (dashed line, top). The variance $D^2_{\mathbf{B}}(V)$ asymptotically scales as $\sim 1/V$ for very large V, as long as h is finite. However, for $h \geqslant 10$, an intermediate regime appears where $D^2_{\mathbf{B}}(V) \sim 1/V^{2/3}$. This scaling law occurs for $V \ll h^3$, i.e. $\ell \ll h$. It is very close to the asymptotic limit (8.45). The change between the two regimes takes place, as expected, when ℓ is of the same order as h. Numerical data indicates $\ell \approx 3h$. A similar behavior happens for $r \gg h$ with $h = 1$ fixed (Fig. 8.6b): when $\ell \gg r$, the scaling law $D^2_{\mathbf{B}}(V) \sim 1/V$ holds, whereas $D^2_{\mathbf{B}}(V) \sim 1/V^{1/3}$

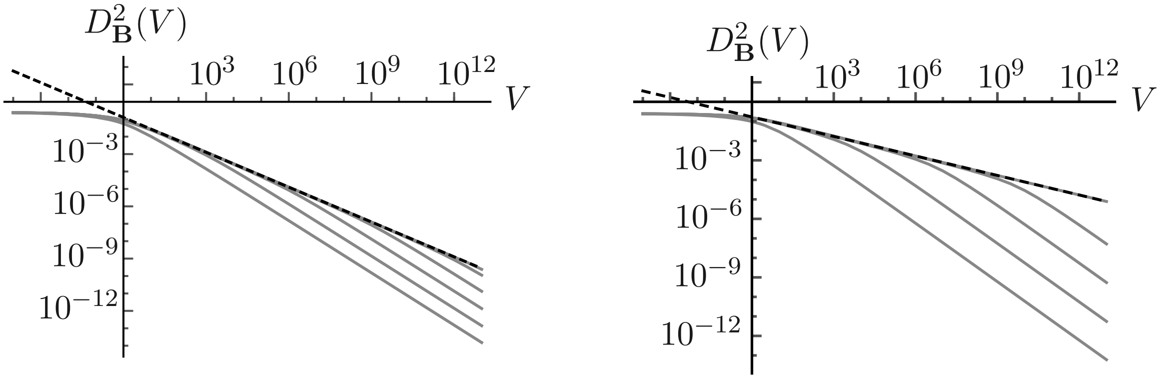

(a) (b)

Figure 8.6: Variance $D^2_{\mathbf{B}}(V)$ of the estimate of the volume fraction measured in a spherical domain W vs. volume size V of the domain, in log-log plot. The cylinders volume fraction is fixed to $p = 1/2$. Grey solid lines, bottom to top : (a) cylinders height $h = 1$, 10, 100, 10^3, 10^4, ∞ with radius fixed to $r = 1/2$; (b) cylinders radius $r = 1$, 10, 100, 10^3, ∞ with height fixed to $h = 1$. Dotted lines in black: expansions (8.45).

when $\ell \ll r$. The change between the two regimes occurs when $r \approx \ell$. Pluging $\ell = 3h$ and $\ell = r$ into (8.45) yields:

$$D^2_{\mathbf{B}}(V) \sim \frac{-27(1-p)^2 \log(1-p) h r^2}{8\ell^3}, \qquad (\ell \gg h \gg r), \tag{8.46a}$$

$$D^2_{\mathbf{B}}(V) \sim \frac{-3(1-p)^2 \log(1-p) h r^2}{5\ell^3}, \qquad (\ell \gg r \gg h). \tag{8.46b}$$

The two expansions above are in good agreement with the numerical data in Fig. (8.6).

8.5 Conclusion

In this chapter, the covariance and integral range of the Boolean model of cylinders have been computed using the geometrical covariogram of cylinders. As expected, the integral range takes the form of a divergent integral for flat (oblate) or highly-elongated (prolate) cylinders. This results in peculiar scaling laws of the variance of the measurement of the volume fraction of cylinders over subdomains of volume V. The latter variance scales as $\sim V^{-1/3}$ for the oblate and $\sim V^{-2/3}$ for the prolate type when $V \to \infty$. The lowest-order correction in the asymptotic expansion for the variance has been derived for domains of volume $V \to \infty$ with a spherical shape. For cylinders with finite (but large) aspect ratio, the scaling law $\sim V^{-1/3}$ or $\sim V^{-2/3}$ occurs in an intermediate region where $L = V^{1/3}$ is comprised between the lowest and highest dimensions of the cylinders. The classical scaling law $\sim 1/V$ is recovered when L is much larger than both cylinders dimensions. Such scaling laws should in turn affect the size of the representative volume element relative to the apparent thermal and elastic response of architectured materials [64, 63], fiber-reinforced [6] or quasi-brittle composites [184].

Chapter 9

Permeability of a Boolean model of cylinders

A rigorous bound on the permeability of Boolean models of randomly-oriented cylinders with circular cross-section is reported. The bound is examined in detail in the case where the fluid flows inside strongly-oblate (flat) cylinders, in the limit of a vanishing volume fraction of obstacles. In such microstructure, the fluid flows around a set of quasi-isolated obstacles. Two regimes are identified for the permeability of such a medium, depending on the aspect ratio of the underlining cylinders and porosity. In one of the regime, the obstacles have a tendency to align with obstacles far from them, resulting in an unusual dilute expansion, which is explicited in this work.

9.1 Introduction

In the recent years, several so-called "Fourier-based" algorithms have been introduced to solve the problem of Stokes flow in heterogeneous media [245, 172, 29, 255] some of which are based on a variational (Hashin-Shtrikman) framework [39, 40]. These methods, which rely on digitized images of the microstructures and do not require meshing, are especially useful for predicting the permeability of materials based on microstructure models or segmented microtomography images. They have been applied to compute the permeability of textiles [201, 88], ceramic foams [199] or anode layers in fuel cells [150], making use of 3D models.

Numerical computations on large-scale 3D microstructures are also useful for investigating theoretical and empirical homogenization estimates, like the classical Carman-Kozeny [45, 129] formula, Doi's upper-bound [65, 238] based on correlation functions or dilute limit expansions [208]. The Boolean model of spheres has been considered in the literature [149] and, as expected, follows the Carman-Kozeny approximation [2], whereas the upper-bound of Doi is valid in the dilute limit only, i.e. for a small volume fraction of obstacles.

The permeability of ordered arrays of cylinders has received considerable interest in experimental, theoretical and numerical works (see e.g. [148, 200, 233, 263, 223]). Attention has also been devoted in the literature to various random fibrous media, where fluid flows around cylindrical obstacles. Many of the theoretical homogenization methods used for regular arrays, however, such as the construction of trial fields, cannot be employed for random media. To study random media, numerical methods, such as the Lattice Boltzmann method, and comparisons with analytical formula for regular arrays have been used. In one of the first such study [113], an analytical estimate, based on numerical predictions, is proposed for disordered fibrous media. The estimate has been found to be accurate for a porosity less than about 25% [50]. A fiber-web material, with a structure similar to that found in fibrous sheets or paper, has been investigated numerically in [126]. Extensive numerical computations have been performed in [49] on models of prolate spheroids with varying aspect ratio. More recently, the efficient Lattice Boltzmann method has been used [234] to compute the permeability fibrous media, where the fluid flows outside of the cylinders. In one such study [177], several models made of random cylinders are investigated. An empirical law is proposed for the permeability, based on the theoretical analysis of the permeability of regular arrays of cylinders [87]. The effect of the cylinders curvature is found to be small compared to straight cylinders. Computations have also been carried out with varying cylinders aspect ratios. The combined numerical and experimental study in [201] considers fibrous media. The authors investigate in particular the domain of validity of the relevant analytical estimates. In another experimental investigation, Darcy and Darcy-Forchheimer laws have been identified on packings of non-spherical particles, including prisms and cylinders [51].

Much less work has been devoted to the “reverse” model of fluid flow through fibers, despite some early works [157]. Systems of random flat cylinders have been investigated in hydro-geological literature on fractured rocks. The permeability of 3D random models of fracture networks has been investigated numerically and theoretically in various works [127, 134]. Among important geometrical factors that influence the permeability, authors have highlighted the role of contact regions [25] or that of a wide size distribution in fractures [175].

This chapter is organized as follows. The micrsotructure model is introduced in Sec. (9.2), the equations to solve for Stokes flow are given in Sec. (9.2). Analytical upper-bounds are derived in Sec. (9.3) for flows in Boolean models of cylinders in the dilute limit. Concluding remarks are given in Sec. (9.4).

9.2 Stokes flow in a Boolean model of cylinders

The microstructures considered hereafter consist in Boolean sets of cylinders. Boolean models [155] are a classical type of random models which depend on a primary grain and on a Poisson point process [165]. In the present work, the primary grain is defined by a distribution of cylinders, and the homogeneous Poisson point process by a spatially-constant intensity n, the mean number of points per unit volume. A cylinder is attached to each point of the Poisson point process, and the Boolean set is the union of cylinders. In the following, we choose to focus on cylinders with high aspect ratio that significantly depart from sphere packings. For such ideal materials, we expect in particular a strong influence of the microstructure on the permeability.

The cylinders have circular cross-section of radius r and height h but their main axis is randomly-oriented. The direction of the axis follows a uniform distribution on the sphere, resulting in (macroscopically) isotropic Boolean sets. Cylinder intersections are allowed so that the volume fraction of cylinder p varies from 0 to 1 and is given by [155]:

$$p = 1 - q = 1 - \exp\left(-nV_0\right), \tag{9.1}$$

where $V_0 = \pi r^2 h$ is the volume of a cylinder. The Boolean sets accordingly depend on n, h

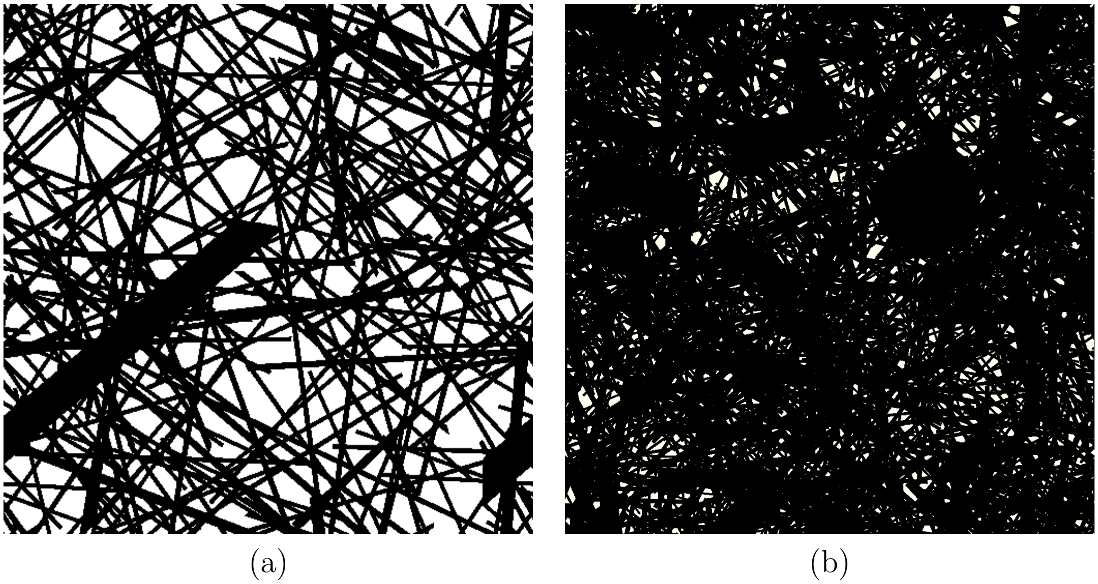
(a) (b)

Figure 9.1: 2D sections of a Boolean models of oblate cylinders (white). The fluid flows in the black phase. (a) and (b): Different volume fractions of cylinders.

and r, or, equivalently q, h and r. In the following, cylinders with very small aspect ratio h/r are considered, with p fixed, as detailed below. All microstructures accordingly depend on two parameters, the cylinders volume fraction q and a characteristic sizes for the cylinder, either r or h.

Let $h \ll r$ and consider oblate cylinders. The configuration of interest is that of "porous cylinders" where the fluid flows inside cylinders. In the case $h \ll r$, the cylinders have asymptotically the same shape as sections enclosed by two (randomly-oriented) parallel planes. The percolation threshold f_c^C again tends to 0 (we refer to [109] for a study on the connectivity of such systems). Accordingly, f is defined in the entire interval $[f_c^C; 1] \approx [0; 1]$. Note that, for $r = \infty$, the "reverse" model where fluids flow outside the cylinders presents no interest as the complementary set does not percolate. A section of the microstructure considered is shown in Fig. (9.1).

We consider hereafter a viscous fluid of velocity $\mathbf{u}$ satisfying the Stokes equation in the pores:

$$\mu \Delta u_i(\mathbf{x}) = \partial_i p(\mathbf{x}), \qquad \partial_i u_i(\mathbf{x}) = 0, \tag{9.2}$$

where $p(\mathbf{x})$ is the pressure at point $\mathbf{x}$ and μ the fluid viscosity. The fluid velocity is zero ($\mathbf{u} = 0$) along the interface with the solid. Periodic boundary conditions are applied on the computational domain, of the form [75]:

$$u\ \#, \qquad \langle \nabla p \rangle = (\Delta P)\mathbf{e}_1, \qquad p^* = p - \Delta P \mathbf{x} \cdot \mathbf{e_1}\ \#, \tag{9.3}$$

here # denotes periodicity and ΔP is the macroscopic pressure drop, oriented along the first axis $\mathbf{e}_1$ of a Cartesian coordinate system. The permeability k is a scalar for isotropic media. It is given by Darcy's law:

$$\langle u_1(\mathbf{x}) \rangle = -\frac{k}{\mu} \langle \partial_1 p(\mathbf{x}) \rangle. \tag{9.4}$$

9.3 Upper-bound for the permeability of Boolean sets of oblate cylinders

The Doi [65] upper-bound for permeability reads:

$$k \leqslant \frac{2}{3}\int_0^\infty \mathrm{d}t\, t \left[\left(\frac{q^2}{s^2} \right) F_{ss}(t) - \left(\frac{2q}{s} \right) F_{sv}(t) + F_{vv}(t) \right], \tag{9.5}$$

where s is the specific surface area of the void-solid interface, and F_{vv}, F_{sv} and F_{ss} are the "volume-volume", "surface-volume" and "surface-surface" correlation functions:

$$\begin{aligned} F_{vv}(t) &= \langle Z(\mathbf{x})Z(\mathbf{x}+t\mathbf{u})\rangle_{\mathbf{u}}, && (9.6)\\ F_{sv}(t) &= \langle |\nabla Z(\mathbf{x})| Z(\mathbf{x}+t\mathbf{u})\rangle_{\mathbf{u}}, && (9.7)\\ F_{ss}(t) &= \langle |\nabla Z(\mathbf{x})| |\nabla Z(\mathbf{x}+t\mathbf{u})|\rangle_{\mathbf{u}}. && (9.8) \end{aligned}$$

In the above, Z is the indicator function for the complementary $\mathbf{B}^c$ of set $\mathbf{B}$ (the obstacles), ∇ is the gradient operator and $\mathbf{u}$ is a unit vector ($|\mathbf{u}| = 1$). The quantity F_{vv} is given by the probability that two points separated by a distance t lie in $\mathbf{B}^c$. The quantities F_{sv} and F_{ss} can also be interpreted in terms of probability, replacing the interface of $\mathbf{B}$ by an interphase of vanishingly small width δ. The quantity F_{sv} is proportional to the probability (divided by δ) that one point lies in $\mathbf{B}^c$ and the other in the interphase. The quantity F_{ss} is related to the probability that the two points lie in the interphase. Formula (9.5) is a rigorous bound which provides the exact lowest-order correction to the permeability for dilute concentration of spherical obstacles $q \to 0$ [208].

The correlation function F_{vv} of a Boolean model of cylinders is given by [156]:

$$F_{vv}(t) = P\left\{ \mathbf{z} \notin \mathbf{B}, \mathbf{z}+\mathbf{t} \notin \mathbf{B}, |\mathbf{t}| = t \right\} = q^{2 - K(t;h,r)}, \tag{9.9}$$

where $K(t;h,r)$ (not to be confounded with k) is the normalized mean cylinder covariogram. The latter is defined as the volume intersected by two cylinders as follows:

$$K(t;h,r) = E\left\{ \frac{|C \cap C_{-t}|}{|C|} \right\}, \tag{9.10}$$

where $|C|$ is the volume of the cylinder C and C_{-t} is C translated by a vector of length t. The quantity is averaged over orientations uniformly distributed on the sphere and normalized by the cylinder volume, so that $k(t = 0; h, r) \equiv 1$.

9.3.1 Case $r = \infty$

We first consider the case of infinitely flat cylinders with $r = \infty$ (Chap. 8). Note that h and q are kept finite in this limit. Accordingly, the Poisson intensity θ (mean number of cylinders per unit of volume) should tend to 0 in a manner inversely proportional to the cylinder volume. Indeed θ is related to q by [156]:

$$q = \exp\left(-\theta\pi r^2 h\right), \tag{9.11}$$

and so $\theta \sim 1/r^2 \to 0$. Accordingly, the microstructure should be understood as a set of randomly-oriented, very large cylinders, with a very low density (in number per unit volume), so that the cylinders volume fraction remains finite. This limit microstructure could be usefully compared to Poisson tessellations (or dilated versions thereof). We refer to [114, 115] for theoretical results on the latter.

The covariogram reads (Sec. 8.2):

$$K(t;h,r)=\begin{cases}1-t/(2h), & t<h,\\ h/(2t), & t>h.\end{cases} \tag{9.12}$$

The formula for F_{sv} and F_{ss} in Boolean media are similar to that of F_{vv} [235, 207] but quite more complex. The formula involve first and second-order derivatives at $h'=h$ of the following functional:

$$K(t;h,h')=E\left\{\frac{|C\cap C'_{-t}|}{|C|}\right\}, \tag{9.13}$$

where, C' is a thick plane of width h'. Straightforward computations lead to:

$$K(t;h,h')=\begin{cases}\frac{1}{t}\left[h/2-h'+(h'+t)^2/(2h)\right], & t<h,\\ \frac{1}{t}\left[h+h'^2/(2h)+(t/h-1)(h+h')\right], & t>h.\end{cases} \tag{9.14}$$

The three expressions for the correlation functions allow one to compute the integrand in (9.5):

$$\left(\frac{q^2}{s^2}\right)F_{ss}(t)-\left(\frac{2q}{s}\right)F_{sv}(t)+F_{vv}(t)\sim\frac{q^2h}{4t},\qquad t\to\infty, \tag{9.15}$$

and so the integral (9.5) diverges and the upper-bound is infinite. The bound accordingly provides no information on the permeability of materials with “infinitely” flat-cylinders. This negative result will nevertheless prove useful for interpreting the results of Sec. (9.3.2).

9.3.2 Case r finite

We now seek for the computation of upper-bounds on the permeability for cylinders of the oblate type but with finite radius r. The isotropized covariogram K of general cylinders with r and h finite has been studied in Chap. (8). The exact form provided in is a rather complicate analytical expression involving incomplete Elliptic functions. Therefore, we use instead the approximate expression taken from (8.27):

$$\begin{aligned}K(t)\approx K_{\text{app}}(t) &= 1-\frac{(r+h)t}{2rh}+\frac{2t^2}{3\pi rh}, \quad \text{if } t<h, & \text{(9.16a)}\\ &= \left(\frac{h^2}{6t^2}-1\right)\frac{h}{2\pi r}\sqrt{1-\frac{t^2}{4r^2}}+\frac{h}{\pi t}\cos^{-1}\left(\frac{t}{2r}\right), \quad \text{if } t>h. & \text{(9.16b)}\end{aligned}$$

The derivation Doi’s bounds for general cylinders requires one to compute the volume of the intersection of two cylinders of different heights and radius averaged over uniformly-distributed directions, which we do not have. Accordingly, hereafter we use the simpler Berryman-Milton bound [27, 208] which reads:

$$k\leqslant\frac{2}{3q^2}\int_0^\infty \mathrm{d}t\,t\left[F_{vv}(t)-q^2\right]. \tag{9.17}$$

For cylinders with $r > h$, replacing F_{vv} with (9.9) and using (9.16) yields, after integrating:

$$\begin{aligned} k \leqslant k^{\mathrm{BM}} &= \frac{h \log q}{3\pi} \left[2h \cos^{-1}\left(\frac{h}{2r}\right) - \frac{1}{3}\left(\frac{h^2}{2r^2} + 4\right)\sqrt{4r^2 - h^2} \right] \\ &\quad + \frac{h^2}{3}\left[\frac{8 + 4\sqrt{q}\,(\log q - 2)}{q(\log q)^2} - 1 \right]. \end{aligned} \tag{9.18}$$

The previous upper-bound may be meaningful in the dilute limit ($q \ll 1$) only as shown in [253], where FFT computations have been carried out for this model. Therefore we focus on the dilute regime $q \to 0$. Fix r and expand the above to zero-order correction $O(1)$ in the dilute limit $q \to 0$ and let $r \to \infty$ *afterwards.* We obtain:

$$k \leqslant \frac{8h^2}{3q(\log q)^2}\left[1 + \left(\frac{1}{2}\log q - 1\right)\sqrt{q}\right] + O(1), \qquad q \to 0. \tag{9.19}$$

At the lowest-order correction, one recovers an asymptotic regime $\sim 1/[q(\log q)^2]$. We remark that this constitutes a higher correction than that predicted by the James-Jackson model [113] which provides:

$$k \sim -\frac{3a^2 \log q}{20q}, \qquad q \to 0, \tag{9.20}$$

for the permeability of fibrous media of radius a and volume fraction q. Estimate (9.20) is itself higher than the dilute expansion for the permeability of a model of hard spheres of volume fraction q, which scales as $\sim 1/q$ when $q \to 0$.

Interestingly, the second leading-order term in (9.19) scales as $1/(\sqrt{q}\log q)$. A similar non-analytic dependence appears in the dilute limit expansion of the permeability of a bed of totally impenetrable spheres, obtained by self-consistent methods [48]:

$$k = \frac{2a^2}{9q}\left[1 - \frac{3}{\sqrt{2}}\sqrt{q} + O(q\log q)\right], \qquad q \to 0, \tag{9.21}$$

where a is the sphere radius. The $\sqrt{q}$ term is related to hydrodynamic screening effects [35, 232]. For a dilute packing of spheres, as shown in [208], no screening term is predicted by the bound (9.17) or by Doi's bound [65]. As shown in expansion (9.19), a screening term is indeed predicted by the variational bound, for the particular highly-elongated shapes considered here. Note that in the dilute limit considered here, the obstacles are not cylinders, but have a variety of shapes with very large surface/volume ratio.

Although the bound (9.17) is in general less accurate than Doi's bound which uses the surface-surface correlation information [208], both are relevant in the dilute limit. Doi's bound predicts the correct leading-order term in the dilute limit for Boolean spherical obstacles. The bound (9.17) predicts the correct scaling law $\sim a^2/q$, with a slightly overestimated prefactor $4/15 \approx 0.27$ instead of $2/9 \approx 0.22$ for the Boolean model of spheres.

Compute now the limit $r \to \infty$ and *afterwards* $q \to 0$ in (9.18):

$$k \leqslant -\frac{8hr}{9\pi}\log q + O(1), \qquad r \to \infty. \tag{9.22}$$

The expansion above depends on r unlike (9.21) and tends to $+\infty$ which explains the result obtained previously for Doi's bound with $r = \infty$. When taking the limits $r \to \infty$ and $q \to 0$,

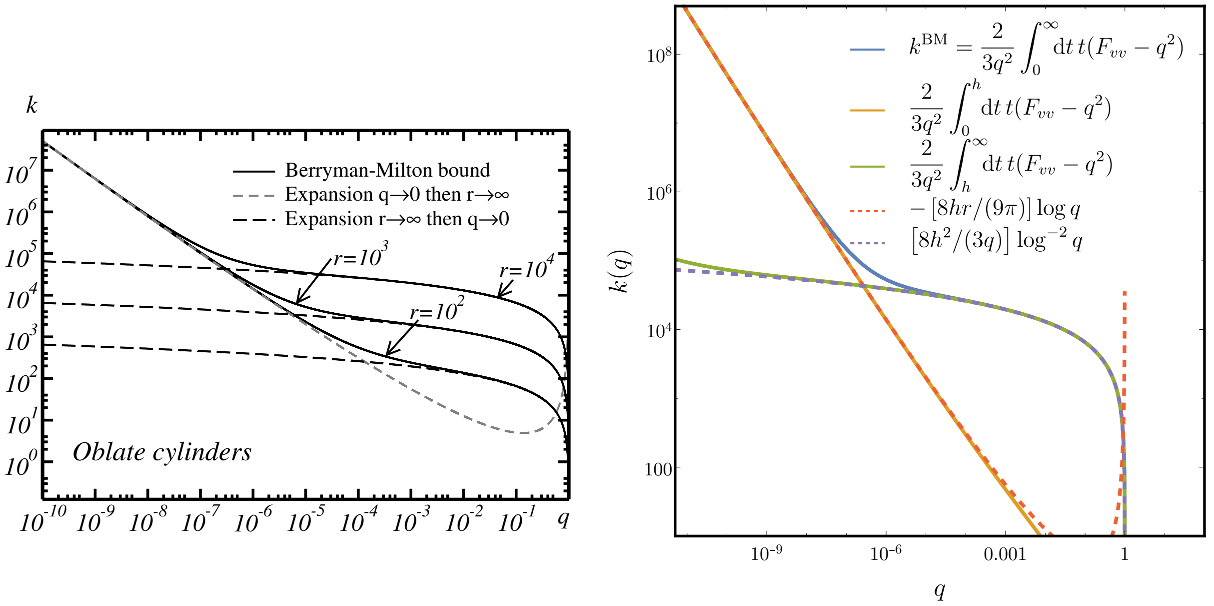

(a) (b)

Figure 9.2: (a) Berryman-Milton upper-bound (9.17) for the permeability k of a Boolean model of flat cylinders with height $h = 1$ and radius $r = 10^2$, 10^3, 10^4 vs. concentration of obstacles q, in log-log plot (black). Dark-gray solid lines: $r \to \infty$ expansion (9.22). Light-gray solid line: dilute limit expansion $q \to 0$ (9.21). (b) Permeability k vs. volume fraction of obstacles q (x-axis) in log-log plot, for a Boolean model of flat cylinders of height $h = 1$ and radius $r = 10^4$ (a.u.). Comparison between the Berryman-Milton upper-bound (9.17, solid blue line), its two contributions over $t < h$ and $t > h$ (orange and green solid lines), and expansions (9.19, blue dashed line) and (9.22, orange dashed line).

different regimes are obtained depending on the order one takes the limits. The two regimes appear when the permeability is plotted as a function of q in log-log plot (Fig. 9.2a). The regime change occurs at some points $r \approx r_c(q)$, $q \approx q_c(r)$ which are obtained by equaling the two highest-order corrections (9.19) and (9.22):

$$r_c = \frac{3\pi h}{q_c(-\log q_c)^3}. \tag{9.23}$$

When $r \gg r_c(q)$, or equivalently $q \ll q_c(r)$, the permeability follows expansion (9.22). Expansion (9.21) holds in the domain $r \ll r_c(q)$ or $q \gg q_c(r)$.

Comparison with FFT data would be needed to confirm the existence of the two regimes, however, accurate computations in the dilute limit requires high computational costs [2]. This is left to future work.

9.3.3 Dilute and "correlated" regimes

To interpret the two regimes identified above, we decompose the Berryman-Milton upper-bound into two contributions, corresponding to near and far-field terms. The integral in (9.17) is split into domains $[0; h]$ and $[h; \infty]$. (Fig. 9.2b, orange and green solid lines). The former and latter contributions match expansions (9.19) and (9.22) rexpectively. As expected, the dilute behavior

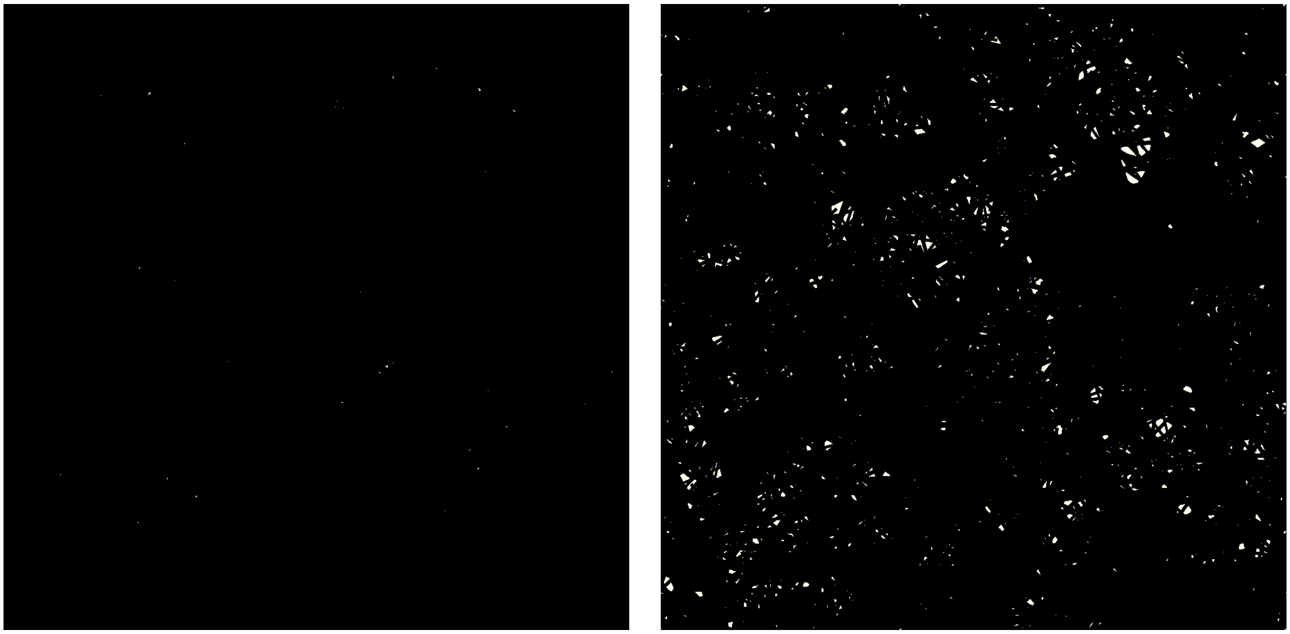

(a) (b)

Figure 9.3: Section (1000×1000 voxels) of a Boolean set of cylinders of height 4 voxels and radius 200 voxels with $q_c \approx 0.04\%$. The fluid flow occurs inside the black phase, obstacles are shown in white. (a): $q \approx 0.009\% \approx 0.2q_c$. (c): $q \approx 1.2\% \approx 30q_c$.

$q \ll q_c$ corresponds to the covariance's main contributions in the range $[0; h]$, whereas the non-dilute regime $q \gg q_c$ is a controlled by the behavior of the covariance in the interval $t \gg h$.

These observations allow us to interpret the two regimes predicted by the covariance bound. On the one hand, when $q \ll q_c$, the medium is made of uncorrelated, isolated obstacles of size $\propto h$ (Fig. 9.3a), and the permeability scales as $k \sim h^2$ (9.19), i.e. the permeability in this regime does not depend on r, at first-order. When $q \gg q_c$, on the other hand, the fluid flow is driven through large-scales structures, which constrain the fluid path into the flat cylinders. This is illustrated in Fig. (9.3b) which shows areas free of obstacles in-between clusters of particles. Some particles are clearly aligned to one another. Accordingly, the permeability in this regime scales as $k \sim hr$ (9.22), highlighting the role of the large-scale structures (of size $\sim r$). Also, the bound predicts that the permeability increases much more with respect to porosity in the highly-dilute regime $q \ll q_c$. This is consistent with our intuition, which suggests that, in the non-dilute regime $q \gg q_c$, the fluid flow inside clusters of particles is much smaller than in zones that are free of particles. Hence, removing obstacles has a lesser effect on the macoscopic flow than in regime $q \ll q_c$.

9.4 Conclusion

In this chapter, the permeability of a Boolean model of very flat cylinders in the case where the fluid flows inside the cylinders. The flat cylinders are tantamount to models of planes of finite width. Because of the cylinder overlap, the resulting microstructure, which consist, in the high porosity limit, of isolated obstacles, displays markedly anisotropic structures and long-range correlations. It should be noted that strongly-anisotropic arrangements are not uncommon in materials, and in fact appear in a wide array of applications [240, 39].

In this chapter we have investigated the behavior of the Berryman-Milton upper-bound in the dilute limit of such a Boolean set, making use of an approximate formula for the covariogram of cylinders. The upper-bound predicts two distinct regimes depending on the diameter of the cylinders relative to the volume fraction of obstacles. In the strongly-dilute regime, a scaling law $\sim 1/[q(\log q)^2]$ is predicted, whereas a much weaker regime $\sim \log q$ arises when $r \gg h/q$.

Chapter 10

Conclusion

The main problem tackled in this manuscript concerns a nonlinear medium in the continuum, in two dimensions, weakened or reinforced by a population of voids or rigid particles. The matrix is rigid perfectly-plastic (in deformation theory) and subjected to anti-plane shear. In the equivalent conducting problem, the particles are either insulating or perfectly-conducting, and the matrix exhibits a threshold-type nonlinear constitutive law. The macroscopic behavior is characterized by an effective plastic yield stress or effective current threshold.

Bounds (4.20) and (4.37), computed in Chap. (4), together with the predictions of nonlinear homogenization theories, have allowed us to gain insights on the effective behavior of such nonlinear medium in the porous case. Namely, in the dilute porosity limit, the effective yield stress relative to the yield stress in the matrix tends to unity with a correction that scales as the porosity to the power 2/3. Although this scaling law holds for Boolean media with homogeneous Poisson point process intensity, it is in fact much more general. The location of particles in random sequential adsorption models, for instance, is asymptotically equivalent to a Poisson point process in the dilute limit, so these models are also identical to Boolean random sets for a dilute concentration of particles [145]. A key for deriving bound (4.20) is the property that the presence of the center of a pore in a given domain is independent of the presence of another pore center in a disjoint domain. As a consequence, the correlation function of the "one-scale" Boolean model $\mathcal{B}_E$ (Chap. 6) vanishes at finite distance. That is, the probability that a point $\boldsymbol{x}$ is in a pore is independent of the probability that point $\boldsymbol{x} + h$ is in a pore, for a finite value of h. This property holds for any media with finite integral range, the integral range being the integral of the correlation function [159]. It would be interesting to investigate if microstructures with finite integral range exhibit a "dilute exponent" equal to 2/3.

The properties of a multiscale dispersion of equisized pores has been studied in Chap. (6), with emphasis on the dilute limit. By tailoring the variation of the volume fraction of clusters with respect to the total porosity in the medium, it has been shown that a non-analytic behavior may be obtained, different from that observed for a homogeneous distribution of pores. This non-analyticity is characterized by a powerlaw with exponent greater than 2/3 and strictly lower than 1, for a two-scale medium. The highest exponent, and consequently the lowest effect of the pores, is attained when the shear bands are flat at the scale of the clusters, but would in fact display rugosity at the largest scale if the porosity was only very slightly increased. By increasing the number of scales, analytical bounds predict that any exponent inbetween 2/3 and 1 may be obtained. For infinitely-many scales, an exponent 1 is obtained for most arrangements (among the ones considered in Sec. 6.3.3).

As predicted by Duxbury et al. [70], the non-analyticity of the effective behavior with respect to the volume fraction is a signature of the localization of the strain field and of the strong interaction of pores along shear bands. Clearly, as shown by the multiscale structures studied in Chap. (6), the exponent depends in general on the tortuosity at the different scales of the minimal path.

Furthermore, analytical bounds obtained in the dilute limit in Chap. (4), in particular (4.31), suggest that the effective behavior depends on the shape of the pores through the width of the inclusion, measured in the direction parallel to the applied load or to the macroscopic direction of the geodesics. As a consequence, according to bounds, elongated inclusions (tantamount to segment of lines, or open cracks) have the most important weakening effect on the effective yield stress at fixed porosity – an unsurprising result. In contrast to this, disk-shaped inclusions have, in the dilute limit, the least important weakening effect on the effective yield stress, in the space of shapes of constant width resulting in an isotropic macroscopic behavior.

Although the bounds on geodesics extend to multidimensional spaces (Sec. 4.4.4), the latter can not be used to predict the behavior of minimal *surfaces* spanning media in three dimensions. Therefore, they can not be used at the moment to assess the validity of the predictions of nonlinear homogenization theories in three dimensions. To achieve this goal, a description of "sufficiently general" surfaces spanning a volume would be required. Another difficulty concerns the extension of the bounds in Chap. (4) to polydisperse inclusions, for instance a population of pores of two different sizes. Such a bound is not available at the moment. Nevertheless, results obtained in Chap. (6) for model $\mathcal{B}_P$ suggest that the exponent 2/3 is unchanged in this case, although the prefactor is not.

The dual problem related to the response of a nonlinear medium containing a population of rigid particles, could not be investigated by the same integral geometry techniques. This is because particles interpenetration is a major difficulty that prevents us from deriving rigorous bounds equivalent to the ones in Chap. (4). The random sequential adsorption model is a random set in which particles interpenetration are forbidden, very few analytical result is known about this model, save in one dimension [236], which prevents us to derive bounds.

To alleviate this difficulty, we have turned to random checkerboard materials where cells do not interpenetrate. A rigorous bound has been obtained for a random checkerboard of square-shaped cells. In the dilute limit of rigid particles volume fraction $f \to 0$, the bound's leading-order term in f scales as $\sim |\log f| f^3$. A markedly different behavior $\sim |\log f| f^2$ was obtained for a random checkerboard of rectangles which are not aligned to each other. We argue that the much lower bound obtained in the former case is an effect of particle alignment and long-range correlations, although long-range correlations are also present in the rectangular case. In any case, the scaling $\sim f^2$ has been numerically confirmed for the RSA model of squares, and is qualitatively close to the predictions of the bound obtained for the random checkerboard of rectangles. Finally, note that the same scaling law $\sim f^2$ is predicted by the "second-order" nonlinear homogenization theory [83], a result which supports our conclusion that a $\sim f^2$ correction holds for spatial distributions without long-range correlations.

Extending our results for multiscale dispersions of rigid particles, it has been found that the exponent in the dilute limit also varies when the number of scales increases. Specifically, for multiscale random materials containing rigid particles, we have shown that any exponent between 1 and 2 may be obtained. In the limit of a material with infinitely-many scales, made of particles arranged into clusters, themselves arranged into superclusters (etc.) an exponent 1 (i.e. a linear correction in f) is recovered. Different regimes are predicted which depend on the fact that shear bands may avoid entire clusters, or pass through them while avoiding rigid particles inside each cluster they go through. The rigid particles have the highest strengthening effect when the length of the minimal path is the same for a path that avoids clusters entirely or for a path that goes through them. This linear correction in the limit of infinitely-many scales explains the behavior of certain rigorous upper-bounds [94]. It would be useful to extend these results to random microstructures in three-dimensions, such as the ones considered in [81] and [82].

The results obtained in the present work also highlight the limits – or the extent – of the domain of validity of linear and nonlinear homogenization theories, as the nonlinearity or heterogeneity contrast becomes large. Chap. (7) has investigated how shear bands may develop from a strictly convex powerlaw potential, in the context of periodic structures. Different regime changes have been identified, in the porous and rigid case, including in plane strain. The study may be usefully compared to [259] and Chap. (2) where a regime change occurring in linear, stongly-anisotropic media is reported. In particular, it would be interesting to generalize these results to randomly-distributed particles.

The two closing chapters (Chaps. 8 and 9) present a study of the behavior of a Stokes flow passing through a medium with statistically-aligned obstacles. In the dilute limit, the fluid avoids a set of obstacles. While the latter are isolated from one another, their positions are correlated to each other so that they form organized patterns corresponding to long-range alignments. In this regime, the Berryman-Milton upper-bound predicts markedly different behavior of the permeability than when the obstacles are isolated and their positions are uncorrelated. Namely, the increase of the permeability with respect to porosity is much smaller in the former case.

References

[1] B. Abdallah. “Analyse morphologique et modélisation pour l’optimisation structurelle d’électrodes”. PhD thesis. Ecole Nationale Supérieure des Mines de Paris, 2015.

[2] B. Abdallah, F. Willot, and D. Jeulin. “Stokes flow through a Boolean model of spheres: Representative volume element”. In: *Transport in Porous Media* 109.3 (2015), pp. 711–726.

[3] B. Abdallah, F. Willot, and D. Jeulin. “Morphological modeling of three-phase microstructures of anode layers using SEM images”. In: *Journal of Microscopy* 263.1 (2016), pp. 51–63.

[4] AA Abrikosov, JC Campuzano, and K Gofron. “Experimentally observed extended saddle point singularity in the energy spectrum of $YBa_2Cu_3O_{6.9}$ and $YBa_2Cu_4O_8$ and some of the consequences”. In: *Physica C: Superconductivity* 214.1-2 (1993), pp. 73–79.

[5] M.J. Alava and P.M. Duxbury. “Disorder-induced roughening in the three-dimensional Ising model”. In: *Physical Review B* 54.21 (1996), p. 14990.

[6] H. Altendorf, D. Jeulin, and F. Willot. “Influence of the fiber geometry on the macroscopic elastic and thermal properties”. In: *International Journal of Solids and Structures* 51.23 (2014), pp. 3807–3822.

[7] M. Amar, G. Crasta, and A. Malusa. “On the Finsler metrics obtained as limits of chessboard structures”. In: *Advances in Calculus of Variations* 2.4 (2009), pp. 321–360.

[8] A. Ambos, F. Willot, D. Jeulin, and H. Trumel. “Numerical modeling of the thermal expansion of an energetic material”. In: *International Journal of Solids and Structures* 60–61 (2015), pp. 125–139.

[9] T. W. Anderson. *An introduction to multivariate statistical analysis.* Vol. 2. Wiley, New York, 1958.

[10] S. Andrieux, Y. Bamberger, and J.J. Marigo. “Un modèle de matériau microfissuré pour les bétons et les roches”. In: *J. Méca. Théor. Appl.* 5.3 (1986), pp. 471–513.

[11] Vladimir I Arnol’d. *Catastrophe theory.* Springer Science & Business Media, 2004.

[12] M. Avellaneda. “Iterated homogenization, differential effective medium theory and applications”. In: *Communications on Pure and Applied Mathematics* 40.5 (1987), pp. 527–554.

[13] M. Avrami. “Kinetics of phase change. I General theory”. In: *The Journal of chemical physics* 7.12 (1939), pp. 1103–1112.

[14] D. Azzimonti, F. Willot, and D. Jeulin. “Optical properties of deposit models for paints:full-fields FFT computations and representative volume element”. In: *Journal of Modern Optics* 60.7 (2013), pp. 519–528.

[15] R. Bargellini, D. Halm, and A. Dragon. “Modelling of quasi-brittle behaviour: a discrete approach coupling anisotropic damage growth and frictional sliding.” In: *Eur. J. Mech. A/Solids* 27 (2008), pp. 564–581.

[16] A. Barroso, D. Vicentini, V. Mantič, and F. París. “Determination of Generalized Fracture Toughness in composite multimaterial closed corners with two singular terms–Part I: Test proposal and numerical analysis”. In: *Engineering Fracture Mechanics* 89 (2012), pp. 1–14.

[17] A Barroso, V Mantič, and F París. “Singularity analysis of anisotropic multimaterial corners”. In: *International Journal of Fracture* 119.1 (2003), pp. 1–23.

[18] A Barroso, V Mantič, and F París. “Computing stress singularities in transversely isotropic multimaterial corners by means of explicit expressions of the orthonormalized Stroh-eigenvectors”. In: *Engineering Fracture Mechanics* 76.2 (2009), pp. 250–268.

[19] M. Barthélémy and H. Orland. “Local field probability distribution in random media”. In: *Physical Review E* 56.3 (1997), p. 2835.

[20] P. J. Basser and S. Pajevic. “A normal distribution for tensor-valued random variables: applications to diffusion tensor MRI”. In: *IEEE Transactions on Medical Imaging* 22.7 (2003), pp. 785–794.

[21] D. Bedrov, O. Borodin, G. D. Smith, T. D. Sewell, D. M. Dattelbaum, and L. L. Stevens. “A molecular dynamics simulation study of crystalline 1,3,5-triamino-2,4,6-trinitrobenzene as a function of pressure and temperature”. In: *Journal of Chemical Physics* 131 (2009), p. 224703.

[22] Y. Benveniste. “A new approach to the application of Mori-Tanaka’s theory in composite materials”. In: *Mechanics of materials* 6.2 (1987), pp. 147–157.

[23] Y. Benveniste. “Universal Relations in Piezoelectric Composites With Eigenstress and Polarization Fields, Part 2: Multiphase Media–Effective Behavior”. In: *Journal of Applied Mechanics* 60.2 (1993), pp. 270–274.

[24] S. Berbenni and M. Cherkaoui. “Homogenization of multicoated inclusion-reinforced linear elastic composites with eigenstrains: Application to thermoelastic behavior”. In: *Philosophical Magazine* 90.22 (2010), pp. 3003–3026.

[25] B. Berkowitz. “Characterizing flow and transport in fractured geological media: A review”. In: *Advances in water resources* 25.8 (2002), pp. 861–884.

[26] J. G. Berryman. “Bounds and self-consistent estimates for elastic constants of random polycrystals with hexagonal, trigonal, and tetragonal symmetries”. In: *Journal of the Mechanics and Physics of Solids* 53.10 (2005), pp. 2141–2173.

[27] J.G. Berryman and G.W. Milton. “Normalization constraint for variational bounds on fluid permeability”. In: *The Journal of chemical physics* 83.2 (1985), pp. 754–760.

[28] James G Berryman. “Long-wavelength propagation in composite elastic media II. Ellipsoidal inclusions”. In: *The Journal of the Acoustical Society of America* 68.6 (1980), pp. 1820–1831.

[29] F. Bignonnet and L. Dormieux. “FFT-based bounds on the permeability of complex microstructures”. In: *International Journal of Numerical and Analytical Methods in Geomechanics* 38.16 (2014), pp. 1707–1723.

[30] M. Bobeth and G. Diener. “Field fluctuations in multicomponent mixtures”. In: *Journal of the Mechanics and Physics of Solids* 34 (1986), pp. 1–17.

[31] V. Bortolussi, B. Figliuzzi, F. Willot, M. Faessel, and M. Jeandin. “Morphological modeling of cold spray coatings”. In: *Image Analysis & Stereology* 37.2 (2018), pp. 145–158.

[32] J.P. Bouchaud, E. Bouchaud, G. Lapasset, and J. Planes. “Models of fractal cracks”. In: *Physical review letters* 71.14 (1993), p. 2240.

[33] B. Bourdin, G. A. Francfort, and J.-J. Marigo. “Numerical experiments in revisited brittle fracture”. In: *Journal of the Mechanics and Physics of Solids* 48.4 (2000), pp. 797–826.

[34] A. Bovier, J. Fröhlich, and U. Glaus. “Lines and domain walls in dilute ferromagnets”. In: *Physical Review B* 34.9 (1986), p. 6409.

[35] J.F. Brady and G. Bossis. “Stokesian dynamics”. In: *Annual review of fluid mechanics* 20 (1988), pp. 111–157.

[36] R. Brenner, O. Castelnau, and L. Badea. “Mechanical field fluctuations in polycrystals estimated by homogenization techniques”. In: *Proceedings of the Royal Society of London* A460 (2004), pp. 3589–3612.

[37] R. Brenner, R.A. Lebensohn, and O. Castelnau. “Elastic anisotropy and yield surface estimates of polycrystals”. In: *International Journal of Solids and Structures* 46 (2009), pp. 3018–3026.

[38] T. Bretheau and D. Jeulin. “Caractéristiques morphologiques des constituants et comportement à la limite élastique d’un matériau biphasé Fe/Ag”. In: *Revue de Physique Appliquée* 24.9 (1989), pp. 861–869.

[39] S. Brisard and L. Dormieux. “FFT-based methods for the mechanics of composites: A general variational framework”. In: *Computational Materials Science* 49.3 (2010), pp. 663–671.

[40] S. Brisard and L. Dormieux. “Combining Galerkin approximation techniques with the principle of Hashin and Shtrikman to derive a new FFT-based numerical method for the homogenization of composites”. In: *Computational Methods for Applied Mechanical Engineering* 217.220 (2012), pp. 197–212.

[41] J. R. Bristow. “Microcracks, and the static and dynamic elastic constants of annealed and heavily cold-worked metals”. In: *British Journal of Applied Physics* 11.2 (1960), p. 81.

[42] B. Budiansky and R. J. O’Connell. “Elastic moduli of a cracked solid”. In: *International Journal of Solids and Structures* 12.2 (1976), pp. 81–97.

[43] F. Cadiou, A. Etiemble, T. Douillard, F. Willot, O. Valentin, J.-C. Badot, B. Lestriez, and É. Maire. “Numerical prediction of multiscale electronic conductivity of Lithium-ion battery positive electrodes”. In: *Journal of the Electrochemical Society* 166.8 (2019), A1692–A1703.

[44] P. Calka, J. Michel, and S. Porret-Blanc. *Asymptotics of the visibility function in the Boolean model.* Online at `https://arxiv.org/abs/0905.4874`. 2009.

[45] P.C. Carman. “Fluid flow through granular beds”. In: *Transactions-Institution of Chemical Engineeres* 15 (1937), pp. 150–166.

[46] G.D. Chakerian and H. Groemer. “Convex Bodies of Constant Width”. In: *Convexity and its applications.* Ed. by PM Gruber and JM Wills. Basel: Springer, 1983, pp. 49–96.

[47] N. Challamel. “A variationally based nonlocal damage model to predict diffuse microcracking evolution.” In: *Int. J. Mech. Sci.* 52 (2010), pp. 1783–1800.

[48] S. Childress. “Viscous flow past a random array of spheres”. In: *The Journal of Chemical Physics* 56.6 (1972), pp. 2527–2539.

[49] I.L. Claeys and J.F. Brady. “Suspensions of prolate spheroids in Stokes flow. Part 2. Statistically homogeneous dispersions”. In: *Journal of Fluid Mechanics* 251 (1993), pp. 443–477.

[50] D.S. Clague, B.D. Kandhai, R. Zhang, and P.M.A. Sloot. “Hydraulic permeability of (un) bounded fibrous media using the lattice Boltzmann method”. In: *Physical Review E* 61.1 (2000), p. 616.

[51] R. Clavier, N. Chikhi, F. Fichot, and M. Quintard. “Experimental investigation on single-phase pressure losses in nuclear debris beds: Identification of flow regimes and effective diameter”. In: *Nuclear Engineering and Design* 292 (2015), pp. 222–236.

[52] F. Cormery and H. Welemane. “A critical review of some damage models with unilateral effect.” In: *Mech. Res. Comm.* 29 (2002), pp. 391–395.

[53] F. Cormery and H. Welemane. “A stress-based macroscopic approach for microcracks unilateral effect.” In: *Comput. Mat. Sci.* 47 (2010), pp. 727–738.

[54] E. Couka, F. Willot, and D. Jeulin. “A mixed Boolean and deposit model for the modeling of metal pigments in paint layers”. In: *Image Analysis & Stereology* 34.2 (2015), pp. 125–134.

[55] N. Cressie and G. M. Laslett. “Random set theory and problems of modeling”. In: *SIAM review* 29.4 (1987), pp. 557–574.

[56] D. Cule and S. Torquato. “Electric-field distribution in composite media”. In: *Physical Review B* 58.18 (1998), R11829.

[57] G. Dantzig and D. R. Fulkerson. “On the max flow min cut theorem of networks”. In: *Linear inequalities and related systems* 38 (2003), pp. 225–231.

[58] L De Arcangelis, A Hansen, HJ Herrmann, and S Roux. “Scaling laws in fracture”. In: *Physical Review B* 40.1 (1989), p. 877.

[59] M. Deijfen. “Asymptotic shape in a continuum growth model”. In: *Advances in Applied Probability* 35.2 (2003), pp. 303–318.

[60] L. Delannay, P. Yan, J. F. B. Payne, and N. Tzelepi. "Predictions of inter-granular cracking and dimensional changes or irradiated polycrystalline graphite under plane strain". In: *Computational Materials Science* 87 (2014), pp. 129–137.

[61] B. Derrida and J. Vannimenus. "Interface energy in random systems". In: *Physical Review B* 27.7 (1983), pp. 4401–4411.

[62] EW Dijkstra. "A note on two problems in connexion with graphs". In: *Numerische mathematik* 1.1 (1959), pp. 269–271.

[63] J. Dirrenberger, S. Forest, and D. Jeulin. "Towards gigantic RVE sizes for 3D stochastic fibrous networks". In: *International Journal of Solids and Structures* 51.2 (2014), pp. 359–376.

[64] J. Dirrenberger, S. Forest, and D. Jeulin. "Computational Homogenization of Architectured Materials". In: *Architectured Materials in Nature and Engineering.* Springer, 2019, pp. 89–139.

[65] M. Doi. "A new variational approach to the diffusion and the flow problem in porous media". In: *Journal of the Physical Society of Japan* 40.2 (1976), pp. 567–572.

[66] A. Donev, C. E. Musolff, and P. M. Duxbury. "Random manifolds in non-linear resistor networks: applications to varistors and superconductors". In: *Journal of Physics A: Mathematical and General* 35.23 (2002), p. L327.

[67] L. Dormieux and D. Kondo. "Stress-based estimates and bounds of effective elastic properties: the case of cracked media with unilateral effects." In: *Comput. Mat. Sci.* 46.1 (2009), pp. 173–179.

[68] D. C. Drucker. "The continuum theory of plasticity on macroscale and microscale". In: *Journal of Materials* 1.4 (1966), pp. 873–910.

[69] R. Durrett and T. M. Liggett. "The shape of the limit set in Richardson's growth model". In: *The annals of Probability* 9.2 (1981), pp. 186–193.

[70] P. M. Duxbury, E. S. McGarrity, and E. A. Holm. "Critical manifolds in non-linear response of complex materials". In: *Mechanics of materials* 38.8 (2006), pp. 757–771.

[71] P.M. Duxbury, P.D. Beale, and C. Moukarzel. "Breakdown of two-phase random resistor networks". In: *Physical Review B* 51.6 (1995), p. 3476.

[72] PM Duxbury, PD Beale, H Bak, and PA Schroeder. "Capacitance and dielectric breakdown of metal loaded dielectrics". In: *Journal of Physics D: Applied Physics* 23.12 (1990), p. 1546.

[73] P. Elias, A. Feinstein, and C.E. Shannon. "A note on the maximum flow through a network". In: *Information Theory, IRE Transactions on* 2.4 (1956), pp. 117–119.

[74] Xavier Emery and Christian Lantuéjoul. "Geometric covariograms, indicator variograms and boundaries of planar closed sets". In: *Mathematical Geosciences* 43.8 (2011), pp. 905–927.

[75] I. Ene H. and E. Sanchez-Palencia. "Equations et phénomenes de surface pour l'écoulement dans un modele de milieu poreux". In: *Journal de mécanique* 14.1 (1975), pp. 73–108.

[76] J. Escoda. “Modélisation morphologique et micromécanique 3D de matériaux cimentaires”. PhD thesis. École nationale supérieure des mines de Paris, 2012.

[77] D. J. Eyre and G. W Milton. “A fast numerical scheme for computing the response of composites using grid refinement”. In: *The European Physical Journal Applied Physics* 6.1 (1999), pp. 41–47.

[78] B. Figliuzzi. “Eikonal-based models of random tesselations”. In: *Image Analysis & Stereology* 38.1 (2019), pp. 15–23.

[79] P. Francescato, J. Pastor, and B. Riveill-Reydet. “Ductile failure of cylindrically porous materials. Part I: plane stress problem and experimental results”. In: *European journal of mechanics-A/solids* 23.2 (2004), pp. 181–190.

[80] G. A. Francfort and J.-J. Marigo. “Revisiting brittle fracture as an energy minimization problem”. In: *Journal of the Mechanics and Physics of Solids* 46.8 (1998), pp. 1319–1342.

[81] F. Fritzen, S. Forest, T. Böhlke, D. Kondo, and T. Kanit. “Computational homogenization of elasto-plastic porous metals”. In: *International Journal of Plasticity* 29 (2012), pp. 102–119.

[82] F. Fritzen, S. Forest, D. Kondo, and T. Böhlke. “Computational homogenization of porous materials of Green type”. In: *Computational Mechanics* 52.1 (2013), pp. 121–134.

[83] J. Furer and P. Ponte Castañeda. “A symmetric fully optimized second-order method for nonlinear homogenization”. In: *ZAMM-Journal of Applied Mathematics and Mechanics/Zeitschrift für Angewandte Mathematik und Mechanik* 98.2 (2018), pp. 222–254.

[84] J.-B. Gasnier, F. Willot, H. Trumel, B. Figliuzzi, D. Jeulin, and M. Biessy. “A Fourier-based numerical homogenization tool for an explosive material”. In: *Matériaux & Techniques* 103.3 (2015), p. 308.

[85] J.-B. Gasnier, F. Willot, H. Trumel, D. Jeulin, and J. Besson. “Thermoelastic properties of microcracked polycrystals. Part I: Adequacy of Fourier-based methods for cracked elastic bodies”. In: *International Journal of Solids and Structures* 155 (2018), pp. 248–256.

[86] J.-B. Gasnier, F. Willot, H. Trumel, D. Jeulin, and M. Biessy. “Thermoelastic properties of microcracked polycrystals. Part II: The case of jointed polycrystalline TATB”. In: *International Journal of Solids and Structures* 155 (2018), pp. 257–274.

[87] B.R. Gebart. “Permeability of unidirectional reinforcements for RTM”. In: *Journal of composite materials* 26.8 (1992), pp. 1100–1133.

[88] P.C. Gervais, N. Bardin-Monnier, and D. Thomas. “Permeability modeling of fibrous media with bimodal fiber size distribution”. In: *Chemical Engineering Science* 73 (2012), pp. 239–248.

[89] W Gille. “The intercept length distribution density of a cylinder of revolution”. In: *Experimentelle Technik der Physik* 35.2 (1987), pp. 93–98.

[90] W. Gille. “The chord length distributions of selected infinitely long geometric figures–connections to the field of small-angle scattering”. In: *Computational materials science* 22.3-4 (2001), pp. 318–332.

[91] W. Gille. *Particle and particle systems characterization: small-angle scattering (SAS) applications*. CRC Press, 2016.

[92] S. Giordano. “Electrical behaviour of a single crack in a conductor and exponential laws for conductivity in micro cracked solids”. In: *International Journal of Applied Electromagnetics and Mechanics* 26.1, 2 (2007), pp. 1–19.

[93] S. Giordano and L. Colombo. “Local elastic fields around cracks and their stress density of states”. In: *Physical Review B* 76.17 (2007), p. 174120.

[94] G.H. Goldsztein. “Bound on the yield set of fiber reinforced composites subjected to antiplane shear”. In: *Discrete & Continuous Dynamical Systems-B* 15.2 (2011), pp. 391–400.

[95] G.H. Goldsztein. “Effects of the Fibers’ Shape and Volume Fraction on the Strength of Ideally Plastic Fiber Reinforced Composites”. In: *SIAM Journal on Applied Mathematics* 72.3 (2012), pp. 713–724.

[96] A. Gray, E. Abbena, and S. Salamon. “Modern differential geometry of curves and surfaces with Mathematica”. In: (2006).

[97] A. Greco, D. Jeulin, and J. Serra. “The use of the texture analyser to study sinter structure: application to the morphology of calcium ferrites encountered in basic sinters of rich iron ores”. In: *Journal of Microscopy* 116.2 (1979), pp. 199–211.

[98] C. Gruescu, V. Monchiet, and D. Kondo. “Eshelby tensor for a crack in an orthotropic elastic medium”. In: *Comptes Rendus Mecanique* 333.6 (2005), pp. 467–473.

[99] H.S. Harutyunyan and V.K. Ohanyan. “Covariogram of a cylinder”. In: *Journal of Contemporary Mathematical Analysis* 49.6 (2014), pp. 366–375.

[100] Z. Hashin. “Analysis of composite materials–a survey”. In: *Journal of Applied Mechanics* 50.3 (1983), pp. 481–505.

[101] Z. Hashin. “Thermal expansion of polycrystalline aggregates: I. Exact analysis”. In: *Journal of the Mechanics and Physics of Solids* 32.2 (1984), pp. 149–157.

[102] R. Haslinger and R. Joynt. “Theory of percolative conduction in polycrystalline high-temperature superconductors”. In: *Physical Review B* 61.6 (2000), p. 4206.

[103] R. Hill. “A self-consistent mechanics of composite materials”. In: *Journal of the Mechanics and Physics of Solids* 13.4 (1965), pp. 213–222.

[104] C. Hoffman. “Geodesics in first passage percolation”. In: *The Annals of Applied Probability* 18.5 (2008), pp. 1944–1969.

[105] H. Horii and S. Nemat-Nasser. “Overall moduli of solids with microcracks: load-induced anisotropy”. In: *J. Mech. Phys. Solids* 31 (1983), pp. 155–171.

[106] C. D. Howard and C. M. Newman. “Euclidean models of first-passage percolation”. In: *Probability Theory and Related Fields* 108.2 (1997), pp. 153–170.

[107] Y. Huang and K. X. Hu. “Elastic moduli of a microcracked composite with spherical inclusions of cubic anisotropy”. In: *Composites science and technology* 50.2 (1994), pp. 149–156.

[108] D. A. Huse and C. L. Henley. “Pinning and roughening of domain walls in Ising systems due to random impurities”. In: *Physical review letters* 54.25 (1985), p. 2708.

[109] O Huseby, JF Thovert, and PM Adler. “Geometry and topology of fracture systems”. In: *Journal of Physics A: Mathematical and General* 30.5 (1997), p. 1415.

[110] M. I. Idiart, H. Moulinec, P. Ponte Castañeda, and P. Suquet. “Macroscopic behavior and field fluctuations in viscoplastic composites: second-order estimates versus full-field simulations”. In: *Journal of the Mechanics and Physics of Solids* 54.5 (2006), pp. 1029–1063.

[111] M. I. Idiart and P. Ponte Castañeda. “Estimates for two-phase nonlinear conductors via iterated homogenization”. In: *Proceedings of the Royal Society A: Mathematical, Physical and Engineering Sciences* 469.2153 (2013), p. 20120626.

[112] M.I. Idiart, F. Willot, Y.-P. Pellegrini, and P. Ponte Castañeda. “Infinite-contrast periodic composites with strongly nonlinear behavior: effective-medium theory versus full-field simulations”. In: *International Journal of Solids and Structures* 46.18 (2009), pp. 3365–3382.

[113] G.W. Jackson and D.F. James. “The permeability of fibrous porous media”. In: *The Canadian Journal of Chemical Engineering* 64.3 (1986), pp. 364–374.

[114] D. Jeulin. “Modèles de fonctions aléatoires multivariables”. In: *Sciences de la Terre* 30 (1991), pp. 225–256.

[115] D. Jeulin. “Modèles Morphologiques de Structures Aléatoires et de Changement d’Échelle”. Thèse de Doctorat d’État. PhD thesis. Université de Caen, 1991.

[116] D. Jeulin. “Power laws variance scaling of Boolean random varieties”. In: *Methodology and Computing in Applied Probability* 18.4 (2016), pp. 1065–1079.

[117] D. Jeulin, W. Li, and M. Ostoja-Starzewski. “On the geodesic property of strain field patterns in elastoplastic composites”. In: *Proceedings of the Royal Society A: Mathematical, Physical and Engineering Science* 464.2093 (2008), pp. 1217–1227.

[118] D. Jeulin, P. Monnaie, and F. Péronnet. “Gypsum morphological analysis and modeling”. In: *Cement and Concrete Composites* 23.2 (2001), pp. 299–311.

[119] V. John, I. Angelov, A. A. Öncül, and D. Thévenin. “Techniques for the reconstruction of a distribution from a finite number of its moments”. In: *Chemical Engineering Science* 62.11 (2007), pp. 2890–2904.

[120] M. E. Johnson. *Multivariate statistical simulation: A guide to selecting and generating continuous multivariate distributions*. John Wiley & Sons, 2013.

[121] M. Kachanov. “Effective elastic properties of cracked solids: critical review of some basic concepts”. In: *Applied Mechanics Reviews* 45.8 (1992), pp. 304–335.

[122] É. Kaeshammer, B. Erzar, S. Belon, F. Willot, P. Dokládal, J. Corbel, and L. Borne. “Étude expérimentale et numérique de la sensibilité de compositions énergétiques : influence de la microstructure et rôle de l’endommagement”. In: Colloque Mécamat, Aussois, France, January 22-26, 2018. `https://hal.archives-ouvertes.fr/hal-01678704`, accessed January 8, 2018. Aussois: Mécamat, 2018.

[123] M. Kardar and Y.-C. Zhang. “Scaling of directed polymers in random media”. In: *Physical review letters* 58.20 (1987), p. 2087.

[124] H. Kesten. “Percolation theory and first-passage percolation”. In: *The Annals of Probability* 15.4 (1987), pp. 1231–1271.

[125] J. R. Kolb and H. F. Rizzo. “Growth of 1,3,5-Triamino-2,4,6-Trinitrobenzene (TATB). I. Anisotropic thermal expansion.” In: *Propellants, Explosives, Pyrotechnics* 4.1 (1979), pp. 10–16.

[126] A. Koponen, D. Kandhai, E. Hellen, M. Alava, A. Hoekstra, M. Kataja, K. Niskanen, P. Sloot, and J. Timonen. “Permeability of three-dimensional random fiber webs”. In: *Physical Review Letters* 80.4 (1998), p. 716.

[127] N. Koudina, R.G. Garcia, J.F. Thovert, and P.M. Adler. “Permeability of three-dimensional fracture networks”. In: *Physical Review E* 57.4 (1998), p. 4466.

[128] N. Kowalski, L. Delannay, P. Yan, and J.-F. Remacle. “Finite element modeling of periodic polycrystalline aggregates with intergranular cracks”. In: *International Journal of Solids and Structures* 90 (2016), pp. 60–68.

[129] J. Kozeny. “Ueber kapillare leitung des wassers im boden”. In: *Sitzungsber Akad Wiss Wien* 136 (1927), pp. 271–306.

[130] D. Krajcinovic. “Damage mechanics”. In: *Mech. Mat.* 8 (1989), pp. 117–197.

[131] W. Kreher. “Residual stresses and stored elastic energy of composites and polycrystals”. In: *Journal of the Mechanics and Physics of Solids* 38.1 (1990), pp. 115–128.

[132] E. Kröner. “Bounds for effective elastic moduli of disordered materials”. In: *Journal of the Mechanics and Physics of Solids* 25.2 (1977), pp. 137–155.

[133] VI Kushch, SV Shmegera, and I Sevostianov. “SIF statistics in micro cracked solid: effect of crack density, orientation and clustering”. In: *International Journal of Engineering Science* 47.2 (2009), pp. 192–208.

[134] P.S. Lang, A. Paluszny, and R.W. Zimmerman. “Permeability tensor of three-dimensional fractured porous rock and a comparison to trace map predictions”. In: *Journal of Geophysical Research: Solid Earth* 119.8 (2014), pp. 6288–6307.

[135] C. Lantuéjoul. “Ergodicity and integral range”. In: *Journal of Microscopy* 161.3 (1991), pp. 387–403.

[136] N Laws. “A note on penny-shaped cracks in transversely isotropic materials”. In: *Mechanics of Materials* 4.2 (1985), pp. 209–212.

[137] R.A. Lebensohn, O. Castelnau, R. Brenner, and P. Gilormini. “Study of the antiplane deformation of linear 2D polycrystals with different microstructure”. In: *International Journal of Solids and Structures* 42 (2005), pp. 5441–5459.

[138] R.A. Lebensohn, Y. Liu, and P. Ponte Castañeda. “On the accuracy of the self-consistent approximation for polycrystals: comparison with full-field numerical simulations”. In: *Acta Materialia* 52 (2004), pp. 5347–5361.

[139] D-Ti Lee and FP Preparata. “Euclidean shortest paths in the presence of rectilinear barriers”. In: *Networks* 14.3 (1984), pp. 393–410.

[140] S. Lee. “The powerlaws of M and N in greedy lattice animals”. In: *Stochastic Processes and their Applications* 69 (1997), pp. 275–287.

[141] S. Levasseur, H. Welemane, and D. Kondo. “A microcracks-induced damage model for initially anisotropic rocks accounting for microcracks closure.” In: *Int. J. Rock Mech. & Mining Sci.* 77 (2015), pp. 122–132.

[142] V. M. Levin, M. I. Rakovskaja, and W. S. Kreher. “The effective thermoelectroelastic properties of microinhomogeneous materials”. In: *International Journal of Solids and Structures* 36.18 (1999), pp. 2683–2705.

[143] T. Lozano-Pérez and MA Wesley. “An algorithm for planning collision-free paths among polyhedral obstacles”. In: *Communications of the ACM* 22.10 (1979), pp. 560–570.

[144] O Mahmood, B Audoly, and S Roux. “Cracks in Tension-Field Elastic Sheets”. In: *Physical review letters* 121.14 (2018), p. 144301.

[145] M. Månsson and M. Rudemo. “Random patterns of nonoverlapping convex grains”. In: *Advances in Applied Probability* 34.4 (2002), pp. 718–738.

[146] V. Mantič, A. Barroso, and F. París. “Singular elastic solutions in anisotropic multimaterial corners: applications to composites”. In: *Mathematical methods and models in composites*. 2014, pp. 425–495.

[147] V. Mantič, F. Paris, and J. Canas. “Stress singularities in 2D orthotropic corners”. In: *International Journal of Fracture* 83.1 (1997), pp. 67–90.

[148] J. J. Martin, W. L. McCabe, and C. C. Monrad. “Pressure drop through stacked spheres. Effect of orientation”. In: *Chemical Engineering Progress* 47 (1951).

[149] N.S. Martys, S. Torquato, and D.P. Bentz. “Universal scaling of fluid permeability for sphere packings”. In: *Physical Review E* 50.1 (1994), p. 403.

[150] D. Masson, B. Abdallah, F. Willot, D. Jeulin, E. Mercadelli, A. Sanson, A. Chesnaud, and A. Thorel. “Morphological modeling of a metal foam SOFC configuration”. In: *ECS Transactions*. Vol. 68. 1. Online at `https://hal.archives-ouvertes.fr/hal-01142056`. Conference on Electrochemical Energy Conversion & Storage with SOFC-XIV, Glasgow, Scotland, July 26-31, 2015. 2015, pp. 2951–2960.

[151] R. Masson. “New explicit expressions of the Hill polarization tensor for general anisotropic elastic solids”. In: *International Journal of Solids and Structures* 45.3-4 (2008), pp. 757–769.

[152] G. Matheron. *Les variables régionalisées et leur estimation: une application de la théorie des fonctions aléatoires aux sciences de la nature*. Masson, Paris, 1965.

[153] G. Matheron. *Eléments pour une théorie des milieux poreux*. Masson, Paris, 1967.

[154] G. Matheron. “Polyédres poissoniens et ensembles semi-markoviens”. In: *Advances in Applied Probability* 4.3 (1972), pp. 508–541.

[155] G. Matheron. “Random sets theory and its applications to stereology”. In: *Journal of Microscopy* 95.1 (1972), pp. 15–23.

[156] G. Matheron. *Random sets and integral geometry*. New-York: Wiley, 1975.

[157] G. Matheron. *L'émergence de la loi de Darcy.* École Nationale Supérieure des Mines, Note Géostatistique No. 592, `http://www.cg.ensmp.fr/bibliotheque/public/MATHERON_Rapport_00216.pdf`, accessed August 21, 2015. 1979.

[158] G. Matheron and J. Serra. *Image analysis and mathematical morphology.* London: Academic Press, 1982.

[159] Georges Matheron. *Estimating and choosing: an essay on probability in practice.* Springer Science & Business Media, 1989.

[160] J.L. Meijering. "Interface area, edge length, and number of vertices in crystal aggregates with random nucleation". In: *Philips Res. Rep.* 8 (1953), pp. 270–290.

[161] P. Meunier and E. Villermaux. "Van Hove singularities in probability density functions of scalars". In: *Comptes Rendus Mécanique* 335.3 (2007), pp. 162–167.

[162] J.-C. Michel, H. Moulinec, and P. Suquet. "A computational method based on Augmented Lagrangians and Fast Fourier Transforms for composites with high contrast". In: *Computer Modelling in Engineering & Sciences* 1.2 (2000), pp. 79–88.

[163] J.-C. Michel, H. Moulinec, and P. Suquet. "A computational scheme for linear and non-linear composites with arbitrary phase contrast". In: *International Journal of Numerical Methods in Engineering* 52.1–2 (2001), pp. 139–160.

[164] C. Miehe, M. Hofacker, and F. Welschinger. "A phase field model for rate-independent crack propagation: Robust algorithmic implementation based on operator splits". In: *Computer Methods in Applied Mechanics and Engineering* 199.45-48 (2010), pp. 2765–2778.

[165] R.E. Miles. "On the homogeneous planar Poisson point process". In: *Mathematical Biosciences* 6 (1970), pp. 85–127.

[166] R.E. Miles. "The random division of space". In: *Advances in applied probability* (1972), pp. 243–266.

[167] G. W. Milton. *The Theory of Composites.* Cambridge: Cambridge Univ. Press, 2002.

[168] J Mitchell. *Shortest rectilinear paths among obstacles.* Tech. rep. Technical Report, Dept. of Operations Research, Stanford University. 1987.

[169] I. S. Molchanov. *Theory of random sets.* Vol. 19. 2. Springer, 2005.

[170] IS Molchanov. "A limit theorem for scaled vacancies of the Boolean model". In: *Stochastics: An International Journal of Probability and Stochastic Processes* 58.1-2 (1996), pp. 45–65.

[171] J. Møller and C. Díaz-Avalos. "Structured spatio-temporal shot-noise Cox point process models, with a view to modelling forest fires". In: *Scandinavian Journal of Statistics* 37.1 (2010), pp. 2–25.

[172] V. Monchiet, G. Bonnet, and G. Lauriat. "A FFT-based method to compute the permeability induced by a Stokes slip flow through a porous medium". In: *Comptes Rendus Mécanique* 337.4 (2009), pp. 192–197.

[173] V. Monchiet, C. Gruescu, O. Cazacu, and D. Kondo. "A micromechanical approach of crack-induced damage in orthotropic media: application to a brittle matrix composite". In: *Engrg. Fract. Mech.* 83 (2012), pp. 40–53.

[174] H. Moulinec and P. Suquet. “A fast numerical method for computing the linear and non linear mechanical properties of the composites”. In: *Comptes Rendus de l’Académie des Sciences Série II* 318 (1994), pp. 1417–1423.

[175] V.V. Mourzenko, J.F. Thovert, and P.M. Adler. “Macroscopic permeability of three-dimensional fracture networks with power-law size distribution”. In: *Physical Review E* 69.6 (2004), p. 066307.

[176] T. Mura. *Micromechanics of defects in solids.* The Hague: Martinus Nijhoff Publishers, 1982.

[177] A. Nabovati, E.W. Llewellin, and C.M. Sousa A. “A general model for the permeability of fibrous porous media based on fluid flow simulations using the lattice Boltzmann method”. In: *Composites Part A: Applied Science and Manufacturing* 40.6 (2009), pp. 860–869.

[178] R. G. Naum and C. K. Jun. “Thermal expansion of polycrystalline graphite.” In: *Journal of Applied Physics* 41 (1970), pp. 5092–5095.

[179] M. Neumann, B. Abdallah, L. Holzer, F. Willot, and V. Schmidt. “Stochastic 3D modeling of three-phase microstructures for the prediction of transport properties in solid oxide fuel cells”. In: *Transport in Porous Media* 128.1 (2019), pp. 179–200.

[180] M. Neumann, O. Stenzel, F. Willot, L. Holzer, and V. Schmidt. “Quantifying the influence of microstructure on effective conductivity and permeability: virtual materials testing”. In: *International Journal of Solids and Structures* (2019). Accepted March 23. DOI: 10.1016/j.ijsolstr.2019.03.028.

[181] A.M. Oberman, R. Takei, and A. Vladimirsky. “Homogenization of metric Hamilton–Jacobi equations”. In: *Multiscale Modeling & Simulation* 8.1 (2009), pp. 269–295.

[182] M. Ortiz. “A constitutive theory for the inelastic behavior of concrete”. In: *Mechanics of materials* 4.1 (1985), pp. 67–93.

[183] CH Papadimitriou. “Shortest-path motion”. In: *International Conference on Foundations of Software Technology and Theoretical Computer Science.* Springer. 1986, pp. 144–153.

[184] C. Pélissou, J. Baccou, Y. Monerie, and F. Perales. “Determination of the size of the representative volume element for random quasi-brittle composites”. In: *International Journal of Solids and Structures* 46.14-15 (2009), pp. 2842–2855.

[185] Y.-P. Pellegrini. “Field distributions and effective-medium approximation for weakly nonlinear media”. In: *Physical Review B* 61.14 (2000), p. 9365.

[186] V. Pensée and D. Kondo. “Micromechanics of anisotropic brittle damage: comparative analysis between a stress based and a strain based formulation.” In: *Mech. Mat.* 35 (2003), pp. 747–741.

[187] C. Peyrega, D. Jeulin, C. Delisée, and J. Malvestio. “3D morphological modelling of a random fibrous network”. In: *Image Analysis & Stereology* 28 (2009), pp. 129–141.

[188] G. Pijaudier-Cabot and Bazant Z. P. “Nonlocal damage theory.” In: *J. Engrg. Mech.* 113 (1987), pp. 1512–1533.

[189] A. N. B. Poliakov, H. J. Herrmann, Y. Y. Podladchikov, and S. Roux. "Fractal plastic shear bands". In: *Fractals* 2.4 (1994), pp. 567–581.

[190] P. Ponte Castañeda. "Second-order theory for nonlinear dielectric composites incorporating field fluctuations". In: *Physical Review B* 64.21 (2001), p. 214205.

[191] P. Ponte Castañeda. "Second-order homogenization estimates for nonlinear composites incorporating field fluctuations. II – Applications". In: *Journal of the Mechanics and Physics of Solids* 50.4 (2002), pp. 759–782.

[192] P. Ponte Castañeda and P. Suquet. "Nonlinear composites". In: *Advances in applied mechanics*. Vol. 34. Elsevier, 1997, pp. 171–302.

[193] P. Ponte Castañeda and P. Suquet. "Nonlinear composites". In: *Advances in applied mechanics*. Vol. 34. Elsevier, 1998, pp. 171–302.

[194] P. Ponte Castañeda and J. R. Willis. "The effect of spatial distribution on the effective behavior of composite materials and cracked media". In: *Journal of the Mechanics and Physics of Solids* 43.12 (1995), pp. 1919–1951.

[195] J. A. Quintanilla and R. M. Ziff. "Asymmetry in the percolation thresholds of fully penetrable disks with two different radii". In: *Physical Review E* 76.5 (2007), p. 051115.

[196] J Quintanilla, S Torquato, and RM Ziff. "Efficient measurement of the percolation threshold for fully penetrable discs". In: *Journal of Physics A: Mathematical and General* 33.42 (2000), p. L399.

[197] F. Rabette, H. Trumel, and F. Willot. "Modélisation multiéchelle par champ de phase de la microfissuration d'un polycristal organique de forte anisotropie cristalline par FFT". In: Colloque National en Calcul des Structures, Giens, France, May 13-17, 2019. Presqu'île de Giens: Computational Structural Mechanics Association, 2019.

[198] C. Redenbach and I. Vecchio. "Statistical analysis and stochastic modelling of fibre composites". In: *Composites Science and Technology* 71.2 (2011), pp. 107–112.

[199] C. Redenbach, O. Wirjadi, S. Rief, and A. Wiegmann. "Modeling a ceramic foam for filtration simulation". In: *Advanced Engineering Materials* 13.3 (2011), pp. 171–177.

[200] F. Richardson J. and N. Zaki W. "The sedimentation of a suspension of uniform spheres under conditions of viscous flow". In: *Chemical Engineering Science* 3.2 (1954), pp. 65–73.

[201] S. Rief, A. Latz, and A. Wiegmann. "Computer simulation of Air Filtration including electric surface charges in three-dimensional fibrous micro structures". In: *Filtration* 6.2 (2006), pp. 169–172.

[202] K. Robb, O. Wirjadi, and K. Schladitz. "Fiber orientation estimation from 3D image data: Practical algorithms, visualization, and interpretation". In: 7th *International Conference on Hybrid Intelligent Systems (HIS), 2007*. 2007, pp. 320–325.

[203] B. W. Rosen and Z. Hashin. "Effective thermal expansion coefficients and specific heats of composite materials". In: *International Journal of Engineering Science* 8.2 (1970), pp. 157–173.

[204] R. Rosenzweig, V. V. Mourzenko, J.-F. Thovert, and P. M. Adler. "Solid matrix partition by fracture networks". In: *Physical Review E* 90.2 (2014), p. 022407.

[205] S. Roux and D. François. “A simple model for ductile fracture of porous materials”. In: *Scripta Metallurgica et Materialia* 25.5 (1991), pp. 1087–1092.

[206] S. Roux and A. Hansen. “Perfect plasticity in a random medium”. In: *Journal de Physique II* 2.5 (1992), pp. 1007–1021.

[207] J. Rubinstein and S. Torquato. “Diffusion-controlled reactions: Mathematical formulation, variational principles, and rigorous bounds”. In: *The Journal of Chemical Physics* 88.10 (1988), pp. 6372–6380.

[208] J. Rubinstein and S. Torquato. “Flow in random porous media: mathematical formulation, variational principles, and rigorous bounds”. In: *Journal of fluid mechanics* 206 (1989), pp. 25–46.

[209] D. Ruer. “Méthode vectorielle d’analyse de la texture”. PhD thesis. France: Université de Metz, 1976.

[210] E. H. Saenger, O. S. Krüger, and S. A. Shapiro. “Effective elastic properties of randomly fractured soils: 3D numerical experiments”. In: *Geophysical Prospecting* 52.3 (2004), pp. 183–195.

[211] P. N. Sævik, I. Berre, M. Jakobsen, and M. Lien. “A 3D computational study of effective medium methods applied to fractured media”. In: *Transport in porous media* 100.1 (2013), pp. 115–142.

[212] P. N. Sævik, M. Jakobsen, M. Lien, and I. Berre. “Anisotropic effective conductivity in fractured rocks by explicit effective medium methods”. In: *Geophysical Prospecting* 62.6 (2014), pp. 1297–1314.

[213] M. Schneider, D. Wicht, and T. Böhlke. “On polarization-based schemes for the FFT-based computational homogenization of inelastic materials”. In: *Computational Mechanics* (2019), pp. 1–23.

[214] R. Schneider. *Convex bodies: the Brunn–Minkowski theory*. 151. Cambridge university press, 2014.

[215] R. Schneider and W. Weil. *Stochastic and integral geometry*. Springer-Verlag, Berlin, Heidelberg, 2008.

[216] J. Serra. “The Boolean model and random sets”. In: *Computer Graphics and Image Processing* 12.2 (1980), pp. 99–126.

[217] J. Serra. “The Boolean model and random sets”. In: *Image Modeling*. Academic Press, 1981, pp. 343–370.

[218] J. Serra and F. Willot. “Special topic on multiscale modeling of granular media: a tribute to Prof. Dominique Jeulin”. In: *Image Analysis & Stereology* 38.1 (2019), pp. 1–2.

[219] J.A. Sethian. “A fast marching level set method for monotonically advancing fronts”. In: *Proceedings of the National Academy of Sciences* 93.4 (1996), pp. 1591–1595.

[220] I. Sevostianov and M. Kachanov. “Explicit cross-property correlations for anisotropic two-phase composite materials”. In: *Journal of the Mechanics and Physics of Solids* 50.2 (2002), pp. 253–282.

[221] I. Sevostianov and V. Kushch. “Effect of pore distribution on the statistics of peak stress and overall properties of porous material”. In: *International Journal of Solids and Structures* 46.25-26 (2009), pp. 4419–4429.

[222] I. Sevostianov, N. Yilmaz, V. Kushch, and V. Levin. “Effective elastic properties of matrix composites with transversely-isotropic phases”. In: *International Journal of Solids and Structures* 42.2 (2005), pp. 455–476.

[223] M.M. Shahmardan, M. Nazari, M. Khaksar, and M. Khatib. “A New Mathematical Model for Permeability of Composites”. In: *Journal of Solid Mechanics Vol* 5.4 (2013), pp. 371–379.

[224] J. A. Shohat and J. D. Tamarkin. *The problem of moments*. Vol. 1. American Mathematical Soc., 1943.

[225] I.J.C. Sillamoni and M.I. Idiart. “Nonlinear ionic transport through microstructured solid electrolytes: homogenization estimates”. In: *Modelling and Simulation in Materials Science and Engineering* 24.7 (2016), p. 075008.

[226] D. Stoyan, W. S. Kendall, and J. Mecke. *Stochastic geometry and its applications*. Second edition. John Wiley & Sons, Chichester, 1995.

[227] G. Strang. “Maximal flow through a domain”. In: *Mathematical Programming* 26.2 (1983), pp. 123–143.

[228] HS Sukiasian and W Gille. “Relation between the chord length distribution of an infinitely long cylinder and that of its base”. In: *Journal of mathematical physics* 48.5 (2007), p. 053305.

[229] C.T. Sun and Z.H. Jin. *Fracture Mechanics*. Vol. 10. Academic Press, 2012.

[230] P. Suquet and H. Moulinec. “Mathematics of multiscale materials”. In: *IMA Lecture Notes 99*. Ed. by K.M. Golden, G.R. Grimmett, R.D. James, G.W. Milton, and P.N. Sen. Springer-Verlag, 1998. Chap. Numerical simulation of the effective elastic properties of a class of cell materials.

[231] J. Talbot, G. Tarjus, P.R. Van Tassel, and P. Viot. “From car parking to protein adsorption: an overview of sequential adsorption processes”. In: *Colloids and Surfaces A: Physicochemical and Engineering Aspects* 165.1-3 (2000), pp. 287–324.

[232] C.K.W. Tam. “The drag on a cloud of spherical particles in low Reynolds number flow”. In: *Journal of Fluid Mechanics* 38.03 (1969), pp. 537–546.

[233] A. Tamayol and M. Bahrami. “Analytical determination of viscous permeability of fibrous porous media”. In: *International Journal of Heat and Mass Transfer* 52.9 (2009), pp. 2407–2414.

[234] M.L.R. Thomas, D.B. Ingham, and M. Pourkashanian. “Prediction of the Permeability of Fibrous Porous Media Using the Lattice Boltzmann Method in Conjuction with Coarse Numerical Lattices”. In: *Open Transport Phenomena Journal* 2 (2010), pp. 80–89.

[235] S. Torquato. “Microstructure characterization and bulk properties of disordered two-phase media”. In: *Journal of Statistical Physics* 45.5–6 (1986), pp. 843–873.

[236] S. TORQUATO. “Nearest-neighbor statistics for packings of hard spheres and disks”. In: *Physical Review E* 51.4 (1995), p. 3170.

[237] S. TORQUATO. “Effect of dimensionality on the continuum percolation of overlapping hyperspheres and hypercubes”. In: *The Journal of chemical physics* 136.5 (2012), p. 054106.

[238] S. TORQUATO and B. LU. “Rigorous bounds on the fluid permeability: effect of polydispersivity in grain size”. In: *Physics of Fluids A: Fluid Dynamics (1989-1993)* 2.4 (1990), pp. 487–490.

[239] L. VAN HOVE. “The occurrence of singularities in the elastic frequency distribution of a crystal”. In: *Physical Review* 89.6 (1953), p. 1189.

[240] H. WANG, A. PIETRASANTA, D. JEULIN, F. WILLOT, M. FAESSEL, Sorbier L., and M. MOREAUD. “Modeling of mesoporous alumina microstructure by 3D random models of platelets”. In: *Journal of Microscopy* 260.3 (2015), pp. 287–301.

[241] E. W. WEISSTEIN. *Polylogarithm.* From MathWorld–A Wolfram Web Resource. Online at `http://mathworld.wolfram.com/Polylogarithm.html`. Accessed 2019, Feb. 21.

[242] E.W. WEISSTEIN. *Complete Elliptic Integral of the First Kind.* Online at `mathworld.wolfram.com/CompleteEllipticIntegraloftheFirstKind.html`, accessed August 4, 2015.

[243] E.W. WEISSTEIN. *Elliptic Integral of the Second Kind.* Online at `http://mathworld.wolfram.com/EllipticIntegraloftheSecondKind.html`, accessed August 4, 2015.

[244] EW WEISSTEIN. *CRC concise encyclopedia of mathematics.* Chapman and Hall/CRC, 2002.

[245] A. WIEGMAN. *Computation of the permeability of porous materials from their microstructure by FFF-Stokes.* `http://kluedo.ub.uni-kl.de/files/1984/bericht129.pdf`, accessed 22 July 2015. 2007.

[246] M. L. WILLIAMS. “On the stress distribution at the base of a stationary crack”. In: *Journal of Applied Mechanics* 24 (1957), pp. 109–114.

[247] J.R. WILLIS. “Bounds and self-consistent estimates for the overall properties of anisotropic composites”. In: *Journal of the Mechanics and Physics of Solids* 25 (1977), pp. 185–202.

[248] F. WILLOT. “Contribution à l’étude théorique de la localisation plastique dans les poreux”. PhD thesis. École Polytechnique, 2007.

[249] F. WILLOT. “Fourier-based schemes for computing the mechanical response of composites with accurate local fields”. In: *Comptes Rendus Mécanique* 343.3 (2015), pp. 232–245.

[250] F. WILLOT. “The power laws of geodesics in some random sets with dilute concentration of inclusions”. In: *Lecture Notes in Computer Science* 9082 (2015), pp. 535–546.

[251] F. WILLOT. “Mean covariogram of cylinders and applications to Boolean random sets”. In: *Journal of Contemporary Mathematical Analysis* 52.6 (2017), pp. 305–315.

[252] F. WILLOT. “The effective conductivity of strongly nonlinear media: the dilute limit”. In: *International Journal of Solids and Structures* (2019). Accepted June 6. DOI: `10.1016/j.ijsolstr.2019.06.006`.

[253] F. WILLOT, B. ABDALLAH, and D. JEULIN. “The permeability of Boolean sets of cylinders”. In: *Oil & Gas Science and Technology* 71.2 (2016).

[254] F. Willot, B. Abdallah, and Y.-P. Pellegrini. “Fourier-based schemes with modified Green operator for computing the electrical response of heterogeneous media with accurate local fields”. In: *International Journal for Numerical Methods in Engineering* 98.7 (2014), pp. 518–533.

[255] F. Willot, F. Bignonnet, A. Wiegmann, L. Chen, and C. Wagner. *Fourier-based schemes for computing the permeability of porous media.* In preparation. 2019.

[256] F. Willot, R. Brenner, and H. Trumel. “Elastostatic field distributions in polycrystals and cracked media”. In: *Philosophical Magazine* (2019). Submitted May 9, accepted November 25.

[257] F. Willot and S. Forest. *Physics & Mechanics of Random Media: from Morphology to Material Properties. A tribute to Dominique Jeulin's contributions to science, research and teaching.* International Workshop in honor of D. Jeulin. Saint-Pierre d'Oléron, France, June 17–22. ISBN 2356715290. Paris: Presses des Mines, 2018.

[258] F. Willot and Y.-P. Pellegrini. “Fast Fourier Transform computations and build-up of plastic deformation in 2D, elastic-perfectly plastic, pixelwise-disordered porous media”. In: *D. Jeulin, S. Forest (eds), “Continuum Models and Discrete Systems CMDS 11”.* Online at `https://arxiv.org/abs/0802.2488`. Paris: École des Mines, 2008, pp. 443–449.

[259] F. Willot, Y.-P. Pellegrini, M.I. Idiart, and P. Ponte Castañeda. “Effective-medium theory for infinite-contrast two-dimensionally periodic linear composites with strongly anisotropic matrix behavior: dilute limit and crossover behavior”. In: *Physical review B* 78.10 (2008), p. 104111.

[260] F. Willot, Y.-P. Pellegrini, and P. Ponte Castañeda. “Localization of elastic deformation in strongly anisotropic, porous, linear materials with periodic microstructures: exact solutions and dilute expansions”. In: *Journal of the Mechanics and Physics of Solids* 56.4 (2008), pp. 1245–1268.

[261] F. Willot, H. Trumel, and D. Jeulin. “The thermoelastic response of cracked polycrystals with hexagonal symmetry”. In: *Philosophical Magazine* 99.5 (2019), pp. 606–630.

[262] Wolfram Research, Inc. *Mathematica software version* 11.3. Champaign, Illinois. 2018.

[263] K. Yazdchi, S. Srivastava, and S. Luding. “Microstructural effects on the permeability of periodic fibrous porous media”. In: *International Journal of Multiphase Flow* 37.8 (2011), pp. 956–966.

[264] Y. B. Yi and K. Esmail. “Computational measurement of void percolation thresholds of oblate particles and thin plate composites”. In: *Journal of Applied Physics* 111.12 (2012), p. 124903.

[265] Y. B. Yi and E. Tawerghi. “Geometric percolation thresholds of interpenetrating plates in three-dimensional space”. In: *Physical Review E* 79.4 (2009), p. 041134.

[266] H. Zhao. “A fast sweeping method for eikonal equations”. In: *Mathematics of computation* 74.250 (2005), pp. 603–627.

[267] Q.-Z. Zhu, J. F. Shao, and D. Kondo. “A micromechanics-based thermodynamic formulation of isotropic damage with unilateral and friction effects.” In: *Eur. J. Mech. A/Solids* 30 (2011), pp. 316–325.

Part IV

Addenda

Appendix A

Summary of recent activities (2016–2019)

This Appendix contains a brief description of my main achievements conducted in three topics of research: micromechanical modeling of polycrystals, probabilistic models of microstructures and Fourier-based methods.

Micromechanical modeling of polycristals

Several studies are currently being conducted regarding the modeling of a 1,3,5-triamino-2,4,6-trinitrobenzen (TATB) polycrystal containing an amorphous thermoplastic polymer used as binder, and to its thermomechanical response, of a quasi-brittle nature [J11]. The material's response is strongly dependent on damage, irreversible deformation, viscoelastic mechanisms and thermal dilation (internship works of A. Ambos, and thesis of J.-B. Gasnier). The material is well characterized at the macroscopic scale, however its behavior is not well understood, although the main mechanisms have been qualitatively identified: inter and transgranular microcracking, viscoelastcicity due to the binder, and inelastic deformation of the TATB. The material is strongly dependent on temperature and stress triaxiality.

A numerical Fourier-based method has been devised [J10] making use of virtual microstructures [J27] representative of the main morphological features of the material (grains size distribution and aspect ratio, lack of geometrical convexity). In the linear thermoelastic case [J11], the important effect of crystal elastic anisotropy of the main phase, the TATB, has been highlighted. Transgranular micro-cracking along the graphitic plane of the monocrystal has been confirmed making use of SEM images, and explains the decrease of the thermal expansion coefficient during cooling-heating thermal cycles. Intergranular cracking, on the other hand, must be present in the material in its initial state [J11].

This work is currently being extended to the modeling of damage, crack initiation and propagation in polycrystals, making use of a numerical approach that combines phase-field and Fourier-based methods [P6] (thesis of F. Rabette). The role of damage and its effect on the macroscopic response of the polycrystal is investigated, in particular during thermal cycles. Image analysis tools have also been developed to assess how intergranular and transgranular micro-cracks propagate through heterogeneous structures.

Modeling of heterogeneous structures

Probabilistic models have recently been developed to represent a variety of heterogeneous microstructures. This includes N-phases random materials [J16] in the context of a European project devoted to fuel cell applications [P15] (thesis of B. Abdallah). The method proposed, which makes used of underlying independent random sets, has been compared to techniques developed elsewhere for the same type of materials, and based on graph-induced random sets [J2, J3]. We compared, in particular, the ability of the virtual microstructures to predict a variety of behavior such as conductivity or permeability, based on SEM images.

A method based on a mixed Boolean-tesselation random structure has been developed to model cold-spray coatings used in materials made for the aeronautical industry [J9] (thesis of V. Bortolussi), with funding from US Air Force. In this study as in others [J13, J18, C1, C2], use is made of automatic images segmentation methods.

Mesoporous structures for catalysis applications have been studied, making use of transmission electron microscopy and porosimetry curves to characterize the multiscale arrangement of alumina platelets (thesis of H. Wang). The two experimental techniques, transmission electron microscopy and porosimetry, have been modeled numerically to infer the material's structure [J14, J12].

Spectral methods

Fourier-based numerical methods have been proposed to predict the viscoelastic behavior of composites in the time-harmonic regime, in heterogeneous media [J18]. Fourier techniques that improve on the field discretization, using specific Green operators specifically adapted to the voxel grid, have been devised [J29]. The Fourier Fortran code has been used at the TSUBAME Japanese cluster to compute the viscoelastic response of virtual models of rubber at a very large scale, to carry out microstructure optimization (about 4 000 problems containing $\sim$ one billion degrees of freedom) [P11]. Learning methods and data mining have been used to infer the main microstructural characteristics. Similar approaches are presently conducted in the context of L. Lacourt's [P4, P10] and É. Kaeshammer's thesis [P9, P2, M2].

Appendix B

Curriculum Vitae

François Willot
École des Mines ParisTech
– Centre for Mathematical Morphology
35 rue St-Honoré, 77300 Fontainebleau
– Centre for Materials P. M. Fourt
63–65 rue Henry Desbruères
BP 87 91003 Évry

Chargé de Recherche
`francois.willot@ensmp.fr`
Tel.: +33 (0)1 64 69 48 07
`www.cmm.mines-paristech.fr/~willot`
ORCID: `0000-0003-1544-6550`[1]
IdHAL: `francoiswillot`[2]

Personal details Born August 1977 (42 years old). French nationality, married. Father of a 4-years old little girl.

Curriculum

- 2018-on: associate researcher at *Centre for Materials, Mines ParisTech*.

- 2011-on: chargé de recherche at *Centre for Mathematical Morphology, Mines ParisTech*. Main research topics: integral geometry, stereology, probabilistic modeling of random structures, physics and mechanics of heterogeneous media, homogenization theories, Fourier-based numerical methods.

- 2008-2010: tenure-track at *Centre for Mathematical Morphology, école des Mines, Paris*.

- 2007: Post-doctoral position. *Department for Mechanical Engineering and Applied Mechanics*, University of Pennsylvania.

- 2003-2007: PhD thesis "Plastic localization in disordered and periodic porous materials", Laboratoire de Mécanique et de Structures, école Polytechnique & Département de Physique Théorique et Appliqué, Commissariat à l'énergie atomique. Thesis directors: P. Ponte Castañeda, Y.-P. Pellegrini.

- 2002: research internship in nonlinear homogeneisation. *Département de Physique Théorique et Appliqué*, Commissariat à l'énergie atomique.

- Previous research internships: *Laboratoire d'informatique*, École Polytechnique (wave equation stabilization, 2002); *Centre de Mathématique et de leurs applications*, ENS Cachan (fluid mechanics, 2001); *Institut de Mathématiques de Luminy* (finite transductors, 2000); *Centre de Mathématique et de leurs applications*, ENS Cachan (Sturm polynomials, 1999).

Education

- 2007: PhD degree, École Polytechnique, in mechanics, "très honorable avec félicitations du jury". Jury: S. Roux, P. Suquet, M. Bornert & P. Gilormini.

- 2002-2003: Diplôme d'études approfondies (∼ research master), École Normale Supérieure de Cachan.

- 1998-2002: Engineering diploma, École Centrale, Lille. Licence of Mathematics, Lille 3 University.

Scientific responsibilities

- 2019-on: responsible of the ECMI (European Consortium of Mechanics and Industry) *Special Interest Group* "Shape and size in medecine and material science" together with J. Angulo & L. Bonilla. URL: `https://ecmiindmath.org/special-interest-groups/shape-and-size-in-medicine-biotechnology-and-materials-science/`.

- Responsible for the "Mécamat" (scientific association) working group "Probabilistic approaches in Mechanics of Materials". Workshops organized in Reims, 2012; S^{t}-Martin d'Hères, 2013; Paris, May 2015; Paris, Dec. 2015; Aussois, 2018.

- Member of the organization comitte of the Mécamat/SF2M (Société française de Mécanique) "Matériaux numériques" from 2016.

- Responsible of the topic "microstructure modeling and analytical methods" for the GDR (CNRS working group) on fibrous media "3MF" (2013-2015) and "MECAFIB" (2018-on).

- Organization of the Euromech symposium "Stochastic & Material Mechanics" (EMMC14, Göteborg, Sweden, 2014, co-chair S. Brisard) and other symposia at EMMC15 (Bruxelles, 2016, co-chair R. Cottereau) et EMMC16 Nantes (2018, co-chair R. Cottereau). Organization of a symposium in Madrid (EMMC17) in 2020 planed.

- Oganisation (together with other researchers) of the symposium "Numerical materials" in Lille, CFM (2017). Organization of the colloquium "Comportement Mécanique", at the conference Matériaux 2014 (Montpellier) and of two colloquia "Endommagement et rupture" and "Matériaux numériques" in Strasbourg (2018). Symposium on "Fourier methods" at ECCOMAS (Crete) in 2015.

- 2018: organization of the international workshop held in honor of D. Jeulin in Oléron (2018), bringing together about 50 researchers (see `cmm.ensmp.fr/~willot/PMRM`).

- 2018-2019: invited editor of *International Journal of Solids and Structures* (Elsevier)

- 2018-2019: invited editor of *Image Analysis & Stereology* (ISSIA).
- Reviewer for Proceedings A (Royal Society), Int. J. of Sol. And Struct. (Elsevier), Comp. Meth. In Appl. Mech. And Eng. (Elsevier), Int. J. for Numer. Meth. In Engng (John Wiley), Phil. Mag. (Taylor and Francis), Engng Comput. (Emerald), J. of Appl. Crystallography (IUCR), Comput. Mat. Sc. (Elsevier), CRC Press Book, Colloids & Surfaces A (Elsevier) and others.
- Reviewer of research projects for ANR (French national research agency) and for the Czech National Foundation.
- Examinateur in PhD jurys for B. Osman-Hoch & D. Komlan Sénam's thesis.
- Invited speaker at EUROMECH 559 (multiscale computational methods, Eindhoven, 2015).
- Editor together with S. Forest of the book "Physics & Mechanics of Random Media: from Morphology to Material Properties. A tribute to Dominique Jeulin's contributions to science, research and teaching", Presses des Mines, Paris, 2018.
- 2008-2012: co-animation with D. Jeulin of the working group "Nanomatériaux" at École des Mines (collaboration for grant applications and teaching).

Involvement in research projects As main contributor:

- Project in collaboration with CEA Gramat (2018)
- Project in collaboration with CEA Le Ripault (2018)
- Project in collaboration with L'Oréal (2016, 2017)
- Project in collaboration with US Air Force (2016)
- Project in collaboration with CEA Le Ripault (2014)
- Project in collaboration with CERIB (2013)
- Carnot Mines (2012)

Participation to various other projects, built with the Centre of Materials, and notably the CEA Valduc (2017), CERN (2016). In collaboration with the Process and surfaces team at centre of materials (A. Thorel, M. jeandin, A. Chesnaud, F. Delloro): european projects on fuel cells (2014) and ANR on colors in paintings (2014), cold-spray modeling (2017).

Teaching

- 2013-2019: organization of the one-week course in Mines ParisTech, in English "Physics and Mechanics of Random Media", for PhD students and to students from the "Athens" european university network. The courses include training session using Fourier methods, linear and nonlinear homogenization theory, and models of random structures.

- 2018-2019: one-week course “option ingénierie et dynamique des systèmes complexes” (organized by D. Ryckelynck and É. Hachem). Participation on a one-week course at École des Mines de Paris (together with H. Proudhon and B. Figliuzzi).
- 2017-2019: PSL master courses “Énergies” `www.psl.eu/formation/master-energie`
- 2014-2019: specialized courses on nanomaterials (organized by J.-F. Hochepied). Course on homogeneisation.
- 2016-2019: PSL master courses “Dynamique et Mécanique des Structures” (organized by F. Azzouz).
- 2011-2017: ESIEE engineering school. Courses on MPI code parallelization.
- 2015: doctoral courses at École des Ponts. Probabilistic modeling in mechanics.
- Various other one-off courses: “Mécanique des matériaux biosourcés” (Aussois, Colloque Mécamat, 2014); “Uncertainty management in Computational Materials Science” (MAI, ÉDF Renardières, 2016); “Random structures and homogenization” (Polytechnique et IFPEN, Rueil-Malmaison, 2018).

Thesis supervision

Defenses held All PhD students have published their works in scientific journals (see Sec. C). Except stated otherwise, the thesis doctoral school is École doctorale ED 432 “Sciences et Métiers de l’ingénieur” which encompasses Arts & métiers, Mines ParisTech and CNAM.

- Jean-Baptiste Gasnier (2015-2017, held in 2017): Étude du comportement thermo-mécanique et de l’endommagement d’un matériau énergétique granulaire par méthodes de Fourier. Thesis director: J. Angulo.
- Vincent Bortolussi (2014-2016, held in 2016) : Étude expérimentale et numérique de la conductivité de revêtements composites métal-polymère déposés par projection dynamique par gaz froid sur substrat composite à matrice organique. Thesis director: M. Jeandin.
- Haisheng Wang (2014-2016, held in 2016) : Morphological modelisation and transport properties of mesoporous alumina. Directeur de thèse : D. Jeulin.
- Enguerrand Couka (2013-2015, held in 2015): Modélisation des propriétés optiques de peintures par microstructures aléatoires et calculs FFT. Thesis director: D. Jeulin.
- Bassam Abdallah (2013-2015, held in 2015): Analyse morphologique et modélisation pour l’optimisation structurelle d’électrodes. Thesis director: D. Jeulin.
- Torben Prill (2012-2014, held in 2014): Caractérisation et modélisation de structures carbonées nanoporeuses. Thesis director: D. Jeulin, M. Spies. ED 432 SMI & Univ. Saarlandes, Allemagne.
- Julie Escoda (2010-2012, held in 2012): Modélisation morphologique et micromécanique 3D de matériaux cimentaires. Thesis director: D. Jeulin.

- Hellen Altendorf (2009-2011, held in 2011): 3D morphological analysis and modeling of random fiber networks: applied on glass fiber reinforced composites. Thesis directors: D. Jeulin, R. Korn. ÉD en cotutelle Paris ENSMP & Univ. Kaiserslautern, Allemagne.

- Aurélie Jean (2007-2009, held in 2009) : étude d'un élastomère chargé, de sa nanostucture à son macro-comportement. Thesis directors: D. Jeulin, S. Forest.

Defenses to be held

- Hugo Launay (started in 2018): Modèles réduits par apprentissage automatique pour l'étude de la nocivité de défauts, Z-ROM Z-learn. Thesis directors: D. Ryckelynck & J. Besson.

- Élodie Kaeshammer (started in 2017): Étude expérimentale et numérique de la sensibilité de matériaux énergétiques (provisional title). Thesis director: P. Dokladal.

- François Rabette (started in 2018): Prise en compte de l'endommagement pour la construction d'un outil de simulation thermomécanique à l'échelle de la microstructure (provisional title). Thesis directors: P. Dokaldal & H. Trumel.

- Laurent Lacourt (started in 2016, defense to be held Oct. 14): Étude numérique de la nocivité des défauts dans les soudures. Thesis directors: S. Forest, D. Ryckelynck.

- Victor-Manuel Monclus (defense planed in 2019): Fabrication et étude de fibres piézoélectriques pour textiles auto-énergétiques (provisional title). Thesis directors: J. Renard, J.-F. Hochepied.

- Lucie Baudin (started in 2017): Structuration de surfaces par technologie Laser pour applications ultra-vide dans l'environnement des accélérateurs de particules (provisional title). Thesis director: M. Jeandin.

Collaborations with other PhD students (no thesis supervision)

- François Cadiou: "Étude de l'impact de la microstructure sur les propriétés électriques des batteries Lithium-Ion" (provisional title). Thesis director: É. Maire.

- Matthias Neumann (ongoing). Thesis director: V. Schmidt.

- Grace Ham (2015-2018): "Propriétés physico-chimiques des oxydes de surface et analyse des données de l'imagerie hyperspectrale" (defense held in 2018). Thesis directors: C. Carteret & J. Angulo. É.D. Université de Lorraine.

Supervision of master students in the context of internships All master students have published their work in scientific journals (see Sec. C), except current internships.

- Siyuan Zhang (2019, in progress), collaboration with L'Oréal (T. Baldeweck).

- Jean-Baptiste Gasnier (2014), collaboration with CEA le Ripault (H. Trumel).

- Andrea Pietrasanta (2013), collaboration with IFPEN (M. Moreaud).

- Andrey Ambos (2013), collaboration with CEA le Ripault (H. Trumel).
- Amaury Vannier-Moreau (2013), collaboration with CERIB.
- Dario Azzimonti (2012), collaboration with PSA (ANR project).

Various

- Administration of the high-performance computing cluster at the Center for Mathematical Morphology in Mines Paristech, made of 9 racks each with 32 to 128 GB RAM, and inbetween 16 and 32 cpu cores.
- Webmaster for `http://cmm.ensmp.fr`
- Articles in anthology of comics (Glénat).
- Excellent knowledge of Fortran, latex PHP, matlab, bash, SQL. Sole contributor of FFT Fortran code ($\sim$ 25K lines of code) used in training session and by PhDs students, and author of a PHP interface for a website (roughly $250,000$ visits per day, $\sim$ 40K lines of code).

Appendix C

List of publications

When I have supervised their work, the name of PhD and master students is underlined. Google scholar: `https://scholar.google.fr/citations?user=Gjv6430AAAAJ&hl=en`, Scopus: `https://www.scopus.com/authid/detail.uri?authorId=23981490600`.

Journals

[J1] F. Cadiou, A. Etiemble, T. Douillard, F. Willot, O. Valentin, J.-C. Badot, B. Lestriez, and É. Maire. "Numerical prediction of multiscale electronic conductivity of Lithium-ion battery positive electrodes". In: *Journal of the Electrochemical Society* 166.8 (2019), A1692–A1703.

[J2] M. Neumann, B. Abdallah, L. Holzer, F. Willot, and V. Schmidt. "Stochastic 3D modeling of three-phase microstructures for the prediction of transport properties in solid oxide fuel cells". In: *Transport in Porous Media* 128.1 (2019), pp. 179–200.

[J3] M. Neumann, O. Stenzel, F. Willot, L. Holzer, and V. Schmidt. "Quantifying the influence of microstructure on effective conductivity and permeability: virtual materials testing". In: *International Journal of Solids and Structures* (2019). Accepted March 23. DOI: 10.1016/j.ijsolstr.2019.03.028.

[J4] J. Serra and F. Willot. "Special topic on multiscale modeling of granular media: a tribute to Prof. Dominique Jeulin". In: *Image Analysis & Stereology* 38.1 (2019), pp. 1–2.

[J5] F. Willot. "The effective conductivity of strongly nonlinear media: the dilute limit". In: *International Journal of Solids and Structures* (2019). Accepted June 6. DOI: `10.1016/j.ijsolstr.2019.06.006`.

[J6] F. Willot, R. Brenner, and H. Trumel. "Elastostatic field distributions in polycrystals and cracked media". In: *Philosophical Magazine* (2019). Submitted May 9, accepted November 25.

[J7] F. Willot and S. Forest. "Preface to a Special Issue of the International Journal of Solids and Structures on Physics and Mechanics of Random Structures: From Morphology to Material Properties". In: *International Journal of Solids and Structures* (2019).

[J8] F. Willot, H. Trumel, and D. Jeulin. "The thermoelastic response of cracked polycrystals with hexagonal symmetry". In: *Philosophical Magazine* 99.5 (2019), pp. 606–630.

[J9] V. Bortolussi, B. Figliuzzi, F. Willot, M. Faessel, and M. Jeandin. “Morphological modeling of cold spray coatings”. In: *Image Analysis & Stereology* 37.2 (2018), pp. 145–158.

[J10] J.-B. Gasnier, F. Willot, H. Trumel, D. Jeulin, and J. Besson. “Thermoelastic properties of microcracked polycrystals. Part I: Adequacy of Fourier-based methods for cracked elastic bodies”. In: *International Journal of Solids and Structures* 155 (2018), pp. 248–256.

[J11] J.-B. Gasnier, F. Willot, H. Trumel, D. Jeulin, and M. Biessy. “Thermoelastic properties of microcracked polycrystals. Part II: The case of jointed polycrystalline TATB”. In: *International Journal of Solids and Structures* 155 (2018), pp. 257–274.

[J12] H. Wang, D. Jeulin, F. Willot, L. Sorbier, and M. Moreaud. “Modelling of the microstructure of mesoporous alumina constrained by morphological simulation of nitrogen porosimetry”. In: *Colloids and Surfaces A: Physicochemical and Engineering Aspects* 553 (2018), pp. 378–396.

[J13] T. Prill, D. Jeulin, F. Willot, J. Balach, and F. Soldera. “Prediction of Effective Properties of Porous Carbon Electrodes from a Parametric 3D Random Morphological Model”. In: *Transport in Porous Media* 120.1 (2017), pp. 141–165.

[J14] H. Wang, F. Willot, M. Moreaud, Rivallan M., Sorbier L., and D. Jeulin. “Numerical simulation of hindered diffusion in $\gamma-$alumina catalyst supports”. In: *Oil & Gas Science and Technology* 72.2 (2017).

[J15] F. Willot. “Mean covariogram of cylinders and applications to Boolean random sets”. In: *Journal of Contemporary Mathematical Analysis* 52.6 (2017), pp. 305–315.

[J16] B. Abdallah, F. Willot, and D. Jeulin. “Morphological modeling of three-phase microstructures of anode layers using SEM images”. In: *Journal of Microscopy* 263.1 (2016), pp. 51–63.

[J17] J. Escoda, F. Willot, D. Jeulin, J. Sanahuja, and C. Toulemonde. “Influence of the multiscale distribution of particles on elastic properties of concrete”. In: *International Journal of Engineering Science* 98 (2016), pp. 60–71.

[J18] B. Figliuzzi, D. Jeulin, M. Faessel, F. Willot, M. Koishi, and N. Kowatari. “Modelling the microstructure and the viscoelastic behaviour of carbon black filled rubber materials from 3D simulations”. In: *Technische Mechanik* 36.1–2 (2016), pp. 22–46.

[J19] F. Willot, B. Abdallah, and D. Jeulin. “The permeability of Boolean sets of cylinders”. In: *Oil & Gas Science and Technology* 71.2 (2016).

[J20] B. Abdallah, F. Willot, and D. Jeulin. “Stokes flow through a Boolean model of spheres: Representative volume element”. In: *Transport in Porous Media* 109.3 (2015), pp. 711–726.

[J21] A. Ambos, F. Willot, D. Jeulin, and H. Trumel. “Numerical modeling of the thermal expansion of an energetic material”. In: *International Journal of Solids and Structures* 60–61 (2015), pp. 125–139.

[J22] E. Couka, F. Willot, P. Callet, and D. Jeulin. “Optical response of a hematite coating: ellipsometry data vs. Fourier-based computations”. In: *Advanced Science, Engineering and Medicine* 7.11 (2015), pp. 925–931.

[J23] E. Couka, F. Willot, and D. Jeulin. “A mixed Boolean and deposit model for the modeling of metal pigments in paint layers”. In: *Image Analysis & Stereology* 34.2 (2015), pp. 125–134.

[J24] E. Couka, F. Willot, and D. Jeulin. “Corrigendum: a mixed Boolean and deposit model for the modeling of metal pigments in paint layers”. In: *Image Analysis & Stereology* 34.3 (2015), p. 145.

[J25] E. Couka, F. Willot, D. Jeulin, M. Ben Achour, A. Chesnaud, and A. Thorel. “Modeling of the Multiscale Dispersion of Nanoparticles in a Hematite Coating”. In: *Journal of Nanoscience and Nanotechnology* 15.5 (2015), pp. 3515–3521.

[J26] J. Escoda, D. Jeulin, F. Willot, and C. Toulemonde. “3D morphological modeling of concrete using multiscale Poisson polyhedra”. In: *Journal of Microscopy* 258.1 (2015), pp. 31–48.

[J27] J.-B. Gasnier, F. Willot, H. Trumel, B. Figliuzzi, D. Jeulin, and M. Biessy. “A Fourier-based numerical homogenization tool for an explosive material”. In: *Matériaux & Techniques* 103.3 (2015), p. 308.

[J28] H. Wang, A. Pietrasanta, D. Jeulin, F. Willot, M. Faessel, Sorbier L., and M. Moreaud. “Modeling of mesoporous alumina microstructure by 3D random models of platelets”. In: *Journal of Microscopy* 260.3 (2015), pp. 287–301.

[J29] F. Willot. “Fourier-based schemes for computing the mechanical response of composites with accurate local fields”. In: *Comptes Rendus Mécanique* 343.3 (2015), pp. 232–245.

[J30] F. Willot. “The power laws of geodesics in some random sets with dilute concentration of inclusions”. In: *Lecture Notes in Computer Science* 9082 (2015), pp. 535–546.

[J31] H. Altendorf, D. Jeulin, and F. Willot. “Influence of the fiber geometry on the macroscopic elastic and thermal properties”. In: *International Journal of Solids and Structures* 51.23 (2014), pp. 3807–3822.

[J32] F. Willot, B. Abdallah, and Y.-P. Pellegrini. “Fourier-based schemes with modified Green operator for computing the electrical response of heterogeneous media with accurate local fields”. In: *International Journal for Numerical Methods in Engineering* 98.7 (2014), pp. 518–533.

[J33] D. Azzimonti, F. Willot, and D. Jeulin. “Optical properties of deposit models for paints:full-fields FFT computations and representative volume element”. In: *Journal of Modern Optics* 60.7 (2013), pp. 519–528.

[J34] F. Dunant C., B. Bary, B. Giorla A., C. Péniguel, J. Sanahuja, C. Toulemonde, B. Tran A., F. Willot, and J. Yvonnet. “A critical comparison of several numerical methods for computing effective properties of highly heterogeneous materials”. In: *Advances in Engineering Software* 58 (2013), pp. 1–12.

[J35] F. Willot, L. Gillibert, and D. Jeulin. “Microstructure-induced hotspots in the thermal and elastic responses of granular media”. In: *International Journal of Solids and Structures* 50.10 (2013), pp. 1699–1709.

[J36] J. Escoda, F. Willot, D. Jeulin, J. Sanahuja, and C. Toulemonde. “Estimation of local stresses and elastic properties of a mortar sample by FFT computation of fields on a 3D image”. In: *Cement and Concrete Research* 41.5 (2011), pp. 542–556.

[J37] A. Jean, F. Willot, S. Cantournet, S. Forest, and D. Jeulin. “Large-Scale computations of effective elastic properties of rubber with carbon black fillers”. In: *International Journal for Multiscale Computational Engineering* 9.3 (2011), pp. 271–303.

[J38] F. Willot and D. Jeulin. “Elastic and electrical behavior of some random multiscale highly-contrasted composites”. In: *International Journal for Multiscale Computational Enginneering: special issue on multiscale modeling and uncertainty quantification of heterogeneous materials* 9.3 (2011), pp. 305–326.

[J39] M.I. Idiart, F. Willot, Y.-P. Pellegrini, and P. Ponte Castañeda. “Infinite-contrast periodic composites with strongly nonlinear behavior: effective-medium theory versus full-field simulations”. In: *International Journal of Solids and Structures* 46.18 (2009), pp. 3365–3382.

[J40] F. Willot and D. Jeulin. “Elastic behavior of composites containing boolean random sets of inhomogeneities”. In: *International Journal of Engineering Science* 47.2 (2009), pp. 313–324.

[J41] F. Willot, Y.-P. Pellegrini, M.I. Idiart, and P. Ponte Castañeda. “Effective-medium theory for infinite-contrast two-dimensionally periodic linear composites with strongly anisotropic matrix behavior: dilute limit and crossover behavior”. In: *Physical review B* 78.10 (2008), p. 104111.

[J42] F. Willot, Y.-P. Pellegrini, and P. Ponte Castañeda. “Localization of elastic deformation in strongly anisotropic, porous, linear materials with periodic microstructures: exact solutions and dilute expansions”. In: *Journal of the Mechanics and Physics of Solids* 56.4 (2008), pp. 1245–1268.

Proceedings

[P1] É. Kaeshammer, P. Dokládal, F. Willot, S. Belon, and L. Borne. “Generation of virtual microstructures of energetic materials based on micro-computed tomography images analysis”. In: Online at `https://hal.archives-ouvertes.fr/hal-02139566`. Karlsruhe: Fraunhofer, 2019.

[P2] É. Kaeshammer, P. Dokládal, F. Willot, B. Erzar, S. Belon, and L. Borne. “A morphological study of energetic materials: analysis of micro-computed tomography images to generate representative microstructures”. In: Online at `https://hal.archives-ouvertes.fr/hal-02139567`. Tours: Af3P, 2019.

[P3] L. Lacourt, S. Forest, F. N’Guyen, D. Ryckelynck, F. Willot, S. Flouriot, V. de Rancourt, and A. Thomas. “Étude numérique de la nocivité des défauts dans les soudures”. In: Colloque Mécamat, Aussois, France, January 21-25, 2019. Aussois: Mécamat, 2019.

[P4] L. Lacourt, S. Forest, D. Ryckelynck, F. Willot, S. Flouriot, and V. de Rancourt. “Étude numérique de la nocivité des défauts dans les soudures”. In: Colloque National en Calcul des Structures, Giens, France, May 13-17, 2019. Presqu’île de Giens: Computational Structural Mechanics Association, 2019.

[P5] F. Rabette, H. Trumel, and F. Willot. “Modélisation multiéchelle par champ de phase de la microfissuration d’un polycristal organique de forte anisotropie cristalline par FFT”. In: Colloque National en Calcul des Structures, Giens, France, May 13-17, 2019. Presqu’île de Giens: Computational Structural Mechanics Association, 2019.

[P6] F. Rabette, F. Willot, and H. Trumel. “Homogénéisation en champs complets par FFT pour un matériau énergétique à forte anisotropie cristalline : prise en compte de la microfissuration par une méthode de champ de phase”. In: Colloque Mécamat, Aussois, France, January 21-25. Online at `https://hal.archives-ouvertes.fr/hal-02311629`. Aussois: Mécamat, 2019.

[P7] H. Trumel, F. Rabette, F. Willot, R. Brenner, E. Ongari, M. Biessy, and D. Picart. “Understanding the thermomechanical behavior of a TATB-based explosive via microstructure-level simulations. Part I: Microcracking and viscoelasticity”. In: Europyro 2019. 44th International Pyrotechnics Seminar, Tours, France, June 3–7. Online at `https://hal.archives-ouvertes.fr/hal-02312483`. Tours: Af3P, 2019.

[P8] F. Cadiou, F. Willot, B. Lestriez, J. Adrien, T. Douillard, O. Valentin, and E. Maire. “Étude de l’impact de la microstructure sur les propriétés électriques des batteries lithium-ion : simulations de microstructures réelles et génération d’architectures numériques”. In: Colloque Mécamat, Aussois, France, January 22-26, 2018. `https://hal.archives-ouvertes.fr/hal-01965255`. Aussois: Mécamat, 2018.

[P9] É. Kaeshammer, B. Erzar, S. Belon, F. Willot, P. Dokládal, J. Corbel, and L. Borne. “Étude expérimentale et numérique de la sensibilité de compositions énergétiques : influence de la microstructure et rôle de l’endommagement”. In: Colloque Mécamat, Aussois, France, January 22-26, 2018. `https://hal.archives-ouvertes.fr/hal-01678704`, accessed January 8, 2018. Aussois: Mécamat, 2018.

[P10] L. Lacourt, S. Forest, F. N’Guyen, D. Ryckelynck, F. Willot, S. Flouriot, V. de Rancourt, and A. Thomas. “Étude numérique de la nocivité des défauts dans les soudures”. In: Colloque Mécamat, Aussois, France, January 22-26, 2018. `https://hal.archives-ouvertes.fr/hal-01678669`, accessed January 8, 2018. Aussois: Mécamat, 2018.

[P11] M. Koishi, N. Kowatari, B. Figliuzzi, M. Faessel, F. Willot, and D. Jeulin. “Computational material design of filled rubbers using multi-objective design exploration”. In: *Proceedings of the European Conference on Constitutive Models for Rubbers X (ECCMR), Munich, Germany (A. Lion, M. Johlitz eds).* Vol. 10. Online at `https://hal.archives-ouvertes.fr/hal-01609886`. CRC Press, 2017, pp. 467–472.

[P12] L. Lacourt, B. Figliuzzi, S. Forest, D. Ryckelynck, F. Willot, S. Flouriot, V. de Rancourt, and A. Thomas. “Étude de la nocivité des défauts dans les soudures et les pièces obtenues par fabrication additive”. In: Colloque Mécamat, Aussois, France, January 23-27, 2017. `https://hal.archives-ouvertes.fr/hal-01678663`, accessed January 8, 2018. Aussois: Mécamat, 2017.

[P13] V. Bortolussi, F. Borit, A. Chesnaud, M. Jeandin, M. Faessel, B. Figliuzzi, F. Willot, K. Roche, and G. Surdon. “Cold spray of metal-polymer composite coatings onto Carbon Fiber-Reinforced Polymer (CFRP)”. In: vol. 324. Proceedings of the International Thermal Spray Conference (ITSC), Shangai, China, May 10-12, 2016. `https://hal.archives-ouvertes.fr/hal-01337696`, accessed June 30, 2016. Shanghai: Deutscher Verlag für Schweisstechnik, 2016, p. 26.

[P14] J.-B. Gasnier, B. Figliuzzi, M. Faessel, F. Willot, D. Jeulin, and H. Trumel. “3D Morphological modeling of a polycrystaline microstructure with non-convex, anisotropic grains”. In: *Acta Stereologica: Proceedings of the 14th International Congress for Stereology and Image Analysis (ICSIA), Liège, July 7-10*. Online at `https://hal.archives-ouvertes.fr/hal-01184811`. 2015.

[P15] D. Masson, B. Abdallah, F. Willot, D. Jeulin, E. Mercadelli, A. Sanson, A. Chesnaud, and A. Thorel. “Morphological modeling of a metal foam SOFC configuration”. In: *ECS Transactions*. Vol. 68. 1. Online at `https://hal.archives-ouvertes.fr/hal-01142056`. Conference on Electrochemical Energy Conversion & Storage with SOFC-XIV, Glasgow, Scotland, July 26-31, 2015. 2015, pp. 2951–2960.

[P16] A. Ambos, H. Trumel, F. Willot, D. Jeulin, and M. Biessy. “A fast Fourier transform micromechanical upscaling method for the study of the thermal expansion of a TATB-based pressed explosive”. In: *Proceedings of the 15th International Detonation Symposium, San Francisco, CA, July 13-18*. Online at `https://hal.archives-ouvertes.fr/hal-1097110`. 2014.

[P17] F. Willot. “Numerical homogenization of random media: the FFT method”. In: Colloque Mécamat, Aussois, France, January 20-24, 2014. `https://hal.archives-ouvertes.fr/hal-01940408`, accessed December 1, 2018. Aussois: Mécamat, 2014.

[P18] J. Escoda, D. Jeulin, and F. Willot. “Simulation of 3D granular media by multiscale random polyhedra”. In: *Proceedings of the International Congress of Stereology (ICS11), Beijing*. Online pre-print: `https://hal.archives-ouvertes.fr/hal-00879260`. 2011.

[P19] J. Escoda, F. Willot, D. Jeulin, J. Sanahuja, and C. Toulemonde. “3D morphological analysis of local elastic fields in a cementitious material”. In: *Advances in Structural Engineering and Mechanics (ASEM11), Seoul*. Online pre-print: `https://hal.archives-ouvertes.fr/hal-00879268`. 2011.

[P20] F. Willot, L. Gillibert, and D. Jeulin. “Étude numérique par FFT et analyse morphologique 3D des points chauds dans les milieux granulaires”. In: *20ème Congrès Français de Mécanique, 28 août/2 sept. 2011-25044 Besançon, France (FR)*. Online at `https://hal.archives-ouvertes.fr/hal-00878998`. Association française de mécanique, PUF de Franche-Comté, 2011, pp. 574–579.

[P21] F. Willot and Y.-P. Pellegrini. “Fast Fourier Transform computations and build-up of plastic deformation in 2D, elastic-perfectly plastic, pixelwise-disordered porous media”. In: *D. Jeulin, S. Forest (eds), “Continuum Models and Discrete Systems CMDS 11”*. Online at `https://arxiv.org/abs/0802.2488`. Paris: École des Mines, 2008, pp. 443–449.

Book chapters

[C1] A. Vannier-Moreau, F. Willot, and D. Jeulin. "Thermal and linear-elastic properties of lightweight concrete". In: *Physics & Mechanics of Random Media: from Morphology to Material Properties.* Ed. by S. Willot F. & Forest. Online at `http://www.cmm.mines-paristech.fr/~willot/publi2018a.pdf`. Paris: Presses des Mines (ISBN 978-2-35671-529-6), 2018. Chap. 20, pp. 169–176.

[C2] F. Willot and S. Guessasma. "Linear-elastic response of starch-based materials: FFT results vs. experimental data". In: *Physics & Mechanics of Random Media: from Morphology to Material Properties.* Ed. by S. Willot F. & Forest. Online at `http://www.cmm.mines-paristech.fr/~willot/publi2018b.pdf`. Paris: Presses des Mines (ISBN 978-2-35671-529-6), 2018. Chap. 21, pp. 177–180.

[C3] F. Willot and D. Jeulin. "The nonlinear response of Boolean models: elasticity and conductivity". In: *Physics & Mechanics of Random Media: from Morphology to Material Properties.* Ed. by S. Willot F. & Forest. Online at `http://www.cmm.mines-paristech.fr/~willot/publi2018d.pdf`. Paris: Presses des Mines (ISBN 978-2-35671-529-6), 2018. Chap. 22, pp. 181–186.

Book (as editor)

[B1] F. Willot and S. Forest. *Physics & Mechanics of Random Media: from Morphology to Material Properties. A tribute to Dominique Jeulin's contributions to science, research and teaching.* International Workshop in honor of D. Jeulin. Saint-Pierre d'Oléron, France, June 17–22. ISBN 2356715290. Paris: Presses des Mines, 2018.

PhD thesis

[T1] F. Willot. "Localization in random media and its effect on the homogenized behavior of materials". Habilitation à diriger des recherches en Sciences pour l'Ingénieur. Sorbonne Université, 2019.

[T2] F. Willot. "Contribution à l'étude théorique de la localisation plastique dans les poreux". PhD thesis. École Polytechnique, 2007.

Miscellaneous

[M1] V. Bortolussi, B. Figliuzzi, F. Willot, M. Faessel, and M. Jeandin. *Electrical conductivity of metal-polymer cold spray composite coatings onto Carbon Fiber-Reinforced Polymer.* Journal of Thermal Spray Technology. Submitted May 22. 2019.

[M2] É. Kaeshammer, F. Willot, P. Dokládal, L. Borne, B. Erzar, and S. Belon. *Analysis of micro-computed tomography images to generate representative granular microstructures.* Manuscript in preparation. 2019.

[M3] F. Willot. *Caractérisation et modélisation probabiliste de milieux hétérogènes.* To appear in “Ingénierie mécanique en contexte incertain – Des approches classiques à quelques développements récents”, ISTE Science Pub. 2019.

[M4] Y.-P. Pellegrini and F. Willot. *Generalized two-body self-consistent theory of random linear dielectric composites: an effective-medium approach to clustering in highly-disordered media.* Online at `https://arxiv.org/abs/1206.0857`. 2012.

Achevé d'imprimer le 9 octobre 2019
par les bons soins de l'École des Mines de Paris

This work is a study in theoretical mechanics devoted to homogenization problems in the context of degenerate (non-strictly convex) local response of one of the phases, which can serve as idealized models for porous or rigidly-reinforced materials exhibiting perfectly-plastic behavior. In these situations plastic flow preferentially concentrates along shear bands; as a result the material effective response is governed by those regions within the material where the field localizes. A form of localization also occurs in linear problems governed by asymptotically hyperbolic partial derivative equations, where the strain field is found to develop banding patterns. The solutions are relevant to strongly-anisotropic elastic or thermoelastic media. Such a linear problem is studied in the present work in the context of a random microstructure, specifically a polycrystal containing cracks. A related topic is whether incipient localization may develop as a result of the microstructure itself. This question is investigated in the case of a Stokes flow occurring in a porous medium around a set of obstacles exhibiting unusual spatial distribution, characterized by long-range correlations. The different model problems are addressed by means of various techniques. Limit analysis bounds are combined with integral geometry to provide insight on the material behavior. Comparisons with rigorous bounds and estimates of homogenization theories, and full-field "Fourier-based" numerical results, allow us to interpret and assess the response of certain random microstructures. Although a complete solution is out-of-reach, the interplay between field localization and microstructure is elucidated in specific cases.